Thomas Bank

Performance and aging analysis of high-power lithium titanate oxide cells for low-voltage vehicle applications

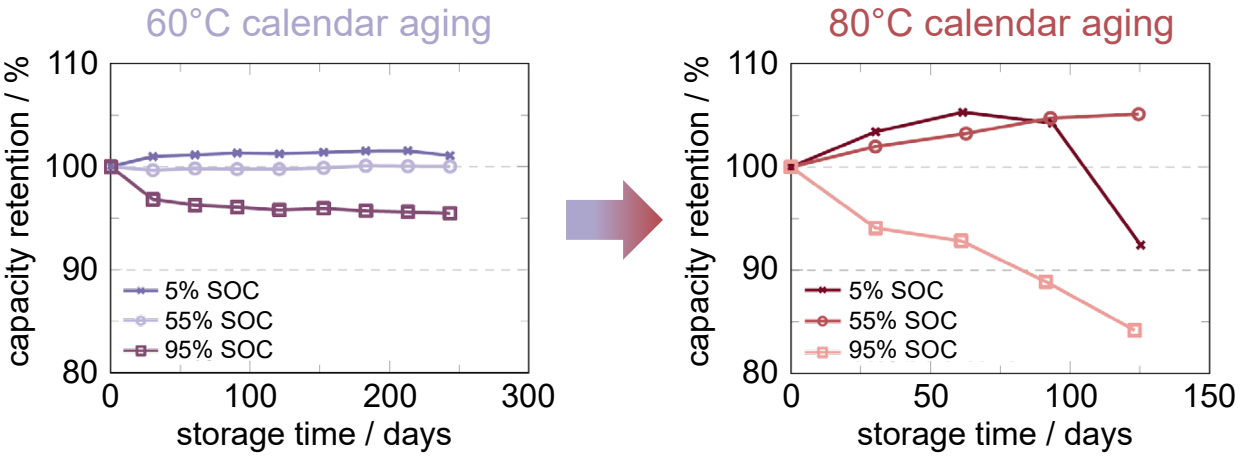

Aachener Beiträge des ISEA Band 160

Performance and Aging Analysis of High-Power Lithium Titanate Oxide Cells for Low-Voltage Vehicle Applications

Von der Fakultät für Elektrotechnik und Informationstechnik
der Rheinisch-Westfälischen Technischen Hochschule Aachen
zur Erlangung des akademischen Grades eines Doktors der
Ingenieurwissenschaften genehmigte Dissertation

vorgelegt von

Thomas Bank, M. Sc.
aus Herford

Berichter:
Univ.-Prof. Dr. rer. nat. Dirk Uwe Sauer
Univ.-Prof. Dr.-Ing. Andreas Jossen

Tag der mündlichen Prüfung: 29. September 2021

AACHENER BEITRÄGE DES ISEA
Vol. 160

Editor:
Univ.-Prof. Dr. ir. Dr. h. c. Rik W. De Doncker
Director of the Institute for Power Electronics and Electrical Drives (ISEA)
RWTH Aachen University

ISSN 1437-675X

Institute for Power Electronics and Electrical Drives (ISEA)
RWTH Aachen University
Jaegerstr. 17/19 • 52066 Aachen • Germany
Tel: +49 (0)241 80-96920
Fax: +49 (0)241 80-92203
post@isea.rwth-aachen.de

Vorwort

Diese Dissertation entstand im Rahmen eines Forschungsprojekts zwischen dem Institut für Stromrichtertechnik und Elektrische Antriebe (ISEA) der RWTH Aachen und der BMW AG. Im Folgenden möchte ich den Personen danken, die essentiellen Anteil am Gelingen dieser Arbeit hatten.

Mein besonderer Dank gilt meinem Doktorvater Prof. Dr. Dirk Uwe Sauer, der mich von der Bachelor-, über die Master- bis hin zur Doktorarbeit fachlich betreut und in vielen gemeinsamen Stunden meine Forschungsvorhaben mit mir diskutiert hat. Prof. Sauer weckte meine Begeisterung für die Batterietechnik und ich bewundere sein außerordentliches Engagement bei der Betreuung von Studierenden. Zudem danke ich Prof. Dr. Andreas Jossen für die Übernahme des Korreferats.

In den vergangenen drei Jahren habe ich bei BMW in der Entwicklung der Niedervoltspeicher nicht nur interessante und vielfältige Entwicklungsprojekte kennenlernen dürfen, sondern bin in ein unheimlich sympathisches, kompetentes und äußerst humorvolles Team aufgenommen worden. Ich danke dem gesamten Team für die wunderschöne Zeit, die vielen wertvollen Eindrücke und die emotionale Unterstützung. Mein ganz besonderer Dank gilt meinem Teamleiter Jürgen Ringler und meinen fachlichen Mentoren Dr. Sebastian Klamor und Dr. Nicholas Löffler. Alle drei haben mich zu jeder Zeit unterstützt und sich dafür eingesetzt, dass genügend Freiraum zur Erstellung dieser Dissertation und der damit verbundenen Publikationen zur Verfügung stand.

Auch wenn diese Arbeit größtenteils in München verfasst wurde, herrschte ein reger wissenschaftlicher und persönlicher Austausch im Rahmen des Forschungsprojekts und bei allen dissertationsrelevanten Themen. Für all die inhaltlichen Diskussionen und die hervorragende Zusammenarbeit möchte ich Stephan Bihn, Dominik Jöst, Florian Ringbeck, Matthias Kuipers, Lennart Alsheimer, Felix Hildenbrand und Meinert Lewerenz danken. Meinerts Erkenntnisse zum „Passive Electrode Effect“ haben mich während meiner Masterarbeit sehr begeistert. Umso mehr freut es mich, mit meiner Dissertation auf seinen Erkenntnissen aufzubauen und dieses Themengebiet weiterzuentwickeln.

Das Gelingen dieser Arbeit ist zu großen Teilen auf die Unterstützung meines Freundeskreises und meiner Familie zurückzuführen. Insbesondere danke ich meiner Freundin Carolin Imbery und meinen besten Freunden Christian Hövels und Marc Altherr. Eure offenen Ohren, die aufmunternden Worte und die vielmals dringend nötige Ablenkung waren essentieller Erfolgsbestandteil. Ich danke meiner Mutter Gabriele und meinem Patenonkel Heinz für all die liebevolle Unterstützung und das Ermöglichen dieses Bildungsweges. Abschließend geht ein großer Dank an meine Schwester Claudia, die mir sowohl emotional als auch fachlich zur Seite stand und für mich seit eh und je ein großes Vorbild ist.

Abstract

Partial electrification of vehicles with conventional combustion engines offers an effective and necessary method for efficiency enhancement and CO_2 emission reduction. One way of adding a so-called mild hybridization to existing vehicle architectures is to extend the conventional 12 V vehicle electrical system by a 48 V voltage level containing a 48 V lithium-ion battery. In addition to the low system costs, this low-to-medium degree of electrification is widely accepted by customers due to the absence of range anxiety and non-required external charging. Purpose of this lithium-ion battery is to recover braking energy and to provide both short-term boost power and energy supply for the vehicle electrical system. Therefore, application-specific requirements such as high-power capability, cycle stability and temperature robustness need to be fulfilled. Despite the rapidly increasing market share of mild-hybrid vehicles, studies of real-world battery loads of vehicles with 48 V system are lacking. Same applies for detailed research results of high-power optimized lithium-ion cells applicable in such mild hybrid vehicle applications.

A promising anode material for such an application is lithium titanate oxide (LTO), which possesses several outstanding material properties including high-power capability, inherent safety and excellent lifetime performance. However, its market availability is comparatively low, as graphite-based cells with higher specific energy density dominate the consumer market. Aging mechanisms of LTO-based lithium-ion batteries are highly controversial and still not fully understood. Known degradation effects of LTO are state of charge (SOC) dependent and strongly accelerated at high temperatures. Extensive scientific studies on mass-produced LTO-based cells are rare, resulting in a lack of essential information on performance and aging behavior of LTO-based cells.

Consequently, through extensive experimental measurements of characteristic mild-hybrid operating points, this thesis aims to assess the suitability of an LTO-based cell type for low voltage vehicle systems by revealing essential performance and aging characteristics.

Real-world battery data from mild hybrid electric vehicles are examined and both characteristic and critical operating conditions of 48 V batteries are derived. The 48 V battery in the investigated system typology is operated in a very wide temperature range (−20 °C to 70 °C) with extremely high average temperatures. In addition, it is mainly burdened with small cycle depths (< 5%), high dynamic current loads (more than 20C) and high energy throughputs over lifetime (> 20,000 equivalent full cycles). Based on these application-specific stress factors, the performance of a 10 Ah nickel manganese cobalt oxide|lithium titanate oxide (NMC|LTO) cell is thoroughly investigated and benchmarked against two high-power graphite-based cells with regard to the sensible begin-of-life parameters open circuit voltage, internal resistance and capacity. A pronounced SOC dependency of the internal resistance of the NMC|LTO cell reduces its power capability, extractable cell capacity

and energy efficiency. This cell, in contrast to the graphite-based cells, exhibits marginal Butler-Volmer dependency and offers high charge acceptance at negative temperatures, which positively affects the CO_2 savings potential.

Cyclic, calendar and drive cyclic aging regimes are defined and applied on a total of 39 NMC|LTO cells. The LTO-based cells show an excellent cycle stability for shallow cycles, even at high ambient temperatures and high current rates. Rise in internal resistance under calendar aging condition has the most detrimental influence on cell lifetime. The aging study demonstrates that the investigated cell is able to meet the vehicle relevant lifetime requirements of 200,000 km. For calendar aging, a part of the SOC dependent capacity retention is attributed to charge equalization processes between active and passive electrode regions. Using a novel descriptive explanatory model, it is illustrated that the passive electrode effect causes a shift in the operating voltage potential of one or both electrode materials. This shift corresponds to a change in electrode balancing. Thus, depending on the potential curves and voltage limits, the extractable cell capacity varies. The analysis of capacities in constant voltage charge phases reveals that equalization processes induced by the passive electrode effect lead to inhomogeneous lithiation of the active material.

To further investigate temperature and SOC dependent aging mechanisms of the NMC|LTO cells, incremental capacity analyses and postmortem examinations are performed that include cell opening, coin cell assembly with aged electrode material and surface examinations. 80 °C storage temperature leads to intense gas formation and a superposition of different degradation modes. These modes are identified in the incremental capacity analysis as predominantly loss of lithium inventory and loss of active material at the positive electrode. At low and medium SOC, the residual cell capacity increases, which is attributable to both added capacity at higher cell voltages caused by extension of the LTO potential plateau and a pronounced passive electrode effect. Irreversible degradation of cell materials is most severe at high SOCs. Surface layer formation is observed on both LTO and NMC, though its composition differs, and its thickness rises with increasing SOC.

For an investigation of the reversibility of capacity effects at 60 °C calendar aging, a passive electrode effect is intentionally induced in ongoing calendar aging tests by changing the storage SOC. Based on the capacity retention, full reversibility of the passive electrode effect is demonstrated. Analysis of the floating currents for maintaining constant cell voltage reveals intensified side reactions at the beginning of the storage phases following a change to higher SOC. These side reactions and thus a distinct drop in capacity occurred only once even with repeated SOC changes. Since the LTO material was limiting the extractable cell capacity, the results confirm the formation of a passivating surface layer on the LTO surface despite the characteristic LTO potential of 1.55 V.

Contents

1 Introduction and motivation

> *"If you always do what you've always done, you'll always get what you've always got."*
>
> – Henry Ford

The automotive industry is facing the biggest transformation in decades. The European Commission's restrictive CO_2 legislation, motivated by rapidly intensifying climate change, forces car manufacturers to reduce their vehicle fleets' emissions. By 2021, a fleet-wide 95 $\frac{g}{km}$ target needs to be met with heavy penalties for non-compliance. By 2030, a further 37.5% reduction compared to the target in 2021 is mandatory [1]. However, given the urgency of mitigating global warming, a tightening of this regulation remains likely. With conventional internal combustion engines, achieving the 2021 targets is ruled out due to thermodynamic limits [2]. A sufficient enhancement in efficiency requires either partial or full electrification of the powertrain. As the quote from Henry Ford emphasizes, it is more important than ever for established car manufacturers to act with an eye to the future and to grow beyond the profound long-term expertise and accomplishments associated with the internal combustion engine.

The transformation to full vehicle electrification requires both sufficient time to market and supply chain capabilities, along with other external factors such as a broad charging infrastructure and a stable energy supply. Ultimately, customer acceptance and thus the interplay between supply and demand is decisive for the rapidity and the success of vehicle electrification [3].

Mild hybridization, meaning partial electrification of the powertrain, represents a cost-effective enabler supporting this transformation process in the short term while maintaining mass acceptance [4]. One way of adding mild hybridization to existing vehicle architectures is to extend the conventional 12 V vehicle electrical system by a 48 V voltage level containing a 48 V lithium-ion battery [5]. The primary purpose of the 48 V system is to recover braking energy to enhance the overall efficiency of the vehicle [6].

Lithium-ion batteries suitable for such an application need to provide high volumetric as well as gravimetric power density due to limited installation space and high braking power. Compared to conventional 12 V lead-acid batteries, 48 V lithium-ion batteries are expected to last as long as the vehicle itself. Compliance with both performance and lifetime requirements needs to be ensured during all development phases of the battery. Non-specific synthetic standard cycles are not suitable for evaluating the relevant operating points and application-specific lifetime performance. For example, testing full cycles at low current rates results most likely in different lifetimes than small cycle depths at high

current rates [7]. Application-oriented lifetime testing always requires detailed information on real-world battery loads, which is difficult to obtain for novel technologies with initially low market penetration [8].

Lithium titanate oxide (LTO) is a promising electrode material for mild-hybrid applications that possesses several outstanding material properties including high power capability, inherent safety and excellent lifetime performance [9]. However, its market availability is comparatively low, as graphite-based cells with higher specific energy density dominate the consumer market [10]. Detailed scientific studies on mass-produced LTO-based cells are scarce [11]. In particular, for a potential application in a 48 V system, experimental studies are needed to identify critical operating conditions and to provide an in-depth understanding of the cell aging behavior.

In this thesis, the following research questions are of primary interest:

- What are characteristic operating conditions of a 48 V battery in a mild-hybrid application? Of these operating conditions, which are critical stress factors that negatively affect cell lifetimes?
- How does the LTO-based cell perform considering these stress factors? Can the cell meet application-specific begin-of-life and end-of-life performance requirements?
- What are the most critical stress factors that limit the lifetime of the LTO-based cell?
- Which aging effects (reversible and irreversible) occur and how dominant are they? By using non-destructive and destructive methodologies, which characteristic aging mechanisms can be identified and what is their impact on the active materials?

Figure 1.1 depicts the structure of this thesis. At the beginning of Chapter 2, the fundamentals of lithium-ion cells are introduced. An overview of design, working principle and cell materials is given. In addition, emphasis is placed on the difference between high-power and high-energy optimized cells. Essential aging mechanisms in lithium-ion cells are described, mainly focusing on lithium-titanate based cells. Finally, criticalities and limitations of aging lithium-ion cells are highlighted.

Chapter 3 elaborates performance-relevant and aging-relevant battery parameters from application-specific load scenarios. As an introduction, basics of low-voltage vehicle electrical systems are outlined. The demand for extending the conventional 12 V voltage level by a 48 V voltage level along with the associated system changes and function enhancements are explained. Based on the analysis of real-world vehicle data, stress factors of a 48 V battery are characterized. This chapter serves as the basis for the performance and aging analysis and defines the key operating points for the cell tests.

Full details on the conducted experiments and applied methods during the course of this thesis are given in Chapter 4. Specifications of the investigated cells, the test benches and the test procedures are provided. Different methods for detailed aging analysis are presented, either based on electrical measurements by regular check-ups or after destructive cell opening followed by dedicated material examination.

Chapter 5 presents a comprehensive comparison of the results of characterization measurements of the LTO-based cell with two other high-power optimized graphite-based cells. The electrical test results both under load-free condition and under high dynamic load are compared and discussed. Based on the begin-of-life performance, the suitability of the investigated cells for use in a 12 V/48 V low voltage vehicle application is evaluated.

This thesis focuses on the analysis of the aging behavior of the LTO-based cell, which is presented in Chapters 6, 7 and 8. Chapter 6 shows the results of the calendar, cyclic, and driving cyclic aging tests separated by each of the relevant stress factors. The impact of the stress factors on the degradation behavior of the cells is assessed and lifetime critical factors are highlighted. Using an explanatory model, the effect of passive electrode areas on electrode operating potentials and extractable cell capacities is illustrated. Finally, it is evaluated if vehicle relevant lifetime requirements can be met with the investigated LTO-based cell.

An in-depth investigation of the effects of calendar aging at a storage temperature of 80 °C and different states of charge is carried out in Chapter 7. An incremental capacity analysis allows for the separation of dominant degradation modes. Aged cells were opened to perform further material studies. Pictures of this cell opening are shown and aging-related material changes are discussed. The measurement of half-cells with aged cell material as well as an investigation of the morphology of this material enable additional insights into degradation effects such as the formation of a cover layer.

The capacity retention during aging tests depends on reversible as well as irreversible capacity effects. In Chapter 8, a differentiation of reversible and irreversible effects is achieved by intentionally adjusting the state of charge during calendar aging at 60 °C. In addition, data from the calendar aging phases and the regular check-ups are used to distinguish between one-time and permanent degradation effects.

This thesis ends in Chapter 9 with a summary of the main findings. Further research topics and open issues are discussed in a brief outlook.

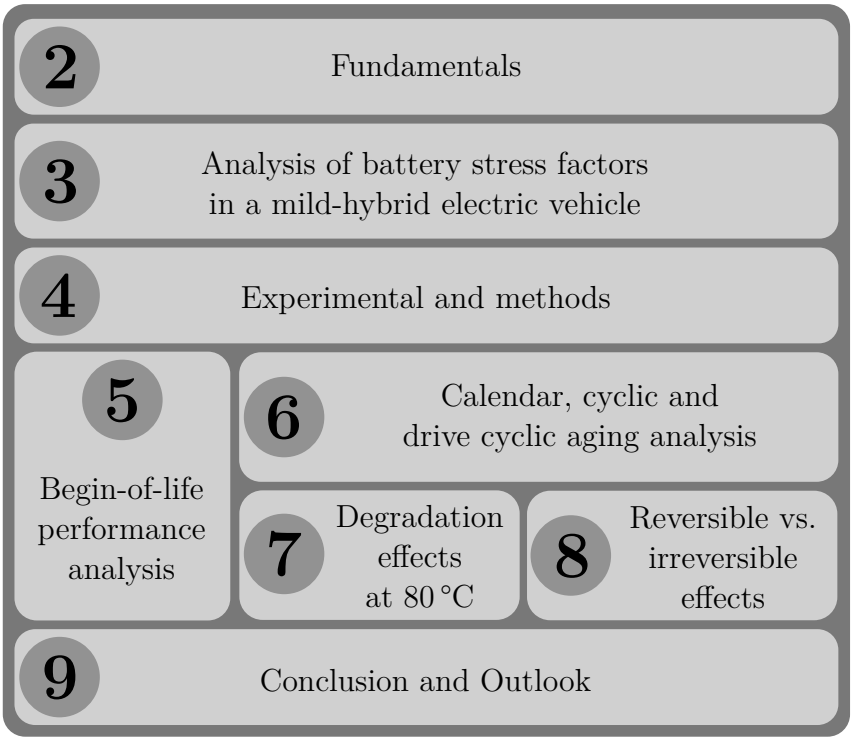

Figure 1.1: Structure of this dissertation on performance and aging behavior of lithium titanate oxide based cells.

2 Fundamentals of lithium-ion batteries

Lithium-ion batteries have become the leading energy storage technology in a variety of applications. No matter whether smartphones, wireless headphones, or electric vehicles, lithium-ion batteries offer a wide area of application and optimization potential in terms of size, performance and safety. A Ragone diagram comparing the performance characteristics of different energy storage systems is shown in Figure 2.1. Lithium-ion technology provides the greatest range of energy and power density. Despite an anti-proportional relationship between energy and power density, lithium-ion batteries are leading in combining both factors. Due to intensive development activities in the field of lithium-ion technology, electrochemical, production-related and design limitations continue to expand, allowing for the depicted area to grow continuously [12].

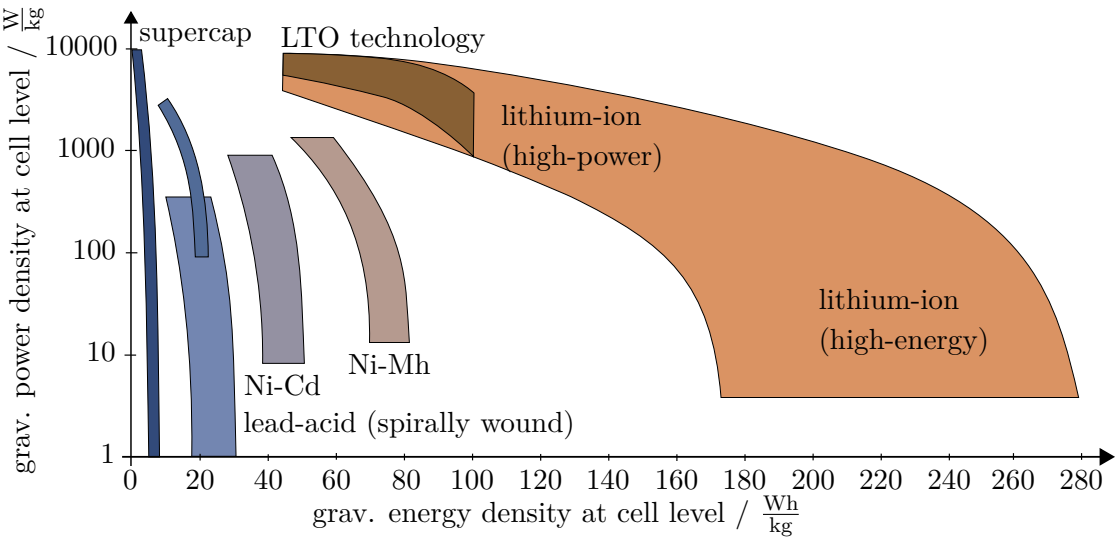

Figure 2.1: Comparison of different commercialized energy storage systems with regard to gravimetric energy and power density at cell level (own illustration, adapted from [12–17]).

In this thesis, the terms lithium-ion battery and lithium-ion cell are distinguished. Lithium-ion batteries are defined as an interconnection of any number of lithium-ion cells in series and/or in parallel. Lithium-ion cells represent the smallest unit of an electrochemical system capable of converting electrical and chemical energy. The lithium-ion cells investigated in this thesis are classified as high-power cells and reach power densities of several thousand watt per kilogram. The following chapter covers the basics of the design and working principle of lithium-ion cells. The explanations aim to enable an understanding of the subsequent chapters. An analysis of the differences between high-power and high-energy

cells highlights the special characteristics of the cells analyzed in this thesis. Common aging mechanisms of lithium-ion cells are briefly outlined. Due to the focus on LTO-based cells, a major part of this chapter is dedicated to this material. The implementation and interpretation of aging tests entails a number of criticalities and limitations, which will be addressed and discussed in conclusion.

2.1 Working principle and components

Lithium-ion cell components can be categorized into two groups: active and passive materials. Active materials take part in the electrochemical reaction both by absorbing and releasing charge carriers and by converting from one oxidation state to another. Despite chemical inactivity, passive materials ensure the functionality of the cell and can have significantly influence the cell behavior. Optimal cell performance for a specific application requires a precise and systematic alignment of active and passive components.

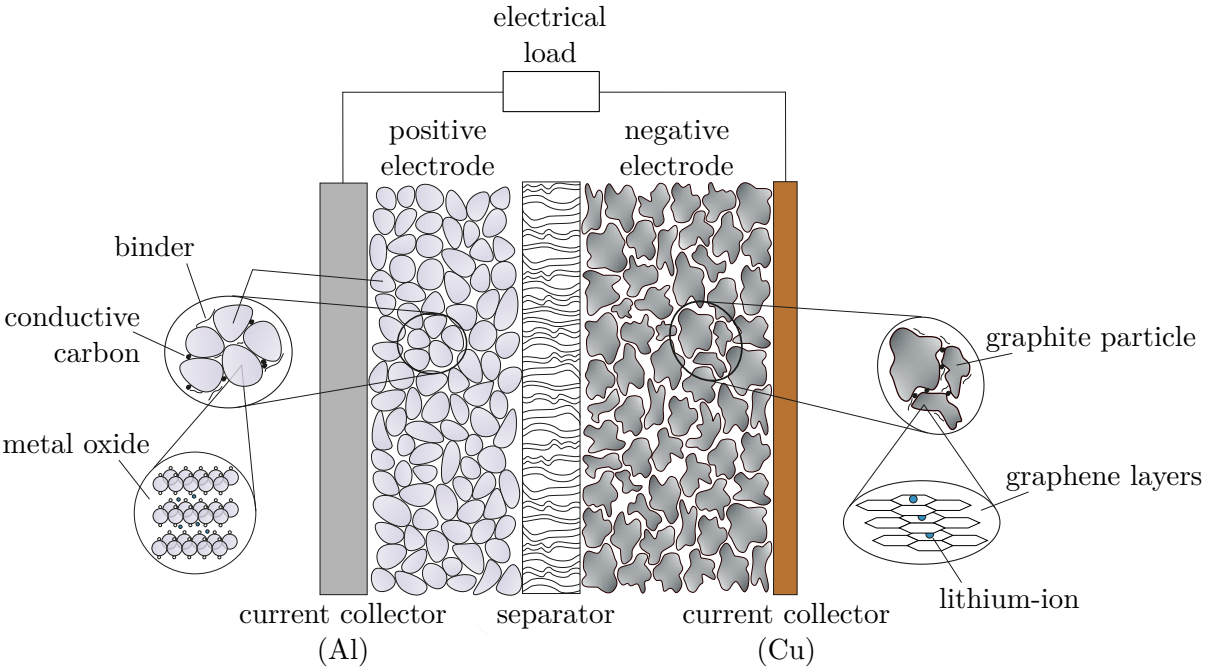

Figure 2.2: Schematic illustration of the components of a lithium-ion cell (own illustration, adapted from [18]).

The fundamental characteristics of lithium-ion cells are part of many books and publications [19–23]. Therefore the essential principle is briefly described below. Figure 2.2 depicts a schematic overview of the components of a lithium-ion cell. The working principle of a galvanic cell and thus a lithium-ion cell is based on a chemical redox reaction of the active materials. During the charge and discharge process, oxidation (emission of electrons) and reduction (absorption of electrons) occur at both electrodes. The electrodes serve as host lattices in which lithium-ions can be reversibly inserted and extracted.

For historical reasons, the positive electrode is referred to as cathode and the negative electrode as anode during both charge and discharge. This nomenclature dates back to the early years of battery technology, when non-rechargeable primary cells were developed [19].

The main electrochemical reactions within the lithium-ion cell, exemplary for a graphite anode and any metal oxide cathode, can be expressed as follows:

$$\mathrm{Li}_{1-x}\mathrm{C}_6 + x\,\mathrm{Li}^+ + x\,\mathrm{e}^- \underset{\text{discharge}}{\overset{\text{charge}}{\rightleftharpoons}} \mathrm{Li}_x\mathrm{C}_6 \tag{2.1}$$

$$\mathrm{Li}_{y+z}\mathrm{MO}_2 \underset{\text{discharge}}{\overset{\text{charge}}{\rightleftharpoons}} \mathrm{Li}_y\mathrm{MO}_2 + z\,\mathrm{Li}^+ + z\,\mathrm{e}^- \tag{2.2}$$

During charge process the metal oxide of the cathode is oxidized by applying an external voltage source. This leads to a transfer of lithium-ions into the electrolyte and a simultaneous release of electrons, so that charge neutrality is preserved. Since the electrolyte acts as both ion conductor and electrical insulator, electrons are forced to flow through the current collector and the external electrical circuit to the anode. Lithium-ions move through electrolyte and separator to the negatively charged anode and insert into the graphite structure. Thus, charging lithium-ion cells implies a conversion of electrical energy into chemical energy. The charging process is completed when the graphite material is filled or the metal oxide is unable to provide more lithium-ions. If an electrical load is connected to the charged cell, all processes proceed in the opposite direction. During the discharge process, the anode oxidizes and releases electrons and lithium-ions, so that in theory the process described above occurs completely reversible. Because of the back and forth motion of lithium-ions between the two electrodes, the process is often called 'rocking-chair' mechanism [18].

Figure 2.3 provides an overview of various anode and cathode materials. Most of the materials differ strongly in their potential versus $\mathrm{Li}/\mathrm{Li}^+$ and their gravimetric capacity density. In the following the characteristics of the most prominent anode and cathode materials are presented.

2.1.1 Anode materials

A variety of materials are suitable for use as an anode within a lithium-ion cell. An overview of the characteristic properties of the most common anode materials is given in Table 2.1. Each of these anode materials offers both advantages and disadvantages, although the electrochemical process of storing energy greatly varies.

2.1.1.1 Lithium metal

The most intuitive and capacity-wise superior material is metallic lithium. Metallic lithium offers the lowest standard electrochemical potential vs. standard hydrogen electrode

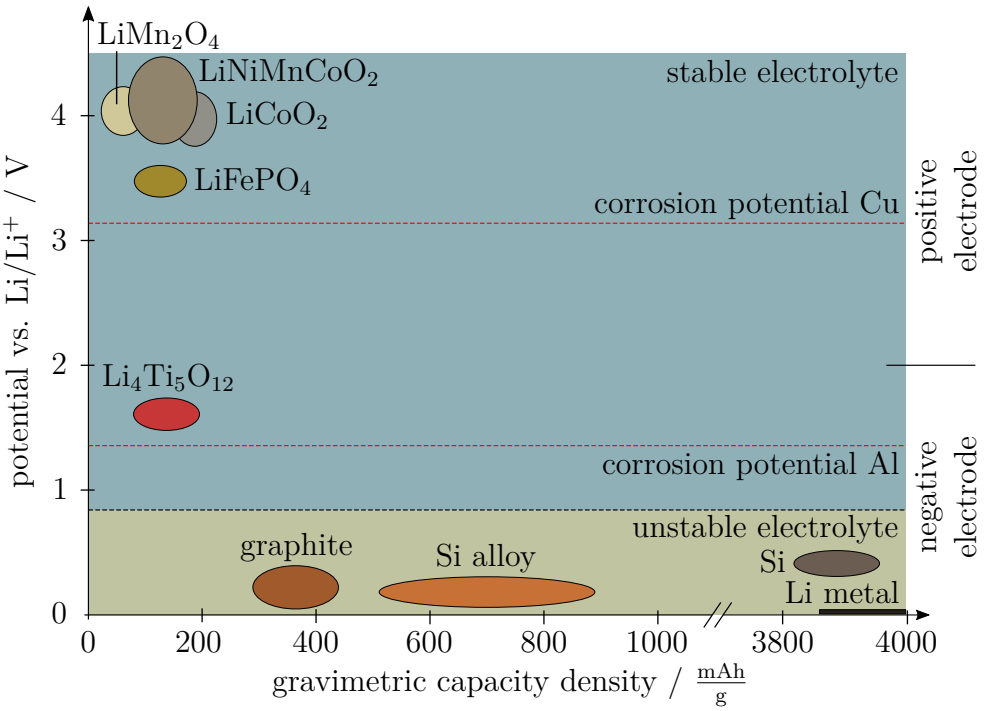

Figure 2.3: Overview of potentials and gravimetric capacity densities of the most common anode and cathode materials. In addition, stability limits of the current collectors and conventional organic electrolytes are highlighted (own illustration, adapted from [19, 24–26]).

(−3.05 V) of all metals, which enables highest possible cell voltages within a lithium-ion cell [27]. The high cell voltages combined with high gravimetric and volumetric capacity density result in the highest energy density of all anode materials. By using a lithium metal anode the entire material actively participates in the process and the potential energy density is not influenced by a passive host lattice structure.

The electrochemical potential of lithium metal, as shown in Figure 2.3, is not within the stability window of the electrolyte, so that a passivation layer is formed on the lithium metal in a continuous process [30]. This surface layer prevents further reactions with the electrolyte. During cyclization of lithium metal anodes, parts of the anode migrate into

Table 2.1: Overview of characteristic properties of different anode materials [27–29].

Material	Li	C	$Li_4Ti_5O_{12}$	Si
Lithiated phase	Li	LiC_6	$Li_7Ti_5O_{12}$	$Li_{4.4}Si$
Gravimetric capacity density $[\frac{mAh}{g}]$	3861	372	175	3579
Volumetric capacity density $[\frac{mAh}{cm^3}]$	2062	756	600	2190
Density $[\frac{g}{cm^3}]$	0.53	2.25	3.5	2.33
Volume change [%]	100	10	0.1	270
Potential vs. Li/Li^+ [V]	0	0.05	1.55	0.4

the electrolyte as lithium-ions. These changes in volume destroy the existing surface layer, resulting in a new layer formation with each cycle. The formation of the surface layer consumes large quantities of electrolyte and lithium, so that an excess of electrolyte needs to be considered in the cell design [31].

In addition, lithium-ions accumulate inhomogeneously at the lithium metal anode. This can lead to the formation of branched lithium metal structures, so called dendrites. Dendrites represent a high safety risk as they can penetrate the separator and thus can reach the cathode [32]. An induced internal short-circuit can result in a spontaneous and uncontrolled heat generation, the so-called thermal runaway, and a complete destruction of the cell [30, 33].

Due to the safety risks and the limited durability, lithium metal batteries have not yet been able to become well-established as secondary batteries. Current research projects try to eliminate the disadvantages by using solid-state electrolytes or by further homogenization of the lithium-ion deposition [27, 34].

2.1.1.2 Graphite

In the last decades, intercalation compounds have gained great success as anode material in lithium-ion batteries. These compounds serve as a stable host lattice in which lithium-ions can be incorporated and extracted. Ideally, the structure of the host lattice remains unaffected by this process, so that a high degree of reversibility and lifetime is given.

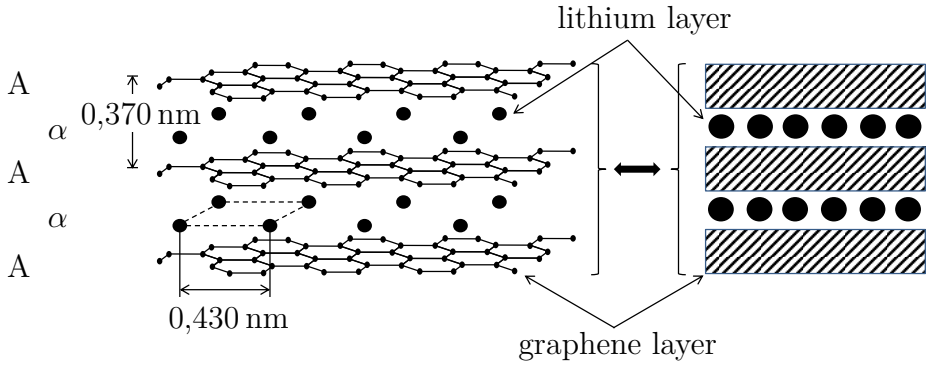

Figure 2.4: Schematic illustration of the position and arrangement of graphene and lithium layers within graphite (own illustration, adapted from [35]).

Especially in applications requiring high energy densities, carbon and in particular graphite (C) has become the preferred anode material [25, 36]. Here, a distinction must be made between soft carbons and hard carbons. The classification is based on the high-temperature behavior and the corresponding graphitizability [37]. Soft carbons posess a more flexible layer structure and are therefore able to form a crystalline structure at very high temperatures (>2300 °C) [38]. The strong layer connections of hard carbons prevent further cross-linking, thus, large amorphous portions remain in the structure. The crystallinity of carbon affects the properties of the lithium-ion cell. As the crystallinity

of carbon increases, the speed of lithiation and thus the cell performance enhances. In contrast, amorphous carbon has the advantage of higher energy density. However, this only applies if charging is done with low current density. Otherwise the potential energy density is significantly reduced [18].

The structure of crystalline graphite material is exemplified in Figure 2.4. It consists of parallel graphene layers, which are arranged and shifted relative to each other. In an unlithiated state two crystallographic forms occur, the predominantly hexagonal form with AB stacking order and the rhombohedral form with ABC stacking order. Since the transformation of both forms into each other is associated with comparatively low activation energy, both arrangements are mostly present simultaneously [35].

The graphene layers are held together by van der Waals forces. If, as shown in Figure 2.4, an insertion of lithium-ions into the structure occurs, the distances between layers increase so that the lithium-ions arrange their position between the layers. Consequently, lithiation causes the graphite material to expand by approximately 10% [35]. In addition, the graphene layers shift to an AA stacking order, see Figure 2.4 [39–41]. In a fully lithiated state graphite offers a theoretical gravimetric capacity density of 372 $\frac{\text{mAh}}{\text{g}}$ [35, 37].

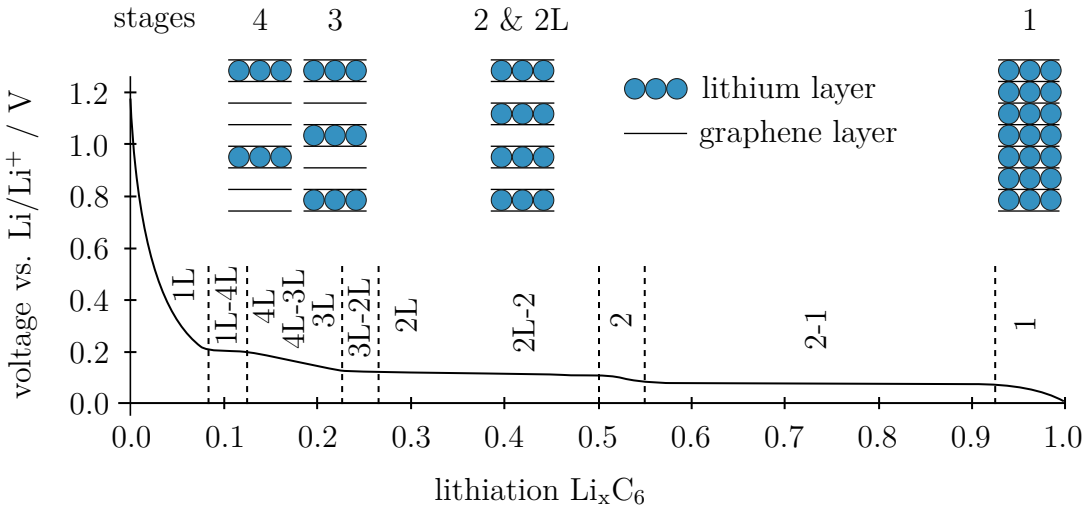

Figure 2.5: Potential of graphite as a function of the degree of lithiation with indication of characteristic stages (own illustration, adapted from [24, 42]).

The lithiation process of lithium-ions into the graphite structure occurs, as shown in Figure 2.5, in a voltage window of 0.25 V to 0 V in the form of a stagewise lithiation of the graphene layers [24]. Here, the number of the stage indicates the distance between the lithiated graphite layers [35]. Two phases can exist simultaneously. This state is indicated by a distinct potential plateau [43, 44]. The mechanism of stage formation is controlled by thermodynamic boundary conditions. The main influencing parameters are on the one hand the energy to overcome the van der Waals forces and on the other hand the repulsive interaction of the embedded lithium-ions. Due to the strength of the van der Waals forces, the formation of single fully occupied layers is energetically preferred to a random lithium-ion distribution [45].

The potential of graphite, similar to that of the lithium metal described above, exceeds the stability window of the electrolyte. The organic electrolyte is reduced due to the chemical potential of graphite, resulting in formation of a hardly soluble surface layer. This protective surface layer, known as solid electrolyte interface (SEI), is formed during the first charge cycles [46]. As an electrically insulating layer, the SEI protects against permanent contact between electrode and electrolyte [39, 47].

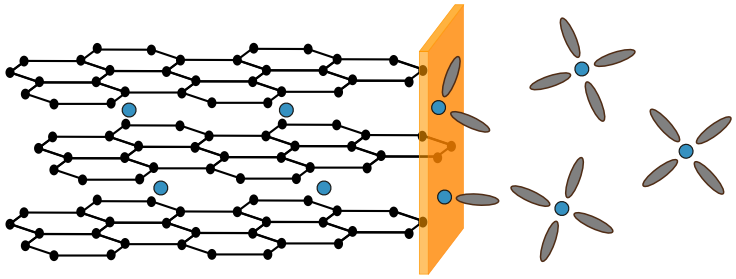

Figure 2.6: Schematic illustration of the position and arrangement of graphene and lithium layers within graphite (own illustration, adapted from [35]).

Further positive characteristic of the SEI is its ability to protect against cointercalation of solvent molecules. As shown in Figure 2.6, solvate shells of intercalating lithium-ions are stripped off at the SEI [48]. Solvate molecules are able to overcome the van der Waals forces that hold the graphite lattices together and subsequently expand them. Thus, each charging process can lead to a permanent damage of the graphite lattice. For the durability of a graphite-based cell a stable and impermeable SEI is of great importance. The thermal and mechanical reliability as well as the uniformity of the SEI can be influenced by modifying the graphite surface or adding additives. Furthermore, the efficiency of the passivation process can be optimized to minimize irreversible capacity losses [18].

A thin copper foil serves as current collector of the graphite anode [42]. Copper foil offers excellent electrical conductivity and high robustness at low potentials vs. Li/Li^+. However, in conventional carbonate-based electrolytes a potential above 3 V vs. Li/Li^+ can dissolve the copper [49, 50]. The dissolved copper can deposit on the cathode surface and can form dendrites, which bear the risk of internal short-circuiting. Therefore, a deep discharge of the anode should be avoided [51].

2.1.1.3 Lithium titanate oxide

Apart from graphite, only few anode materials have made it to a wide market penetration and mass production. A highly promising alternative is LTO, which is ideally suited for high-power applications requiring high cycle stability over extended temperature ranges, high rate capability and inherent safety [52–54].

The lithiation process of the spinelstructured $Li_4Ti_5O_{12}$ to the rock-salt-structured $Li_7Ti_5O_{12}$ takes place in a two-phase process under absorption of three electrons, according to the following equation 2.3 [55, 56]:

$$\mathrm{Li_4Ti_5O_{12}} + 3\,\mathrm{Li^+} + 3\,\mathrm{e^-} \underset{\text{discharge}}{\overset{\text{charge}}{\rightleftharpoons}} \mathrm{Li_7Ti_5O_{12}} \tag{2.3}$$

LTO reaches a theoretical gravimetric capacity density of 175 $\frac{\mathrm{mAh}}{\mathrm{g}}$. The insertion and extraction of lithium-ions takes place on a potential plateau of approx. 1.55 V vs. $\mathrm{Li/Li^+}$, as illustrated in Figure 2.7 [54, 57]. Thus, LTO offers the highest potential of all commonly used anode materials, which negatively affects achievable lithium-ion cell voltages. Consequently, LTO-based cells are limited in their energy density and are not commonly used in high-energy applications, such as EVs, where installation space is limited [58].

The reversible insertion and extraction of lithium-ions into the crystal structure of the LTO occurs without significant expansion of the material (less than 0.1%) [59, 60]. This characteristic is the origin for the commonly used term as 'zero-strain' material [55, 56, 59]. Low material expansion benefits both cycle life and stability against high-rate cyclization, since mechanical stress within the material is minor and high reversibility is ensured [36, 58].

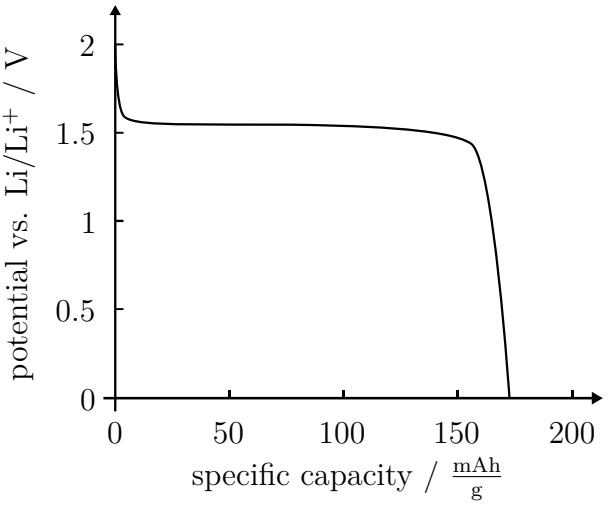

Figure 2.7: Characteristic potential profile of an LTO electrode.

However, both commercial and scientific interest is driven by the high operating voltage, not least because essential aging mechanisms of graphite do not apply to LTO. The electrolyte is stable in the operating range of the voltage plateau of 1.55 V vs. $\mathrm{Li/Li^+}$, so that in principle no protective SEI is formed on the LTO. The high potential prevents deposition of metallic lithium and dendrite growth, even if the cell is temporarily overcharged. Thus, LTO provides high charge capability at negative temperatures and a high level of safety [56, 61, 62].

In the event of thermal breakdown of cell or pack, LTO is thermally more stable than graphite at above 200 °C and therefore offers an increased level of safety [63].

The low electrical conductivity ($<10^{-13}\,\frac{S}{cm}$) and the low lithium diffusion coefficient (approx. $10^{-8}\,\frac{cm^2}{S}$) are a challenge for the usage of LTO and restrict the high rate capability [64]. Various methods for optimizing kinetic performance of LTO have been proposed in the past. One method is the use of nano-sized particles [58, 65]. Smaller particles greatly shorten diffusion paths for lithium-ions and electrons as well as increase the contact area between active material and electrolyte. In addition, conductive coatings can enhance the conductivity at the material surface, resulting in enhanced high rate capability. Further measures include in-situ structure modification, ion-doping and morphology control [61, 66, 67].

A major safety risk and aging mechanism of LTO-based cells is the formation of gas (H_2, CO, CO_2 etc.), which leads to an inflation of the cells [57]. Gas formation occurs already at room temperature and is not linked to cyclization of the cell [68]. A detailed consideration of this behavior and potential causes of gassing are provided in Chapter 2.2.1.

The high potential of LTO allows for the use of aluminum as current collector. Aluminum is commonly used for cathode materials that are operated at high potentials (>3 V) since copper would decompose [41]. Although aluminum offers both weight and cost advantages, its electrical conductivity is lower than that of copper. Aluminum forms a stable passivation layer consisting of Al_2O_3 [69]. Along with other stabilizing layers, which emerge from reactions with lithium hexafluorophosphate ($LiPF_6$) containing electrolytes, they protect the aluminum from oxidative processes [50, 70, 71].

2.1.2 Cathode materials

A wide spectrum of materials qualifies as cathode in a lithium-ion cell, but few of them fulfill all key properties. On the one hand, excellent electrochemical characteristics regarding reversibility of ion insertion, insolubility in the electrolyte, high specific capacity, high potentials vs. Li/Li^+ and good ion conductivity are required. On the other hand, low material costs, non-toxicity, high availability and good reusability are essential for a large-scale industrialization [41, 72].

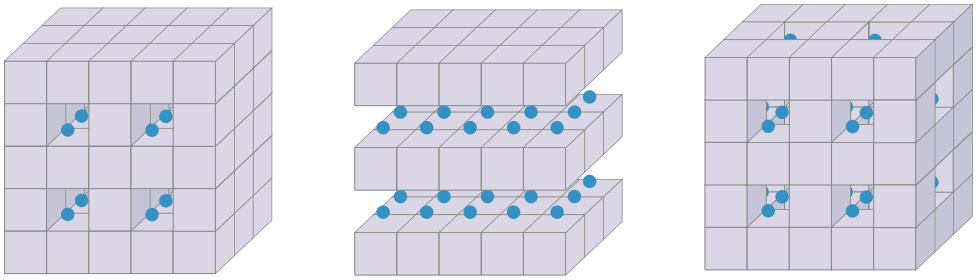

Figure 2.8: Schematic illustration of the different crystalline structures of cathode materials (own illustration, adapted from [73]).

Generally, cathode materials can be grouped based on their crystallographic structure. As shown in Figure 2.8, a distinction is made between olivine, layered oxide and spinel materials. The grouping is derived from the number of dimensions through which lithium-ions insert into the material and diffuse within the material. The most prominent representatives of the individual groups are introduced below.

Olivine-type materials Lithium iron phosphate (LFP) is the best-known material of the olivine structured group, offering only 1-dimensional lithium transport. The insertion and extraction of lithium-ions occurs at a potential of 3.45 V vs. Li/Li^+. Here, LFP exhibits a flat voltage plateau over a wide state of charge (SOC) range, which is caused by the two-phase lithiation process [74]. The voltage profile of LFP exhibits a pronounced hysteresis, which is separately discussed in Chapter 5.1.2. The low working potential of LFP, see Figure 2.3, and its theoretical capacity of 170 $\frac{\text{mAh}}{\text{g}}$ results in lower energy densities compared to other cathode materials. Similar to LTO, untreated LFP lacks electrical and ionic conductivity, so that additional material optimizations are required. Different strategies are pursued to overcome these constraints. Bulk properties are adjusted, e.g. by using nanometer-sized particles (<1 µm), to keep diffusion paths in the material short [75, 76]. Further, the electrical and ionic conductivity is improved by surface treatment, including methods such as carbon coating and metal doping [77–80].

LFP material exhibits high stability and negligible material expansion upon lithiation, which is beneficial for cycle stability and durability [38]. Complete delithiation is permitted due to the excellent structural stability. Additionally, the strong P-O bonds inside the material prevent the release of oxygen during deep discharge, making LFP thermally extremely stable and inherently safe [79, 80]. Raw material costs of LFP are low and it is considered as non-toxic. All these properties make LFP extremely attractive for automotive applications. Consequently, LFP has been used for example in lithium starter batteries and in the BMW Active Hybrid 3 and 5 series [81, 82].

Spinel-type materials An example of a commercially available cathode material with three-dimensional diffusion of lithium-ions is the spinel-structured lithium manganese oxide (LMO). With 148 $\frac{\text{mAh}}{\text{g}}$, the theoretical capacity density of LMO is relatively low [28]. Due to its high structural stability, LMO shows also a high thermal stability [83]. Lithiation and delithiation occurs in the range of 4.1 V vs. Li/Li^+ at minimal volume expansion and highly reversible, resulting in good cycle stability. Its three-dimensional diffusion paths enable high rate capability, thus offering excellent suitability for high-power applications [79]. Production of the non-toxic LMO is carried out at relatively low costs due to the high availability of raw materials.

Pure LMO exhibits certain characteristics that negatively affect cycle stability, especially in terms of capacity loss. Firstly, a manganese dissolution can occur at elevated temperatures [84]. The transition metal dissolved in the electrolyte is freely moving and bears the risk of deposition on all cell components. The deposition of manganese on the anode can lead to increased formation of surface layers and bind active lithium. This

reduces both the available capacity and the maximum performance of the cell. Various research projects have shown that coatings can limit or stop manganese dissolution [85, 86]. Secondly, the LMO structure loses much of its stability if the specified cell voltage limits are exceeded. The resulting effect, known as Jahn-Teller distortion, describes the development of mechanical stress inside the crystal structure, which can cause a release of manganese ions [84, 87]. A combination of manganese with other transition metals, as it is the case with the lithium nickel manganese cobalt oxide (NMC) described below, allows for the reduction of negative properties while intensifying positive material properties.

Layered-type materials NMC is the most commonly used layered oxide material in lithium-ion batteries. In principle, NMC offers a good balance between safety, performance and lifetime. Due to these characteristics, both scientific and commercial interest in NMC is great, which is why many research and development projects aim to optimize this material.

While maintaining an upper end-of-discharge voltage of 4.2 V to 4.4 V, the cyclization process of NMC takes place under minor volume expansion and with high cycle stability [62, 88, 89]. Up to 70% of the inserted lithium is extracted within this operating range.

Delithiation of the NMC beyond 4.5 V enables an extension of the theoretical capacity to over 200 $\frac{\text{mAh}}{\text{g}}$ [90]. However, the stability of the layer structure is too weak to withstand such a high degree of delithiation. Such a condition can provoke severe material expansion and, in the worst case, a collapse of the layer structure [91]. In fully lithiated state, NMC exhibits low electrical conductivity, negatively affecting the performance of the material [44].

Since the proportion of the various transition metals (nickel, manganese, cobalt) in the material is flexible, different material characteristics result depending on the weighting. The material can be optimized in consideration of requirements and operating conditions for specific applications. A higher nickel content increases the capacity in lower voltage ranges, which is due to the oxidation reaction from Ni^{2+} to Ni^{4+} with the release of two electrons [90]. Manganese is electrochemically inactive in the regular operating range of the cell, thus it enhances the thermal stability and safety of the material. In addition, low raw material costs of manganese reduce the total cost of cathode material [62]. In the triple combination, cobalt offers critical and versatile properties that enhance both material stability and performance [92]. Firstly, cobalt reduces the probability of nickel ions and lithium-ions changing positions in the layered structure, reinforcing the two-dimensional layered structure [93]. The stable structure enables a high diffusion rate, which has a positive effect on performance and capacity. Secondly, it is assumed that cobalt increases the electrical conductivity thanks to its redoxactitvity at high potentials [38, 94].

Primary focus of this thesis is to investigate the aging behavior of NMC|LTO cells. Therefore, aging mechanisms of NMC are discussed in detail in Chapter 2.2.

2.1.3 Separator

The separator is a thin and porous membrane that is located between the electrodes and fulfills both an ion conducting and electrically insulating function. In addition to sufficient thermal and mechanical stability, the separator is required to provide high chemical stability against the electrolyte and the active materials [21]. A high and uniform porosity of the separator positively affects the ion conductivity and thus the performance of the cell. The size of the pores represents an important optimization parameter. On the one hand, a reduction in pore size reduces the probability of dendrite formation and thus increases safety. On the other hand, if the pores are too small, the ion conductivity may be limited, which in turn increases the internal resistance of the cell [95].

Another important criterion is the wettability of the separator. During the production process, good wettability ensures that the cell can be quickly filled with electrolyte. Further, it guarantees a homogeneous electrolyte distribution over the entire cell lifetime. [96].

Often polymers, such as polyethylene (PE) or polypropylene (PP), with a thickness between 10 and 25 µm are used as microporous separator [18]. A combination of PE and PP in PE-PP or PP-PE-PP separators can provide an additional shut down mechanism due to the different melting points of both materials. If the melting point of the inner PE layer is exceeded, ion paths close locally, whereas the mechanical stability is guaranteed by the PP layers. Depending on the intensity of heating, this mechanism can prevent a complete thermal runaway [96].

For a detailed overview of requirements, characteristics and challenges of separators in liquid electrolyte lithium-ion batteries, it is referred to [97, 98].

2.1.4 Electrolyte

The electrolyte enables an ion conductive connection between all cell components. Therefore, various performance characteristics of the cell, both new and aged, depend on an optimal design of the electrolyte. Ideally, the electrolyte should offer high ionic conductivity and electrical insulation as well as a wide electrochemical stability window, so that neither reductive nor oxidative processes occur at the electrodes. It should further not react with other cell components, be stable against electrical, mechanical and thermal abuses, and possess environmental friendliness [99]. Compliance with the stability window of the electrolyte and a continuous passivation of the anode by the SEI significantly enhance the lifetime of the electrolyte.

Electrolytes can be subdivided into three main categories: liquid, gel and solid electrolytes. Since this thesis exclusively investigates cells with liquid electrolyte, it is referred to the following reviews for further information on the other electrolyte categories [34, 100–102].

Common liquid electrolytes consist of a mixture of organic solvents, a dissolved lithium salt and additives. Due to the strongly reducing anode and the strongly oxidizing cathode, only aprotic solvents are used within the electrolyte [99, 103]. These solvents lack functional

groups from which hydrogen could be split off. In addition, the solvent should provide low viscosity, late boiling, non-toxic, flame-retardant and electrically insulating properties. Most often organic solvents such as ethylene carbonate (EC), ethyl methyl carbonate (EMC), propylene carbonate (PC), dimethyl carbonate (DMC) are utilized. These are typically combined in order to achieve optimum electrolyte behavior for each specific application [99]. Such solvent blends are unable to provide the required performance under all conditions. Therefore, additives are added to systematically modify electrolyte characteristics while maintaining the main characteristics of the electrolyte. For example, additives can support the formation of the SEI or reduce the flammability of the electrolyte [104]. The share of additives in the electrolyte can reach up to 10% [104, 105].

The lithium salt commonly used is $LiPF_6$. It ensures high ionic conductivity and contributes to stable SEI formation. In addition, it forms a passivation layer on the surface of the aluminum current collector, protecting it from material dissolution [105, 106].

$$LiPF_6 \rightleftharpoons LiF + PF_5 \tag{2.4}$$

$$PF_5 + H_2O \longrightarrow 2\,HF + POF_3 \tag{2.5}$$

$LiPF_6$ dissociates at room temperature to solid lithium fluoride (LiF) and gaseous phosphorus pentafluoride (PF_5) (see Equation 2.4) [104]. Thus, direct contact with water or residual moisture can result in the development of highly reactive hydrofluoric acid (HF), according to Equation 2.5. The latter in turn corrodes most cell components. To guarantee long-lasting and safe batteries, requirements for residual moisture contents of the components are high, which is why cell production is carried out under certain dry room conditions [51].

2.1.5 Key distinctions between high-power and high-energy cells

In this thesis lithium-ion cells are investigated, which were explicitly designed and developed for high-power applications. In the literature it is often neither obvious nor explicitly emphasized what kind of cell type is analyzed. Usually high-energy cells are used, since they represent the majority of cells produced worldwide [107]. As illustrated in Figure 2.1, cell performance can differ by a factor of 5 in energy density and by a factor of 1000 in power density. These performance differences between high-power and high-energy cells result from a variety of degrees of freedom available in material selection, cell design and cell production.

In the following, a number of these degrees of freedom are described and their influence on cell properties is characterized. Many electrochemical material optimizations take place on atomic and particle level. Nevertheless, a differentiation of high-power and high-energy cells can even be made by optical examination of the electrode materials.

For a comparison of electrode materials from different cell types, Figure 2.9 shows optical microscope images of the cross-section of anode and cathode. Both are NMC|C cells from the same cell manufacturer. These cells are suitable for automotive applications: the high-power cell for low-voltage applications (vehicle electrical system) and the high-energy cell for high-voltage applications (electrical drive system). The most obvious difference between the electrodes is the layer thickness of the active material. Both anode, see Figure 2.9a, and cathode, see Figure 2.9b, of the high-power cell feature a 50% lower layer thickness. Even in the case of an identical active material composition, this electrode dimension would lead to greatly shortened diffusion paths and enhanced electron transport, which greatly increases the cell performance.

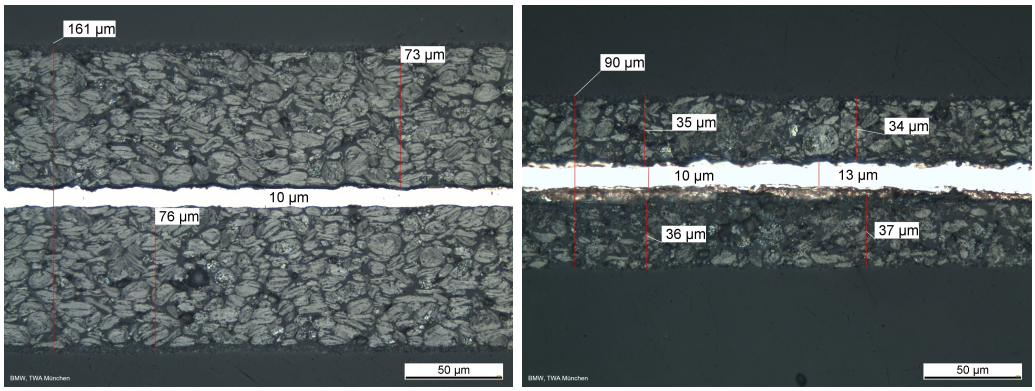

(a)

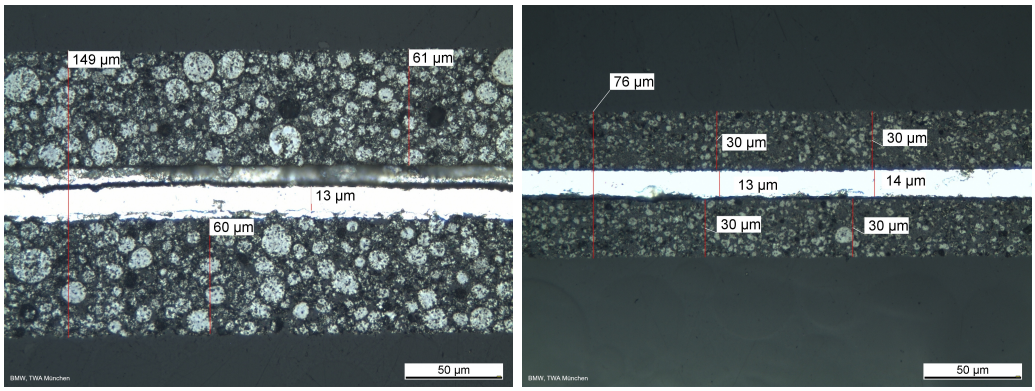

(b)

Figure 2.9: Optical microscope images of cross sections from a) anode and b) cathode of high-energy (left) and high-power cells (right) produced by the same cell manufacturer. Both sides of the centered current collector (10 µm to 15 µm) are coated with active material. Depending on the cell type, both thickness and composition of the active material layer differ. The microscope images were created by the technology material and process analysis (TWA) of BMW AG.

The thickness of the current collectors of anodes and cathodes is comparable with 10 µm and 13 µm respectively. A similar observation was reported by Lain et al. [108] when they

analyzed cell components from different high-power and high-energy cells. Due to lower surface capacity of the high-power electrode, current load is not significantly increased even at high-power input and output, so that no larger current collector is required. In addition, having a lower active to passive material ratio of the high-power cell allows for better heat transport to the outside, thus enabling more effective cooling of the cell and the battery pack.

In contrast to the current collectors, cell tabs in high-power cells should be enlarged. Current loads of several 100 A generate high ohmic losses at the cell tabs, which heat them up. This heat can damage surrounding components within the pack and can cause strong heat transfer into the cell. The latter entails a risk of permanent local damage as well as accelerated aging of the cell material, which, depending on its characteristics, may pose a safety risk. In addition, high contact resistances at electrical junctions, such as between the current collector and the cell tab, should be avoided. This can be achieved by special welding techniques such as laser welding or ultrasonic welding [109, 110].

The high-power anode is characterized by a lower particle density than the high-energy anode. For the latter, a high particle density is desired in order to be able to store as many lithium-ions as possible and to achieve high energy densities. One major drawback of high particle densities is that diffusion processes are slowed down drastically.

The material specific diffusion rate can be quantified by the effective diffusion coefficient. This coefficient is derived from the material properties porosity and tortuosity as follows [111]:

$$D_{\text{eff}} = D \cdot \frac{\epsilon}{\tau} \tag{2.6}$$

Porosity ϵ describes the ratio of particle volume to total volume, tortuosity τ the degree of winding in the particles within a material and D the diffusion coefficient from the electrolyte. In high-power cells, where porosity is higher and tortuosity is lower, diffusive lithium-ion transport can proceed at high speed.

The black areas between graphite particles of the high-power anode indicate an intensified use of conductive carbon. This guarantees proper contact both between individual particles and between particles and the current collector, thus enhancing the electrical conductivity. Large differences in the size of the graphite particles are not apparent.

This is contrary to the NMC particles of the individual cathodes. These are significant larger in the high-energy cell than in the high-power cell. The larger a particle is, the longer the lithiation and delithiation process takes. Limiting material parameter is the speed of solid diffusion and thus the concentration equalization within a particle. The difference in size between adjacent particles is also large for the high-energy cathode, which prevents uniform and rapid lithiation. Here, Käbitz [112] used laser microscope images of graphite to prove that neighboring particles and even areas within a particle can exhibit

strongly differing SOCs[(i)]. Such inhomogeneities worsen the aging behavior of the material, for example as a result of increased mechanical stress or local overcharge [113]. Apart from a few exceptions, the high-power cathode seems to have a more homogeneous particle size distribution.

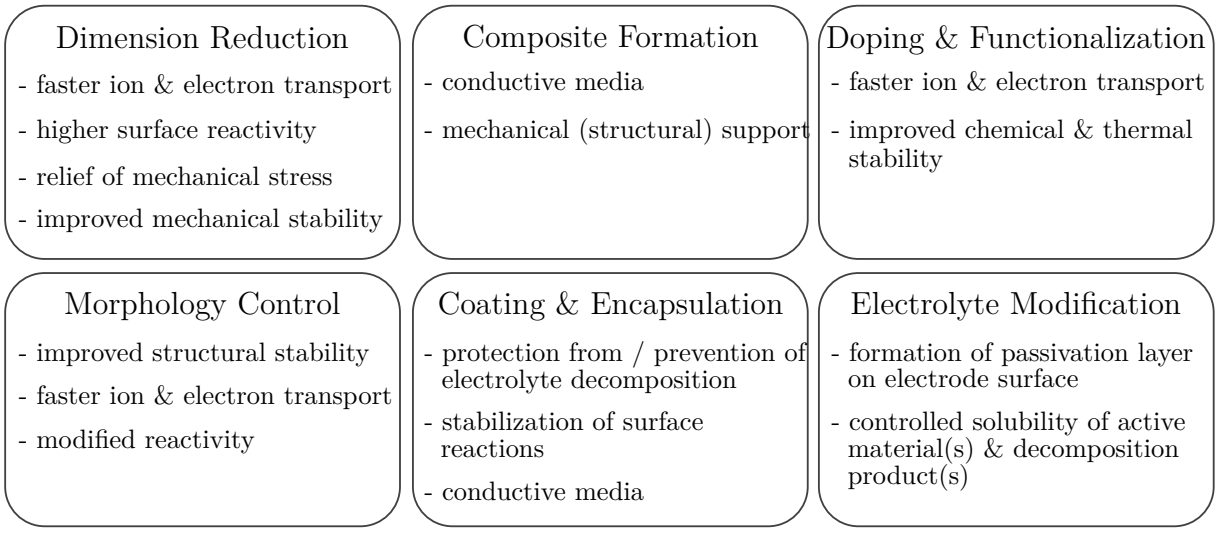

Figure 2.10: Methods for optimizing cell materials to improve their power performance (own illustration, adapted from [28]).

In addition to the aforementioned optically detectable material changes, further electrochemical optimizations can be applied to the bulk material. An overview of different methods is shown in Figure 2.10. Some of these methods have already been mentioned in Chapters 2.1.1 and 2.1.2.

For the optimization of LTO within high-power cells, an improvement of the electrical and ionic conductivity is a key criterion. Therefore, the categories dimension reduction (nanoparticles), composite formation (LTO|C, LTO|graphene), doping & functionalization (Zr, Al, Nb) as well as coating & encapsulation (carbon) have been investigated within the scope of various research projects and are partly commercialized [64].

2.2 Aging of lithium-ion cells

Parts of this section are based on a publication created during the course of the dissertation. The use of the article content including illustrations from [114] is permitted with the consent of Elsevier.

[(i)] Lithiation of graphite takes place in a stepwise process, in which it undergoes different characteristic colorations based on the degree of lithiation. Thus, optical material analysis allows for an estimation of the SOC.

A lithium-ion cell is subject to various aging processes over its lifetime, which affect the structural, chemical and physical properties of the cell components [115]. The rate at which a lithium-ion cell ages depends on the usage behavior and the environmental conditions the cell is exposed to [116, 117]. Cell aging is manifested in a loss of electrochemical performance, which includes both power capability and energy availability. A long-term aging process can result in a complete failure of the lithium-ion cell. In addition, single cell damaging events, such as short circuit, thermal runaway or abusive usage behavior, can cause sudden cell failure.

The aging condition of a lithium-ion cell is commonly assessed by monitoring the loss of capacity and the rise in internal resistance. In high-energy applications, the remaining capacity is crucial for the full functionality of the application, such as the range of an electric vehicle. For this reason, 80% remaining capacity is widely established as a conservative end-of-life criterion [118, 119]. Further usage of the cell beyond this condition is still possible and might have negligible limitations depending on the application [120]. There is no binding standard for a uniform end-of-life criterion [121]. Since the requirements concerning energy and power availability differ greatly depending on the application, this criterion should be variably adjusted to ensure full functionality in all relevant fields of operation. Therefore, in high-power applications an end-of-life criterion related to a maximum rise in internal resistance can be appropriate and sometimes necessary. For the design of the cell this question is of great importance, as it has implications for both manufacturing costs and potential warranty costs.

The aging processes within a cell and the intensity with which they occur depend largely on the cell components used and on the operating conditions. Generally, two categories of aging conditions are distinguished: calendar and cyclic aging. Calendar aging covers all effects occurring in a non-operating state without external load. Decisive for the aging characteristics under this condition are the interactions between active materials and electrolyte. Additionally, thermodynamic instabilities cause side reactions [116]. The influencing operating parameters are temperature, cell voltage/SOC and time [124–127].

Cyclic aging is induced by repetitive lithiation and delithiation processes, which result in a variety of kinetic and structural effects. For example, changes in volume within the lithiation process can trigger mechanical stress or structural changes up to dissolution can degrade the electrode material [116]. Main operating conditions that induce cyclic aging processes are current rate, depth of discharge and energy throughput [128–131]. In addition, the operating voltage limits of the cell affect material stress and aging processes [132].

Figure 2.11 provides a schematic overview of the most common aging mechanisms. The importance of each individual mechanism depends strongly on the respective components and the design of the lithium-ion cell as well as the relevant load scenario. Most of the aging processes are associated with the active materials. Nevertheless, lithium-ion cells represent highly complex electrochemical systems with strong interdependencies between different aging mechanisms. These interdependencies can lead to overlapping and mutual reinforcement.

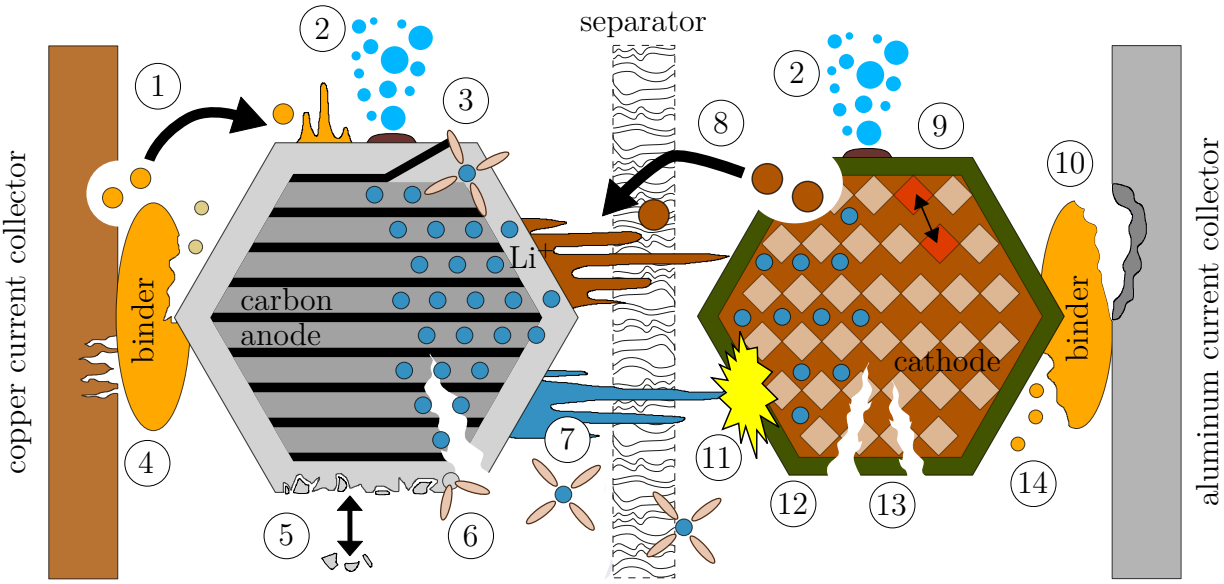

1. copper dissolution and dendrite formation
2. gassing and surface film
3. solvent co-intercalation and graphite exfoliation
4. copper cracking and contact loss
5. SEI decomposition and precipitation
6. particle cracking, SEI formation and build up
7. lithium plating and dendrite formation
8. transition metal dissolution and dendrite formation
9. structural disordering
10. aluminum corrosion and contact loss
11. internal short-circuit
12. cathodic surface film
13. particle cracking
14. binder decomposition and contact loss

Figure 2.11: Schematic illustration of the most commonly reported aging mechanisms of a lithium-ion cell (own illustration, adapted from [122, 123]).

Therefore, in battery diagnostics clusters are built, which connect measurable performance degradation with different aging mechanisms. Two so-called degradation modes are well accepted in the literature: loss of lithium inventory (LLI) and loss of active material (LAM) [133, 134].

LLI comprises the loss of usable lithium-ions due to irreversible side reactions, which cause both the formation of surface layers on the electrodes and the formation of compounds within the electrolyte [135]. Primarily, LLI covers the aging mechanisms ⑤, ⑥, ⑦ on anode side for a graphite anode and ⑫ on cathode side. All these phenomena occur at the

interface between electrode and electrolyte. Lithium-ions that are bound by such processes are not available for further reactions, which reduces the usable cell capacity. In addition, cover layers slow down charge transfer processes and thus increase the internal resistance, which limits the power capability of the cell [136].

In contrast to LLI, LAM is inherently associated with material degradation, meaning a permanent damage of the material. In the case of LAM, the volume of the active material that is involved in the storage of lithium-ions decreases. Most of the underlying aging mechanisms of LAM originate from repeated lithiation and delithiation processes. These mechanisms include, for example, mechanical material defects (see ③, ⑤, ⑬) or structural material changes (see ⑧, ⑨). Often LAM and LLI occur simultaneously and are partly mutually dependent.

Both modes can cause capacity as well as power fade. The latter is induced by a deterioration of the cell's kinetics, reflected by a decrease in electrical and ionic conductivity. This degradation can be determined via the ohmic internal resistance. During charge and discharge processes, an increased internal resistance leads to higher overvoltages. Because of these additional overvoltages, voltage limits of the cell are reached earlier, so that less capacity is usable. In addition, ohmic losses are increased, which is why the heat generation inside the cell rises [41].

Since this thesis concentrates on the aging behavior of LTO-based cells, few of the graphite-specific aging processes from Figure 2.11 are of interest. An essential aging mechanism, which has been extensively investigated in the literature, is the gassing behavior of LTO-based cells. This mechanism heavily affects lifetime and safety of the cell. Hence, it will be addressed separately in the following section. In addition, cell geometric properties can provoke a reversible capacity effect within aging tests. Since this effect can be very pronounced for long-lasting LTO-based cells, it is an important element of this thesis. Consequently, background and relevance of this effect are clarified in Section 2.2.2.

2.2.1 Degradation of lithium titanate cells

In general, LTO-based cells are known for their outstanding lifetimes, both cyclic and calendaric. Unfortunately, few comprehensive aging studies of mass-produced LTO cells exist in the literature [137]. Reasons for this are, among others, the low spread of LTO cells in commercial applications and the high price of the material [28]. In addition, aging studies of LTO cells are very time and cost intensive due to high cycle and calendar lifetimes. For this reason, cyclic aging has been accelerated using higher C-rates[ii] (2C to 10C) and temperatures (20 °C to 55 °C) [138–142]. All investigations showed high cycle stability, even at elevated temperatures. Hall et al. [139] and Svens et al. [142] were able to prove that the cathode was the more lifetime-critical material in the examined cells.

[ii] The term C-rate enables a normalization of the charge or discharge current to the nominal cell capacity. Thus, current loads of cells with different capacities can be compared. For example, with 2C a 10 Ah cell can be discharged in half an hour. The unit of the C-rate is 1/h.

Calendar aging tests also showed an outstanding lifetime of LTO-based cells [126, 142]. Dubarry et al. [143] found no loss of capacity during storage of LTO|(LCO+NCA) cells at 25 °C for over one year regardless of SOC. In contrast, 55 °C storage temperature resulted in a distinct capacity loss, which was most pronounced at low SOC. The loss of capacity at elevated temperatures was primarily attributed to LLI. Additionally, high temperatures in combination with high SOC have been found to shorten the battery lifetime due to strong gassing behavior [144].

In LTO-based cells, certain aging mechanisms that are dominant in graphite-based cells can be neglected. For example, mechanical stress within the active material is greatly reduced by its 'zero strain' characteristic, even when cycled at high current rates. Thus, the risk of particle cracking, which could result in poor electrical contacting and LAM, is low. Reactions at the electrode/electrolyte interface are attenuated due to the high potential of LTO (see Section 2.1.1.3).

The assumption that no SEI or cover layer is formed on the surface of LTO has been contradicted by various scientific studies [145]. Dedryvère et al. [146] were able to prove through electrochemical impedance spectroscopy measurements that a passivation layer is built on LTO during cyclization. Both inorganic (LiF, phosphates) and organic species (carbonates, polyethylene oxides) were detected as compounds within this surface layer [146–148]. Further studies by Kitta et al. [149] and He et al. [150] confirmed the formation of a protective and lifetime extending passivation layer. The thickness of this layer increases with rising cyclization temperature. Reasons for this are an intensified decomposition of $LiPF_6$ and, specific for the investigated cell, an increased manganese dissolution of the LMO cathode [148].

A key aging mechanism of LTO is gas formation (H_2, CO, CO_2 and other gaseous hydrocarbons), which is accelerated at elevated temperatures and can already occur during storage phases [138, 151]. Here, the volume expansion in a cell induced by gassing reactions can be so strong that the cell casing bursts. This phenomenon represents a serious safety risk for potential applications, which is why much scientific research focuses on this issue. The origin of the gassing characteristic is attributed to various electrochemical reactions. Three explanatory approaches have become established, which are briefly described below [152].

One theory suggests that $LiPF_6$ is responsible for the main gassing process [104, 152, 153]. As described in Chapter 2.1.4, $LiPF_6$ dissociates into LiF and PF_5 at room temperature, causing the release of HF upon contact with residual moisture. HF can decompose solvents and thus can cause gassing reactions which comprise the above mentioned gassing products [152]. Residual moisture content in the electrodes or the electrolyte significantly accelerate gas formation. Fell et al. [144] could prove a correlation between the residual moisture content and the amount of gas produced within the cell.

Another theory is based on the assumption of TiO_2 impurities in the LTO material, which can arise during the synthesis process of material production [154, 155]. TiO_2 is highly catalytic and is used to obtain hydrogen through water splitting. It is believed that TiO_2 can decompose carbonate electrolytes [152].

Lastly, interfacial reactions between the LTO surface and the electrolyte can cause gas formation. Here LTO acts as a catalyst and decomposes electrolyte components. A general decomposition of the electrolyte has been proven by the discovery of an SEI-like structure on the LTO surface (see above). Gao et al. [156] also demonstrated that the potential of the lithiated LTO surface exceeds the stability window of the electrolyte, particularly at high temperatures. These results are consistent with calendar aging tests conducted by He et al. [29] at various SOCs. Cells in a fully charged state exhibited stronger gassing behavior, mainly consisting of C_2H_4 and CO_2.

Various material optimizations have been investigated to suppress and minimize the gassing behavior of LTO. Their primary purpose is to form a stable, protective surface layer on the LTO and thus to inhibit critical reactions at the electrode/electrolyte interface. Established methods include particle coatings of various materials or the addition of electrolyte additives [152].

2.2.2 Reversible aging - Passive electrode effect

Several aging studies in the past showed unexpected capacity rises and drops in initial phases of the tests [157, 158]. The large majority of these phenomena can be explained by the anode overhang or, in a broader sense, the passive electrode effect (PEE), which has already been postulated by various authors [159–161]. According to these publications, this effect occurs if the graphite anode is geometrically oversized compared to the opposing cathode. This dimensioning provides a reserve in case of production-related inaccuracies, for example during the stacking process of the electrodes [33]. It ensures that the cathode is always opposite an anode area. The anode overhang allows for a more homogeneous current distribution during lithiation of the edges of the acitve graphite material [162]. Thus, the danger of lithium plating due to excessive accumulation of lithium-ions in the edge areas is reduced [159].

The overlapping passive anode material causes lithium-ion flow from the active to the passive area and vice versa. Those passive electrode areas act as lithium-ion sources and sinks. As a result, the lack or excess of lithium-ions in the active area of the anode affects the usable capacity, which can be extracted from the cell. This effect is completely reversible, since these lithium-ions are available for further lithiation processes. A precise capacity determination is impeded since the availability of capacity depends on the pre-condition of the cell. For example, in high-precision measurements of the coulombic efficiency values of over 100% were obtained [159, 163]. Additionally, in calendar aging tests, in which cells with low and high SOC had been stored, capacity differences of 3.6% were attributed to the overhang [163].

Depending on the cell geometry, the size of the overhang can vary from less than one millimeter to more than one centimeter [159, 161, 163]. According to Dagger et al. [164], major oversizing should be avoided. On the one hand, SEI is also formed in the passive regions of the graphite, which leads to a loss of usable lithium-ions and thus to a loss of cell capacity. On the other hand, with an increasing proportion of passive regions, the

amount of lithium-ions increases, which are reversibly stored in these regions and which are not immediately available for cyclization. In addition, coulombic efficiency and capacity retention decrease as the overhang size rises [164].

The strength and direction of this balancing process depends on the voltage difference between the two areas. Depending on the half-cell potential of the graphite and the location on a plateau or a variable flank, different gradients occur. This can be identified by characteristic kinks of the charge flow, which occur during the equalization process [161]. In addition, a rise in temperature accelerates the lithium-ion flow into and out of the passive area. Hüfner et. al [161] could demonstrate that the lithium-ion flow increases by a factor of 1.4 per 10 K.

The execution and interpretation of aging tests, both calendar and cyclic, requires an evaluation and consideration of the impact of PEE based on the individual cell geometry and operating points. A detailed investigation of this phenomenon for the examined cells and applied aging tests is provided in Chapter 6.1.2.

2.2.3 Criticality and limitations of aging studies

The execution of aging tests with lithium-ion cells requires high expenditures, which are mainly caused by long test durations and high investment costs for test benches. In addition, for an extensive investigation several operating points have to be determined. Ideally, these points form a solution space, which can be used to draw conclusions about further operating points and specific aging behavior. Aging tests should be designed redundantly with several cells per operating point in order to exclude measurement errors or production-related cell variations and thus to obtain stochastically valid statements. However, due to the variety of relevant operating points, the limited availability of test cells respectively test benches and the long test duration, this cannot be realized in most cases. By using high quality mass-produced cells, like those examined in this thesis, variations between individual cells from one production batch are minimal. These cells undergo an automated end-of-line test specified by the supplier ensuring proper production process capability and condition. Compared to prototype cells or cells from pilot plants, frequently used in aging studies, these cells offer superior quality and uniformity [165]. Results with high consistency can be achieved in such cases even with smaller test volumes. In addition, plausibility of the results of individual operating points can be verified by related operating points.

A unified test routine, commonly called check-up, should be used for the aging monitoring of all cells, regularly assessing the performance of all cells under test. The stress experienced by the cell during a check-up can have an impact on cell aging. Both calendar and cyclic load are given during a check-up. A trade-off between a high level of detail and a minimal cell load must be resolved. External influential variables such as ambient temperature and cell contacting are another important factors to ensure a reliable and accurate determination of the cell condition.

The battery lifetime in commercial applications reaches several years, which can not be tested under real conditions with aging studies. For this reason, the test duration is shortened by changing certain aging conditions. Usually, the temperature is elevated under the assumption of a so-called Arrhenius dependency. This dependency describes, especially for chemical processes, a rise in reaction speed with increasing temperature. Aging processes within a lithium-ion cell, such as side reactions between electrolyte and active materials, are to some extent also linked by such a relationship. The temperature dependency is expressed by the following equation [24]:

$$t_{\text{eff}} = t_{\text{ref}} \cdot e^{\frac{E_A}{R} \cdot (\frac{1}{T_{\text{eff}}} - \frac{1}{T_{\text{ref}}})} \tag{2.7}$$

Here t_{eff} describes the effective time at temperature T_{eff} to reach the same aging state as after a reference time t_{ref} at temperature T_{ref}. E_A indicates the activation energy and R the general gas constant. Extreme aging mechanisms caused by certain triggers, such as mechanical damage, lithium plating or gassing reactions, limit the simplified assumption of an Arrhenius relationship.

Further ways to shorten test durations are an adjustment of SOC, current rate or cycle depth (ΔDOD). However, for all three parameters direct cause-effect relationships are difficult to determine and vary greatly depending on the cell chemistry. In addition, higher current rates lead to enhanced self-heating of the cell, which in turn accelerates cell aging, if the temperature in the climatic chamber is constant or not controlled. It is necessary to ensure that aging effects associated with modified operating parameters remain clearly distinguishable.

Aging tests represent an essential part of battery component development, both in terms of design and safety. Understanding of application-specific load scenarios is essential to obtain relevant information about real-world aging behavior and to identify corresponding aging mechanisms. In vehicle applications, long downtimes as well as highly dynamic loads occur, which on their own are responsible for significantly different aging processes. For this reason, it is necessary to use a vehicle-related vehicle-cyclic load scenario in addition to the isolated cyclic and calendar load scenarios. In this way, an understanding of actual aging behavior in real applications is generated, so that misinterpretations, both overestimating and underestimating, are prevented.

3 Lithium-ion batteries in low-voltage vehicle applications

This chapter is based on a publication created during the course of the dissertation. It contains minor modifications with respect to the original publication. An introduction to electrical vehicle systems and a detailed overview of 48 V *systems are added. The use of the article content including illustrations from [166] is permitted with the consent of Elsevier.*

This chapter focuses on the application of low-voltage lithium-ion batteries in passenger cars and identifies characteristic stress factors to which the battery is exposed. First of all, the structure of a vehicle electrical system is introduced. Differences between a 12 V micro hybrid electric vehicle and a 48 V mild hybrid electric vehicle (MHEV) are illustrated. Both setup and functionalities are explained.

Since lithium-ion batteries have been installed in low-voltage vehicle applications for only a few years, few information exist regarding battery load scenarios during vehicle operation. Such information is essential for conducting application-oriented aging tests on cell level. For this reason, critical stress factors for the battery are characterized using real-world vehicle data from current 48 V development vehicles. Both a qualitative analysis and a quantitative analysis of the 48 V battery data from the vehicles are performed. Additionally, 48 V battery loads are compared to those of battery electric vehicle (BEV) applications. In Section 4.4 these insights are used to define aging matrices, which allow for a comprehensive analysis of battery aging. The resulting application-related aging matrices form the basis for the extensive aging studies performed during the course of this thesis.

3.1 Design of a vehicle electrical system

The purpose of the vehicle electric system is to link all electrical components and to ensure a sufficient power supply. Figure 3.1 shows a schematic structure of a vehicle electrical system including its connection to the combustion engine. Generally, a vehicle electrical system consists of a generator acting as energy converter, a battery acting as energy storage and a multitude of electrical consumers. In the following, a brief overview of the key functions of each component is provided.

In engine operation, the generator is responsible for maintaining a stable energy supply to the vehicle electrical system and additionally charges the battery. A belt drive connects the generator to the engine. While driving, the generator is controlled in order to guarantee

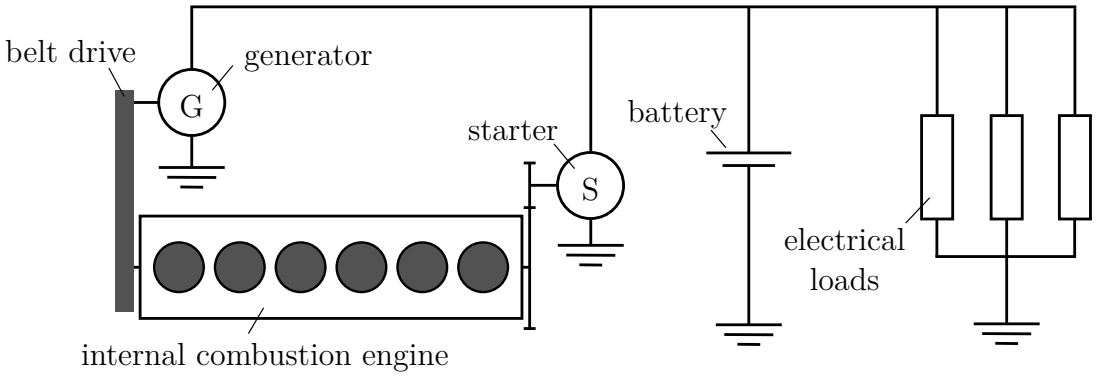

Figure 3.1: Schematic structure of a conventional vehicle electrical system including engine-related electrical components (own illustration, adapted from [167]).

a constant system voltage of about 14 V. However, due to the operating voltage of the battery, the conventional vehicle electrical system is referred to as 12 V vehicle electrical system [168].

For many decades, lead-acid batteries have become an integral part of vehicle electrical systems and are no longer used only as starter batteries, but also as on-board power supply batteries with enhanced vehicle electrification capabilities for improved efficiency. Lead acid technology offers various advantages explaining why it has been predominantly applied in vehicles in the past decades. Due to its high robustness against both high and low temperatures, it allows for flexible installation in different installation spaces. Furthermore, it offers high safety, low costs and a closed loop value chain [82]. Due to the increasing number of vehicle electrical system components and comfort functions, the energy demand and battery load in the vehicle have increased significantly [169]. In addition, stricter CO_2 regulations require a fleet-wide reduction in fuel consumption, which can only be achieved by additional vehicle electrification. Therefore, energy recovery, storage, and availability play a decisive role in low-voltage applications. The energy window required for these measures cannot be provided by a conventional lead-acid battery. An upsizing of the lead-acid battery is impossible due to installation space and weight putting the technology at its limits. In addition, regulatory discussions exist about a general ban on lead, which accelerates the transition to the use of lithium-ion batteries [170, 171]. A substitution of lead-acid batteries by high-power optimized lithium-ion batteries offers various technical advantages. On the one hand, lithium-ion batteries are more resistant to cycling and possess higher energy densities, both volumetrically and gravimetrically, which allows for a reduction in installation space and weight. On the other hand, large parts of the SOC range are usable with negligible consequences on the aging behavior. This provides a wide and flexible energy window for potential CO_2-reducing functionalities. A broad aging and performance comparison of six different 12 V batteries with different battery technologies, including both lead-acid and LFP batteries, was performed by Kollmeyer et al. [172]. They conclude that the LFP battery is superior to the other battery types both in terms of charge/discharge power and cycle life. However, costs of the LFP battery are the highest. A detailed discussion on the transition from lead-acid batteries to lithium-ion batteries

and the associated challenges was reported in a review by Ferg et al. [82].

The starter, an electric motor, accelerates the engine to the speed required to start the engine. The power is transmitted via a pinion directly to the engine's flywheel. Consequently, the starter is often referred to as pinion starter. A relay closes the electric circuit between battery and starter during the starting process. The battery is directly connected to the armature winding of the electric motor, so that a short circuit occurs. This short circuit enables the transmission of maximum currents to the electric motor. The voltage drop at the battery is determined by the resistance of the battery, the wires and the armature winding [167]. To obtain high starting power, these resistances have to be as low as possible. At low temperatures, both the internal resistance of the battery and the drag torque of the motor rise sharply, making it difficult to start the engine. Therefore, cold start capability is a critical requirement for the battery. In advanced vehicle network topologies the engine is usually started by the generator, see Chapter 3.2.1. Such systems require significantly higher power for the start of the engine, since the transmission ratio is lower compared to the pinion starter. Here, 12 V systems reach a power limit due to high currents and the low system voltage [167]. In addition, during recuperation phases the charge power is limited, resulting in little energy being recovered and CO_2 saving potentials not being fully exploited. Consequently, higher voltage levels are required.

3.2 48 V mild hybrid systems

A higher voltage level, which has become generally accepted among European car manufacturers, is the 48 V voltage level. Reason for the choice of the 48 V are the regulations concerning the touch protection voltage, which allows up to 60 V within vehicle components. This voltage limit also serves to distinguish between low-voltage and high-voltage components in the automotive sector. A direct current (DC) voltage greater than 60 V poses an imminent danger to life requiring additional regulations regarding personal protection measures, insulation monitoring, etc. [173].

48 V refers exclusively to the nominal voltage of the vehicle electrical system. During normal operation, voltage values between 36 V and 52 V can occur within the system without causing functional limitations [174]. Neither generating nor recuperating components may exceed the 60 V voltage limit. Therefore, a nominal voltage of 48 V includes a margin for short-term overvoltages, which ensures compliance with these regulations [175].

High electrical losses caused by high currents in the 12 V system can be significantly reduced by raising the system voltage to 48 V. In addition, both electrical cables as well as 48 V components can be designed smaller, which reduces weight and installation space in the vehicle [176]. Due to the higher electrical power capability, vehicles with a 48 V system are capable of performing additional consumption-reducing functions. Thus, these vehicles are so-called hybrid vehicles in which the electric motor performs subfunctions while the actual drive energy is provided by the internal combustion engine. The term MHEV has become generally accepted for such vehicle types.

3.2.1 System configuration

A mild hybrid system can be implemented through different system layouts. The different typology names of these MHEV systems, usually referred to as P0 - P4, are derived from the position of the generator [173]. Basically, with increasing number, the generator is further separated from the powertrain and thus enables both more electrified operating modes as well as higher powertrain system efficiency. Figure 3.2 shows a schematic structure of the powertrain installed in the 48 V vehicles, whose battery loads were analyzed in this thesis. The only difference to a pure internal combustion engine (ICE) vehicle is the more powerful belt-driven starter generator (BSG) operated with 48 V. The BSG is directly connected to the motor and cannot be operated independently. In the scope of this thesis exclusively a P0 system is considered.

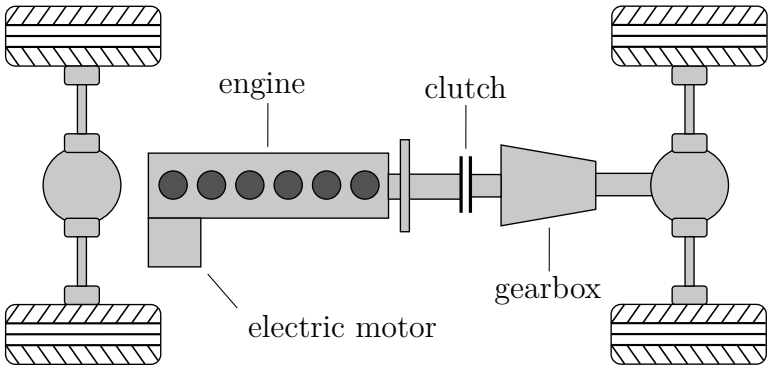

Figure 3.2: Schematic structure of a P0 system typology for the implementation of a 48 V vehicle electrical system. A comparable system is installed in the considered development vehicles.

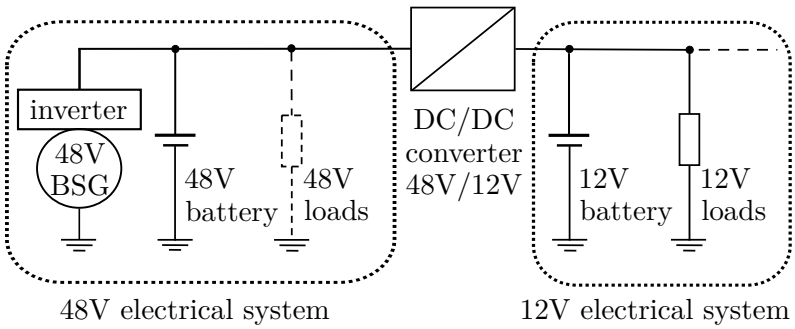

Figure 3.3: Schematic structure of a 48 V electrical system with a P0 typology.

A schematic structure of the electrical system of the analyzed vehicles is illustrated in Figure 3.3. The 48 V level is connected to the usual 12 V level by a DC/DC converter. Thus, it is an extension of the conventional 12 V vehicle electrical system. This approach allows for the use of existing components and structures so that fundamental developement of all components is unnecessary. Depending on the power demand and the market availability

of the component, electrical loads can be connected to 12 V or 48 V. This flexibility lowers the development costs of 48 V MHEV. The 12 V battery is usually a conventional lead-acid battery, whereas a lithium-ion battery is used at the 48 V level. Redundant availability of two energy storage devices enables a high level of safe energy supply for safety-related functions such as dynamic stability control or electric power steering.

3.2.2 Functions and efficiency enhancements

For a classification of MHEVs into the various levels of vehicle electrification, Figure 3.4 shows the different types of vehicle electrification including some characteristic functions. Here, system complexity is defined both by the number and diversity of system components and by the relationships between these components. [177]. In addition, the system complexity is proportional to the added expenses required for the given system. The reference for the CO_2 savings potential is a conventional internal combustion vehicle without further electrification functions.

Vehicles with minor electrification at 12 V level, as described in Chapter 3.1, are called micro-hybrids. In addition to a start-stop function, they offer a limited energy recuperation capability up to 5 kW and represent the lowest form of vehicle electrification [179]. The start-stop function allows for the combustion engine to be switched off during stop periods, for example at a red light. In these periods the energy demand of the electrical consumers is fully covered by the 12 V battery. Micro-hybrid systems are extremely attractive for automobile manufacturers due to their low system complexity and ease of integration into existing vehicle architectures. Such systems allow for fuel savings of 5 % to 10 % with little additional cost and effort [175].

Further enhancement of the degree of electrification and the CO_2 savings potential requires substantial changes to the conventional vehicle electrical system. This is where MHEVs and full hybrid electric vehicles (FHEVs) are located. The main difference between these two systems is the electrical power capability and the battery capacity. In addition, FHEVs offer separate use of the drive systems, internal combustion engine and electric motor, so that short distances (<5 km) can be driven electrically.

PHEV focus on increasing the electrical range and power capability. In PHEVs, two complete and independent drive systems are installed, so that most of the day-to-day driving distances are covered electrically. The aim of this system is to enable local emission-free driving while simultaneously taking advantage of the long-range advantages of the internal combustion engine. However, the existence of two independent drive systems and a high-voltage battery pack with external charging capability lead to a significant rise in system complexity in terms of safety requirements, software functions and component needs. In addition, external charging capability requires significant technical and software development and validation activities. With the use of a fully electrical drivetrain architecture, where fewer components and integration needs as well as cross-functional dependencies exist, the complexity of the system drops.

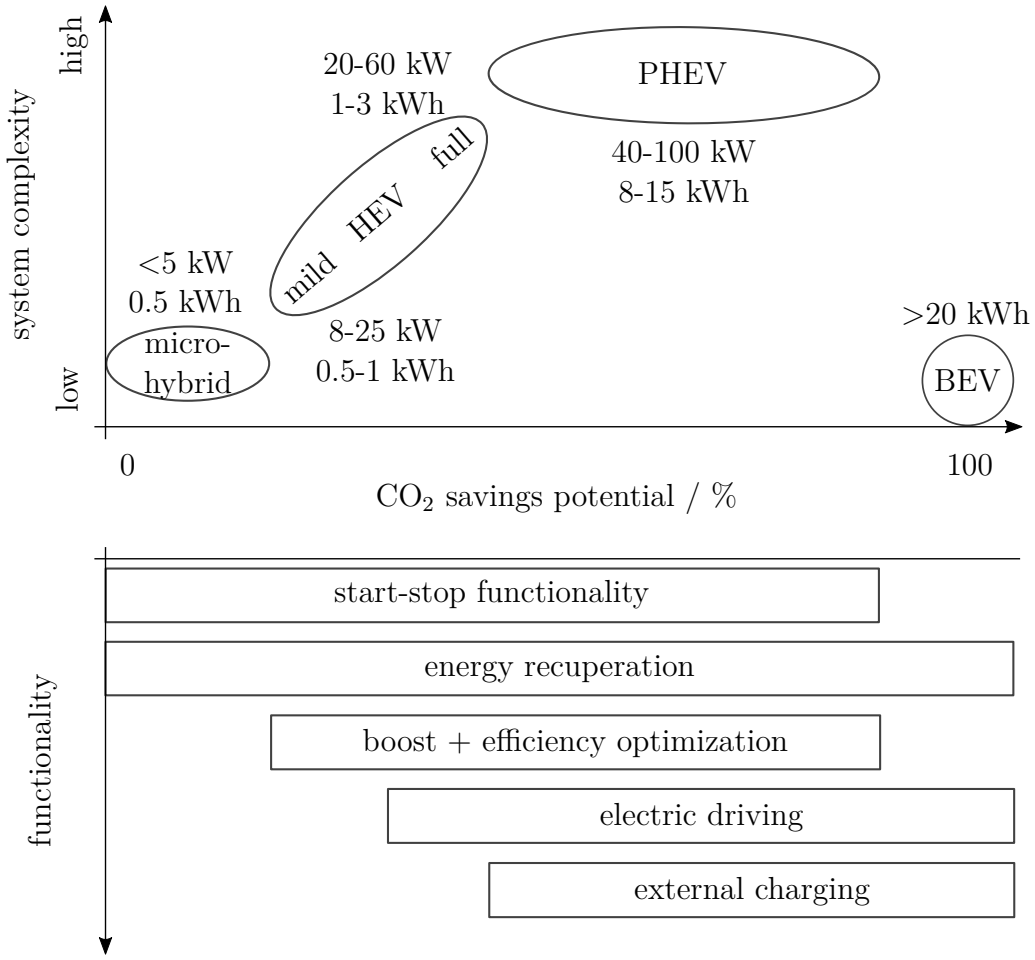

Figure 3.4: Classification of different electrification levels of passenger cars (micro hybrid, mild/full hybrid electric vehicle (HEV), plug-in hybrid electric vehicle (PHEV), BEV) regarding both system complexity versus CO_2 savings potential as well as related vehicle functions (own illustration, adapted from [178]).

Unlike PHEVs and BEVs, MHEVs do not offer external charging. Charging of the 48 V battery is done by recuperation phases or the internal combustion engine. MHEVs offer a high cost-benefit ratio, especially considering potential CO_2 fines [175]. With this electrification level a reduction of fuel consumption of up to 15% is feasible [180, 181]. Further functions of a MHEV system can be clustered into the categories comfort, efficiency and dynamics:

Comfort Substantial enhancement of comfort is achieved due to the more powerful 48 V generator affecting both general motor starts and the start-stop function. The 48 V generator accelerates the engine to higher rotating speeds faster which reduces engine vibrations. In addition, higher electrical system power enables the engine to be switched off at low speeds during deceleration. This minimizes the perception of start-stop events.

Efficiency The 48 V system can systematically adjust the load point of the motor. Thus, the engine can mostly operate with high efficiency reducing fuel consumption. In situations without thrust, the vehicle is able to operate in sailing mode with the engine switched off. In this mode the on-board power supply is provided by the 48 V battery. Sailing mode is energetically beneficial, as unlike in recuperation phases, no energy conversion losses occur.

Dynamic Under peak load conditions, the 48 V system can boost the combustion propulsion and provide additional system power. The electrical torque is provided even at low engine speeds where a conventional turbocharger is unable to reach its full power. In addition, the 48 V system allows for the integration of additional power-intensive components such as electric turbochargers for further optimization of driving performance[(i)].

The additional functions of the 48 V system result in characteristic loads on the 48 V battery. In the following, battery stress factors are analyzed and their criticality regarding battery aging is evaluated.

3.3 Determination of application-specific aging conditions

For vehicle manufacturers, there is an ambivalence between achieving the lifetime requirements of the overall system and the objectives for manufacturing cost and vehicle weight. Since the installation space in the vehicle is extremely limited and, moreover, not flexibly selectable, different requirements arise for the high-power lithium-ion battery used in such a system. With regard to the electrical loads, the power to be supplied and absorbed by the battery in a 48 V system is usually limited by the generator power and can be up to 25 kW [182]. At pack level this can result in charge and discharge currents of up to 500 A. By using small battery pack sizes and capacities with typically one serial string, peak currents of up to 30C for several seconds can occur at cell level. In addition to significant self-heating of the pack because of high loads, installation space in many vehicles is located in the engine compartment or the rear end of the car, in which the pack is exposed to high temperatures. Only state-of-the-art high-power lithium-ion batteries are able to endure these conditions for an extended period of time. The fulfillment of all mentioned requirements must be taken into account in the validation process of the component development.

In previous publications the 48 V mild hybrid technology has already been addressed. A basic overview of the components and functions of a 48 V system was presented by Mahr et al. [176]. Kuypers et al. [181] evaluated the technical integration of the 48 V system into an existing 12 V system and discussed the handling of possible failure modes. An

[(i)] The 48 V vehicles examined as part of the following analysis were not equipped with additional 48 V consumers.

optimal operating strategy for the parallel connection of a 12 V lead-acid battery and a 48 V lithium-ion battery was analyzed by Bae et al. [183]. A detailed introduction of potential 48 V system topologies and operating modes was postulated by Bao et al. [173]. In addition, they demonstrated the impact of the system layout on the efficiency of the powertrain system. Liu et al. [184] investigated the influence of external factors, such as the aggressiveness of the driving style, on the vehicle consumption. They found that hybridization is relatively more beneficial when driving aggressively.

The outlined studies explore in depth various topics related to the 48 V system. Nevertheless, a comprehensive, application-oriented investigation of the load scenarios of a 48 V battery in driving operation is missing. These stress data are essential to improve the component design and to avoid serious durability issues. In addition, they enable application-oriented aging tests in the course of cell validation.

For a study of battery aging by application-specific load, a distinction between three different categories has to be made. Most commonly, artificial cycles with constant load are used. These cycles allow for the best separation between different aging factors. In most cases they have no real application relevance, but instead are easy to define and apply. Secondly, cyclization can be based on high-resolution real world duty cycles. These load profiles are created using real driving profiles. They can represent the entire complexity of real-world usage such as operating strategies and driving behavior. However, a statistical analysis is needed to extract correlations between aging phenomena and operating conditions. The third type, which tries to combine the advantages of the first two methods, is the use of application-oriented artificial duty cycles. These cycles are usually compiled using statistical evaluation of real-world data from vehicles. Their comprehensible structure and clarity make it easier to draw conclusions about aging phenomena and their origins [185].

Frequently, the term real-world data refers exclusively to the underlying driving profiles, which serve as an input for system simulations. Speed data of vehicles have comparatively good availability, especially if powertrain topology and vehicle type are of minor interest. By using full vehicle simulations, large amounts of data can be generated that include the individual component data of the virtual vehicle. This involves various risks and potential errors. On the one hand, the vehicle model does not completely cover the complexity of the entire vehicle system, in particular with regard to the operating strategy. On the other hand, the simulation of all operating parameters involves the risk of systematic errors. Such errors can only be prevented through comparison with real vehicle data from the corresponding component. Ideally, logged data are used for the entire drive cycle and load analysis. On the one hand, these data can serve to characterize the criticality of the various operating parameters. On the other hand, it can enable a transfer of the individual operating conditions into testable synthetic cycles.

3.3.1 Scope of the 48 V vehicle data and data processing

The vehicle data, which are analyzed subsequently, were obtained from 48 V development vehicles. Here, vehicles of two vehicle classes (midsize, large) were used for testing, all of which had installed a comparable 48 V system with identical components. Thus, differences in system behavior can only result from the vehicle characteristics themselves, such as engine type, additional equipment or weight. This can lead to small deviations in terms of the overall vehicle electrical system and battery loads. The data were collected in two large-scale trials, which are categorized in hot climate and cold climate based on the given outer climatic conditions. During more than 60 test drives over 7000 km were driven. Indicated by the driving speed, the car rides cover all relevant scenarios of urban, intercity and motorway travel. Due to speed limits in the respective countries, extreme trips with more than 150 $\frac{\text{km}}{\text{h}}$ could not be accomplished. The average trip time was 127 min and the average distance traveled was 111 km. This is far higher than the average travel distance by private customers. Therefore, the data are solely called customer-oriented, although this will have a neglectable impact on the results presented in this thesis.

The battery pack data were read out directly from the battery management system via controller area network (CAN) interface and stored with the help of in-vehicle measurement technology. The signals examined are current, voltage, temperature, SOC and vehicle speed. Since the measuring electronics was not able to store different signals with a uniform frequency, all data signals were normalized to a frequency of 50 Hz.

Figure 3.5 shows data of a 250 s cutout of an exemplary trip. In the upper plot both speed and acceleration of the vehicle are illustrated. The corresponding charge and discharge power of the battery is depicted in the lower graph, with the colored area below the curve reflecting the energy balance. The constant power output of approx. 600 W corresponds to the base vehicle electrical system load. In addition, boost and recuperation phases of several seconds are recognizable by acceleration values and corresponding power peaks of the battery. However, the power profile is less volatile than the acceleration curve. In addition to data from 48 V vehicles with 10 Ah batteries, battery data from a BMW i3 with a 60 Ah battery are used for comparative purposes. Data recording was done in the same way as described above.

3.3.2 Evaluation of critical stress factors

48 V batteries are exposed to various load scenarios within the vehicle, which affect the aging of a lithium-ion battery in different intensities (see Chapter 2.2). Detailed understanding of these loads is essential to identify potential degradation mechanisms and to perform relevant lifetime tests. In the following, main stress factors occurring in a 48 V application are analyzed and classified.

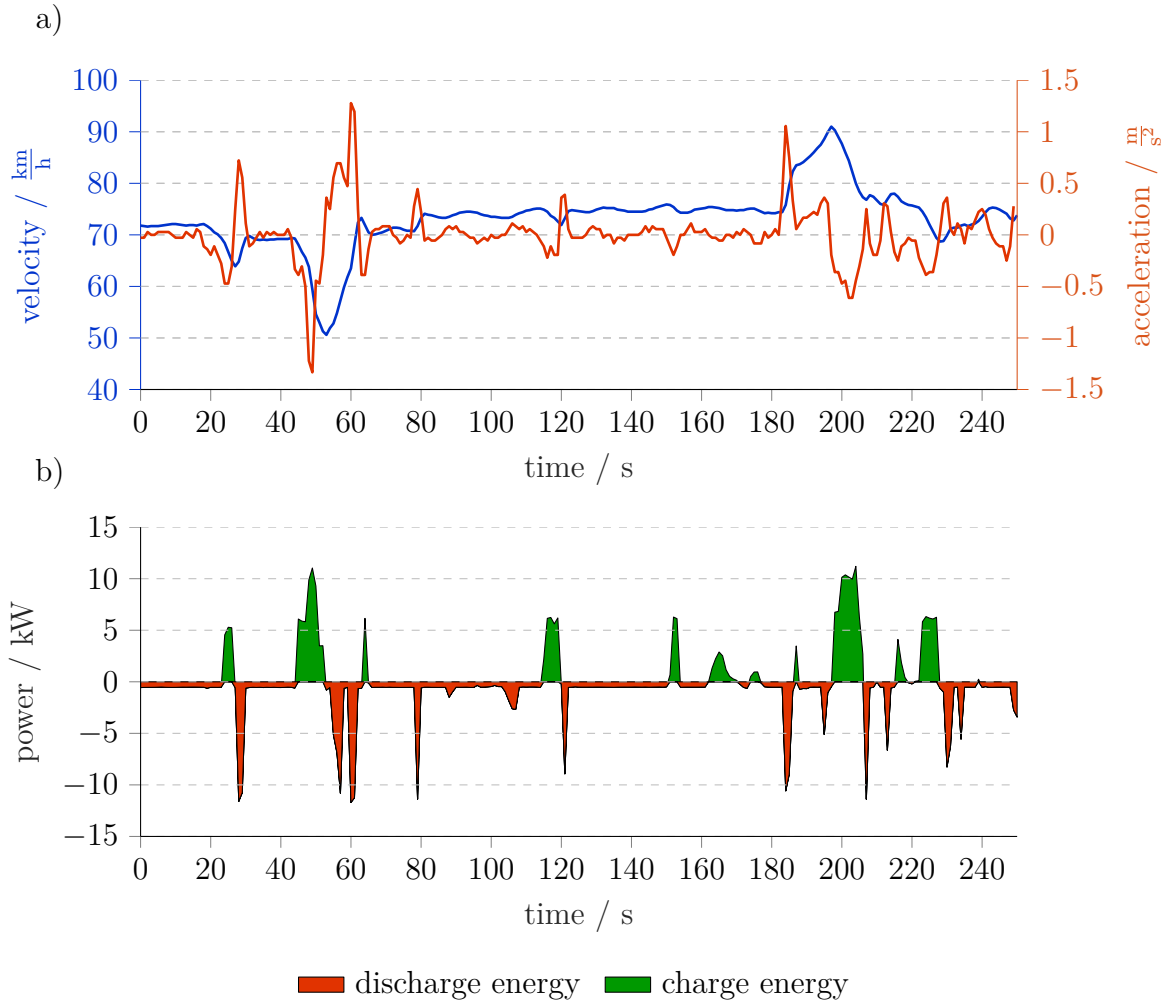

Figure 3.5: Exemplary part of a drive cycle. (a) shows the speed and associated acceleration values. (b) illustrates the resulting load and energy throughput of the 48 V battery.

3.3.2.1 Temperature

The use of lithium-ion batteries in common ICE vehicles poses major challenges, especially with regard to temperature. So far, lead-acid batteries have been used for electrical power supply, technically engineered as a wearing part with relatively low replacement costs and high temperature resistance. Due to significant higher costs of lithium-ion batteries, their lifetime is designed to be equivalent to that of the vehicle. This lifetime is usually defined as 8 years or 200.000 km. By integrating the battery into existing vehicle architectures, an optimum space for the component is not available. Usually, the battery is installed within the engine compartment or trunk. Both spaces are characterized by very high temperatures due to waste heat of the engine and the exhaust system.

Under cold climatic conditions, the variance of the battery temperature is extremely high. Figure 3.6 shows a frequency distribution of the battery temperatures that occurred during

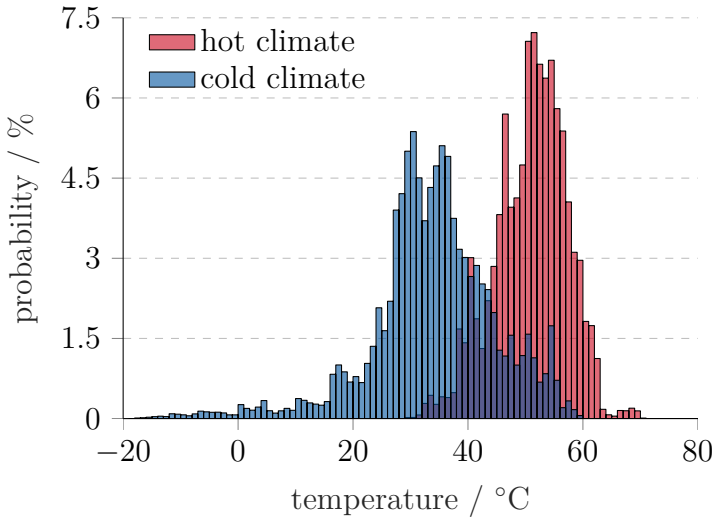

Figure 3.6: Frequency distribution of the temperature of the 48 V batteries while driving. A differentiation is made between temperatures during hot and cold country trips.

the test drives. The results from the hot countries are separated from those of the cold countries. In cold countries the battery reaches temperatures between −18 °C and 60 °C. However, the likelihood of occurrence of very low temperatures less than 0 °C is below 2%. The most common temperature is 30 °C. The high variance demonstrates the need to use electrolytes and additives with a large temperature operating window. Here, the electrolyte has to exhibit a sufficiently low viscosity and ionic conductivity at low temperatures and at the same time be stable enough to resist decomposition at high temperatures [104, 105]. In addition, electrical and aging tests within the relevant temperature window have to ensure that short-term and long-term battery performance requirements are met. This can, for example, allow for a minimization of the risk of lithium plating in case graphitic anode materials are used and charging processes in cold temperatures are performed. [186]. Knowledge of the high temperature span assists in long-term assurance of operational stability and minimization of failure probabilities.

Under hot climatic conditions, severely high battery temperatures occur. Here, a most common temperature of 52 °C and a mean temperature of 50.4 °C are measured. In 5% of the time the battery temperature exceeds 60 °C. In addition, temperatures higher than 70 °C do not occur due to forced power degradation, which is implemented within the operating strategy. The results suggest that either the cooling is undersized or the heat dissipation from the battery pack is insufficient. Most battery cells available on the market are not applicable in such temperature ranges or do not reach the required lifetimes. Thus, the development of special high-power batteries with high robustness against high temperatures and with very low internal resistances to minimize self-heating is required. In addition, an improved battery cooling strategy or a different installation space for the battery, for example within the passenger compartment, can lower the temperature conditions. At this point, a trade-off between costs and benefits has to be made to meet

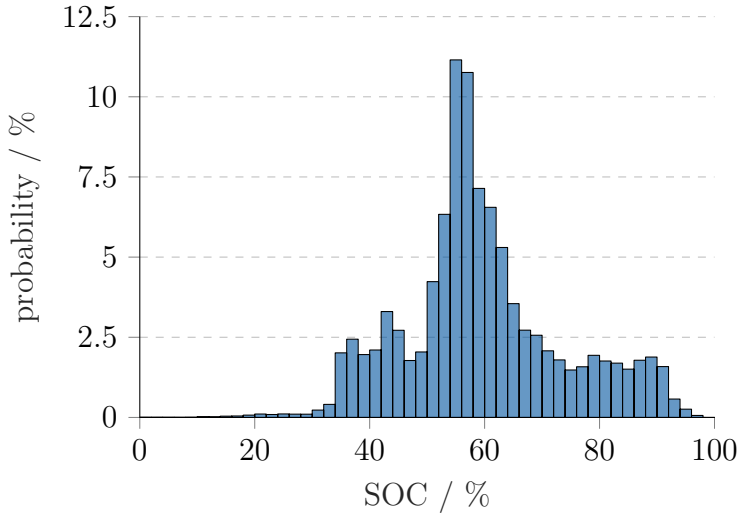

Figure 3.7: Frequency distribution of the states of charge of the 48 V batteries reached during the test drives.

the battery lifetime requirements.

Since the temperature in the surrounding areas greatly influences the battery temperature, the distribution will be different for every powertrain technology and component installation space under consideration. Therefore, a repetition of this temperature investigation is essential for every relevant vehicle architecture.

3.3.2.2 State of charge

Various authors have found that the SOC has a strong impact on the aging processes within the battery [124, 128, 187, 188]. However, the level of influence varies depending on the cell chemistry.

In the MHEV application, not the full SOC range is used. Figure 3.7 depicts the frequency distribution of all SOCs that occurred during the test drives are plotted. The used SOC range is, apart from rare outliers, between 34% and 92%. The mean SOC is 55%. This shows that the operating strategy implemented in the battery management system is designed to hold the battery in a middle region preferably. Some of the considered test drives took place in mountainous terrain. These conditions may favor the likelihood of higher states of charge due to long recuperation phases. The avoidance of low SOCs, even if these are favorable in terms of aging, is necessary to ensure sufficient energy reserves and peak power for sudden emergency situations, such as a failure of the combustion engine. Higher SOCs at cold temperatures increase the risk of lithium plating, but enhance power reserves in discharge direction [189]. However, it is essential that the operating strategy effectively prevents high charging currents in these conditions. Overall, the measured SOCs of the 48 V battery do not represent critical operating parameters with respect to aging.

3.3.2.3 Current rate

High charge and discharge rates have been identified as one of the causes of accelerated aging [131, 132]. Rapid lithiation and delithiation processes intensify the mechanical stress which can cause fatigue and destruction of crystal structures within the active material. Further, inhomogeneous particle sizes can among other factors induce local overcharging, resulting in lithium plating. High current rates increase the ohmic losses within the battery leading to higher temperatures and the acceleration of side reactions.

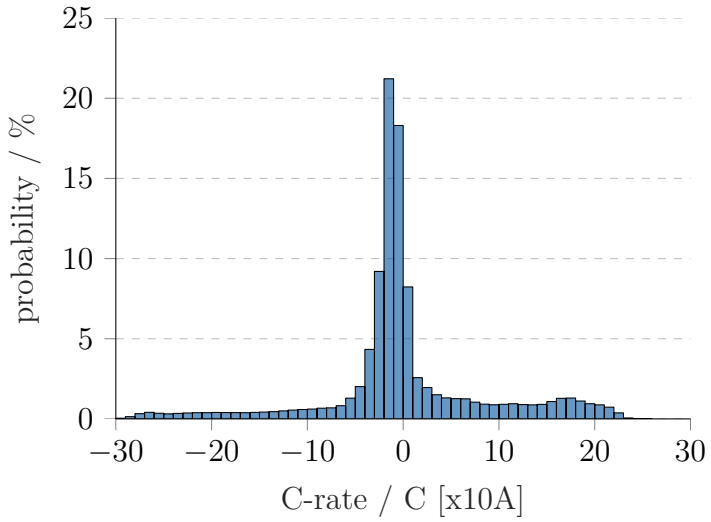

Figure 3.8: Frequency distribution of the current load on the 48 V 10 Ah batteries in charge and discharge direction during the time of vehicle operation. Positive current corresponds to charging.

The 48 V application is characterized by high charge and discharge currents requiring the use of high-power batteries. Figure 3.8 shows the frequency distribution of all battery currents in charge and discharge direction measured in the vehicles. The case of a current $I = 0\,A$ is not integrated in the consideration, since it has no significance for the cyclic stress of the battery. Further, it significantly improves the clarity of the figure. The bandwidth of current loads is between -30C in discharge direction and 24C in charge direction. Although the range of discharge currents is wider, current rates greater than 5C are more likely to occur in the charge direction. Overall, the likelihood of currents higher than 5C is 30%. This means that nearly one third of the time, current rates are present that conventional lithium-ion cells can only withstand for short periods of time.

High currents lead to large ohmic losses that must be dissipated from the battery. At the same time, it is the goal of car manufacturers to minimize the battery size both in terms of package and capacity. For this reason, only state-of-the-art high-power lithium-ion batteries with extremely low internal resistance ($\ll 1\,\mathrm{m\Omega}$ at 25 °C, 1C, 50% SOC) can be used in such an application. The high occurring currents must be part of both electrical begin-of-life characterization tests and aging tests. Appropriate tests must be executed exclusively with suitable measuring equipment.

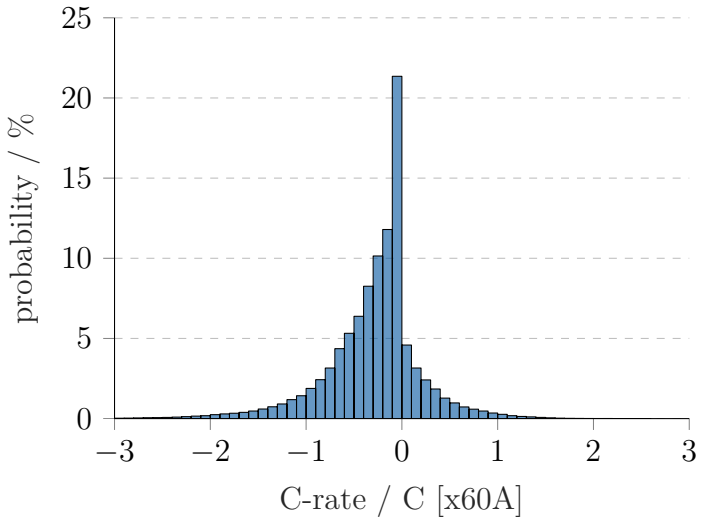

Figure 3.9: Frequency distribution of the current load of the high-voltage battery in a BMW i3 in charge and discharge direction during the time of vehicle operation. Positive current corresponds to charging. Periods of external charging are not included.

Both the system topology and the battery can limit the performance of the system. For batteries, these limits are defined in the operating strategy. The aim of this strategy is to keep the battery within the operating range approved by the manufacturer and thus to protect it from long-term damage. In the investigated vehicles the generator limits the power rating within the system topology. If the battery is not restricted by SOC, temperature, or aging and no buffer is kept in the operation strategy, maximum currents can be calculated by the power limits of the generator.

The cell-specific electrical load of the 48 V battery is significantly higher than that of a battery in a BEV. As can be seen in Figure 3.9, the currents within the battery pack of a BMW i3 are almost entirely smaller than 2C. In the MHEV application, most frequent currents are between 1C and 2C. This corresponds to the base load in the electrical on-board network, which was also apparent in the power curve of the driving profile in Figure 3.5. This load is caused, for example, by the air conditioning, the steering system, or the brake. In BEV applications, the entire energy supply takes place via the battery and the focus of battery design is on energy density. By using high voltage levels, usually 400 V or 800 V, and multiple strings in parallel, resulting cell-specific current loads can be kept comparatively low even at peak power. A simple transfer of test specifications from BEV to MHEV batteries is therefore not possible.

3.3.2.4 Cycle depth

Due to short recuperation and boost processes in the range of seconds, average ΔDODs of the battery within a 48 V system are small. This observation is visualized in Figure 3.10, where a frequency distribution of all ΔDODs is plotted. Here, the ΔDOD is calculated

with a rainflow algorithm. Over 50% of all cycles are smaller than 2%. The stress on the active material, for example due to the volumetric expansion of the graphite, is significantly lower than for full cycles (100% ΔDOD). The influence of the ΔDOD on the cycle life is often shown in the literature by a Wöhler curve. Here, battery lifetime, indicated by number of full cycles equivalents[(ii)] till the end-of-life criterion is reached, increases with decreasing ΔDOD. Frequently, full cycles are used to test and validate battery lifetimes in order to obtain worst-case lifetime estimations. These results can be relevant for the design of begin-of-life battery capacities and performance capabilities.Thus, knowledge of the application-relevant ΔDODs and their impact on battery lifetime is essential to prevent an over-dimensioning.

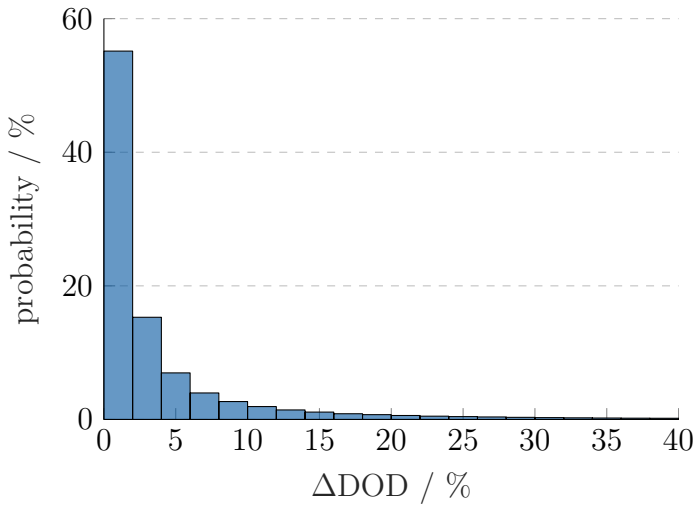

Figure 3.10: Frequency distribution of the ΔDOD of the 48 V batteries for all investigated trips during the time of vehicle operation. The calculation of the ΔDOD is done using a rainflow algorithm.

3.3.2.5 Energy throughput

The total energy throughput, in analogy to full cycle equivalents, is a good indicator for the durability of a lithium-ion battery. In applications such as the 48 V system where no long-term observations exist, the energy throughput of the battery component over lifetime is difficult to determine. In addition, the operating strategy and system topology have a major impact on energy throughput. In the new product development process, component requirements are defined by applying complete vehicle simulations. For this reason, it is important to use real-world data from pre-series vehicles as early as possible to validate simulation data and to prevent improper technical designs.

[(ii)] Full cycle equivalents normalize the charge throughput of cycles with different ΔDODs to the nominal capacity (C_N) of the battery and thus provide better comparability. For one full cycle equivalent, the cell has to undergo a charge throughput of 1 C_N in both charge and discharge direction.

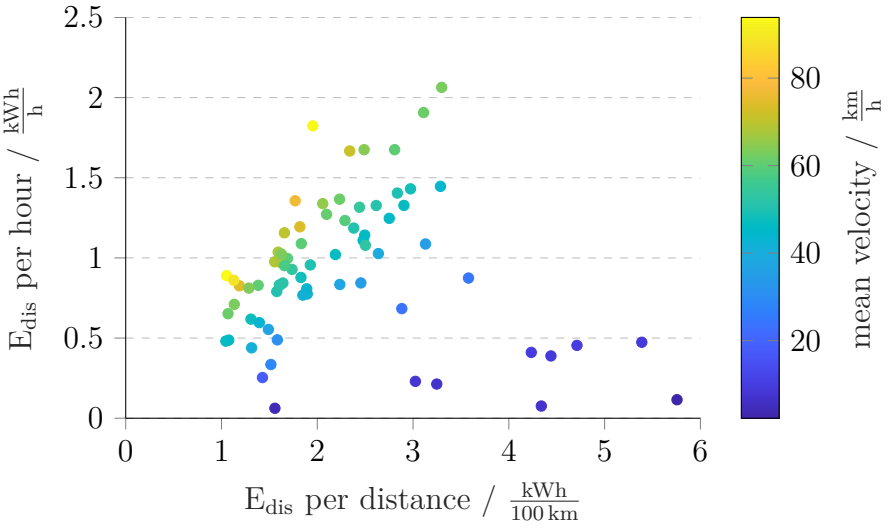

Figure 3.11: Representation of the average energy throughputs per trip in discharge direction (E_{dis}) as a function of average speed. A differentiation is made between energy throughput per unit of time and energy throughput per distance.

Single drive cycles do not provide the data basis for battery designs due to a large variance in specific energy throughputs. The energy throughputs in discharge direction of all test drives are shown in Figure 3.11 as a function of distance and time. In addition, the average speed is highlighted in color. Based on the energy throughput per distance, the values vary between 1 $\frac{\text{kWh}}{100\,\text{km}}$ and almost 6 $\frac{\text{kWh}}{100\,\text{km}}$. In terms of time, energy throughputs arise between 0.05 $\frac{\text{kWh}}{\text{h}}$ and 2.07 $\frac{\text{kWh}}{\text{h}}$. The data illustrate that a conclusion of individual car rides on a universally applicable load of the battery storage is not given. For statistically valid statements regarding the design of MHEV batteries, as much driving data as possible have to be analyzed. Alternatively, it must be examined which influencing factors have the greatest impact on the energy throughput.

For the lithium-ion battery, very high energy throughputs arise over the lifetime of a vehicle. Taking the lifetime requirement of 200,000 km into account, energy throughputs of up to 12 MWh at pack level can be achieved in a worst-case scenario. Based on the values shown in Figure 3.11 and on the assumption of having installed 20 NMC|LTO cells in a battery pack, energy throughputs between 200 kWh and 600 kWh can be obtained at cell level. For a 10 Ah cell with a rated voltage of 2.2 V, this results in over 27,000 equivalent full cycles. Therefore, the lithium-ion battery used has to be extremely cycle-resistant. Due to limited testing time, this energy throughput can only be achieved with an increase of the current rates in cycling aging tests.

The average speed during the documented rides is an indication of the time or distance-related energy throughput only in the border areas. Trips at very low speeds generate a high energy throughput in relation to the distance. The same applies to the relationship between high speeds and time. However, even at high speeds a base energy throughput of approximately 1 $\frac{\text{kWh}}{100\,\text{km}}$ is measurable. For the development of a 48 V battery, it must be

determined whether a lifetime criterion related to distance or operating hours should be defined. If, as described above, 200,000 km are used as lifetime requirement, consideration of car rides with low average speeds is appropriate.

3.3.3 Conclusion of the application-specific aging conditions

Real-world battery data from MHEV were examined and both characteristic and critical operating conditions of 48 V batteries were derived. For this purpose, vehicle data of over 70 test drives were statistically evaluated and analyzed with regard to cell aging affecting battery parameters.

The 48 V battery in the considered P0 typology is operated at a very wide temperature range (−20 °C to 70 °C) with extremely high average temperatures. In addition, it is mainly burdened with small ΔDODs (<5%), high short term current loads (more than 20C) and high energy throughputs over lifetime (>20,000 equivalent full cycles). The factors temperature, current rate and energy throughput are considered most critical with respect to aging. The variance of the energy throughput, normalized by distance or time, was very high for the investigated trips. For this parameter, a large sample size is important to ensure high validity and thus to provide a worst-case estimate for vehicle-relevant lifetime requirements.

In comparison to the battery cyclization within a BEV application, significant differences in current rates and ΔDODs were identified. The special requirements of a 48 V system must be taken into account in the development process and validation management. The data analysis carried out in this chapter enables an improvement of application-oriented aging studies and is thus able to reduce test effort. At the same time, the findings regarding load parameters facilitate the screening of possible cell candidates for a 48 V application.

4 Experimental and methods

Parts of this chapter are based on four publications created during the course of the dissertation. It contains minor modifications with respect to the original publications and supporting data. The use of the article content including illustrations from [114, 166, 190, 191] is permitted with the consent of Elsevier.

The analysis of battery data from the investigated 48 V vehicles in Chapter 3.3 showed that the loads of lithium-ion batteries in MHEVs are exceptionally high and different from those in high-energy applications. The wide operating range, for example regarding power capability and temperatures, has to be provided by a cell candidate both at begin-of-life and throughout the specified lifetime. To ensure compliance, cell tests have to be designed specifically for these load scenarios.

In the light of the previous findings, this section presents an overview of the cell tests and analysis methods that were conducted during the course of this thesis.

The cell tests can be divided into electrical characterization tests and aging tests. Although this thesis focuses on the performance and aging characteristics of a LTO-based cell type, two additional cell types with other cell chemistries were investigated to obtain a broad electrical performance benchmark. All aging tests were performed exclusively on the LTO-based cells. For this purpose, calendar, cyclic and drive-cyclic aging experiments were defined and implemented, which were both application-specific and cell chemistry specific. A uniform and detailed aging monitoring allowed for the identification of critical operating parameters as well as the determination of dominant degradation mechanisms. Reversible and irreversible aging effects were investigated using non-invasive and destructive methods, all of which were described in detail below.

4.1 Cells under investigation

In this thesis three different cell types were investigated, which differ particularly with respect to cell chemistry and form factor. A detailed overview of the cell properties is shown in Table 4.1. With power densities of about 2300 $\frac{\mathrm{Wh}}{\mathrm{kg}}$ to over 8000 $\frac{\mathrm{Wh}}{\mathrm{kg}}$ all three cells are classified as high-power cells (see Figure 2.1). Here, the manufacturers' specifications for peak power are not necessarily the absolute power limits of the cells but rather a conservative estimate. High quality and uniformity of the cells was assumed, since all cells were mass produced on high volume production lines, which underwent an automated end-of-line test specified by the supplier.

The NMC|LTO cell has a nominal capacity of 10.6 Ah and is the smallest both volumetrically and gravimetrically. Its active material and electrolyte composition is designed for extremely high pulse currents (>100C) and a wide temperature window ($\Delta T = 100\,°C$). Compared to the prismatic NMC|C cell and the pouch LFP|C cell, the pouch NMC|LTO cell provides the lowest capacity. However, the energy density of the NMC|LTO cell differs only slightly from that of the LFP|C cell.

Table 4.1: Specifications of the investigated cell types according to the manufacturers' data sheets. The size of the electrode sheets of the NMC|LTO cell has been measured after cell opening.

Cell type	NMC|LTO	NMC|C	LFP|C
Nominal capacity (Ah)	10.6	16	20
Cell format	Pouch	Prismatic	Pouch
Weight (g)	296	487	836
Size w/h/d (mm)	150/137.5/8.8	149/77/24.5	137/295/8.9
Nominal voltage (V)	2.2	3.7	3.3
Upper voltage limit (V)	2.65	4.2	3.6
Lower voltage limit (V)	1.9	2.8	2.0
Max. pulse discharge current ((A), 1 s, 25 °C)	1,100	1,010	600
Max. pulse charge current ((A), 1 s, 25 °C)	1,100	940	600
Max. continuous discharge current ((A), 25 °C)	200	240	300
Max. continuous charge current ((A), 25 °C)	200	240	300
Max. pulse discharge power density ($(\frac{W}{kg})$, 25 °C)	8,175	7,673	2,368
Energy density ($\frac{Wh}{kg}$)	78.8	121.5	78.9
Operating temperature (°C)	-30 - +70	-30 - +55	-30 - +60
Clamping torque (Nm)	1.75	-	0.4
Anode sheet area (mm^2)	130.29	-	-
Cathode sheet area (mm^2)	137.28	-	-

As discussed in Section 2.2.2 regarding the PEE, the anode of graphite-based cells is typically geometrically oversized. For the examined NMC|LTO cell this is not the case. Here, the size of the cathode sheets is approximately 7 cm^2 larger. Due to the high electrochemical potential of LTO, inhomogeneities of the current distribution in LTO edge areas are not critical for the cell lifetime (low risk of plating). The extent to which this geometrical arrangement affects the PEE is investigated in Section 6.1.2.

4.2 Test setup and measuring equipment

The pouch cells (NMC|LTO and LFP|C) were clamped with constant-path between two aluminum bracing plates with torque specified by the manufacturer (see Table 4.1). No external pressure was applied to the prismatic NMC|C cell, as the metal casing itself

applies pressure to the cell. Clamping of cells is a common procedure and has a beneficial effect on cell performance. The pressure ensures a good electrical contact between the cell materials, which is important, for example, in case of strong gas formation. Moreover, it simulates the application scenario in a battery pack where the cells are exposed to a similar level of pressure. Due to the low internal resistances of the examined cells and the testing with high current rates, all measurements were carried out using the four-pole measuring principle to increase measuring accuracy. In addition, two temperature sensors were attached in the middle of the cell and between the cell tabs. For this purpose, small holes were drilled in the clamping plates of the pouch cells. To prevent inhomogeneities, these holes were leveled with filling compound after the sensors had been attached. Exemplary for a NMC|LTO cell, Figure 4.1 shows a basic test bench setup within the temperature chamber.

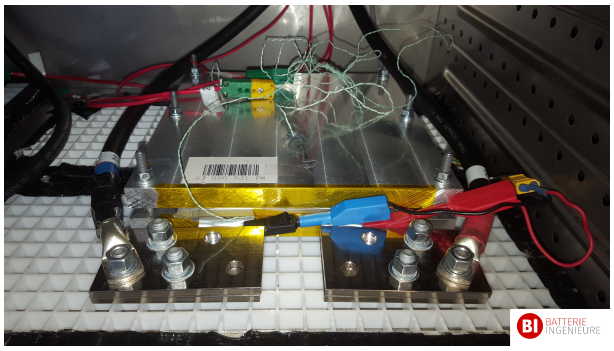

Figure 4.1: Test bench setup with a tightened NMC|LTO pouch cell. All measurements were carried out using the 4-pole measuring principle. Temperature was recorded in the middle of the cell and towards the top of the cell between the tabs. The test setup and the shown picture were created by the BatterieIngenieure GmbH in Aachen.

The formation of the cells was carried out by the cell manufacturer and the cells were in an unused state prior to test start. At the beginning of each test a short characterization test was performed, which includes both capacity tests and pulse tests. This routine verifies the proper electrical connection and cell functionality. The measuring equipment used for the different tests is listed in Table 4.2 and 4.3. Except for the second test series of the calendar aging, all cell tests were conducted by BatterieIngenieure GmbH in Aachen as specified.

Table 4.2: Technical data of the measuring equipment used for the characterization tests, the calendar aging tests (test series 1) and the cyclic tests.

Device	Manufacturer	Accuracy
Cell tester	Digatron MCT 300-06-12 RE S	0.1% of full scale (I), 0.05% of full scale (V)
	Digatron MCT 300-06-4(3)ME	0.1% of full scale (I), 0.1% of full scale (V)
	Neware CT-4008-5V 100A-NA	0.1% of full scale (I), 0.1% of full scale (V)
External data logger	Gantner Q.Station 101	0.01% - 0.05% (I), 0.01% - 0.05% (V)
Climate chamber	Binder model MK 240	up to ±2K

Table 4.3: Technical data of the measuring equipment used for the calendar aging tests (test series 2).

Device	Manufacturer	Accuracy
Cell tester	Scienlab SL6/300/1.8BT4C	±0.05% of measured value, ±60 mA (offset) ±1 mV
Climate control	CTS T-40/350/Li	±0.3K

4.3 Electrical characterization measurements

The three different cell types were subjected to a series of electrical characterization tests, which are described below. Each of these measurements was performed with two NMC|LTO, one NMC|C and two LFP|C cells. The studies aimed to quantify both the characteristic behavior in electrochemical equilibrium and the highly dynamic behavior under load in a uniform and comparable way. The loads in the dynamic measurements were chosen according to the requirements in a low-voltage vehicle application. Thus, the cell performances can be compared with each other and the usability of the cells in a corresponding application can be evaluated.

4.3.1 Open circuit voltage

Two methods are commonly applied to determine characteristic open circuit voltage (OCV)-curves. For the first method, a very small current (usually smaller C/20) is used to measure the voltage response during charge and discharge. This type of OCV is often called quasi-stationary open circuit voltage (qOCV), because it is observed exclusively in the unrelaxed state. Deviations can be expected due to the kinetic influences and the associated overvoltages, in particular in boundary areas of the SOC [192]. For this reason the second method, the so-called incremental OCV method, was used in this study, in which a stepwise measurement of the OCV is performed [193]. The significantly higher time expenditure of this method is subordinated to the considerably increased accuracy. Thereby a relaxation time of several hours is set after each defined SOC level. This allows for the cell to reach a state close to equilibrium before the actual OCV measurement

takes place. As shown in previous publications, further electrochemical changes can be neglected [193, 194].

This test routine was used for the measurement:

1. Temper the cell to target temperature for 6 h
2. Constant current (CC) discharge and constant current-constant voltage (CC-CV) charge with $\frac{1}{3}$C and $\frac{1}{50}$C cutoff till the lower/upper voltage limit
3. Pause for 30 min
4. Repeat step 2 to determine a reference discharge capacity (C_{ref})
5. Pause for 3 h, or 6 h when T<10 °C
6. Sampling of OCV
7. Discharge Ah-based (using C_{ref}) with $\frac{1}{3}$C to target SOC
8. Repeat steps 5 to 7 for each SOC

The determination of the OCV was performed at seven temperature settings (−25 °C, −10 °C, 0 °C, 10 °C, 25 °C, 40 °C, 55 °C). At temperatures higher 0 °C the SOC change to the next step was done in 5% steps. At low temperatures the OCVs were measured in 10% SOC steps due to extended relaxation times. After the lower cut-off voltage was reached and the pause time had elapsed, the charge direction was measured using the same procedure and the identical Ah-based SOC-steps. As Barai et al. [195] describe in detail, errors in hysteresis observation can be avoided by directly linking the measurement of discharge and charge direction.

4.3.2 Capacity

The extractable battery capacity strongly depends on temperature and current. To investigate this dependency, the same temperature levels as in the OCV measurement were used. Charging and discharging was carried out by applying at least five different C-rates (1C, 3C, 5C, 10C, 15C (and 20C for cell A and B)) within the following test procedure:

1. Temper the cell to target temperature for 6 h
2. CC discharge and CC-CV charge with 1C and $\frac{1}{50}$C cutoff till the lower/upper voltage limit
3. Pause for 30 min, or 60 min when T<10 °C
4. CC discharge with predefined current rate till the lower voltage limit
5. Pause for 30 min
6. CC-CV charge with 1C and $\frac{1}{50}$C cutoff till the upper voltage limit
7. Repeat steps 3 to 6 for each discharge current rate

8. CC discharge with 1C till the lower voltage limit
9. Pause for 30 min, or 60 min when T<10 °C
10. CC-CV charge with predefined current rate and $\frac{1}{50}$C cutoff till the upper voltage limit
11. Pause for 30 min
12. Repeat steps 8 to 11 for each charge current rate
13. Repeat steps 1 to 12 for each temperature level

4.3.3 Internal resistance

To determine the internal cell resistances an extensive pulse characterization was carried out [196, 197]. For this purpose, the following test procedure was used:

1. Temper the cell to target temperature for 6 h
2. CC discharge and CC-CV charge with $\frac{1}{3}$C and $\frac{1}{50}$C cutoff till the lower/upper voltage limit
3. Pause for 30 min
4. Repeat step 2 to determine a reference discharge capacity (C_{ref})
5. Pause for 30 min, or 60 min when T<10 °C
6. Discharge pulse for 10 s with predefined current rate and subsequent equalizing charge with 1/3C
7. Pause for 30 min, or 60 min when T<10 °C
8. Repeat steps 6 to 7 for each current rate (1C, 3C, 5C and multiples of 5C)
9. CC-CV charge with $\frac{1}{3}$C and $\frac{1}{50}$C cutoff till the upper voltage limit
10. Pause for 30 min
11. Discharge Ah-based (using C_{ref}) with $\frac{1}{3}$C to target SOC
12. Repeat steps 5 to 11 for each SOC

The measurement was performed in 10% SOC steps. Additionally 5% SOC and 95% SOC were tested. The temperature steps were identical to those in the OCV and capacity measurement. To shorten the test time, pulse measurements were carried out separately in charge and discharge direction with one cell each. Charge pulses were tested identically to discharge pulses, though the test procedure started in discharged condition.

The calculation of the internal resistance at a certain time t, SOC and temperature T depends on the OCV prior to the pulse (U_{OCV}), the measured pulse voltage (U_{p}) and the pulse current ($I_{\mathbf{p}}$) according to the following equation:

$$R(t,SOC,T,I) = \frac{U_{\mathrm{p}}(t,SOC,T,I) - U_{\mathrm{OCV}}(SOC,T)}{I_{\mathrm{p}}} \tag{4.1}$$

All internal resistances presented in this thesis were evaluated after a pulse duration of 1 s. Therefore, a pulse induced shift of the SOC as well as a strong rise in cell temperature can be neglected even at high current rates.

4.4 Aging test strategy

Based on the findings of the vehicle data analysis in Section 3.3, calendar, cyclic and drive cyclic aging matrices were defined. The goal was to enable shortened, application-oriented cell aging tests with the possibility of building an semi-empirical aging model. The defined matrices do not claim to be universally applicable. Rather, they illustrate a methodology that can be used to validate the fulfillment of cell lifetime requirements of a 48 V vehicle battery. The aging matrices of Schmalstieg et al. [128] served as a basis for the definition. Each cross in the matrix represents one cell to be measured (see Table 4.4, 4.5 and 4.6).

Although measuring multiple cells per operating point can lead to more valid results, this is difficult to apply in a development process in terms of effort and test benches. Since NMC|LTO cells were used in the 48 V battery of the considered vehicles, boundary conditions of the aging matrices, such as the absolute temperatures, will differ for other cell chemistries. Cell candidates have to be tested according to the limits specified by the cell manufacturer and additionally specifically tailored to the application context. Nevertheless, the stress factors analyzed in this thesis are identical for each cell candidate, since a suitable battery is developed in the development phase for a given 48 V system.

Figure 4.2 shows the begin-of-life condition in terms of capacity and resistance of all NMC|LTO cells within the aging tests. Based on the initial capacity, the cells vary by 2.3%. The variation in internal resistance is significantly higher at 17.7% but within the range specified by the cell manufacturer. No noticeable influence with regard to the following aging tests can be found. All aging tests were carried out in accordance with the conditions of use specified by the cell manufacturer.

4.4.1 Calendar aging

The calendar aging tests focused on the investigation of dependencies regarding temperature and SOC. As part of the calendar aging tests (test series 1), 12 aging conditions were examined, which are shown in Table 4.4. The average SOC was set to 55% SOC, as it was most likely to occur in the 48 V batteries (see Figure 3.7). Due to high temperatures in the

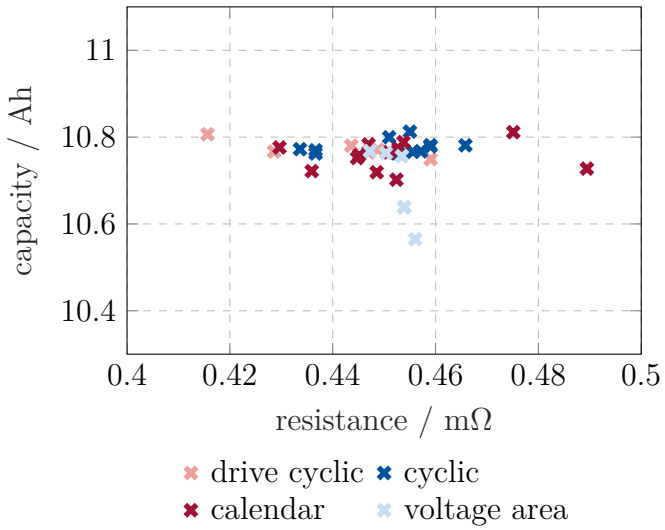

Figure 4.2: Overview of the begin-of-life condition of all NMC|LTO cells in terms of discharge capacity (1C, CC, 2.65 V-1.9 V, 25 °C) and resistance (5C, 1 s, 50% SOC, 25 °C) prior to test start. The cells are assigned to the different aging tests by color. The variation in capacity is much smaller than the variation in resistance.

application and their impact on cell aging, only 40 °C, 60 °C and 80 °C were tested. On the one hand, this allowed for shorter test durations, while on the other hand, it offered the possibility to integrate an Arrhenius dependency in an aging model. In addition, an SOC dependency can be demonstrated by testing different SOCs. The SOC boundaries were set to 5% and 95%, since these were the application-related extreme cases. Although low SOCs were not observed during the battery data analysis (see Figure 3.7), they are expected at longer standing phases and with increasing battery aging.

Table 4.4: Calendar aging matrix based on the investigation of the real-world 48 V system data.

T/SOC	5%	10%	55%	70%	90%	95%
40 °C	X		X			X
60 °C	X	X	X	X	X	X
80 °C	X		X			X

A check-up was carried out every 30 days to determine the aging progress. The cell voltage during storage was kept constant. This floating current condition was achieved by a test configuration, which was similarly used by Lewerenz et al. [198]. The SOC setting after every check-up was based on the latest measured capacity and was done Ah-based.

The cells at 80 °C burst in the test chamber during the aging test. Due to the direct exposure to air, these cells were not suitable for further ex-situ investigations. For this reason, a second series of calendar aging tests (test series 2) was performed, in which three

cells were aged at 2.03 V (approx. 3% SOC), 2.2 V and 2.65 V (100% SOC) at 80 °C for 40 days in a floating condition. To enhance SOC-dependent aging effects, the investigated voltage range was extended in the second test series. It was assumed that essential aging mechanisms were identical for both test series at each of the voltage levels.

4.4.2 Cyclic aging

The cyclic aging tests aimed to investigate dependencies with respect to ΔDOD and current rate. An overview of all test conditions is shown in Table 4.5. The mean SOC for all ΔDODs smaller than 100% was 55% SOC and was approached via constant-voltage step. Cyclization around this SOC took place Ah-based, with a reset of the mean SOC every 20 equivalent full cycles. According to the occurrence in the application, testing of different current rates was necessary. In this test, three constant current rates (2C, 5C and 10C) were chosen to examine a possible current rate dependency. A ΔDOD variation enabled the quantification of the influence of shallow cycles, as this was one of the special operating conditions in a mild hybrid application. Even if full cycles were not observed in the real application, it was useful to test them as a worst-case reference. All cyclization profiles consisted exclusively of constant-current charging and discharging processes. The asterisk (*) indicates an operating point at which two cells were tested. One cell was cycled at 5C/5C and 70% ΔDOD. The load profile of the other cell was expanded by a sawtooth profile, so that every change of 4% SOC was superimposed by a microcycle of 2% in the opposite direction. The aim was to get a better understanding of overlapping aging effects and to generate essential knowledge regarding battery lifetime in dynamic real-world applications. After every 500 equivalent full cycles a check-up was performed.

If the 48 V system under consideration provides a cold-start capability, low temperatures shell be part of special aging tests regarding lithium plating. This is particularly important when cells with graphite anode are to be used within a low-voltage battery.

Table 4.5: Cyclic aging matrix based on the investigation of the real-world 48 V system data. Cyclization at ΔDODs less than 100% took place at an average SOC of 55%. At (*) an additional cell was loaded with a sawtooth profile, where a microcycle of 2% SOC overlaped every 4% SOC change.

Current	2C/2C		5C/5C		10C/10C	
ΔDOD/T	40 °C	60 °C	40 °C	60 °C	40 °C	60 °C
100%			X			
70%	X		X	X*		
20%			X			
10%			X			
5%	X		X	X		X
2%			X			

Further cyclic aging tests were defined to investigate the criticality of the upper and lower voltage ranges. For this purpose, 6 cells, 2 per test condition, were cycled in different voltage ranges with 5C/5C at 60 °C. The test conditions are given in Table 4.6. Every 250 cycles the cell performance was checked by a check-up.

Table 4.6: Additional cyclic aging tests to investigate the aging behavior at low and high SOC in combination with different ΔDODs. The listed lower and upper voltages defined the limits of the CC step.

U_{lower}/U_{upper}	2.4 V	2.5 V	2.65 V
2.0 V	X		
2.1 V		X	X

4.4.3 Drive cyclic aging

As described in Chapter 3.3, a clear differentiation of individual aging phenomena is difficult when cells are exposed to real driving cycles. However, aging data of such profiles offer the chance to verify results of individual operating points and to investigate potential interdependencies. Further, the results can be used for the validation of an aging model, even though this is not content of this thesis. To validate the cyclic and calendar aging tests as well as for a realistic prognosis regarding the battery lifetime within a 48 V application, three cells were loaded with a driving cycle at different temperatures. The drive cycle included a combination of real battery loads during city, country and highway driving and had a duration of 16 h. With the variable temperature profile a temperature level between 20 °C and 60 °C was set weekly. A total of ten temperature levels were tested with an average temperature of 37.3 °C. As Ah-neutrality could not be guaranteed due to the cycle itself and measurement inaccuracies, a SOC reset was performed after each drive cycle. A check-up was performed every 32 cycles.

4.4.4 Check-ups

Check-ups were carried out at defined intervals to monitor the aging behavior. The entire measurement routine was performed at 25 °C. An exemplary voltage curve of a check-up is shown in Figure 4.3. At the beginning of the check-up, the examined cell was charged with CC of 1C to 2.65 V followed by a constant voltage (CV) step until the current fell below $\frac{1}{50}$C. Then a capacity test was performed in discharge and charge direction with CC of 1C, concluded with a CV step. A qOCV at $\frac{1}{8}$C is performed for further electrical studies, followed by another capacity test at 1C [192]. Deviations between a qOCV and a real OCV are assumed to be very small considering the low current rate in combination with the extremely low internal cell resistance [195]. The qOCV, which was recorded with 2 Hz during the check-up, was filtered to eliminate any identical consecutive voltage values.

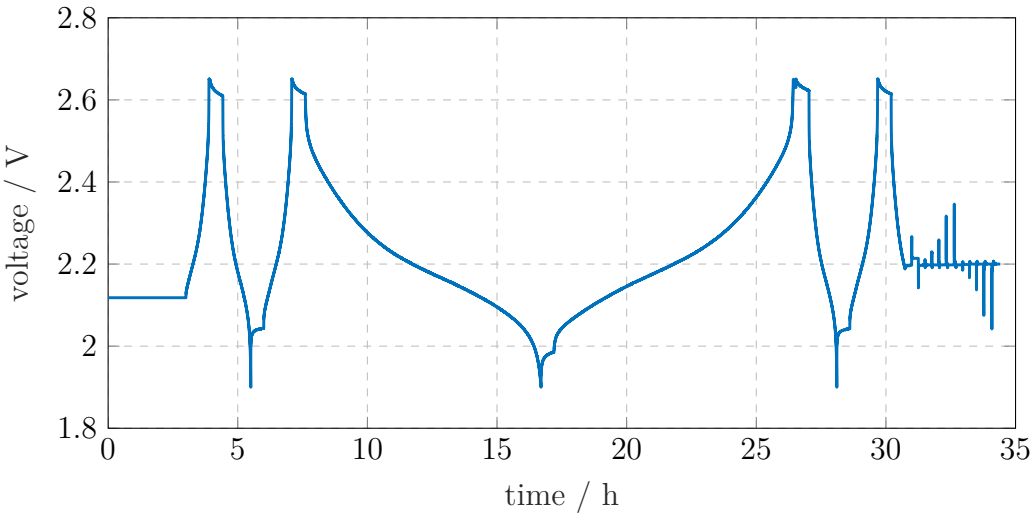

Figure 4.3: Exemplary voltage profile of a cell during the regular check-up at 25 °C. Due to the high-power characteristic of the NMC|LTO cells, the CV phases following the CC charging are very short (1-2 minutes) in comparison to the total duration of the check-up. For this reason, they are not distinguishable in this plot.

At 50% SOC a pulse power characterization profile was performed. First, a charge and a discharge pulse were applied to the cell for 20 s with a 15 min rest in between. After another 15 min rest period, a sequence of charge and discharge pulses with current rates of 2C, 5C, 10C, 20C and 25C and a pulse duration of 10 s was applied with a directly connected equalizing charge of 1C. The relaxation time between the respective pulses was 15 min. In this work, the analysis of the internal resistance increase is based on the 5C pulse behavior, which is evaluated after 1 s pulse duration. To calculate the internal resistance, the difference between the cell voltage before the pulse and 1 s after the start of the pulse is divided by the applied current (see Equation 4.1). In the following aging analysis, all values concerning the capacity retention refer to the extractable capacity in the first capacity test in discharge direction within the CC phase.

4.5 Incremental capacity analysis and differential voltage analysis

Both incremental capacity analysis (ICA) and differential voltage analysis (DVA) represent in-situ and thus non-invasive electrochemical techniques to study the aging behavior of lithium-ion cells by investigating their characteristic voltage profiles.

Basis for both analysis techniques is the characteristic qOCV, which is recorded during regular check-ups. The qOCV is measured with a small constant current, usually lower $\frac{1}{8}$C, to ensure that characteristic electrochemical characteristics such as phase transitions

within the material are not distorted by overvoltages and concentration gradients. The choice of the current depends strongly on the kinetics of the measured cell. Relaxation processes in high-power cells, for example, are highly accelerated, so that higher current rates can be applied for measurement. It is necessary to weigh up the maximum level of detail in the measurement against the time required for the check-up. Long rest periods bear the risk of influencing the aging behavior, for example due to a PEE.

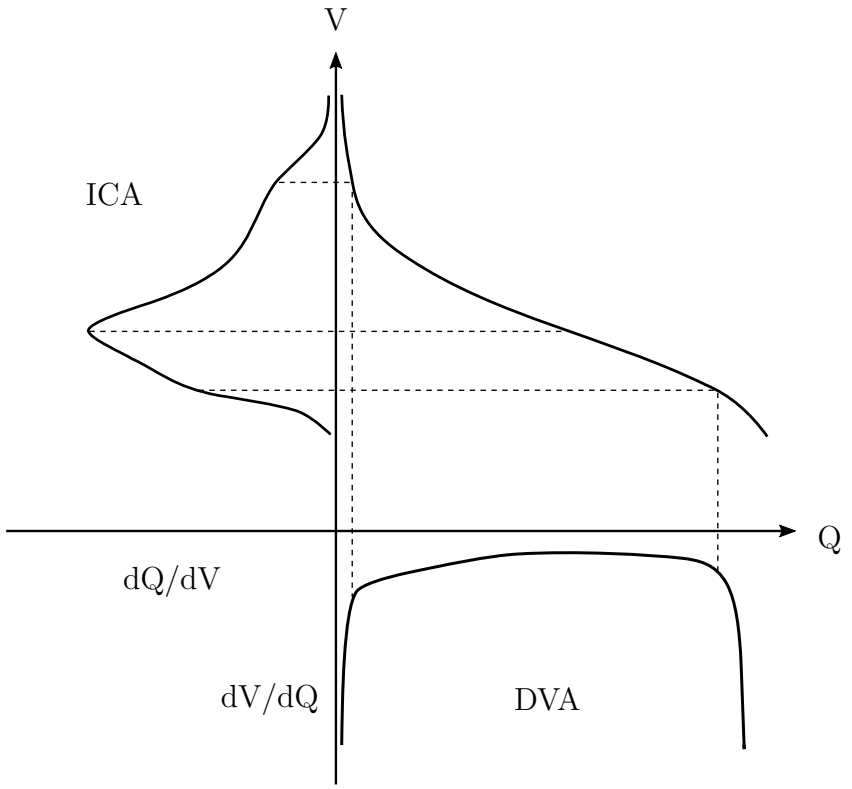

Figure 4.4: Qualitative visualization of the relationship between the qOCV obtained during the check-up of an NMC|LTO cell and the derived ICA and DVA.

Figure 4.4 shows qualitatively the relationship between the logged qOCV data and the incremental capacity (IC) and differential voltage (DV) curves for the examined NMC|LTO. DV curves are the derivative of the voltage curve with respect to the capacity. In a DV analysis of graphite-based cells, characteristic minima are obtained, which can be assigned to stage transitions of the graphite. Since the graphite anode is usually the main source of aging mechanisms, diverse changes of the DV curves can be observed during the aging process, which allow for identification of degradation modes, primarily LAM of the anode and LLI [199].

IC curves are calculated using the derivative of the incrementally charged capacity ΔQ with respect to the changed unit of voltage ΔU. Typically, IC curves are plotted over cell voltage or SOC. Depending on the characteristic phase transitions of the active materials and the cell balancing, distinct dQ/dV peaks result, which differ in height, position and

intensity. An investigation of the peak progressions during the aging process provides key information regarding cell aging state and aging mechanisms [200].

As shown in Figure 4.4, the characteristic qOCV of the NMC|LTO cell exhibits a strictly monotonous profile without any plateaus or sharp gradient changes. Multiple phase transitions, as they are present in graphite-based cells, are not observed for LTO due to the constant potential plateau at 1.55 V vs. Li/Li^+. When the qOCV is derived according to capacity, DV curves in an inverted U-shape without pronounced minima are obtained, which are of limited value for an analysis of potential degradation mechanisms.

Here, an ICA offers several advantages. The values dQ/dV indicate how much capacity can be charged into or discharged from the cell at a particular voltage. Especially 2-phase materials like LTO are clearly distinguishable by characteristic peaks [199]. Same applies for aging-related variations in the qOCV, for example due a change in electrode potential caused by surface layers. Devie et al. [201] have qualitatively shown how the effects of the degradation modes loss of active material at the negative electrode (LAM_{NE}), loss of active material at the positive electrode (LAM_{PE}) and LLI are reflected in the characteristic IC curves of an NMC|LTO cell. Further, as it is demonstrated in Chapter 7.1, an ICA can be used to identify the occurrence of the reversible PEE. For the reasons given above, only ICA were carried out in the course of this thesis.

4.6 Post-mortem analysis

The previous section provided a detailed description about which cells were subjected to aging tests and how these tests were performed. In addition, the methodology for monitoring the aging process by means of external measurements of electrical battery parameters was introduced. However, most aging mechanisms are not directly identifiable by such methods, not least due to the high complexity of electrochemical reactions within the cell. For this reason, further methods are introduced in this section, which allow for a specific and isolated analysis of aged cell materials after cell opening. Since further use of the cell after disassembly is not possible, these types of investigations are often referred to as post-mortem or ex-situ analyses.

For the post-mortem analysis the aged cells along with a fresh reference cell were discharged until the lower cut-off voltage of 1.9 V was reached. The cells were opened in an argon-filled glovebox. During the opening process, photos of the cell materials were taken and optical changes or abnormalities were documented. The electrodes were separated for further investigations of the material and the assembly of half-cells. The electrolyte residues on anode and cathode sheets were washed off with DMC. The electrodes were dried in a vacuum oven at 80 °C for at least 24 h.

The technology material and process analysis (TWA) of BMW AG, among others represented by Dr. Michael Leitl, was responsible for cell opening and ex-situ investigations. The assembly and testing of the coin cells was performed by Lennart Alsheimer (Münster Electrochemical Energy Technology (MEET)) as part of a collaborative project.

4.6.1 Half-cell assembly

To study the performance degradation of the separate electrode materials, half-cells were assembled as coin cells in a dry room. Anodes and cathodes from the 40-days aged cells (test series 2) were punched out of the dried electrode sheets with a diameter of 14 mm. From a 1 mm thick lithium foil lithium metal electrodes were punched out with a diameter of 15 mm serving as counter electrode. Since no information regarding the electrolyte composition of the NMC|LTO was available, a standard electrolyte (LP57 - 1 mol $LiPF_6$ in EC:EMC 3:7) was used. Cellguard 2500 with a thickness of 25 µm was selected as separator.

After sealing of the coin cells, a break of 6 h ensured an even electrolyte distribution. Two formation cycles were performed with $\frac{1}{10}$C to enable the completion of potential equalization processes. For the qOCV measurement the assembled cells were charged and discharged with CC of $\frac{1}{10}$C followed by a CV step until $\frac{1}{50}$C was reached. The voltage limits for the LTO|Li cells were 1.0 V and 2.0 V and for the NMC|Li cells 3.0 V and 4.2 V.

4.6.2 Scanning electron microscopy

Scanning electron microscopy (SEM) is a widely used analytical technique for the characterization of surface typologies, crystalline structures and chemical compositions [202]. Here, the specimen is exposed to a high-energy electron beam. The penetrating electrons interact with the sample material inducing an emission of secondary electrons, backscattering electrons and X-rays, which are subsequently collected by different detectors. Secondary electrons are generated by inelastic scattering with atoms in a narrow region near the surface. In contrast, backscattering electrons originate from elastic scattering in deeper material layers. These electrons can provide information about the material composition, indicated by differences in brightness on SEM images. Here, elements with high atomic mass produce larger grayscale variations [202]. X-rays are emitted due to the shifting of electrons from outer shells to locations in inner shells vacated by the electron beam. From the X-ray radiation, the atomic composition can be deduced [88].

In this thesis, the morphology of electrode material was investigated with a scanning electron microscope from Zeiss (model EVO 10). The SEM images were taken with an acceleration voltage of 15 kV at a beam current of 250 pA.

4.6.3 X-ray photoelectron spectroscopy

An X-ray photoelectron spectroscopy (XPS) was performed to examine elements and chemical bonds of the surface layer on the electrode samples. In this method the sample material is irradiated with X-rays and thus energetically excited. Impinging X-rays interact with electrons of the sample elements and cause an emission of characteristic photoelectrons (photoelectric effect). The emitted photoelectrons are detected and their kinetic energy is determined. From these energy values, reliable information about the elements of the

surface layer is obtained. Since the X-ray radiation only permeates the outermost layers of the material, the measuring depth is limited to 2 nm to 10 nm [88, 203].

For the XPS measurements, samples were cut out of the dried electrodes and applied to the sample holder. The measurement was performed with a PHI VersaProbe II, using an Al anode to generate the $Al_{K\alpha}$ radiation (1486.6 eV). Prior to measurement, two neutralizers (BaO electron and Ar^+ ion neutralizer) compensated residual charges on the sample surface. At each test point a section of 100 µm was examined with an X-ray beam of 100 W. The measurement of each test point was repeated at least once to detect and exclude incorrect measurements. The C1s signal at 285 eV served as reference for the evaluation of resulting spectra and binding energies.

5 Performance benchmark of high-power cells

This section is based on a publication created during the course of the dissertation. It contains minor modifications with respect to the original publication. The use of the article content including illustrations from [190] is permitted with the consent of Elsevier.

The following investigation aims to present a consistent and comprehensive performance benchmark of state-of-the-art high-power cells. For this purpose, characterization measurements with respect to OCV, internal resistance and capacity were performed on three cell types with different cell chemistries covering a wide operating window. This includes vehicle relevant operating conditions, indicated by temperatures between −25 °C and 55 °C as well as by charge and discharge current rates up to 30C.

In the literature, high-power cells have only occasionally been subjected to specific investigation. Thus, Schröer et al. [9] have characterized three different LTO-based cells electrically on the basis of frequency domain and time domain measurements. Both general conclusions regarding the electrical behavior and a model parameterization were accomplished, which enabled a state of available power analysis. Additionally, a current dependency of the internal resistance of LTO-based cells was shown [204]. Andre et al. [205] have elaborated essential dependencies regarding temperature and SOC by extensive impedance measurements of a nickel cobalt aluminum and graphite based cell. In a similar study, which included time domain measurements with a variation of the current (up to 3C), Farmann et al. [206] studied a LTO-based cell. A Butler-Volmer correlation was found especially for negative temperatures. Waag et al. [207] have quantified the impact of aging on the above mentioned dependencies using a NMC|C-based cell. A detailed analysis of the performance and the aging behavior including the application of ex-situ methods was carried out for nine different commercially available high-power cells with less than 4 Ah by Schmidt et al. [129].

A comprehensive investigation of the electrical characteristics of battery cells suitable for low-voltage applications (larger 10 Ah) to begin-of-life has not yet been carried out, especially under consideration of the relevant operating conditions presented in Section 3.3. Necessary information regarding the cell behavior, which is indispensable for system design and operation in a highly dynamic application, is therefore missing.

In the following, first, the results of the load-free characterization tests are presented, in which the cell is in a relaxed state. Second, dynamic load scenarios are analyzed and performance variations are discussed. The electrical behavior of the cells is examined regarding the respective cell chemistry and is compared to findings from the literature. Furthermore, implications for the use of these cells in low-voltage applications are identified.

However, results and conclusions refer exclusively to the analyzed cells. If cell chemistry specific generalizations are appropriate, this is highlighted at the corresponding passage.

5.1 Load-free characteristics

5.1.1 Open circuit voltage

The intensity of the temperature dependency of the OCVs varies strongly with the cell under consideration. In Figure 5.1 the characteristic OCVs of the three examined cells are shown as a function of SOC at different temperatures. For the sake of simplification, the three investigated cells are abbreviated as cell A (NMC|LTO), cell B (NMC|C) and cell C (LFP|C) in this chapter. Cell A shows an increasing OCV for decreasing temperatures over the entire SOC. Particularly at low SOC ranges, the curves for high and low temperatures diverge significantly. The result is similar for cell B, where deviations mainly occur at low SOCs smaller than 40%. Baccouche et al. [208] achieved similar results for the temperature dependency of the OCV of a high-energy NMC cell. Cell C shows an approximately identical OCV for all temperatures. Small discrepancies are observed at high SOCs greater than 80%. At this position the phase transition of graphite from stage 2 to stage 1 is significantly less pronounced for low temperatures.

In principle, the electrode potential can be determined at any time by energetic evaluation, taking into account a change in the chemical potential using the Nernst equation [209–211]:

$$E = E_0 - \frac{RT}{zF} \cdot log \frac{a_{ox}}{a_{red}} \tag{5.1}$$

Here E_0 describes the standard redox potential, R the gas constant, T the temperature, z the number of electrons ($z = 1$ for lithium-ion systems), F the Faraday constant and a_{ox} respectively a_{red} the activities of the chemical species participating in the redox reaction. Accordingly, an increase in temperature is expected to cause a decrease in the equilibrium voltage in both chemical equilibrium states and phase transitions. Since the OCVs of LFP and LTO electrode materials, for example, are slightly dependent on the lithium concentration, the Nernst equation cannot always correctly reflect the conditions [209, 212]. The results for cell C reveal these limitations. Up to about 40% SOC the OCV is lower for higher temperatures. This changes after the phase transition, so that from 40% to 80% the OCV is higher with increasing temperature.

For potential applications precise SOC determination is essential, since it is an integral part of strategic operating decisions. Battery management systems often use an OCV-SOC relation to estimate the real SOC. Misjudgment of the SOC can lead to inaccurate power prediction, resulting in power degradation, loss of CO_2 savings potential, or even partial functional failure. Shifts in the operating window, such as towards higher SOCs, can negatively affect cell aging, thus, shortening the lifetime of low-voltage batteries. As the findings of the OCV measurement show, considerable inaccuracies can be expected if

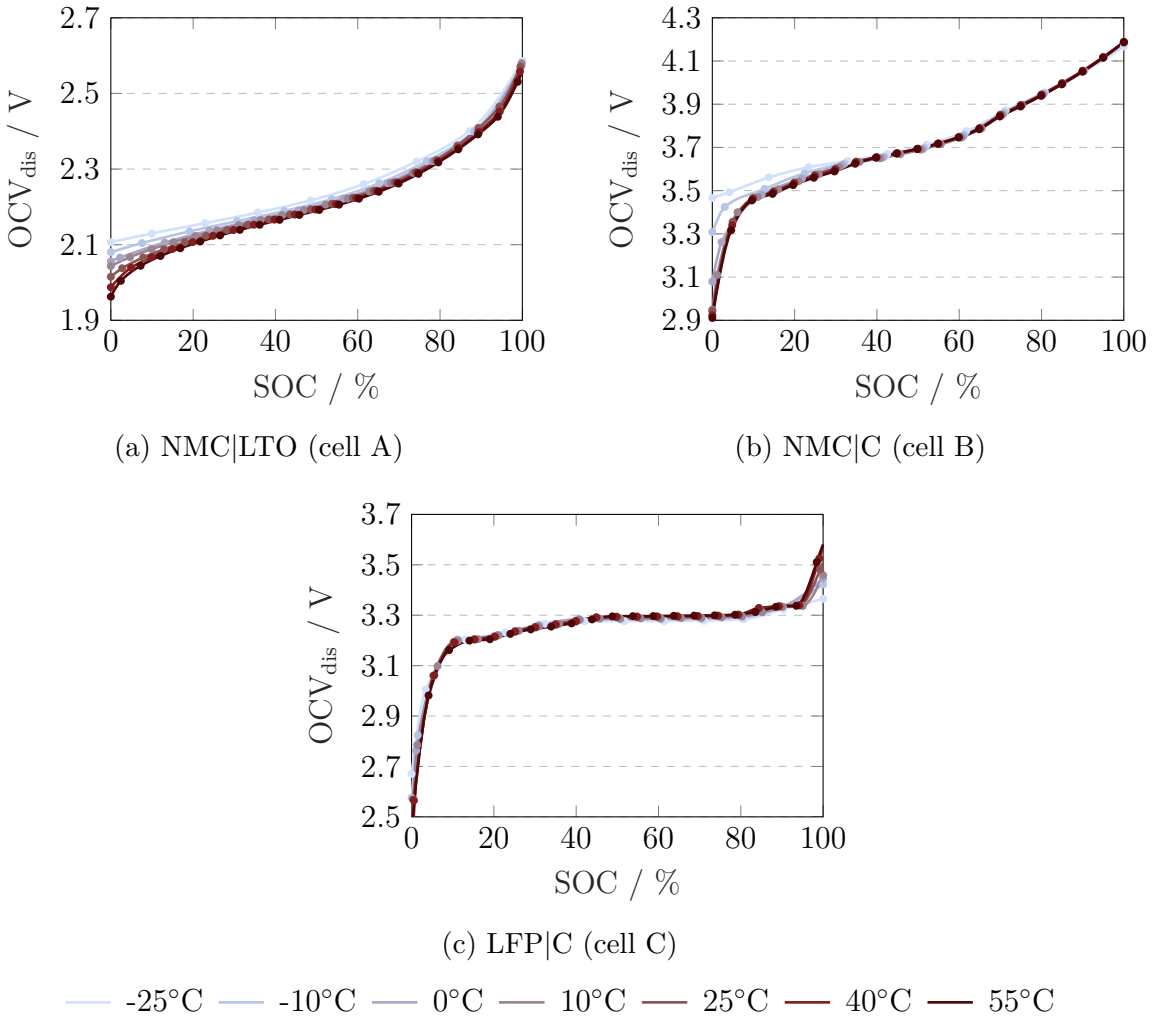

(a) NMC|LTO (cell A)

(b) NMC|C (cell B)

(c) LFP|C (cell C)

Figure 5.1: OCVs of cells A, B and C as a function of SOC, measured stepwise in discharge direction and normalized to the available capacity at the corresponding temperature level. Cell A and cell B show a clear temperature dependency in lower SOC ranges, whereas the OCVs of cell C are roughly congruent, with the exception of very high SOCs.

temperature dependencies are neglected. Absolute SOC errors can be up to 20% for cell A and B in low SOC ranges and even 35% for cell C at the voltage plateau. This does not include hysteresis behavior, which will be investigated in the following.

5.1.2 Hysteresis behavior

The OCV measurements presented above allow for a detailed analysis of the hysteresis behavior of all three cells. OCV hysteresis appears when the cell voltage differs at identical charge state (same stoichiometric lithium content) depending on prior charging or discharging processes. The occurrence of hysteresis has been extensively investigated in

the literature and its definite origin is still unknown. Sranivasan et al. [213] describe the origin of hysteresis using a shrinking-core model, in which different degrees of lithiation are formed within the particle layers. Dreyer et al. [214] provide a thermodynamic explanation, which considers the connection of neighboring particles with non-monotonic chemical potential curves as the cause. In addition, some theories suggest that mechanical stress between phase boundaries is responsible. A potential reason for mechanical stress is different lattice constants for lithiated and delithiated phases, which cause a voltage drop within the particle. Further, lattice distortions due to doping compounds can hinder the propagation of phase boundaries, leading to an increase in mechanical stress [74, 215, 216].

However, the effects of hysteresis are more tangible and include large inaccuracies in SOC determination using the previously mentioned OCV/SOC relation. Especially for high-power batteries, in which the focus is on short-term performance and reliable power prediction, a complete and thus temperature-dependent investigation of the hysteresis is necessary.

The hysteresis behavior of the three investigated cells is strongly dependent on the anode material, which allows for a separation into two groups [217]. Figure 5.2 shows the hysteresis for all temperatures and SOCs between 10% and 90%. Figure 5.2a shows that cell A has an approximately SOC-independent hysteresis for each temperature, which does not exceed 11 mV and slightly increases with decreasing temperature. Compared to cell B and C, this hysteresis is the least pronounced, which is due to the indistinct phase transitions of the LTO and NMC material. The outlier at about 50% SOC and 10 °C was reproducible in a second measurement of an alternative cell and could not be explained so far. In principle, the results are in good agreement with those for NMC|LTO cells by Barai et al. [195], but are higher than those of Farmann et al. [218].

The LFP|C cell C has the highest hysteresis with about 35 mV, comparable with the values reported in [74, 218, 219]. Interestingly, the results of cell B and cell C, shown in Figure 5.2b and 5.2c, are qualitatively similar. Both show two distinct peaks due to the characteristic phase transitions of the graphite. The position of the peaks differs. Cell B peaks at approximately 30% and 60% SOC while cell C peaks at 35% and 80% SOC. These variations in the position indicate that both cells differ in their cell balancing. Despite this shift, the height and shape of the hysteresis are similar for temperatures greater than 0 °C. At temperatures less than 10 °C the height of the first peak decreases significantly. An explanation for this characteristic might be a more inhomogeneous lithiation of the active material, so that on the one hand phase transitions in the OCV are less evident and on the other hand the hysteresis is flattened.

Remarkably, the hysteresis of cell C increases at negative temperatures in the middle SOC range. A hysteresis, which rises with decreasing temperature, as postulated by Barai et al. [219], cannot be confirmed by the findings. A possible explanation for their diverging results may be ongoing relaxation processes due to the applied relaxation time of four hours independent of temperature. The measurement routine within this work, however, used pause times of six hours at temperatures less than 10 °C. In addition, faster

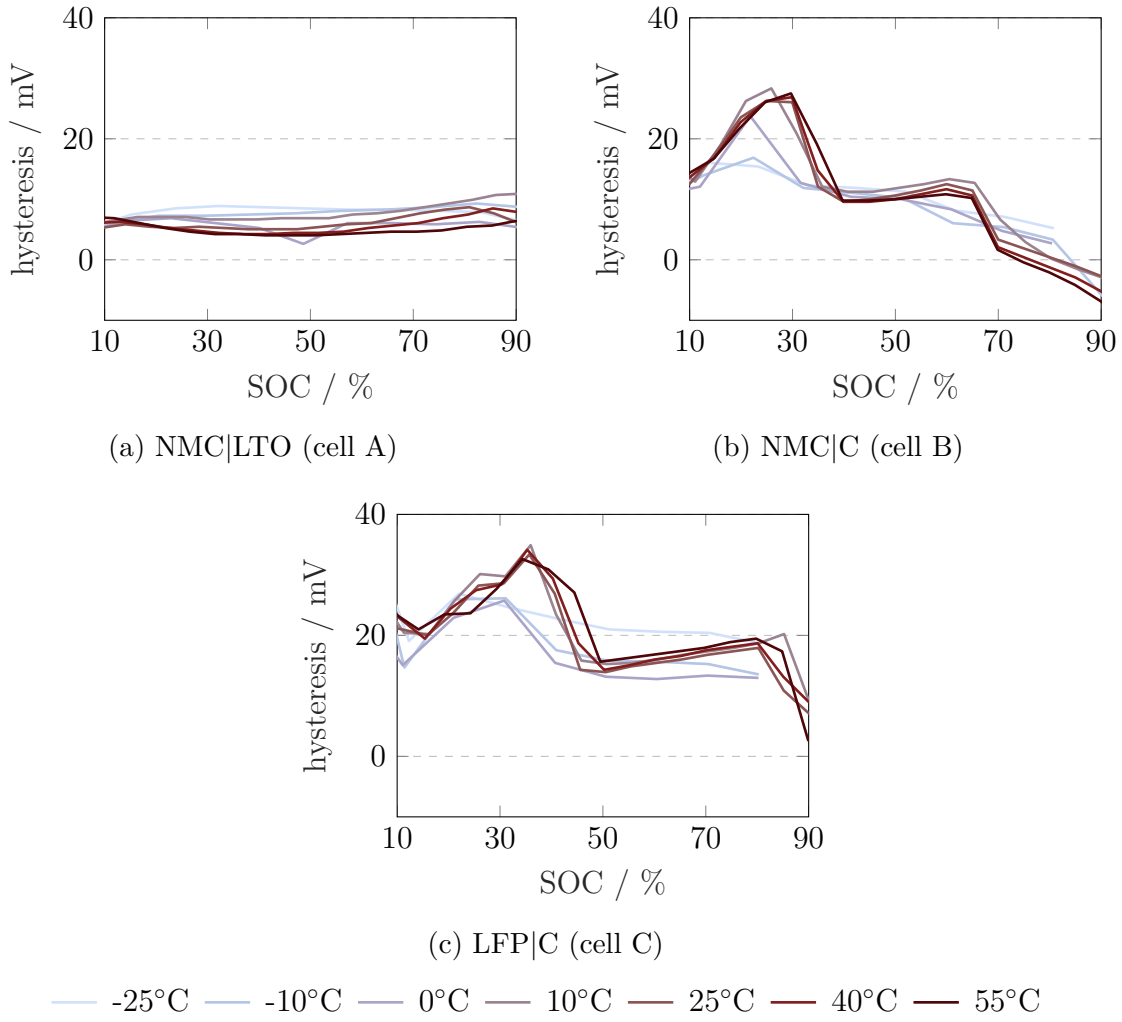

(a) NMC|LTO (cell A)

(b) NMC|C (cell B)

(c) LFP|C (cell C)

Figure 5.2: Hysteresis behavior of the examined cells as a function of SOC and temperature. The hysteresis of cell A is approximately constant for SOCs between 10% and 90% and rises with decreasing temperature. In contrast, the hysteresis of cells B and C is highest at medium to high temperatures and peaks at the characteristic phase transitions of graphite.

relaxation processes can be assumed due to the properties of high-power cells and their good kinetics.

A suitable integration of the hysteresis behavior in a battery simulation needs to be cell chemistry specific. In addition, model simplifications are recommended for the investigated cells. For cell A, a temperature-independent, constant hysteresis can be considered depending on the accuracy requirements of the model. For cells B and C it is conceivable to assume a constant SOC-dependent hysteresis for temperatures above 0 °C.

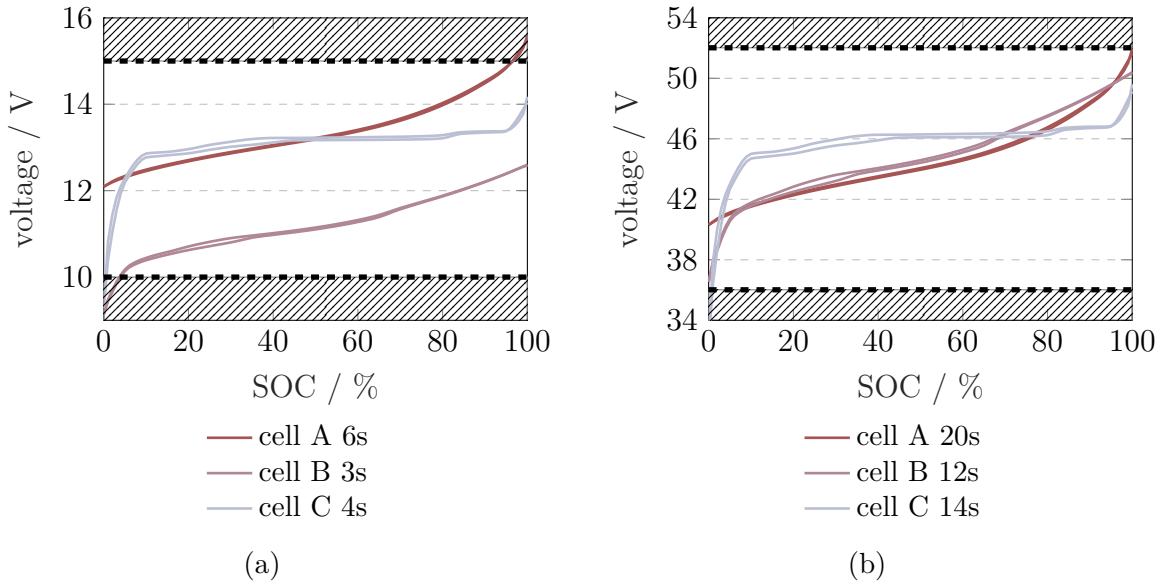

Figure 5.3: Potential series connection of the examined cells for a) 12 V and b) 48 V applications. For each configuration the number of cells connected in series ("s") is specified. To ensure the functionality of the electrical components, the vehicle electrical system requires a normal operating range, which is marked with a dotted line. This restricts damaging operating points and prevents the use of an arbitrary number of cells.

5.1.3 Compatibility with low-voltage applications

A critical key requirement for the use of lithium-ion batteries in low-voltage vehicle electrical systems is the supply of an application-specific operating voltage. The required voltage range is mainly pre-defined by upstream and downstream components, such as generators, electric motors and other loads. The operating voltage of the battery results from the series connection of any number of cells, taking into account their voltage limits. Therefore, it is necessary to assess whether certain cell chemistries can be prioritised or excluded in advance. Figure 5.3 shows the characteristic voltage curves of a serial connection of the examined cells. Additionally, the upper and lower voltage limits of 12 V and 48 V systems are included by dotted lines: For 12 V systems the voltage range is 10 V to 15 V, for 48 V systems the voltage range is 36 V to 52 V (VDA 320 standard). The identifier "6s", as an example for cell A in Figure 5.3a, refers to six cells connected in series.

The illustrated topologies offer the greatest overlap with the permitted voltage range. Nevertheless, other configurations are conceivable. As shown in Figure 5.3a none of the three configurations allows for full use of the battery capacity in the voltage range from 10 V to 15 V. The (starter) generator, which charges the battery using energy from the combustion engine or from recuperation periods, provides an operating voltage in the range of 14 V [168]. Hence, a battery pack with any 3s configuration of cell B requires the integration of additional voltage limiting components such as a DC/DC converter. The

voltage level of any 6s configuration of cell A is so high that it is impossible to fully charge the battery without voltage-boosting components. Otherwise the operating voltage limits the available battery capacity.

Since the 12 V battery is used for engine starts, short-term power fluctuations within the system and start-stop functionalities, the operating strategy provides for comparatively high average SOCs, just as with the use of a lead-acid battery [82, 169]. It is essential to ensure that all cold start requirements are met even at cold climatic conditions. This implies that the lower cut-off voltage must not reached during operation, which can not be assured for the 3s configuration of cell B due to the low operating voltage. Moreover, this cell would have to deliver higher current rates for required power outputs, which leads to higher losses and more stress for downstream components. Taking the aforementioned criteria into account, cell C in a 4s configuration appears to be the most suitable candidate for a 12 V application.

Figure 5.3b illustrates the wider permitted voltage range in a 48 V application. This wider range allows for greater flexibility in cell selection and configuration. The serial connection of 20 cells A, 12 cells B or 14 cells C fulfills completely or to a high degree the specified voltage range, with the voltage curves of cells A and B being similar. 48 V batteries are strained with high dynamic currents in a medium SOC range in order to achieve the highest CO_2 savings potential [166]. At 30% to 70% SOC, all three cells offer a sufficiently wide energy window to ensure high charge or discharge currents during long recuperation or boost phases. Cell C has the advantage of its flat OCV characteristic and thus a constant and, compared to the other cells, higher charge and discharge power in lower and medium SOC ranges. In high SOC ranges, cells B and C offer increased discharge performance, however, a power degradation in charge direction is possible. None of the three cells stands out from this investigation.

Cost-related aspects are not discussed at this point. It should be noted, however, that different numbers of cells per pack cause significant cost differences, which represent an important additional decision criterion. Due to the higher flexibility in the voltage level, 48 V applications allow for a more complex optimization of the cell configuration in order to fulfill vehicle specific requirements regarding boost capability, CO_2 savings potential and energy throughput over lifetime.

5.2 High-power capability

From an electrical point of view, high-power capability is primarily influenced by the internal resistance of a cell. Under load, a high internal resistance leads to large overvoltages and thus to increased ohmic losses. These overvoltages affect the time at which the cell-specific voltage limits are reached, which in turn determines the available cell capacity. In cell design, the internal resistance can be influenced by a variety of customizable parameters. For example, the thickness of the active material coating can be reduced to shorten the length of diffusion paths, or materials such as conductive carbon can be added

to the active material to increase the electrical conductivity [129]. The following section presents and discusses the measurement results for internal resistances and capacities of the investigated cells.

5.2.1 Impact of SOC on internal resistance

The results of the pulse measurements reveal significant differences in cell performance at low temperatures. Figure 5.4 shows the dependency of the internal resistances on SOC and temperature for discharge direction (left) and charge direction (right). For all cells the values were determined using a 3C current pulse, which were evaluated with a duration of 1 s. All three cells exhibit extremely low resistances from 0.1 mΩ to 0.5 mΩ for temperatures higher than 25 °C. To our knowledge, no commercial cells have been reported in the literature to reach such a low level.

In Figure 5.4a the internal resistance of cell A rises sharply in outer SOC regions in both charge and discharge direction. Thus, for temperatures lower than 40 °C and from 10% to 50% SOC an increase of more than 50% is apparent. Ovejas et al. [220] obtained qualitatively similar results in their study, which examined the occurrence of overvoltages in a NMC-based cell. They observed an increase of overvoltages in low SOC ranges, mainly caused by intensified concentration polarization. As shown in [114] for the same cell, the half-cell potentials of anode and cathode exhibit large gradients at low states of charge. Inhomogeneities during delithiation, especially at low temperatures and high currents, can cause increased internal resistance and local overvoltages. Within an application, strong SOC dependency can lead to reduced system performance and therefore requires explicit consideration in the operating strategy.

For temperatures below 10 °C and medium SOCs between 30% and 90%, cell A offers the lowest internal resistance. In charge direction an advantage of the LTO cell chemistry is apparent. Its high robustness against lithium plating enables cell A to be the only one tested at −25 °C with charge pulses greater than or equal to 3C [56]. Accordingly, cell A is capable of accepting recuperation currents within a vehicle application and hence has a higher CO_2 savings potential.

Cell B shows the strongest temperature dependency of the internal resistance and the highest values at negative temperatures, both in charge and discharge direction (see Figure 5.4b). For example, charge resistances at −10 °C are at least twice as high as those of the other two cells. In contrast, it provides the lowest discharge resistances at high temperatures. Similar to cell A, the internal resistance increases with declining SOC. The performance characteristics described above suggest that the focus during cell development was on discharge capability and that, compared to the other cells, fewer optimizations (e.g. electrolyte additives, conductivity improvements) were made for low-temperature operation. In low-voltage applications, functional limitations are to be expected, especially regarding cold start capability and energy recuperation at negative ambient temperatures.

Cell C, shown in Figure 5.4c, is characterized by an almost SOC-independent internal resistance, particularly in charge direction. Because of the constant resistances, cell C

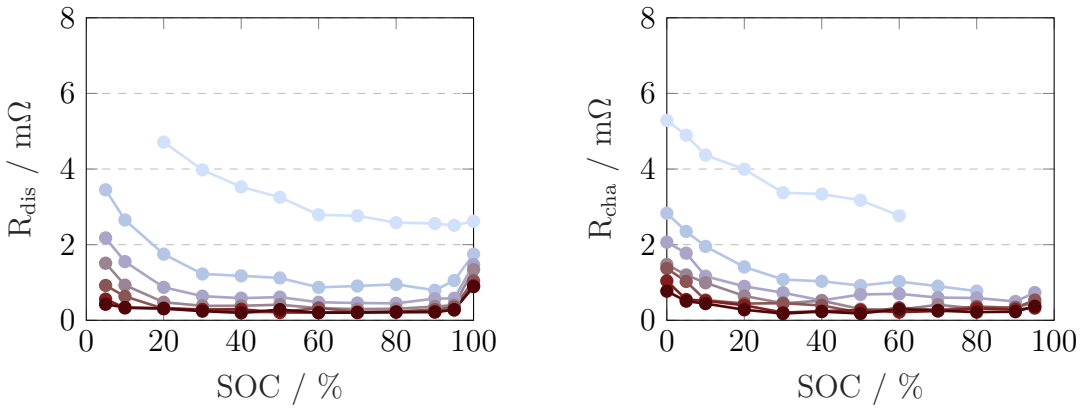

(a) NMC|LTO (cell A)

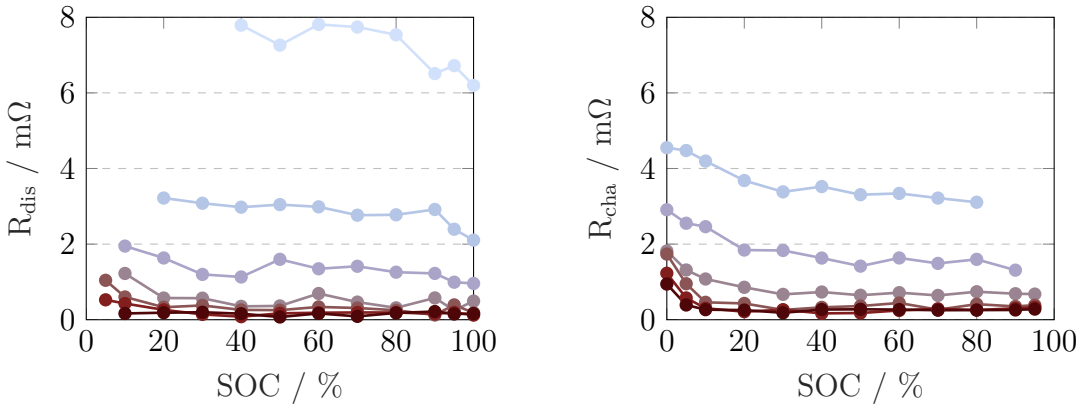

(b) NMC|C (cell B)

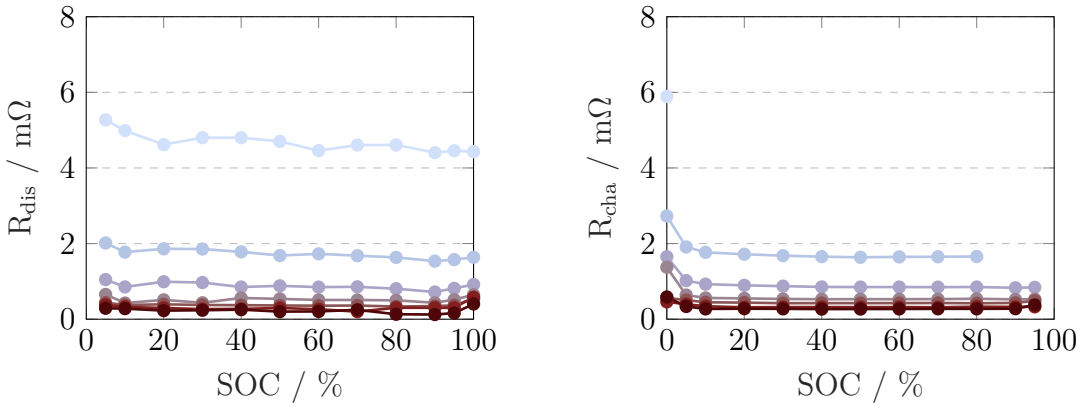

(c) LFP|C (cell C)

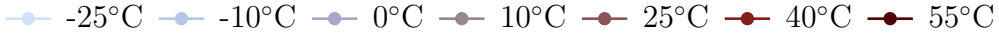

Figure 5.4: Overview of the internal resistances as a function of SOC and temperature. All internal resistances were calculated for 3C current pulses, evaluated after a pulse duration of 1 s in discharge direction (left) and charge direction (right). In general, the internal resistances of the three high-power cells are extremely low. However, major deviations in temperature and SOC dependency require cell-specific analyses.

performs better than cell A at low SOCs. The olivine structure of the LFP material seems to allow for extremely consistent lithiation and delithiation. In addition, particle sizes in nanometer scale and conductivity enhancing measures such as carbon coating enhance the performance of modern LFP cells [62, 221]. Since the OCV, see Figure 5.1c, is approximately constant over a wide SOC range, constant power output can be obtained at constant current load. This enables the use of simplified algorithms for power prediction and increases the general accuracy of power estimations. The overall predictability of the electrical behavior is higher compared to the other cells, which allows for rough calculations even without the need of simulations.

5.2.2 Impact of current rate on internal resistances

Current dependency of the internal resistance can be described by the general Butler-Volmer equation [222]. According to this equation, the speed of an electrochemical reaction increases exponentially with the driving force. Such a relationship for the current load has often been postulated for different cell chemistries. However, it is open to question how the specific properties of high-power cells, such as the low thickness of the active materials, the smaller particle sizes or the increased conductivities, influence the intensity of this effect.

Figure 5.5 summarizes the results of the internal resistances of the three cells, evaluated at 50% SOC after 1 s pulse duration as a function of current rate. All cells show approximately constant internal resistances for temperatures greater than 0 °C regardless of the current load. Waag et al. [207] achieved significantly stronger dependencies at these temperatures when testing a 40 Ah high-energy cell. This suggests that the good kinetics of the investigated cells not only have an effect on the amplitude of occurring overvoltages, but also lead to reduced activation energies for charge transfer processes. Therefore, it seems reasonable to neglect the Butler-Volmer relationship in these temperature ranges in the development of a battery management system or a simulation model.

Figure 5.5a reveals that cell A stands out from the other two cells indicating a marginal increase in resistance at low current rates even at −25 °C. The graphite-based cells (Figure 5.5b and 5.5c) show a characteristic rise in resistance, which is most pronounced for cell B. Besides the different cathode materials, the type of graphite can significantly affect the cell performance. A detailed analysis of the electrode materials and their electrochemical properties is beyond the scope of this work.

An application use of cell B or C while neglecting the current dependency can lead to increased costs in the vehicle development due to battery oversizing. For example, cold start capability of low-voltage systems requires high discharge currents at negative temperatures. If the power prediction within the battery management system is based on low-current internal resistances, functional restrictions may result. Cost-intensive measures to reach the power requirements could be to either increase the battery capacity or to reduce the low current resistance.

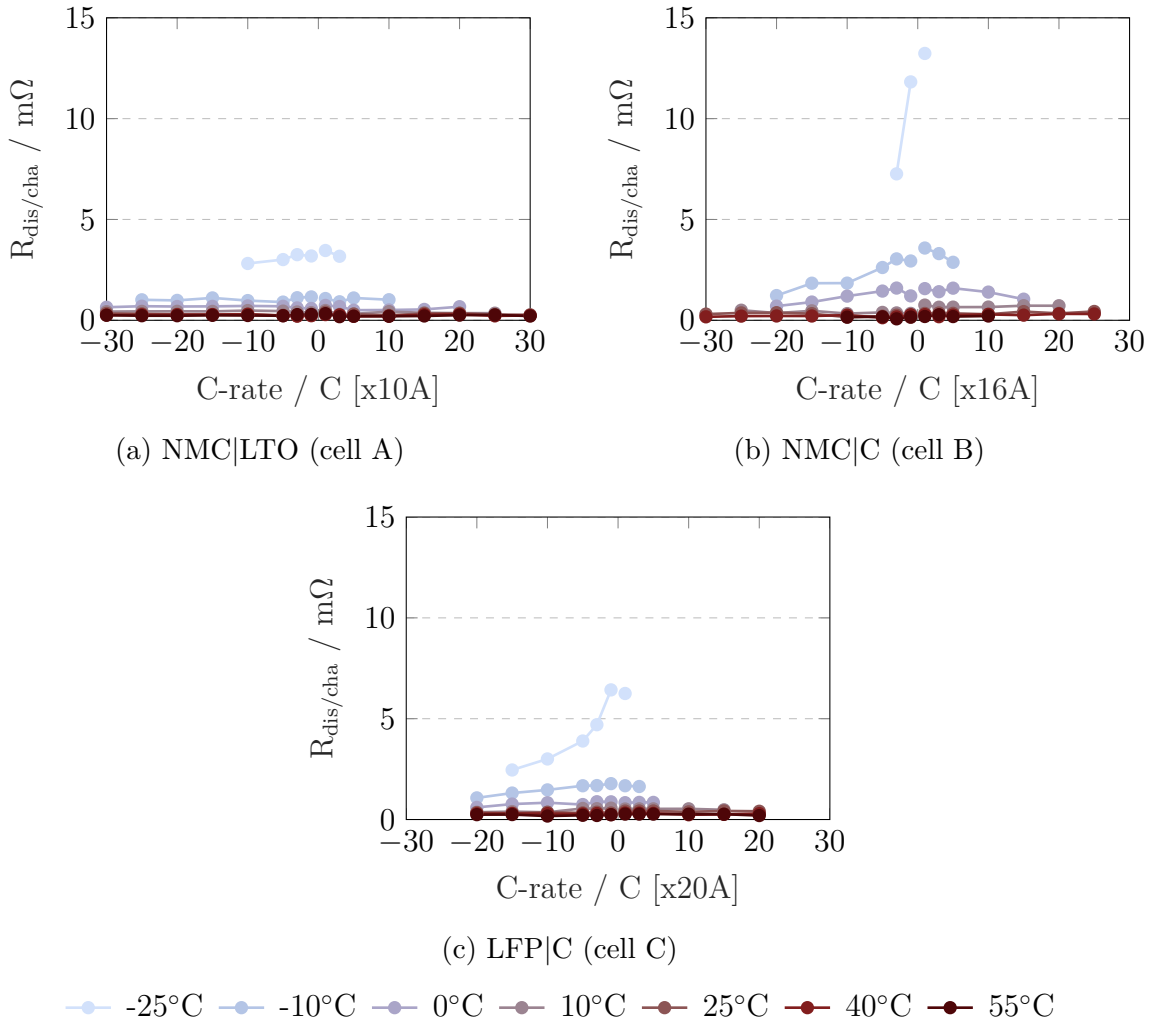

(a) NMC|LTO (cell A)

(b) NMC|C (cell B)

(c) LFP|C (cell C)

Figure 5.5: Current dependency of the internal resistances for different ambient temperatures. All internal resistances were evaluated for pulses at 50% SOC with a pulse duration of 1 s. Cells B and C show a strongly pronounced Butler-Volmer relation for −25 °C. For all three cells this dependency can be neglected at positive temperatures.

5.2.3 Capacity and energy availability

To ensure safety-relevant and comfort-oriented 48 V vehicle functions, sufficient capacity under continuous high load is required. The investigated cells show large differences in their robustness against temperature and current rates. Figure 5.6 illustrates the results of the capacity tests, which were carried out by applying a constant current in charge (positive) and discharge (negative) direction. Cell A, see Figure 5.6a, exhibits the most pronounced temperature and current dependency in discharge direction. The latter is less distinct in charge direction. Cell A can accept high charge currents of up to 15C at −25 °C, allowing for a charge of more than 50% of its rated capacity. The observed temperature dependency causes limited discharge capacities below 10 °C. Only cell A can be used in

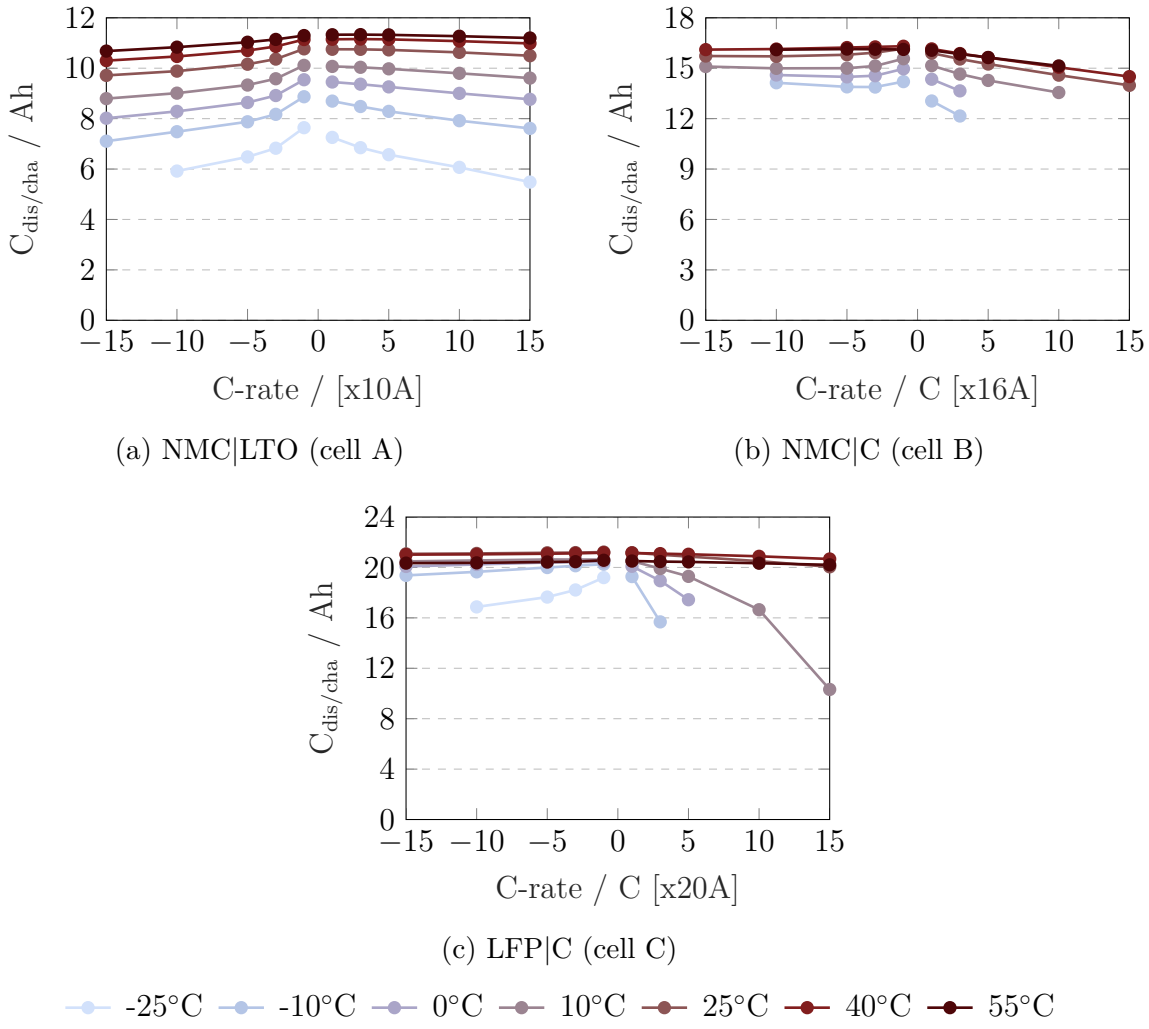

(a) NMC|LTO (cell A)

(b) NMC|C (cell B)

(c) LFP|C (cell C)

Figure 5.6: Cell capacities in charge and discharge direction as a function of current rate and ambient temperature. All capacities were determined by a CC step (cut-off voltages 1.9 V and 2.65 V), with negative currents representing a discharge process.

charge and discharge direction at any temperature, offering the largest operating range within a low-voltage application.

The narrowest operating range is provided by cell B, see Figure 5.6b, where no capacity test can be performed for −25 °C in neither charge nor discharge direction. The kinetic limitations in charge direction are in line with the results of the pulse tests shown in Figure 5.4b.

The usable capacity of cell C, see Figure 5.6c, is approximately constant and greater than the nominal capacity for temperatures greater or equal 25 °C for all current rates. Below 25 °C, the available charge capacity decreases disproportionately with increasing current intensity.

The ratio between discharged and charged capacity or energy in a complete cycle is defined as coulombic efficiency (CE) and energy efficiency (EE). In the literature CE is often used as an indicator to quantify charge losses, such as reversible/irreversible side reactions and internal micro short circuits, and to predict cell lifetime. EE further incorporates the impact of cell voltage so that, for example, thermal losses are taken into account. In principle, the CE of lithium-ion cells is approximately 100% and the ongoing processes are almost completely reversible. However, the measurement of the CE requires high-precision measuring equipment and is carried out by using very small currents. Fundamental findings for the application-oriented performance of the investigated cells might not be expected.

More relevant for the high-power cells focused on in this thesis is the amount of capacity and energy that can be extracted from the cell at high load. For a comparison of the three cell types, Figure 5.7 illustrates the results for the capacity availability (CA) and energy availability (EA). The calculation of these two performance values is based on the following equations:

$$CA = \frac{Q_\mathrm{d}(I_\mathrm{CC},T)}{Q_\mathrm{c}(I_\mathrm{CC\text{-}CV},T)} = \frac{\int_0^{t_\mathrm{d}} I_\mathrm{d}\,dt}{\int_0^{t_\mathrm{c}} I_\mathrm{c}\,dt} = \frac{I_\mathrm{d} t_\mathrm{d}}{\int_0^{t_\mathrm{c}} I_\mathrm{c}\,dt} \tag{5.2}$$

$$EA = \frac{E_\mathrm{d}(I_\mathrm{CC},T)}{E_\mathrm{c}(I_\mathrm{CC\text{-}CV},T)} = \frac{\int_0^{t_\mathrm{d}} U_\mathrm{d} I_\mathrm{d}\,dt}{\int_0^{t_\mathrm{c}} U_\mathrm{c} I_\mathrm{c}\,dt} = \frac{I_\mathrm{d} \cdot \int_0^{t_\mathrm{d}} U_\mathrm{d}\,dt}{\int_0^{t_\mathrm{c}} U_\mathrm{c} I_\mathrm{c}\,dt} \tag{5.3}$$

Here I_c and I_d represent charge/discharge currents, which are applied for periods t_c and t_d and thus result in capacities Q_c and Q_d. In discharge direction only a CC step was performed, whereas in charge direction a 1C CC-CV step with 1/50C cutoff is applied. By further considering the cell voltage U_c and U_d the charge/discharge energy E_c and E_d is calculated.

Cell A, see Figure 5.7a, shows the strongest drop in CA and EA for rising current rates. This could be related to the SOC dependency of the internal resistance, which prevents the cell from being fully discharged. CA and EA improves with increasing temperature. Exceptions are the results at 1C, where the order is reversed and CA values greater than 100% are obtained. Such values may be due to measurement inaccuracies or an influence of electrode overhang [159, 163]. At low C-rates, general deviations can have a greater effect since integration is performed over a larger number of time steps. Interestingly, differences between CA and EA are very small, indicating that overvoltages play a minor role. This is in line with the low internal cell resistances and the high-power capability of the cell.

In 48 V application use, limitations in EA can be highly relevant for vehicle operation, for example during longer parking periods at low ambient temperatures with subsequent cold start. Therefore, battery capacity as well as EA needs to be addressed in battery development and dimensioning.

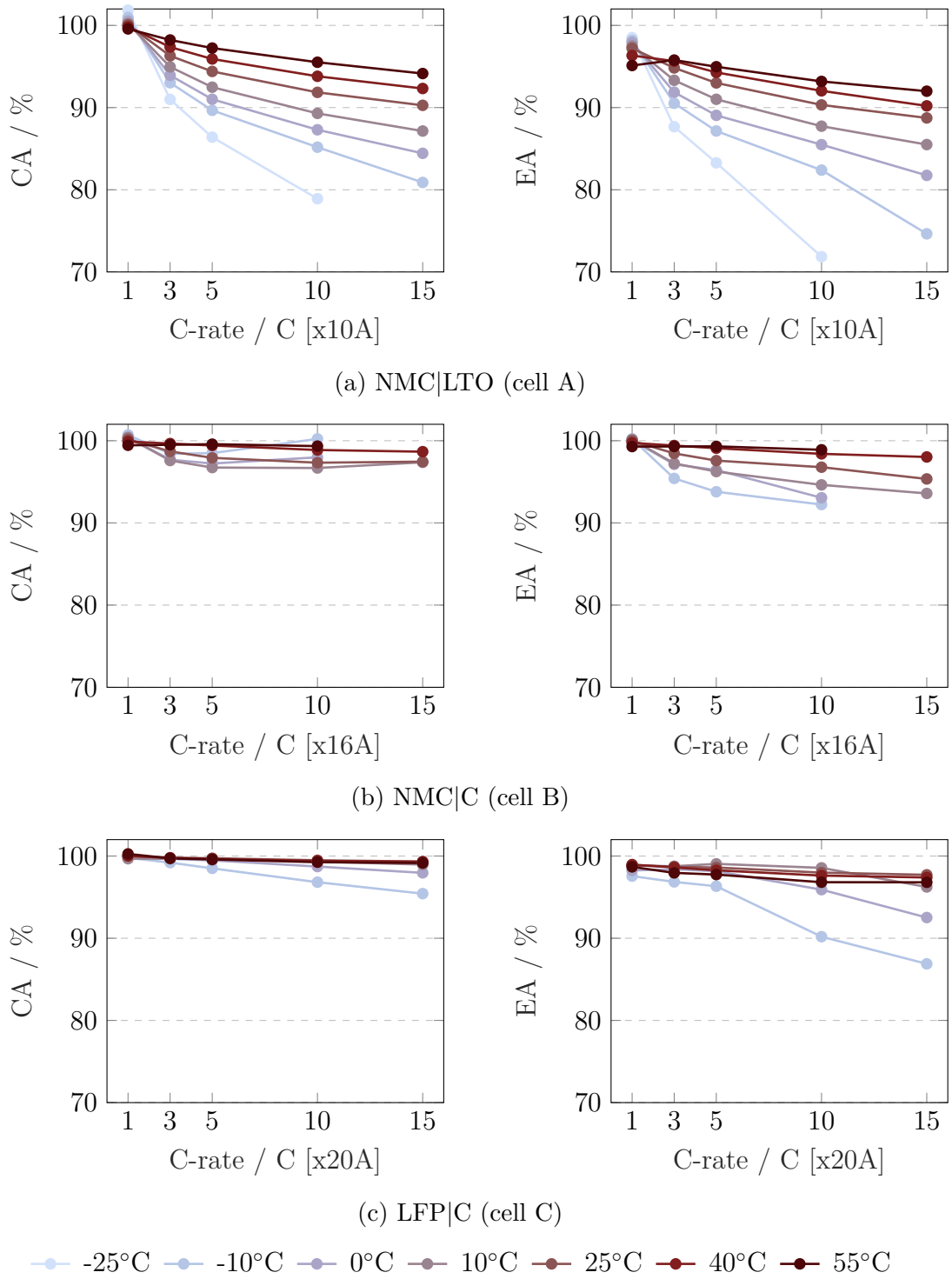

(a) NMC|LTO (cell A)

(b) NMC|C (cell B)

(c) LFP|C (cell C)

Figure 5.7: Overview of the CA (left) and the EA (right) of the investigated cells. In comparison to the graphite-based cells, cell A exhibits the worst CA and EA, which indicates limited discharge capability. The results for cells B and C mostly show over 90% even for high current rates at low temperatures.

Cell B (Figure 5.7b) and cell C (Figure 5.7c) are characterized by high CA and EA of over 90% at positive temperatures. The results are outstanding, especially since a 1C CC-CV charge is considered as a reference.

At higher current rates, the EA of cell B decreases slightly and the CA even increases, which is due to the current dependency of the internal resistance, see Figure 5.5. The non-linear decrease in internal resistance at increased current rates influences the occurring overvoltages. This affects the EA, which likewise declines non-linearly. In case of the CA, this effect becomes apparent in the rising curves at negative temperatures. The heating of the cell might positively affect the available capacity as well.

The CA of cell C, as shown in Figure 5.7c (left), reveals a linear trend with increasing current rate. At low temperatures and high current rates overvoltages increase disproportionately, affecting the EA (Figure 5.7c (right)). It is likely that the electrode materials reach kinetic limitations under these conditions.

With regard to continuous load, cells B and C are well suited for 12 V applications, where large amounts of energy are needed in the short term. The limited operating window at low temperatures restricts the use in a 48 V application, or requires additional measures such as a larger storage dimensioning or a battery heating system. Further, the results of the capacity tests and corresponding CA and EA analysis can be used to parameterize a simplified model for energy prediction.

5.3 Conclusion of the performance benchmark

A benchmark analysis of three commercially available high-power cells was performed to assess their characteristic properties at begin-of-life regarding low-voltage applications. The three cells with different cell chemistries were tested regarding their relaxed (OCV, hysteresis) and loaded characteristics under boundary conditions of low-voltage vehicle applications (1C to 30C, −25 °C to 55 °C).

The internal resistances (50% SOC, 3C) at the temperature operational limits are very low, which proves the exceptional performance of the three cells: above 40 °C internal resistance is lower than 0.5 mΩ, at −25 °C it is lower than 8 mΩ. The internal resistance of the graphite-based cells showed a strong temperature dependency and at temperatures below 0 °C a pronounced current dependency. The NMC-based cells exhibited a SOC-dependent resistance, most evidently in the NMC|LTO cell. For this cell high overvoltages in SOC boundary areas limited the CA and EA.

Hysteresis behavior depended strongly on the anode material and was little affected by ambient temperatures greater than 0 °C. For the NMC|LTO cell hysteresis was almost constant and rose with decreasing temperature. In contrast, for temperatures less than or equal to 0 °C the hysteresis of the graphite-based cells tended to decrease, especially the characteristic graphite phase-related peaks.

It can be concluded that the LFP|C cell is best suited for usage in a 12 V application. This is mainly due to the accessible operating voltage window. The SOC-independent power capability and the high achievable discharge rates further support this choice. This means that a 12 V LFP|C battery system is able to provide the required power for cold start capability, on-board power requirements etc. For 48 V applications, both the NMC|LTO and the LFP|C cell are recommended. The NMC|LTO cell represents the most powerful cell in medium to high SOC regions regardless of temperature and it possesses the highest charge acceptance at negative temperatures enabling high recuperation capability. Nevertheless, the LFP|C cell offers advantages with respect to EA in discharge direction and constant power output over the full SOC range. The new insights serve as a benchmark for battery researchers from a wide range of disciplines. They can be used as dimensioning-relevant information in battery modeling, cell and system design, and battery management system development.

Additional investigations should aim at determining performance influencing material parameters such as porosity, diffusion constants and eletrical conductivity. A direct cell comparison of these parameters could uncover the origin of the observed electrical characteristics and thus make a substantial contribution to cell development and design.

6 Evaluation of aging characteristics

This chapter is based on a publication created during the course of the dissertation. It contains minor modifications with respect to the original publication and aging results are updated to recent findings. The use of the article content including illustrations from [114] is permitted with the consent of Elsevier.

The performance analysis in the previous chapter deals exclusively with the begin-of-life characteristics of the NMC|LTO cell. However, studies on long-term effects of application-specific cell loads are essential to ensure the long-term robustness of the investigated cells.

In general, LTO-based cells as described in Section 2.2.1, have rarely been subjected to extensive aging tests. All investigations existing in the literature consider only single, partly arbitrarily chosen operating parameters for the aging analysis. There is a lack of holistic, multi-dimensional aging measurements that attempt to cover all essential dependencies of the calendar and cyclic aging behavior of LTO-based cells.

The aim of the aging studies is to evaluate the lifetime of prospective NMC|LTO cells for highly relevant MHEV applications and to identify critical operating conditions. For this reason, 36 NMC|LTO cells were subjected to various aging tests in an application-oriented 48 V context. Building on the insights of the vehicle data analysis in Section 3.3, the impact of the stress factors temperature, current rate, SOC, ΔDOD and energy throughput is investigated.

As far as known this study is the first to report and explain the PEE in cells with a geometrically oversized cathode. The PEE affects the availability of lithium-ions within the active area and thus influences the balancing of anode and cathode. An explanatory model is developed that allows for a differentiation of the consequences of floating and non-floating test conditions. Considering the PEE is particularly important for the study of stable LTO-based cells, in which under normal operating conditions of up to 60 °C hardly any loss of capacity can be observed as a result of calendar aging. Here, neglecting the PEE can lead to significant misinterpretations and incorrect state-of-health predictions.

In the following, the results of the calendar aging tests are presented, including the insights on PEE. Considering these findings, the effect of additional exposure to cyclization, synthetic or with real driving cycle, is described. A discussion of the findings and an evaluation of the criticality with respect to a 48 V application conclude this, mostly quantitative, aging analysis.

6.1 Impact factors on calendar aging

The calendar lifetime of the battery has a high degree of relevance in a vehicle electrical system. On the one hand, vehicles are required to have high durability and, on the other hand, are mainly stationary, so that the cells are not subject to cyclization. Essential battery operating parameters during these standstill periods are the SOC and the temperature, the impacts of which are analyzed in detail below. Both irreversible and reversible degradation behavior is quantified.

6.1.1 State of charge

With regard to capacity retention over aging, the examined cells exhibit a strong dependency on the storage SOC at which the test was performed. Figure 6.1a shows the remaining capacity of the cells stored at 60 °C and different SOCs. During the first check-up, a delta of 4% between the best (5% SOC) and worst (95% SOC) performing cell is found with respect to the initial capacity. Up to a test duration of about 100 days this difference increases and reaches a maximum value of over 5%. The difference in capacity is larger than the 2.3% spread of cell capacity at the beginning of the tests. Especially the rise of usable capacity cannot be explained by common aging mechanisms. The sequence of the residual capacity curves corresponds in exact order to the storage SOCs under floating conditions. Over the period under consideration, low SOCs lead to an increase and high SOCs to a decrease in residual capacity. Considering the aging trend over time, the NMC|LTO cells behave steadily despite high temperatures and perform significantly better than other cells reported in the literature [141]. Even after more than 300 days, no degradation behavior in terms of capacity is recognizable in cells with a SOC smaller than 70%. The results illustrate the challenge of aging tests of LTO-based cells in terms of time requirements and speed-up possibilities.

The internal resistance, as shown in Figure 6.1b, rises from 6% to 14.5%. Here, the internal resistances of the cells with medium SOC increase the most and those of the cells with low SOC the least. It is difficult to make a general statement regarding this observation, since the deviations between the individual cells with similar SOC are high and measurement inaccuracies due to the very low internal resistances of high-power cells may have a great influence. However, the calendar aging tests at 60 °C emphasize that the cells are very well suited for applications where high temperatures occur over long periods of time. Under the assumption of an end-of-life at 150% relative internal resistance and a linear aging trend, a total battery lifetime of three years at constant 60 °C is realistic. During the aging test slight gassing behavior has been observed, but it was difficult to be detected optically due to the clamped test setup.

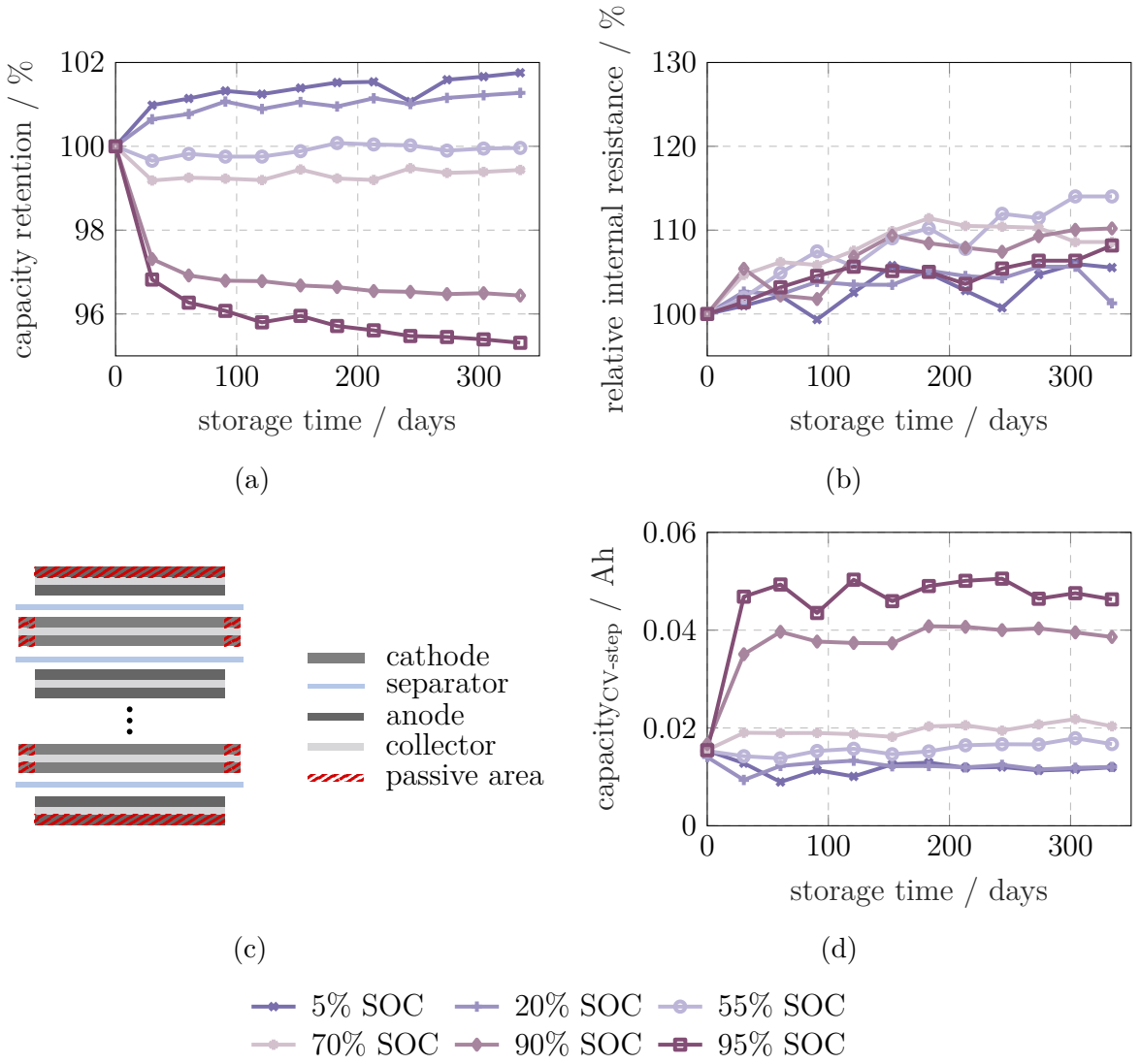

Figure 6.1: a) Normalized capacity over time and b) normalized resistance over time for calendar aging tests at 60 °C and different SOCs. Depending on the storage SOC during the aging tests, the remaining capacity in the first check-up changes significantly. High SOCs lead to a decrease and small SOCs cause an increase of the residual capacity. c) Schematic representation of the geometric arrangement within the cell. The cathode is geometrically oversized on all sides compared to the anode. All sheets are coated on both sides, whereby anode sheets represent the first and last layer of the cell. All areas that are not actively involved in charge and discharge processes are declared as passive areas. d) Capacity added in the CV step of charging during the first capacity test in the check-up. With increasing storage SOC, this capacity rises sharply. The homogeneity of the lithiation of the cathode is decisive for the magnitude of capacity.

6.1.2 Passive electrode effect

The cell investigated in this work represents a novelty and thus an extension of the prevailing theory in two aspects. In Figure 6.1c a schematic illustration of the inner cell geometry is shown. A distinction must be made between two different areas which do not actively participate in charge and discharge processes and thus also in capacity determination. On the one hand, there is an edge area of the cathode, which is directly connected to the active area of the cathode and is a few millimeters wide. Since LTO-based cells exhibit an extremely low lithium plating risk and LTO material is likely to be more costly than NMC material, the anode is dimensioned smaller. On the other hand, double-sided coated anode sheets are used within the whole cell. Therefore, the anode side facing the pouch foil at the beginning and end of the cell stack is only indirectly involved in the lithiation processes. Based on the geometric conditions within the cell, the anode and cathode overhang result in different diffusion paths for equalization processes. Within the cathode, the diffusion path into the passive region is short, whereas large distances of several centimeters must be bridged by solid-state and electrolyte diffusion within the anode. This leads to the assumption that two individual time constants result for the speed of the equalization processes.

As can be deducted from the data in Figure 6.1, the impact of the PEE is quite large for the given cell. According to the formula published by Lewerenz et al. [160], the following value results for the cathode overhang:

$$\text{Share of PE}_{\text{Cathode}} = \frac{A_{\text{C}_{\text{activepassive}}}}{A_{\text{C}_{\text{active}}}} - 1 \approx 5.4\,\% \tag{6.1}$$

Here, $A_{\text{C}_{\text{activepassive}}}$ refers to the total area and $A_{\text{C}_{\text{active}}}$ to the active area of a cathode sheet. The anode overhang can be calculated by the ratio of numbers of anode sheets $N_{\text{A}_{\text{sheets}}}$ and cathode sheets $N_{\text{C}_{\text{sheets}}}$:

$$\text{Share of PE}_{\text{Anode}} = \frac{N_{\text{A}_{\text{sheets}}}}{N_{\text{C}_{\text{sheets}}}} - 1 \approx 2\,\% \tag{6.2}$$

Figure 6.2 qualitatively shows how these overhangs affect the capacitive performance of the cells using the half-cell potential curves. As with the tested cells, a completely relaxed system with approximately 30% SOC is assumed as initial condition. The adjustment of the storage SOC to 95% only affects the active areas of cathode and anode at first. The concentration and voltage gradient between the active and passive regions of the cathode results in a balancing ion flow, which increases the charge of the active cathode material. In this context, a distinction must be made between calendar aging tests under floating and non-floating condition. Since there is an electrical connection between the anode and cathode in the case of floated cells, an external current flow can occur. As the potential of the active cathode area decreases, the potential and thus the SOC of the anode must increase to maintain the externally applied full cell voltage. This takes place via a current flow from anode to cathode or an ion flow from cathode to anode respectively, which is monitored as floating current. The entire process leads to a change in charge of

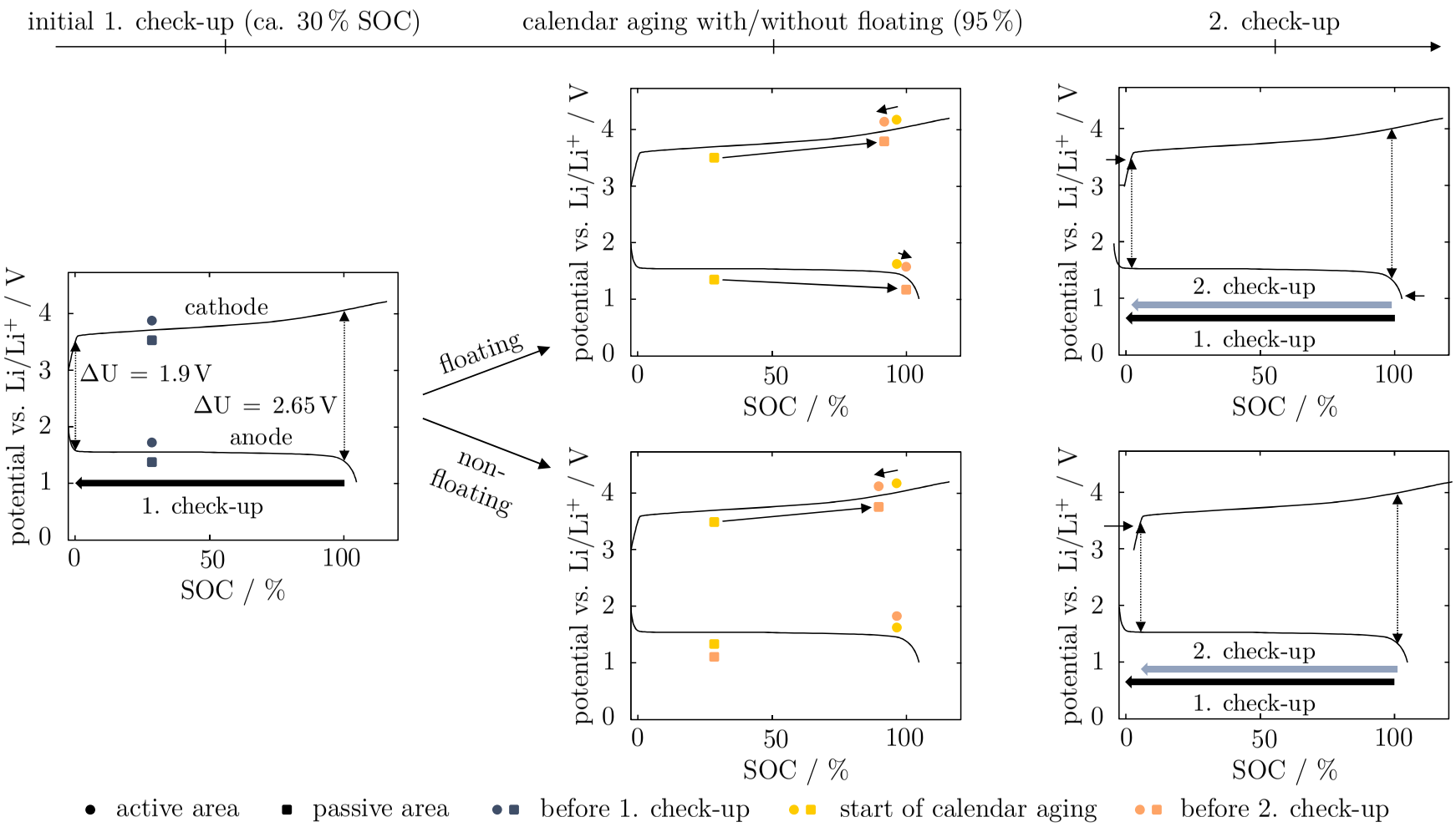

Figure 6.2: Qualitative explanation for the influence of the passive areas on the resulting discharge capacities in the first and second check-up using anode and cathode potential curves. A fully relaxed system is assumed for the first check-up. At the beginning of calendar aging, the examined cells are at approximately 30% SOC. An increase of the cell SOC leads to a concentration and voltage gradient between the active and passive area and a lithium-ion flow from the passive to the active area. Depending on the test procedure (floating, non-floating), one or both potential curves shift and thus reduce the discharge capacity in the defined operating voltage window.

anode and cathode, which corresponds to a shift of the half-cell voltage curves. This shift, taking into account the upper and lower cell voltage limits, leads to significantly lower extractable capacity in the second check-up. In the case of non-floating test conditions, the equalization process only takes place on the cathode side, thus causing a shift of the half-cell potential. However, in the end this has similar effects on the available cell capacity.

The overall influence of the passive area of the anode is most likely to be low, not only because of the small proportion of 2%. On the one hand, the potential of the LTO is nearly constant over the entire operating window, so that balancing processes between the active and passive areas of the anode are small. On the other hand, the aforementioned long diffusion paths have an inhibiting effect.

The half-cell potential curve of the cathode is decisive for the majority of the equalization processes within the cell. Since NMC vs. Li/Li^+ has no potential plateaus compared to graphite considered in previous works, the influence increases strictly monotonically with increasing difference between storage SOC before test and during test [160, 161]. This results in a distinct arrangement of the capacity curves for the examined cells according to their storage SOCs during the test. As becomes apparent from the level of the capacity differences and the corresponding SOC level, the intensity increases in the higher SOC boundary area, where the OCV of the full cell has a steep gradient.

Additionally, the passive area of the cathode has an effect on the homogeneity of lithiation of the active cathode area. An indicator of this is the capacity that is charged into the cell during a constant voltage phase. In Figure 6.1d, the capacities measured in the constant voltage phase of the charging step during the first capacity test of the check-up are illustrated for the calendar aging tests at 60 °C. Nearly identical values are observed in the first check-up due to similar SOC start values of all cells. From the second check-up onwards, large differences in CV capacities are observed depending on the storage SOC. Particularly noticeable are high storage SOCs, which require the largest CV phase. This can be explained by the degree of lithiation of the passive cathode area. For the calendar aging test with high SOC, the degree of lithiation of the passive cathode regions is low. During the capacity test the anode is discharged and the active area of the cathode is charged. Due to the high potential gradient between lithiated and delithiated cathode material, the passive edge region of the cathode facing the active region is slightly charged. In addition, during the 30-minute break, more ions diffuse into the passive area, further reducing the degree of lithiation in the edge area of the active NMC part and thus increasing the inhomogeneity. During the subsequent charging phase, the anode cannot be lithiated over its entire surface until the cut-off voltage is locally reached, so that a more extensive CV phase is necessary. As Grimsmann et al. [223] theoretically explained for graphite-based cells as well as demonstrated by cell openings, these local inhomogeneities in the active edge areas of the graphite material can lead to lithium plating and thus to significantly shortened cell lifetimes. Due to the high stability of the LTO and the capacitive oversizing of the NMC, no strong influence on aging is to be expected from the shift of the used potential ranges. This is consistent with the available measurement data.

Regarding the internal resistance, the PEE has no quantifiable influence. On the one hand, at high temperatures during the test, the equalization process is largely completed by the second check-up. On the other hand, the internal resistance of the tested NMC|LTO cell is nearly SOC-independent in the SOC range between 5% and 95% at 25 °C.

For a systematical analysis of cell aging, the PEE must be considered and quantified in the test design. Ideally, the cells have to be long-time stored at a defined storage SOC prior to test start if no information on the cell history is available. If a determination of the geometric arrangement within the cell is impossible, methodologies as described by Lewerenz et al. [224] and Warnecke et al. [31] enable a rough quantification of the share of passive area. In the application context, the resulting inaccuracies can cause significant misjudgments regarding the remaining capacity. However, it should be mentioned at this point that the standard transport of lithium-ion batteries is carried out at SOCs between 30% and 50% and that the average SOC in application operation is often in the medium SOC range. This leads to lower deviations and calculation errors. To reduce the impact of the PEE, one goal of cell design should be to minimize the overhang.

6.1.3 Temperature

The examined NMC|LTO cells show a clear temperature dependency only with regard to the increase in internal resistance. As shown in Figure 6.3a, the cells perform identically at 40 °C and 60 °C in terms of capacity retention. After more than 300 days of testing, approximately 100% of the initial capacity is still available. The capacity of the cell stored at 80 °C increases to about 105% before the cell had to be removed from the test due to bursting of the pouch bag, caused by strong gassing behavior. The PEE does not explain the sharp and continuous rise in capacity for two reasons. Firstly, all three cells had a similar initial state from 2.11 V to 2.124 V the test started. Secondly, according to the theory of the PEE, the subsequent calendar aging phase at 55% SOC, which approximately corresponds to 2.2 V, should lead to a slight decrease in available capacity. In the examined cell, the LTO material determines the cell capacity due to the cell balancing. Perhaps the gassing behavior caused increased pressure within the LTO active material and in consequence cracking, which lead to an increase of the active surface area ('electrochemical milling') [225–227]. A permanent structural change of the LTO material due to the high ambient temperature may also be conceivable. In Chapter 7, these capacity effects induced by calendar aging at high temperatures are investigated in more depth.

Regarding the internal resistance increase, presented in Figure 6.3b, the three tested cells indicate significant differences depending on the storage temperature. The internal resistance of the cell at 40 °C increases by 5% in the observation period of 240 days, at 60 °C by 14% and at 80 °C even by 35% after 120 days. Considering the strong gassing behavior of the cell at 80 °C up to venting, the internal resistance increase is low and a good cell performance is still given. The continuous compression of the cells allows for a large part of the gases produced to be displaced into the peripheral areas where the gas reservoirs are located. Assuming an Arrhenius dependency, the relationship between temperature and internal resistance rise is usable for aging simulations and lifetime predictions.

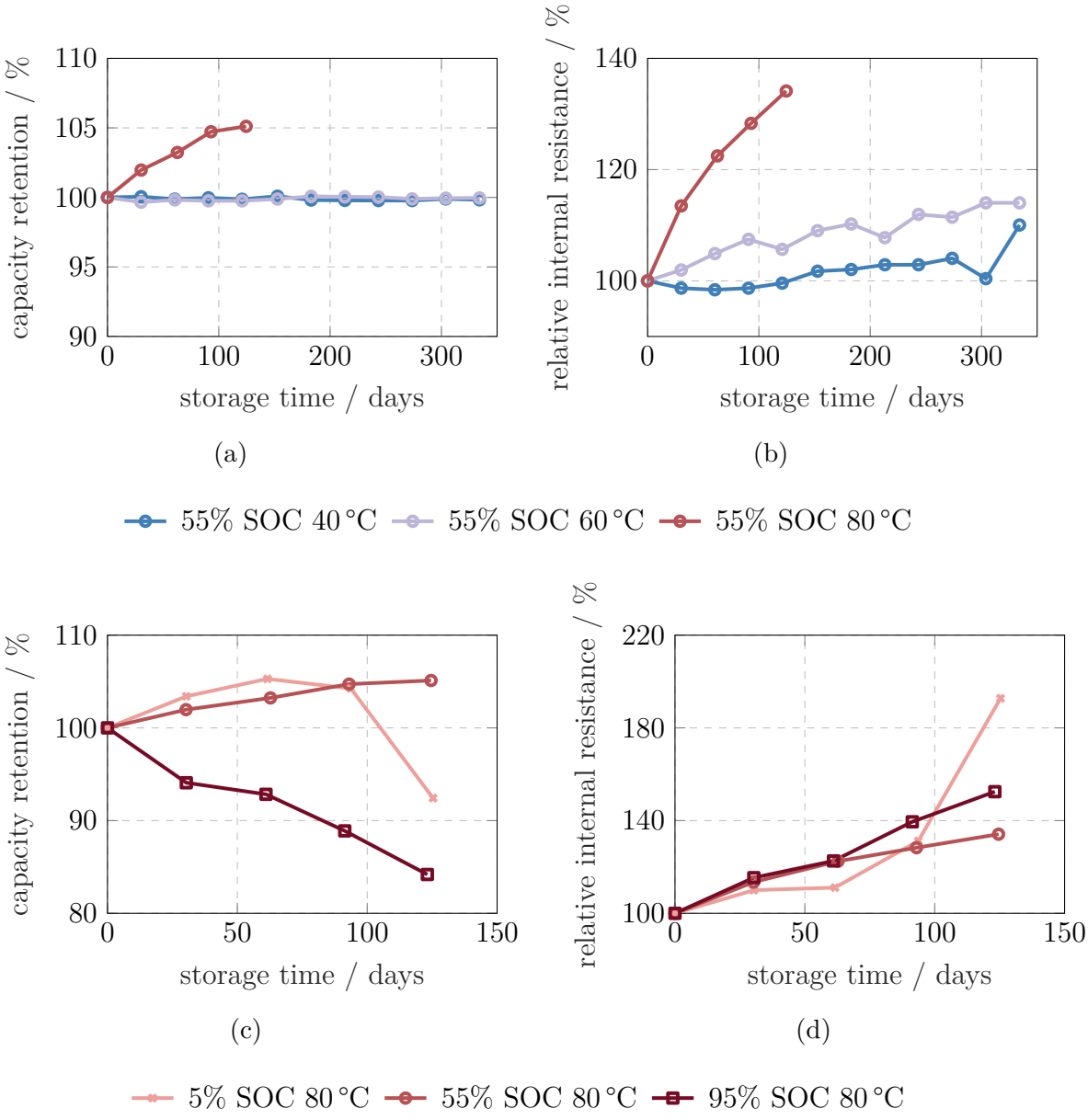

Figure 6.3: a) Normalized capacity over time and b) normalized resistance over time for calendar aging tests at 55% SOC and different temperatures. Only the cell at 80 °C shows a change in capacity. The resulting internal resistances suggest a temperature dependency. c) Normalized capacity over time and d) normalized resistance over time for calendar aging tests at 80 °C and different SOC. Due to strong gassing behavior, all three cells show a large increase in internal resistance. The cells were removed from the test after the pouch bag film had burst.

At very high temperatures, the NMC|LTO cells show a strong gassing behavior independent of SOC, with both the upper and lower SOC range being particularly critical. Figure 6.3c and 6.3d show the capacity and internal resistance curves of the cells stored at 80 °C. As 80 °C represents the highest storage temperature approved by the cell manufacturer, it is not to be described as an abuse scenario. In the first 60 days, both the PEE and the previously described abnormal behavior at 55% SOC predominate in relation to the residual capacity. At this point, the capacities of the cells stored at 5% SOC and 95% SOC decrease significantly. A possible reason for this could be a loss of contact within the cell caused by gassing [123]. This loss of contact could be caused by electrolyte displacement on the one hand and by cracking of the active material on the other hand. This theory coincides with the significant increase in internal resistance from 60 days test duration for cells with 5% SOC and 95% SOC. For these two cells a direct correlation between residual capacity and internal resistance increase exists. With respect to the internal resistance, the cell stored at 55% SOC appears to be the least noticeable.

As already postulated in [29, 61], the results suggest that different gassing reactions take place within the cell depending on the SOC. However, such a strong gassing in low SOC areas has not been observed so far. It remains to be investigated which electrochemical reaction at which of the two active materials is mainly responsible for the detected gassing behavior. Generally, when using the cells in an application, temperatures beyond 70 °C should be avoided for safety reasons in order to prevent the cells from swelling or, in extreme cases, venting. In addition to high SOCs, which are often described as critical to battery lifetime, the focus should also be on low SOCs in combination with high temperatures. This should also be considered for the definition of the operating strategy.

6.2 Impact factors on cyclic aging

In the following sections, the effects of aging are mainly shown by means of changes in residual capacity. This is due to the fact that the measured internal resistances often do not show a clear aging trend. Especially cyclic aging tests at 40 °C do not lead to a significant increase of the internal resistance. In addition, despite the four-pole measuring principle, measuring inaccuracies are still present due to the extremely low internal resistances of the NMC|LTO cells. The number of equivalent full cycles is calculated on the basis of the available capacity in the first check-up before test start. All cyclic tests, including the SOC setting at test start and at SOC reset, were Ah-based. The initial loss of capacity observed in all tests from Table 4.5 is assumed to be attributable to the PEE. Prior to test start, the cells in these cyclic aging tests had SOCs between 15% and 20% (2.11 V to 2.124 V). Since during cyclization the average SOC was 50% or 55% an initial drop in usable capacity is expected. For this reason, the capacity drop after test start is not addressed for every illustration. Instead the focus is on the long-term aging trend.

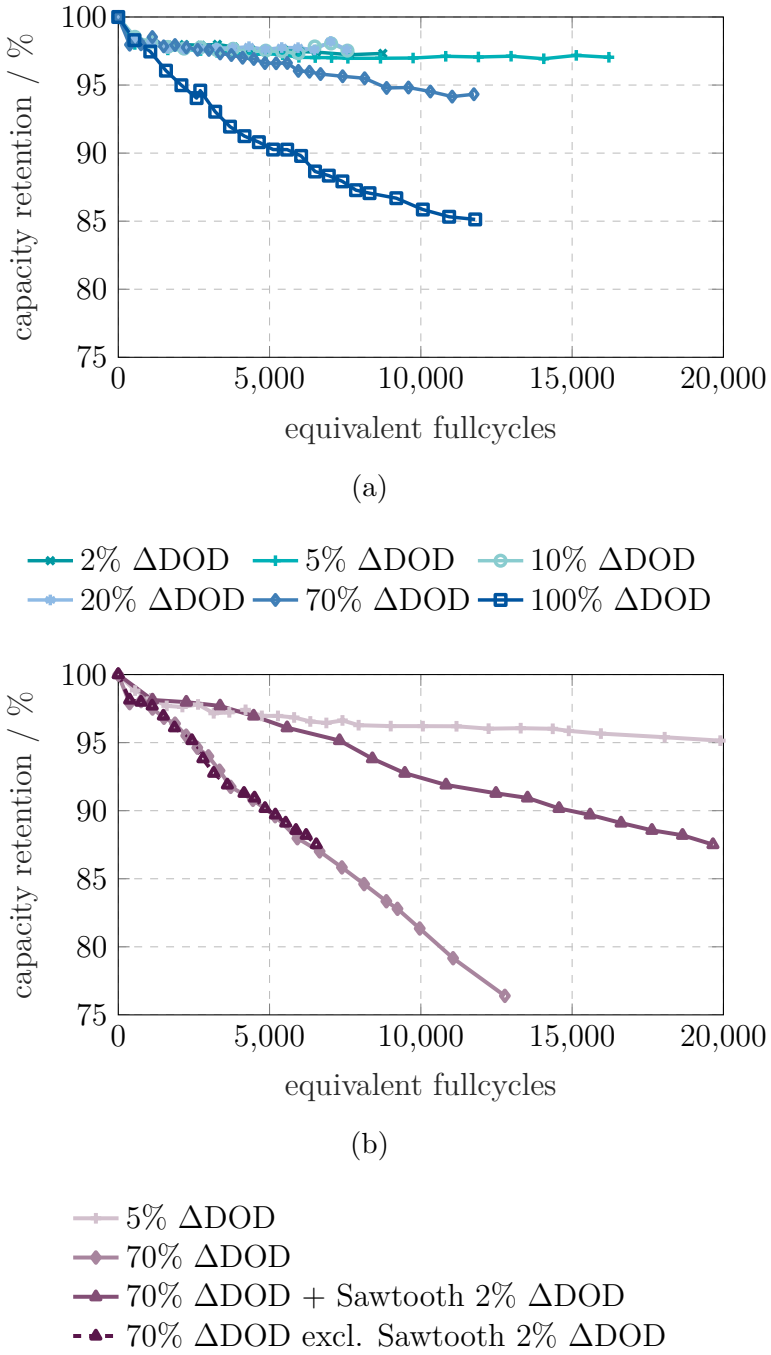

Figure 6.4: Normalized capacity over time for cyclic aging tests with different ΔDODs at a) 40 °C and b) 60 °C. The mean SOC for fractional cycles was 55% SOC. For both temperatures the capacity loss increases with greater ΔDOD. The dependency on ΔDOD becomes stronger with increasing temperature. In b), the charge throughput of the superimposed microcycles was both included and excluded. There is no noticeable capacity loss due to the microcycles of 2% in the cyclized SOC range between 20% and 90%.

6.2.1 Cycle depth

Despite the 'zero-strain' property of LTO, the aging behavior of the examined cells reveals a clear dependency on the ΔDOD. For 40 °C and 60 °C the residual capacity curves for different ΔDODs are shown in Figure 6.4. For the tests at 40 °C (see Figure 6.4a), significant differences between the ΔDODs 100%, 70% and the rest are apparent. Small ΔDODs (ΔDOD ≤ 20%) only lead to a slight loss of capacity, whereas full cycles accelerate the aging process by a large factor. Taking into account an end-of-life criterion for the remaining capacity of 80%, the cell with 100% ΔDOD has an estimated cycle life of approximately 20,000 equivalent full cycles. This number is substantially high under the present boundary conditions (40 °C, 5C/5C, 100% ΔDOD).

At 60 °C, see Figure 6.4b, the cell at 70% ΔDOD ages in a comparable order of magnitude as the cell at 40 °C with 100% ΔDOD. Interestingly, the 60 °C cell with a ΔDOD of 70% and an overlaid sawtooth profile of 2% ΔDOD shows a significantly lower aging rate. This rate is stronger than that of the cell cycled at 5% ΔDOD. The superimposed sawtooth profile is responsible for approximately two thirds of the charge throughput. For illustrating the influence of the superimposed large cycle, in Figure 6.4b the charge throughput of the microcycles was both included and excluded. The obtained capacity curves reveal that the microcycles with 2% ΔDOD do not noticeably affect the capacity retention. On the one hand, this demonstrates that small ΔDODs generally lead to lower stress for the examined cell. On the other hand, these results, in line with the results of SOC-related calendar aging, indicate that some aging processes are induced by SOC. Further investigations of these processes are carried out in Chapter 7.

The NMC|LTO cell offers an excellent lifetime when cycled in medium SOC ranges, espacially when small ΔDODs are applied. The results illustrate the difficulties associated with aging tests of LTO-based cells. Despite an operating point just below the maximum allowed temperature limit (70 °C at cyclization), high-current testing is necessary to allow for a test period of a few months to a few years. This leads to high costs for test bench occupation and also requires parallelization of test equipment, depending on the cell capacity.

6.2.2 Current rate

Based on the existing results, the stress factor current rate cannot be clearly classified as lifetime shortening. In Figure 6.5a, the remaining capacity of two cells is shown, which were cycled with two C-rates each and two different test temperatures at 5% ΔDOD. The capacity loss after the first capacity drop caused by the PEE can be described as approximately linear for all cells. After 12,000 equivalent full cycles, the 10C/10C current load causes approximately 20% more capacity loss than the 5C/5C cycles, however, this corresponds to only 1% of capacity difference. The different self-heating of the cells at the various current rates must be taken into account. These were 0 °C to 2 °C at 2C/2C, 2 °C to 4 °C at 5C/5C and 4 °C to 6 °C at 10C/10C. As shown in Figure 6.3a, this difference should have a minor impact on the capacity degradation of the cell.

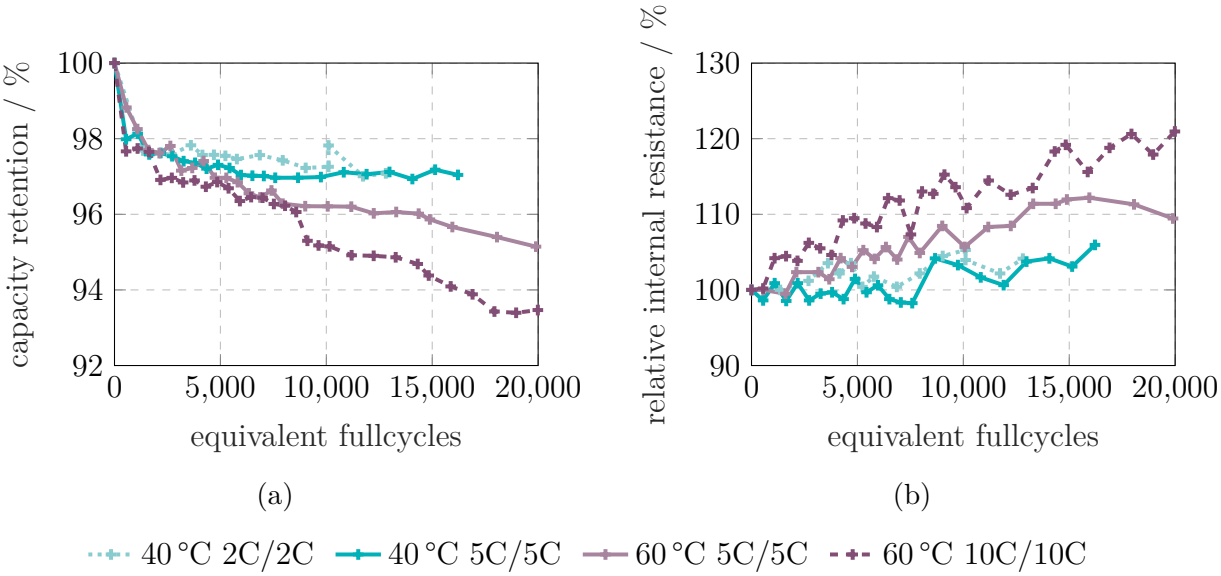

Figure 6.5: a) Normalized capacity and b) normalized resistance over equivalent fullcycles for cyclic aging tests at 40 °C and 60 °C with three different current rates and 5% ΔDOD at an average SOC of 55%. An influence of the current rate as well as the temperature on the aging behavior is noticeable. The self-heating of the cells is very low due to low internal resistances and good heat dissipation via the pressure plates.

Regarding the internal resistance, see Figure 6.5b, the findings are similar. The increase in internal resistance does not exceed the calendar aging effect shown in Figure 6.3b over the period under consideration. Nevertheless, at 60 °C 10C/10C seems to lead to stronger resistance increase than 5C/5C. It is possible that cyclization might lead to greater current dependency at greater ΔDODs, since the probability of concentration gradients as well as the mechanical stress within the active material increases. Conversely, at shallower ΔDODs, the duration of exposure to potentially damaging high and low voltage ranges is reduced, since overvoltages are smaller. A variation of the current rate affects a series of other aging relevant parameters, so that isolated examinations are difficult.

Nevertheless, the given results are highly relevant in the application context and demonstrate the suitability of the investigated NMC|LTO cells for dynamic high-power applications. Furthermore, the superior resistance to high current rates allows for accelerated aging tests in terms of overall energy throughput.

6.2.3 Voltage level

Low voltage ranges cause severe performance degradation of the examined cells and should be considered at least as critical as high voltage ranges. As can be seen in Figure 6.6, the cells in the lower voltage range (2.0 V to 2.4 V) show the strongest aging trend. As with calendar aging at low SOCs, the reason for this behavior is not clear. In the literature,

accelerated aging is often associated with high SOCs at cell level. This is reported for both lithiated LTO and delithiated NMC. These states possess an increased electrochemical reactivity as well as structural instability and thus accelerate possible side reactions [61, 228].

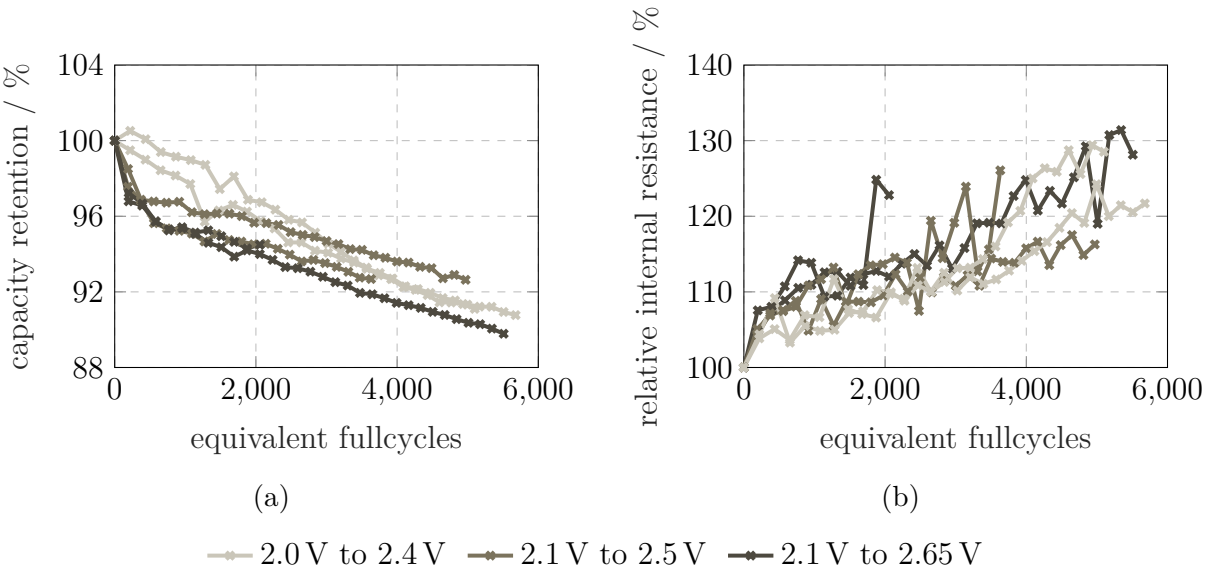

Figure 6.6: a) Normalized capacity over time and b) normalized resistance over time for cyclic aging tests at 60 °C, 5C/5C and different voltage ranges. The impact of the cut-off voltage is low. However, the rapidity of the capacity loss of cells cycled in lower voltage ranges is most critical. No distinct statement can be made regarding the increase in internal resistance.

The PEE is clearly evident in the results presented. All cells in this test were stored at about 5% SOC before test start. The differences of the cells cycled between 2.0 V and 2.4 V in the first 500 cycles are due to an unintentional full charge phase of 2.5 and 4 days respectively prior to test start. This emphasizes the importance of the consideration of the cell history. Otherwise, misjudgments of almost 4% capacity difference in this case are possible after a few hundred cycles. Therefore, if the history of the cells is unclear and a PEE could potentially be present, the aging trend should always be taken into account, neglecting the initial drop.

The upper cut-off voltage seems to have little influence on the aging rate. From the 1000th equivalent full cycle onwards, the cells with an upper voltage limit of 2.5 V or 2.65 V age almost identical. With regard to the change in internal resistance, no differentiation between the tested voltage ranges is possible, partially because of the high scattering.

6.2.4 Aging by drive cycle

Aging with real drive cycles illustrates the positive effect of small ΔDODs on the remaining cell capacity. As shown in Figure 6.7a, the three tested cells exhibit a similar capacity

loss of less than 3% after almost 10,000 equivalent full cycles. On the one hand, this temperature-independency of the capacitive aging behavior corresponds to the results in Figure 6.3a. On the other hand, the aging impact of high pulse currents in connection with low ΔDODs is small for the investigated NMC|LTO cells. Thus, achieving the application-relevant lifetime requirement of more than 27,000 equivalent full cycles, see [166], is not critical. The PEE described above is minor, since on average the cells were cycled in the middle SOC range and were previously stored at approximately 30% SOC.

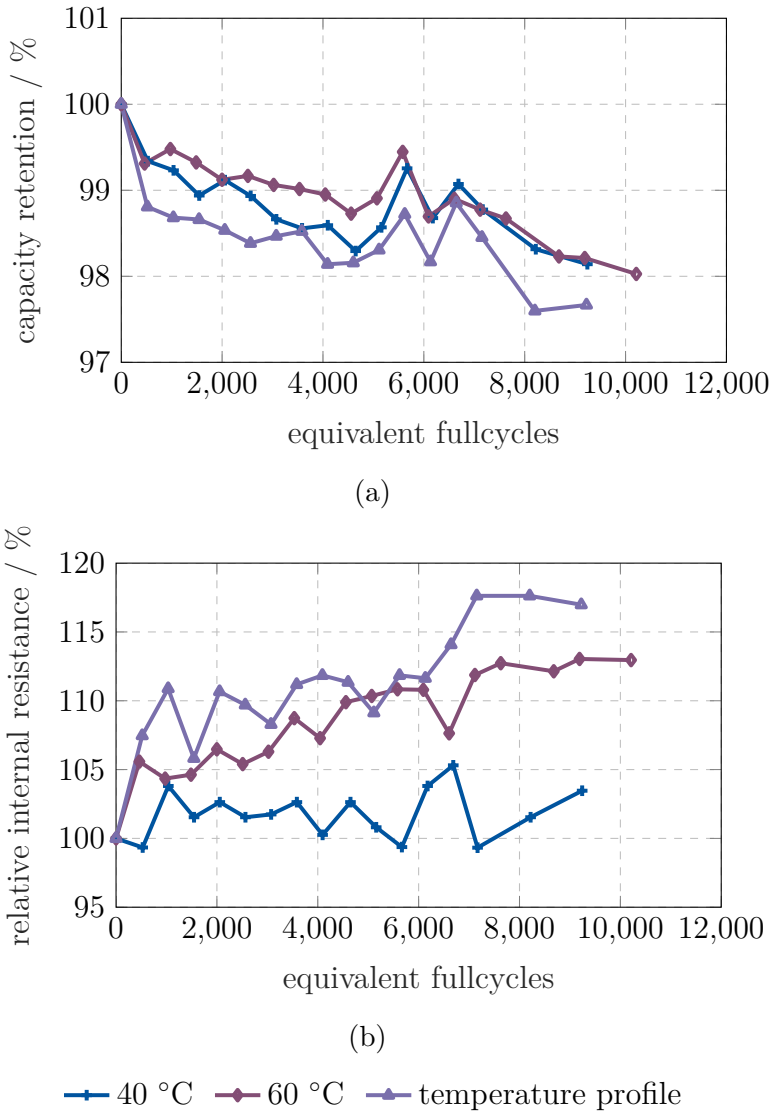

Figure 6.7: a) Normalized capacity over time and b) normalized resistance over time for drive cyclic aging tests at different ambient temperatures. The capacity retention is almost temperature-independent. In contrast, the results for the internal resistances for the cells at 40 °C and 60 °C show a clear influence of temperature. The increased aging behavior of the cell with variable temperature profile is surprising and cannot be explained so far.

The increase of the internal resistance is temperature-dependent and lifetime-critical and should therefore be a prioritized criterion in battery development. All three cells experience a rise in internal resistance with increasing number of equivalent full cycles as shown in Figure 6.7b. The internal resistance of the cell at 60 °C increases about three times as much as the internal resistance of the cell at 40 °C. The reason for this may be accelerated and additional side reactions, which can lead, for example, to the formation of a covering layer on the electrodes or gassing. Since the results of the calendar aging tests were quite similar (compare Figure 6.3b), the cyclic stress seems to only have a negligible effect on the internal resistance. Interestingly, the cell with the variable temperature profile shows the largest increase, although the average temperature in this profile is below 40 °C. No explanation for this could be found so far. Perhaps the temperature changes have a negative effect on degradation. To exclude the risk of the cell being an outlier, additional measurements need to be carried out. Under the condition of a maximum increase of 50% over the battery lifetime and the assumption of a linear progression, 27,000 equivalent full cycles are realistic. Depending on the ambient temperature within the application, special attention must therefore be paid to the internal resistance in the development process.

6.3 Resulting implications for 48 V applications

For the application-based context, the results of the aging tests have several, mostly positive, implications. On the one hand, it was shown that small ΔDODs, which predominantly occur in 48 V applications, have a negligible impact on cell aging. No explicit deterioration in cell performance can be detected after deduction of calendar aging. In addition, other stress factors such as high current rates and high energy throughputs have a low influence on aging. It must be ensured that low and high SOCs are avoided, as these accelerate the aging process and, depending on the ambient temperature, gassing reactions. In spite of the high temperature stability of the tested cells, the ambient temperature in the application is decisive with regard to the increase in internal resistance. For this reason, special attention must be paid to the expected battery temperature in the development process. The high capacitive stability of the NMC|LTO cells can be used to minimize capacitive reserves, which serve to achieve the defined end-of-life performance. For example, a 10% reduction of the nominal capacity could be considered while simultaneously increasing the frequently used 80% end-of-life requirement. The opposite applies to the internal resistance according to the illustrated cycle life results. For the cell design it is essential to ensure that the end-of-life performance defined for the application is guaranteed. Since the calendar aging represents the more severe challenge for the examined cell in the application-related operation, relevant stress factors have to be minimized or greater reserves have to be ensured. It may be necessary to improve the battery cooling or to make cell-specific changes.

6.4 Conclusion of the aging analysis

Quantifying the influential parameters relevant for battery aging in an 48 V system is necessary for a large-scale and error-free application in the vehicle. Within the aging analysis, 36 state-of-the-art NMC|LTO cells were exposed to cyclic, calendar and drive cyclic aging regimes. The chosen load scenarios had previously been derived from real vehicle data and therefore cover the application-relevant operating conditions of the cells in the vehicle.

The calendar aging tests indicated little to no loss of capacity at temperatures of less than or equal to 60 °C independent of the SOC. If a change in capacity was observed in the first weeks of the test, this was predominantly caused by the PEE. Importantly, for the first time, the PEE is reported for a cell with geometrically oversized cathodes. A theoretical and descriptive explanatory model is presented, which highlights the unavoidable relocation of lithium-ions into and out of passive electrode areas. This relocation alters the initial cell balancing and thus explains the reversible loss or increase of capacity. The presented argumentation is transferable to graphite-based cells and shows, for example, the increased risk for lithium plating due to CV phases during cyclization.

Storage of cells at extremely high temperatures (80 °C) led to a strong gassing behavior, which occurred at both high and low SOCs. The latter has not been reported in the literature previously. In addition, a greater loss of capacity was observed under systematic cycling at lower voltage ranges. This confirmed the assumption that operation at lower voltage ranges triggers additional aging processes.

Exposure to real drive cycles demonstrated the capacitive stability of the NMC|LTO cells. An increase in internal resistance, which was mainly influenced by calendar aging at high temperatures, was the lifetime-determining factor. Thus, with respect to cell development for a 48 V system, special attention must be paid to performance fulfillment at end-of-life.

In a next step, the aging results from this publication can serve as a data base for a parameterization of a semi-empirical aging model. This could cover an open niche in the field of aging models for high-power cells and in particular NMC|LTO-based cells. Especially with regard to the PEE, a concrete breakdown of the impacts of cathode and anode is needed. In addition, it remains to be investigated how rapidly the concentration gradient between the active and passive area equalizes and how the effect can be adequately integrated into an aging model. Additional investigations should attempt to determine the cause of gassing at low SOCs.

7 SOC-dependent degradation effects at severly high temperatures

This chapter is based on a publication created during the course of the dissertation. It contains minor modifications with respect to the original publication. The use of the article content including illustrations from [191] is permitted with the consent of Elsevier.

The aging results in the previous chapter revealed outstanding calendar lifetimes for the 10 Ah NMC|LTO cells at elevated temperatures, exhibiting irreversible and reversible aging effects as well as strong gas formation with abrupt end-of-life. However, when stored at 80 °C, the cells showed a capacity retention that cannot be attributed to common aging mechanisms.

To illustrate the peculiarities, the results of calendar aging at 60 °C and 80 °C from Chapter 6 are consistently normalized in Figure 7.1. The capacity retention greatly differs depending on storage temperature and SOC. Due to high calendar aging robustness of the NMC|LTO cells, the PEE strongly influences the residual capacity within the 60 °C calendar aging tests (see Figure 7.1a). At 60 °C the change in capacity is strongest within the first 30 days mainly attributed to the PEE. After the balancing process has subsided, the cell capacity remains approximately constant over the observation period shown.

The three cells at 80 °C (see Figure 7.1b) exhibit a different capacity retention. During the first 90 days, capacity grows significantly at 5% SOC and 55% SOC, whereas at 95% SOC capacity drops. After 60 days of testing, a capacity gap of more than 12% between the cells at low and high SOC occurs.

Such a deviation is not explainable by the PEE for two reasons. Firstly, the capacity difference exceeds any value that can be assigned to the cell geometry and the potentially usable capacity in the boundary areas (see Section 6.1.2). Secondly, at 80 °C, where balancing processes run at higher speed, faster equalization processes than at 60 °C are to be expected.

This chapter aims to improve the understanding of calendar aging effects and their impact on cell performance of the investigated 10 Ah NMC|LTO cells. Main focus is to identify SOC-dependent aging mechanisms and to enable a differentiation between reversible and irreversible aging effects. Taking advantage of the previously described aging study results in Chapter 6 and complementary calendar aging tests, in-situ and ex-situ analysis methods are applied. The results of an ICA show that an increase in temperature from 60 °C to 80 °C strongly enhances degradation effects, which are highly SOC-dependent. The conducted post-mortem analysis comprises a cell opening, the assembly of coin cells with aged electrode material and a surface investigation by SEM and XPS. In particular, the

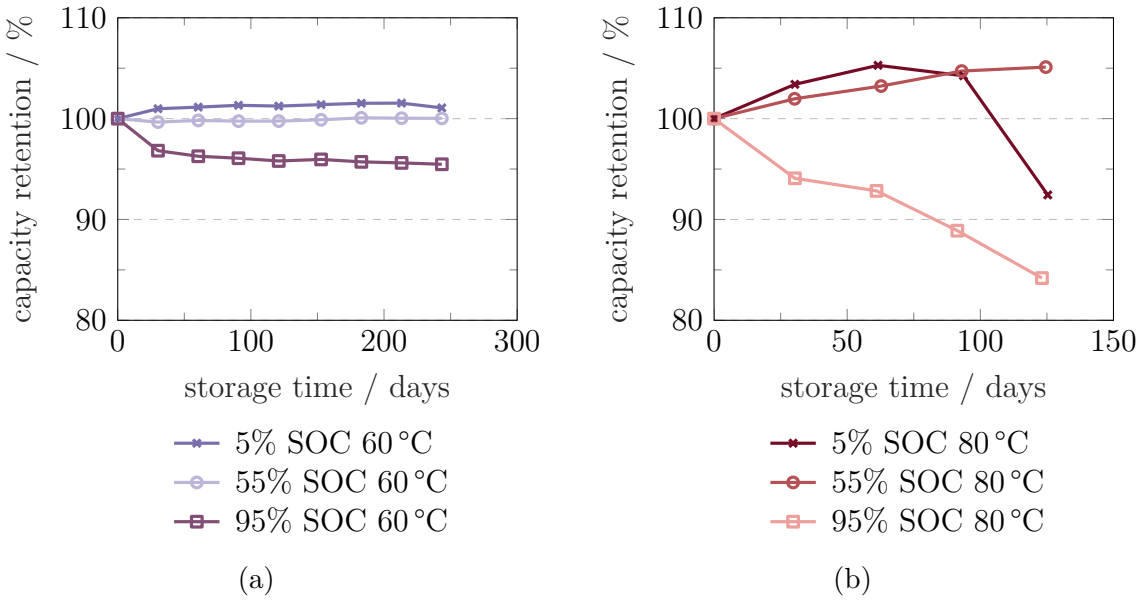

Figure 7.1: Normalized residual capacity of calendar-aged cells at a) 60 °C and b) 80 °C at three different SOCs under floating condition. Capacity was evaluated with a CC discharge of 1C. The cells at 60 °C show a pronounced PEE. At 80 °C this effect is superimposed by further capacity-reducing and capacity-increasing aging effects.

impact of SOC on cell degradation as well as the formation of cover layers on LTO and NMC is analyzed. Potential aging mechanisms are elaborated and discussed.

7.1 Results of incremental capacity analysis

The effects of calendar aging, which were illustrated in Figure 7.1 by means of capacity loss, are strongly dependent on temperature and SOC. An elevation of the storage temperature from 60 °C to 80 °C triggers additional aging mechanisms, which are revealed by ICA.

An overview of the IC curves of the calendar aged cells at 60 °C is given in Figure 7.2. IC curves of the examined NMC|LTO cells exhibit a characteristic peak at about 2.17 V with a shoulder at about 2.08 V. This shoulder is only observable for the charge direction, which might be related to differences in the process of lithiation as well as delithiation of spinel- and rocksalt-structured LTO [229]. A second shoulder extends over a voltage range of 2.25 V to 2.45 V. The area below the IC curve corresponds to the cell capacity during the CC phase of the qOCV measurement.

For storage at 5% SOC (Figure 7.2a), the IC curves are approximately constant during the 240-day aging test. At 55% SOC (Figure 7.2b) and 95% SOC (Figure 7.2c) a major shift of the IC curve occurs between first and second check-up. For 55% SOC primarily the position of the peak shifts towards lower voltage, with hardly any changes of the

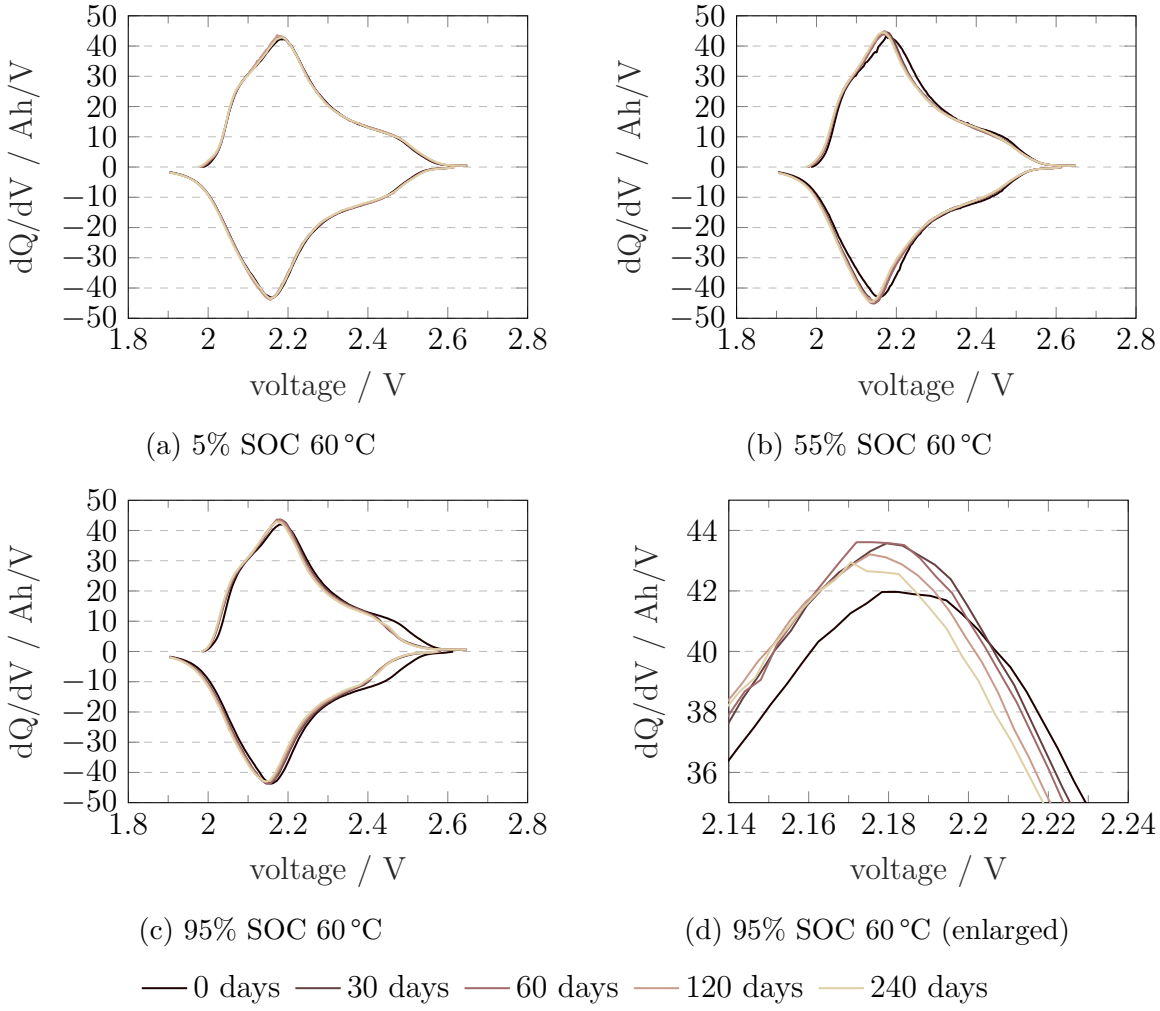

(a) 5% SOC 60 °C

(b) 55% SOC 60 °C

(c) 95% SOC 60 °C

(d) 95% SOC 60 °C (enlarged)

Figure 7.2: Results of the ICA of the calendar aged 10 Ah NMC|LTO cells at 60 °C at a) 5% SOC, b) 55% SOC and c) 95% SOC. An enlargement of the peak of c) at 2.18 V is given in d). The shift from first to second check-up at 55% SOC and 95% SOC is induced by the PEE and an associated shift in cell balancing. Besides this shift, the cells exhibit minor irreversible aging characteristics.

distinctive shoulder positions. In contrast, a significant shift of the shoulder in the upper voltage range is observed at 95% SOC indicating a loss of capacity. As aging proceeds, the IC curves at 55% SOC and 95% SOC gradually shift towards lower voltages (enlarged for 95% SOC in Figure 7.2d), which might be caused by a beginning loss of active material at the positive electrode in the delithiated state (LAM_{dePE}).

As described in detail in Section 6.1.2, the shape of the characteristic OCV can deviate as a result of a pronounced PEE. Diffusion of lithium-ions into passive electrode areas affects the working potential of the individual electrodes and the overall cell balancing. Variations in cell balancing influence the characteristic OCV of the cell, which is subsequently reflected in the ICA. Thus, the presented IC curves prove the impact of the PEE on the cell balancing and illustrate the source of the reversible capacity rise and capacity drop, which

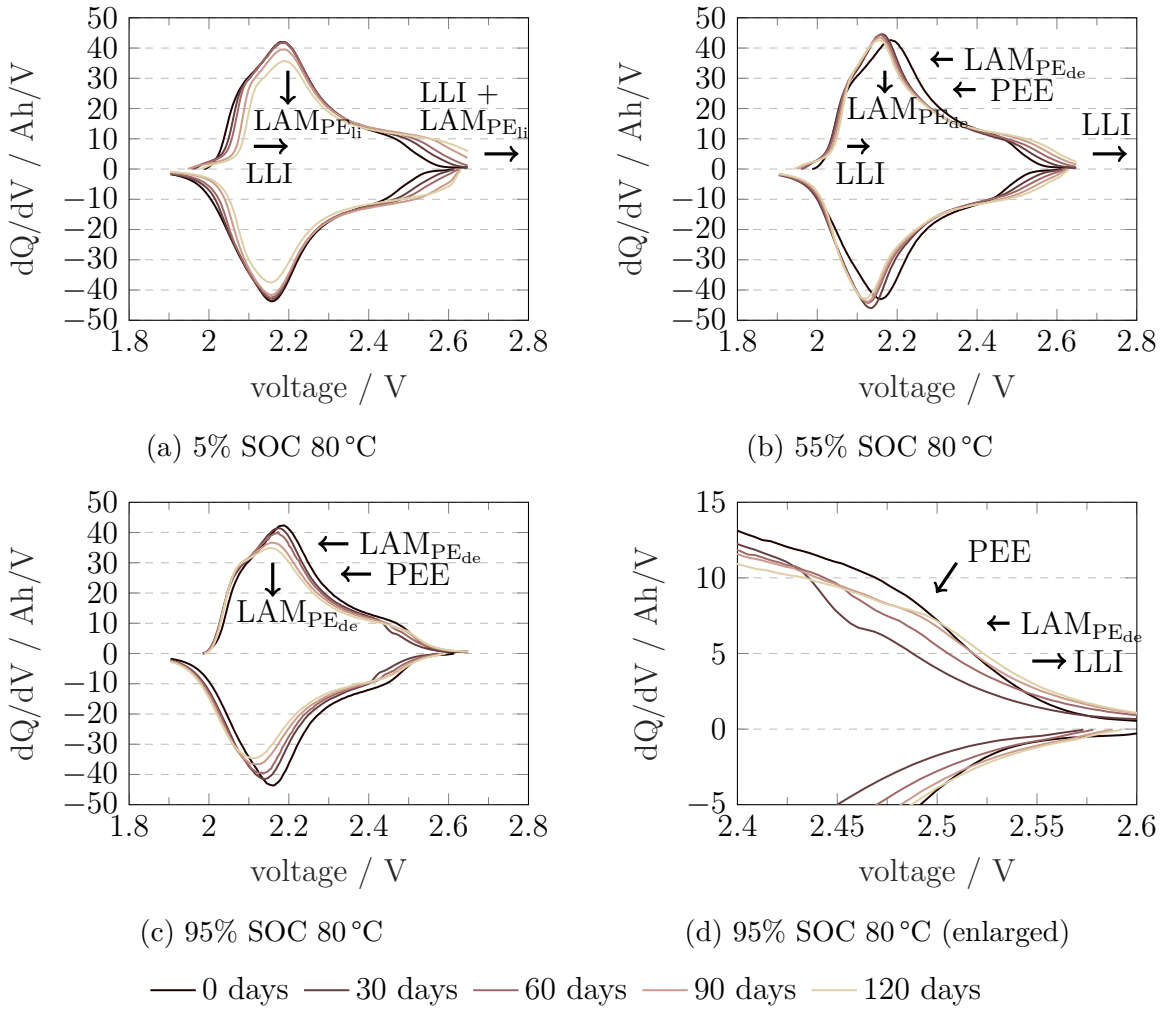

Figure 7.3: Results of the ICA of the calendar aged 10 Ah NMC|LTO cells at 80 °C at a) 5% SOC, b) 55% SOC and c) 95% SOC. Potential degradation modes are marked with arrows. The aging behavior depends strongly on the storage SOC, with changes in the IC curves most pronounced at high and low SOC. In d) a detailed section of the IC curves at 95% SOC is shown, which illustrates the shifts in high voltage ranges. Multiple aging processes, including the reversible PEE, overlap and cause opposing displacements.

can be identified in Figure 7.1a.

After the second check-up the shape of the IC curves for all SOCs remains almost unchanged, which corresponds to the constant capacity values given in Figure 7.1a. An irreversible loss of capacity caused by calendar aging at 60 °C is largely negligible for all tested SOCs. In this experiment the influence of the PEE outweighs possible irreversible aging effects of the stable NMC|LTO cells and causes SOC-dependent capacity deviations of more than 4%. In general to prevent misinterpretations, findings from calendar aging tests including subsequent ICA should be interpreted with awareness of this effect.

An increase of the storage temperature to 80 °C leads to detectable irreversible aging processes. IC curves of the corresponding aging tests (capacity trends shown in 7.1b) are illustrated in Figure 7.3. The IC curves shift continuously over the test duration so that distinct trends can be identified for each storage SOC. Essential changes are marked with arrows and complemented by associated degradation modes.

At 5% SOC, see Figure 7.3a, the height of the peak decreases and the shoulder at 2.05 V shifts to the right, resulting in a reduction of the available capacity in the medium voltage range. In higher voltage ranges the values for dQ/dV rise. According to [201], such behavior can be attributed to a LLI and a loss of active material at the positive electrode in the lithiated state (LAM_{liPE}). LLI is caused by parasitic side reactions which bind lithium charge carriers and make them unavailable for further lithiation processes. These parasitic side reactions might contribute to the strong gassing behavior which was not only observed for a low SOC of 5% but also for SOCs of 55% and 95%. The LAM_{liPE} can be attributed to an increasing inactivity of active material [201]. Gassing might lead to local displacement of electrolyte reducing the ionic conductivity at these spots. However, contrary to expectations, the IC shifts of cells aged at 5% SOC reveal an overall increase in cell capacity in the first four check-ups. Only between 90 and 120 days of test duration, the cell has noticeably lost capacity, which becomes apparent from the height of the peak and most likely originates from LAM_{liPE}.

The IC curves at 55% SOC and 80 °C, see Figure 7.3b, experience a peak shift induced by the PEE, which is qualitatively comparable to the results at 55% SOC and 60 °C but more pronounced. LLI and LAM_{dePE} result in opposing shifts, reducing the area between 2.05 V and 2.25 V. The slightly reduced peak height might also be attributed to these two degradation modes. Similar to the cell stored at 5% SOC the cell aged at 55% SOC exhibits an enhanced capacity at higher cell voltages. However, this effect is less pronounced than for the cell aged at 5% SOC, see Figure 7.3a, which is in good agreement with [201] as the ratio of lithiated NMC (potentially contributing to an increased plateau along with LLI) is reduced at 55% SOC.

The cell at 95% SOC, see Figure 7.3c, shows a capacity reduction, which is mainly caused by a left shift and a decrease of the IC peak. Both originate from LAM_{dePE} and LLI. Additionally, the left shift of the peak is enhanced by the PEE. This superposition of different capacity influencing processes becomes even more noticeable at higher cell voltages. Figure 7.3d provides a magnification of this area. On the one hand, a capacity-reducing left shift occurs from the first to the second check-up, which is caused by the PEE. On the other hand, a capacity increasing effect similar to the one reported for the other two SOCs is observed. As NMC is not lithiated the effect is reduced by the missing influence of LAM_{liPE}. Instead a LAM_{dePE} counteracts this effect and mitigates the right shift significantly.

The remarkable increase in overall cell capacity, especially in the higher voltage range, is not explainable by similar observations from other publications. In the cell under investigation, LTO represents the capacity-limiting active material. An increase in cell capacity must therefore be accompanied by an increase in the areal capacity of LTO. A possible explanation could be an enhancement of the active surface area of LTO. Due to

the strong gassing behavior at 80 °C under permanent tension, the pressure inside the cell rises. This high pressure could potentially lead to electrochemical milling, a cracking of the material, and thus an increase in available areal capacity [225–227]. Increased pressure on the LTO bulk material might also improve the electrical connection of LTO particles allowing for additional particles to participate in the lithiation process.

An assignment of the observed effects to the electrode materials is strongly limited by means of a full cell investigation approach. The following half-cell investigations enable a detailed analysis of the individual electrode materials and contribute to the identification of aging mechanisms.

7.2 Half-cell investigation

A comparison of the characteristic half-cell potentials of fresh and aged anodes/cathodes reveals material degradation and allows for conclusions on aging mechanisms. In Figure 7.4 half-cell potentials of coin cells built from aged cell materials (test series 2) with lithium metal as counter electrode are illustrated. Each figure includes the half-cell potential curve of the reference anodes/cathodes for comparison purposes. The cell balancing was determined according to the measured full cell qOCV. Here, the characteristic rises and drops of LTO and NMC potential curves in low SOC ranges allow for high accuracy.

The potential of the NMC|Li cell at 3% SOC, see Figure 7.4a, exhibits no shift and especially no change in areal capacity. The areal capacity of LTO decreased slightly and the slope of the half-cell potential in lithiated state became steeper. On full cell level, considering the voltage limits of 1.9 V and 2.65 V, this leads to a reduction of the cell capacity. At first glance, this does not correspond to the results in Figure 7.1b, where the cell at 5% SOC reaches a remaining capacity of 92% after about 120 days. As shown in Figure 7.3a, LAM_{liPE} is mainly responsible for the severe capacity loss. Reason for this could be the strong gassing behavior, which locally displaces electrolyte and inactivates parts of the NMC. The gas reservoir of the pouch bag captures gas only as long as the pressure of the cell clamping is sufficiently high compared to the internal cell pressure. Thus, by opening the cell and letting the gas escape, the capacity limiting effect of the LAM_{liPE} might be reversible, so that NMC keeps its original capacity. Interestingly, LTO seems to dominate the performance degradation when aging in low SOC ranges.

For the cells aged at 2.2 V and 2.65 V both LTO and NMC show a visible change in the potential curve and the areal capacity. For the cell aged at 2.2 V, see Figure 7.4b, both NMC and LTO are subject to a distinct capacity change. The areal capacity of the aged LTO exceeds that of the unaged reference LTO. In addition, the typical half-cell potential plateau of the LTO declines. The formation of covering layers on the LTO surface might lead to overpotentials which cause a reduction of the potential. It is also conceivable that gassing within the cell locally displaces electrolyte and greatly deteriorates conductivity. These kinetic limitations can lead to overvoltages in the NMC|LTO cell system lowering

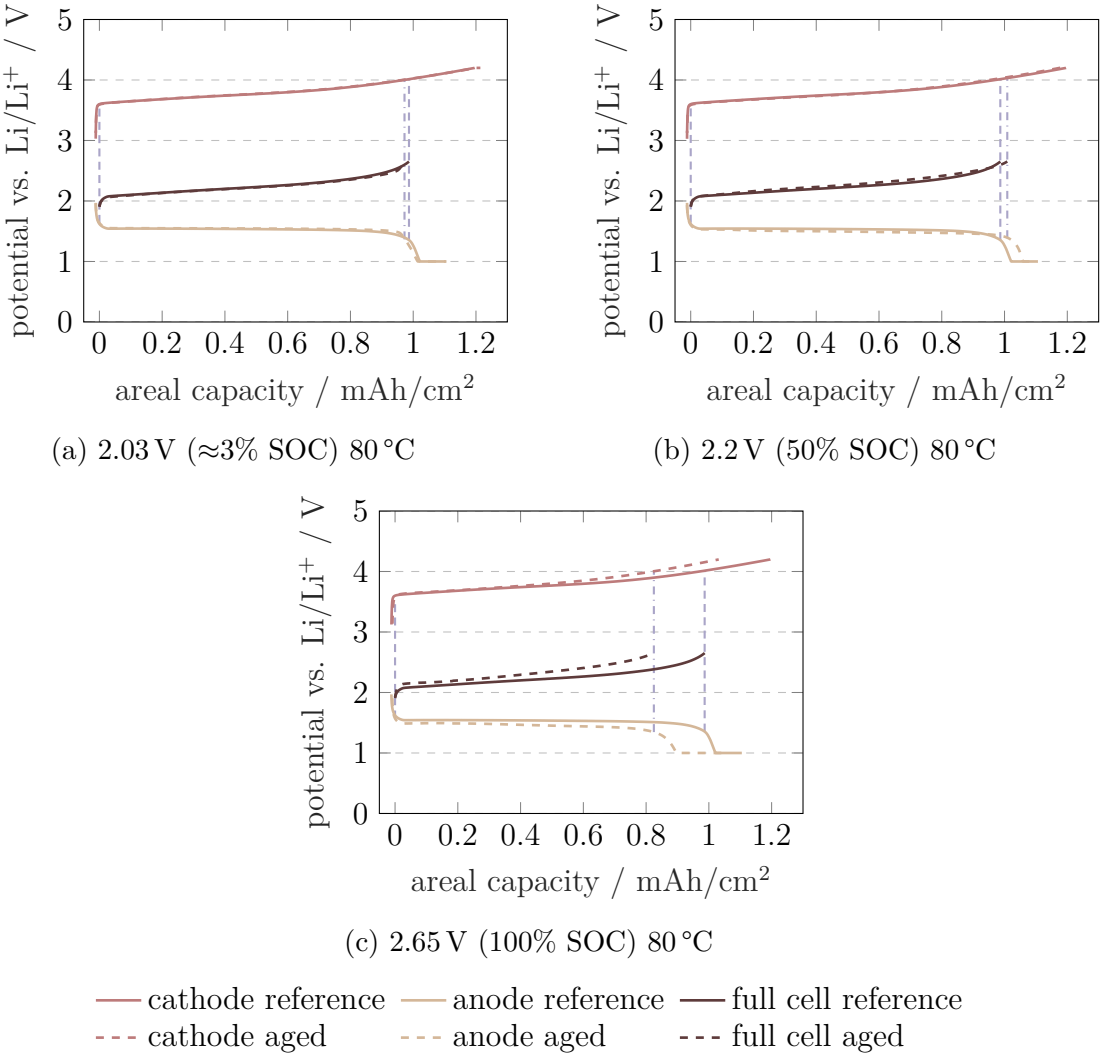

(a) 2.03 V (≈3% SOC) 80 °C

(b) 2.2 V (50% SOC) 80 °C

(c) 2.65 V (100% SOC) 80 °C

Figure 7.4: Comparison of qOCVs of coin cells, which were assembled as half-cells with aged electrode material with lithium metal as counter-electrodes. Reference measurement data of the unaged cell material is indicated as a solid line. At a cell voltage of a) 2.03 V and b) 2.2 V the voltage characteristics of the electrode materials show little degradation due to aging. In case of b) the areal capacity of LTO increases. For the fully charged cell at c) 2.65 V both the areal capacity of LTO and NMC are reduced.

the potential of LTO cycled vs. lithium. A detailed analysis of the existing surface layer will be carried out in the course of the XPS investigation in Section 7.4.

The NMC aged at a cell voltage of 2.2 V loses marginally in areal capacity, so that the half-cell potential slightly shifts to the left. Overall, the increased areal capacity of the LTO leads to an increase in the available cell capacity while the upper voltage limit of the full cell remains constant at 2.65 V. The altered potential curve characteristics make NMC the capacity limiting electrode, since for the aged cell the cut-off potential is now

reached at the LTO plateau and is determined by the potential rise of the cathode. With reference to ICA, such a shift of the cut-off voltage implies a rise in the IC curve in the same area and thus agrees with the results of the ICA in Figure 7.3b.

The LTO and NMC electrodes stored at 80 °C at a cell voltage of 2.65 V clearly reveal a capacity loss recognizable by the shortened potential curves in Figure 7.4c. Similar to LTO stored at 2.2 V (Figure 7.4b) an even more intense potential drop for the characteristic 1.55 V potential plateau can be observed, which is due to electrolyte decomposition products on the surface of the LTO electrode. This passivating decomposition layer might not only cause a capacity decrease by overpotentials but also by blocking lithium insertion sites at the LTO electrode. The potential curve of NMC cycled vs. lithium shows an intense capacity loss most likely due to LAM_{dePE}. At high temperatures delithiated NMC electrodes tend to experience cation mixing which leads to severe and irreversible capacity loss.

Even though both anode and cathode are responsible for the dramatic capacity loss at a storage voltage of 2.65 V, one can assume, that the cathode contributes more to the capacity decrease of the stored NMC|LTO cell. The potential curve of LTO reveals a capacity increase of 9.5% by a CV step after the CC charge, whereas for the cathode no additional capacity appears with a subsequent CV step. Considering the CV step at the end of the CC charge process LTO only loses 7.5% of its original capacity whereas NMC suffers from a capacity loss of 14%.

However, these measurements were realized at a coin-cell level using electrodes with a diameter of only 14 mm punched out of a ca. 130 cm^2 pouch cell electrode. Figure 7.5 clearly demonstrates optical differences within one electrode sheet. Thus, these coin cell results are very sensitive to statistical errors, which must be considered for the interpretation of the potential curves of LTO and NMC especially when there are only slight differences in the curves.

7.3 Insights from cell opening

At the end of the 40-day calendar aging test, all three cells showed bulges in the area of the cells' gas reservoirs. The gas reservoir of these pouch bags is located on the side of the current collectors. In Figure 7.5a and 7.5b the reference cell and the cell aged at 2.65 V are shown prior to opening. In the latter, a swelling is evident between the isolated tabs. The inflated area extends over the entire cell width, hence a change in volume is visible in the lower right corner of the cell. The cells at high and low voltage exhibited the largest bulging of the gas reservoirs.

The physcial appearance suggested that the cells would have likely bursted shortly after the 40-day testing period. The clamping of the cells between two aluminum plates and, in the case of application, in the battery pack ensures that gas is displaced into the designated area. This minimizes the effects of gassing on cell performance and extends the cell lifetime. From a safety point of view, detection of gassing based on electrical cell data becomes

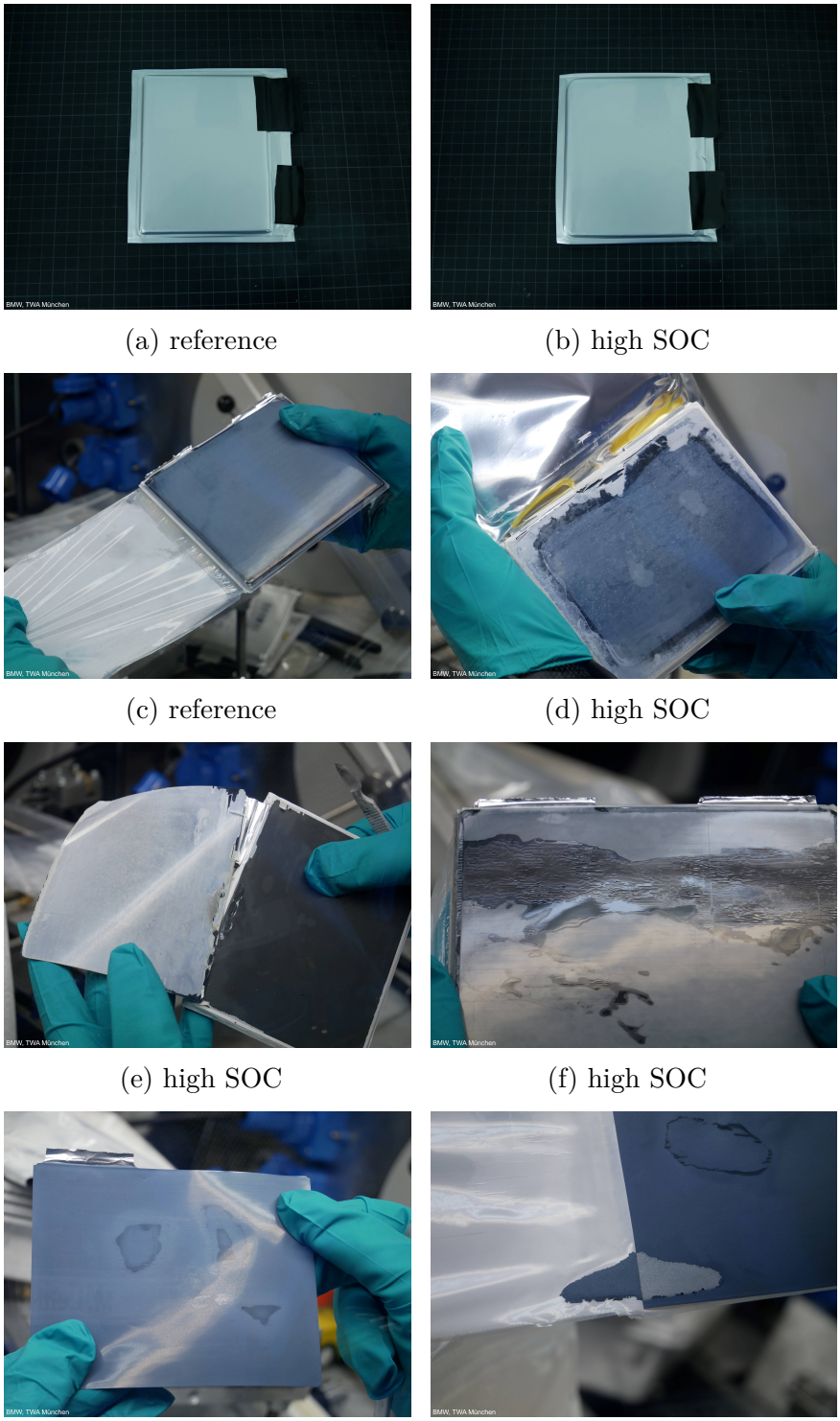

(a) reference (b) high SOC

(c) reference (d) high SOC

(e) high SOC (f) high SOC

(g) middle SOC (h) low SOC

Figure 7.5: Optical images during cell opening of the reference and the three calendar aged cells.

more complex. The aged cells (test series 1) possessed large parts or even more than their nominal capacity until the time of degassing (see Figure 7.1b), so that the remaining capacity is no indicator for critical gassing conditions. Additional sensors for detection or safe degassing paths in cell modules and battery packs are necessary and should be integrated into the pack design.

The cells were opened in a glove box under argon atmosphere to avoid reactions with the ambient air. Previously, all cells had been discharged to 0% SOC at the end of the calendar aging period. Figure 7.5c shows a picture of the reference cell. The electrode material of this cell revealed no abnormalities. Electrode and separator sheets could be easily separated. The cell materials of all calendar-aged cells exhibited optically detectable aging effects, which differed in intensity and type.

Figure 7.5d, 7.5e and 7.5f show cell images of the cell exposed to high SOC (100%, 2.65 V). Two gas bubbles were apparent in the middle of the cell. The edge of the separator of the outermost electrode layer, see Figure 7.5d, was fragile in the area of the current collectors. The moisture penetration with electrolyte was less than in the other two cells. Especially in the chapped edge areas the cell material was dry, which is in good agreement with the observation of gas allocations in the edge areas (Figure 7.5b). As illustrated in Figure 7.5e, some separator sheets showed a brownish discoloration indicating increased electrolyte decomposition at these spots, which was more pronounced in the area of the current collectors.

The separator was difficult to detach from the electrode material. In some places this led to delamination of the active material from the current collector. Reasons for delamination include reduced adhesion of the active material to the current collector as well as increased adhesion between separator and electrode. In this case the cell opening does not allow for a precise allocation. The separator, see Figure 7.5f, exhibited a wave-like structure in deeper layers of all three cells.

Figure 7.5g showed an example of an anode sheet of the cell at low SOC (≈3%, 2.03 V). Both anodes and cathodes revealed darker spots that remained on the material after drying. During cell opening, it was found that these spots appeared in areas where gas bubbles had previously been observed. A detailed analysis of these spots is provided as part of the XPS investigations in Section 7.4. A delamination of the active material, see Figure 7.5h, was mainly observed in the corner areas of the electrode sheets. In the cells with 2.2 V and 2.65 V both cathode and anode were affected, whereas in the cell with 2.03 V only the anode was delaminated.

The cell opening proves that aging at high temperatures leads to optically detectable material degradation in the investigated NMC|LTO cells. Striking are the decomposition effects at the separator and the dark spots on the electrodes. Clamping of the cells does not ensure full gas displacement, resulting in local accumulation of gas bubbles in front of the active material. High SOCs cause the most severe material degradation and aging characteristics.

7.4 Surface layer analysis

In the following, results of ex-situ surface examinations of aged anodes and cathodes are presented. The aim is to identify potential causes for the performance degradation described above and to gain a deeper understanding of the aging processes involved.

7.4.1 Anode

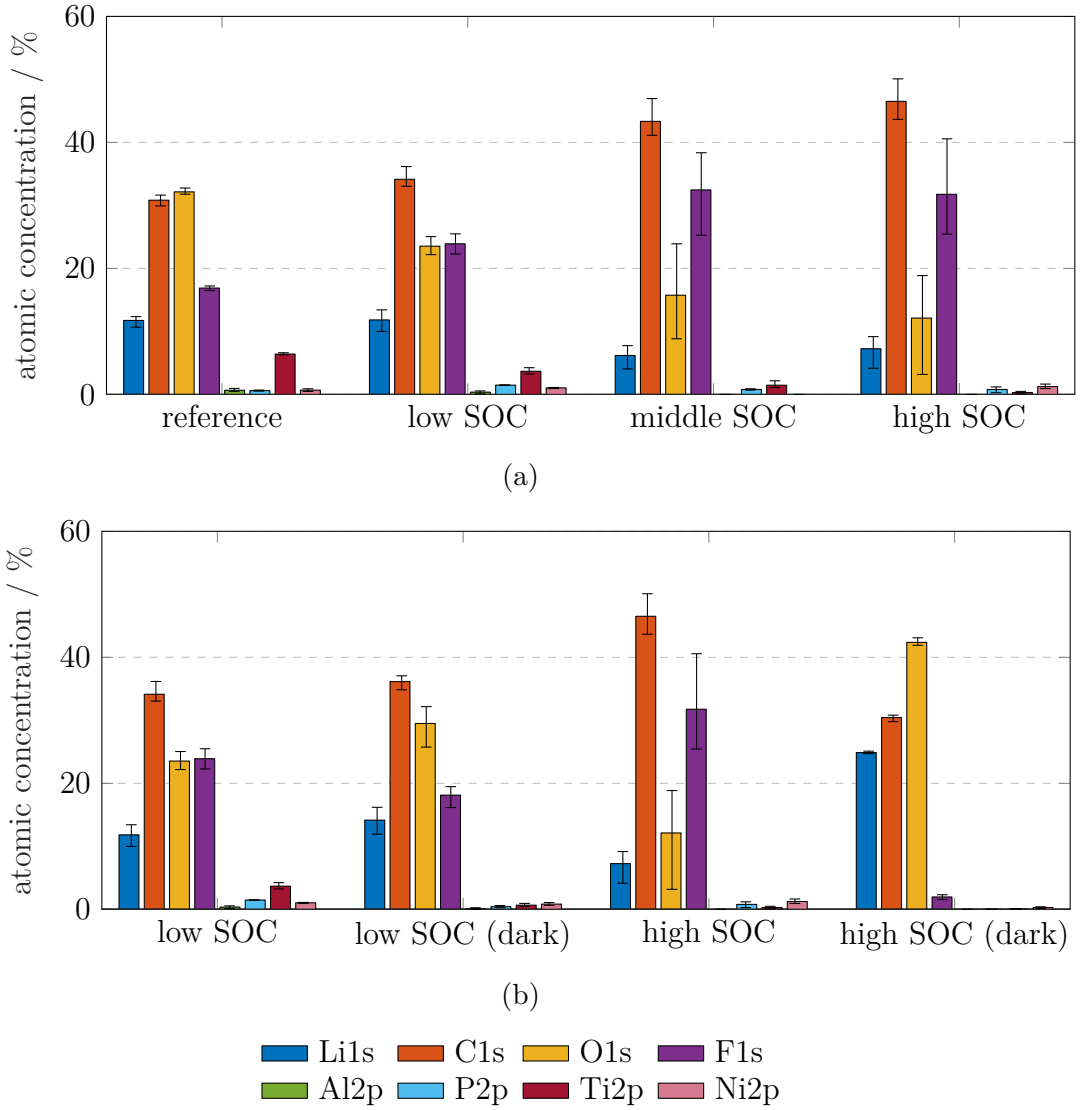

Figure 7.6: Composition of the anode surface film of all aged cells including reference material were determined by XPS measurements. In a) the atomic concentrations of the individual components for the different anodes (bright, inconspicuous areas) are shown. A comparison of cover layer components of light and dark areas is illustrated in b).

The XPS results of the LTO electrodes stored at different SOCs at 80 °C, see Figure 7.6a, clearly show a rise of the C1s and a reduction of the Ti2p signal intensity with increasing SOC. This allows for the assumption that with a higher degree of anode lithiation a thicker deposition layer is formed on the LTO electrode surface more and more covering the Ti2p signal of titanium from LTO. Considering the increasing C1s signal and the decreasing O1s and Li1s signal (probably ascribed to Li_2O) the composition of the thicker growing deposition layer seems to be dominated by carbonaceous decomposition products overlaying the inorganic decomposition products with higher SOC. The slight increase of the Li1s signal at higher SOCs might correlate to a higher repulsion of inserted lithium when LTO is fully charged. Especially at high temperatures this effect could lead to more lithium containing oxidation products because of a thermal induced delithiation of LTO.

During the optical investigation isolated dark spots are observed at the electrode surfaces. For the dark spots on the LTO, Li1s and O1s signals are intensified (Figure 7.6b). The atomic concentration increase from normal spots to dark spots is much more intense for the electrodes stored at high SOC. The dark spots might be associated with local accumulation of CO_2 gas and its reduction to Li_2CO_3. The effect is intensified at higher SOC, since lithium, as mentioned above, might be more mobile due to more intense lithium-ion repulsion.

However, as the XPS measurement only indicates the atomic concentration, an explicit and certain assessment of the surface compounds and the detailed composition and distribution of reaction products is not feasible. The results described above have to be interpreted in terms of possible assumptions.

7.4.2 Cathode

From the XPS measurements of the NMC surface, see Figure 7.7a an increasing atomic concentration of carbon can be observed with an increasing SOC while the O1s and Li1s signals decrease. The increasing C1s signal could be attributed to an increased oxidative decomposition of electrolyte to organic polymers, promoted especially at high voltages and elevated temperatures [123]. As not only the signals for oxygen and lithium but also the atomic concentration of cobalt and manganese get reduced with an increasing SOC, one can assume that these signals might be attributed to the growing decomposition layer of organic polymers gradually covering the NMC surface. However, the signal intensity of nickel shows only small fluctuations but no clear decreasing trend. It is reported in the literature that Ni^{4+}, present at higher SOCs, tends to react with the electrolyte in side reactions significantly thickening cathode-electrolyte interfaces [230]. Probably this side reaction effect counteracts the actual trend of the Ni2p signal to decrease.

Similar to LTO, optical investigation of the positive electrode revealed some dark spots at the surface (Figure 7.7b). However, for NMC these spots were only found at low SOC. The XPS measurements at these spots show a reduced C1s and O1s signal whereas the signal for lithium, fluorine and phosphorus increase. This trend might be associated with an increased content of $LiPF_6$ decomposition products like LiF.

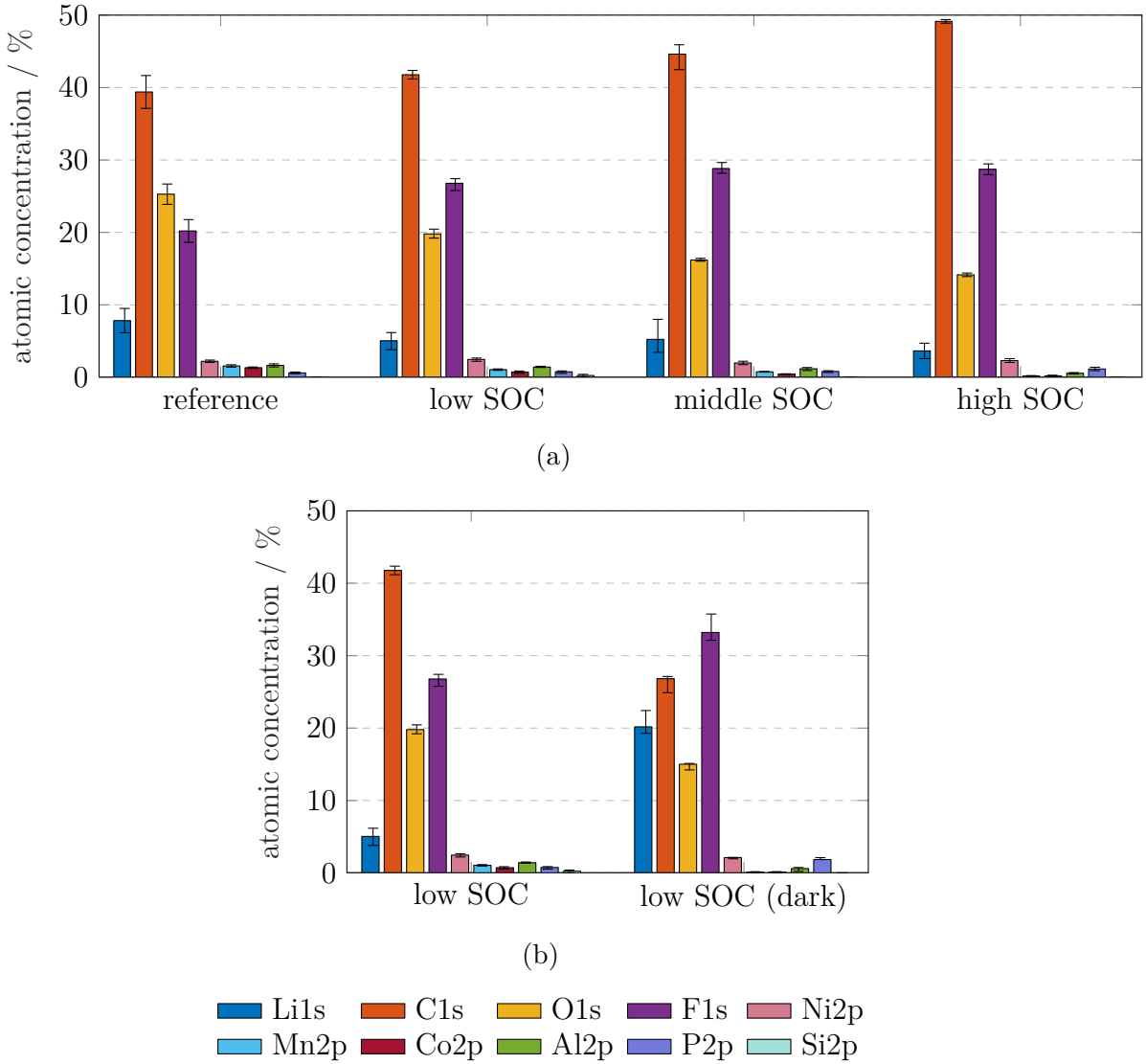

Figure 7.7: Composition of the cathode surface film of all aged cells including reference material were determined by XPS measurements. In a) the atomic concentrations of the individual components for the different cathodes (bright, inconspicuous areas) are shown. A comparison of cover layer components of light and dark areas of the cell at low SOC is illustrated in b).

Overall, the decomposition processes at the cathode can be influenced by various factors that interact with each other. This makes it difficult to draw reliable conclusions only on basis of atomic concentration ratios.

As the half-cell potential curves of NMC aged at a cell voltage of 2.65 V clearly reveal an intense loss of capacity, SEM measurements were performed to investigate the surface morphology. Comparing the SEM images of the reference NMC electrodes with NMC stored at 100% SOC at 80 °C, see Figure 7.8, the aged surface shows some darker spots which are not observable during optical investigation with the naked eye. Furthermore,

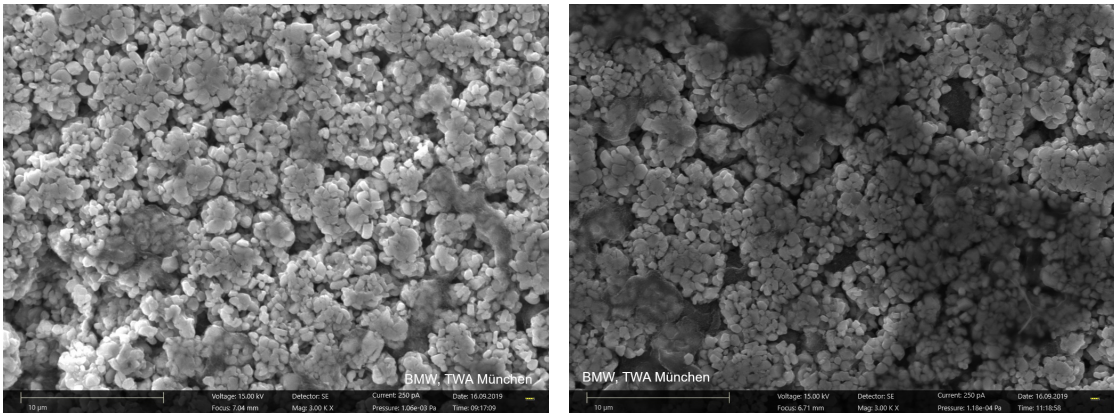

(a) (b)

Figure 7.8: SEM Analysis of the NMC material of the fresh (a) and aged (b) cells stored at 100% SOC.

compared to the reference the surface exhibits a few more cracks and holes in between the agglomerated secondary particles.

Previous research has reported that NMC tends to produce oxygen containing gases like CO_2, CO and O_2 at higher degrees of delithiation [231]. At high SOCs these gases might aggravate in between the secondary particles until they finally reach a critical volume and lead to local surface cracking. The reactions, leading to gas generation at the cathode, might be accompanied with the formation of solid decomposition products, which could be responsible for the darker spots, observable from the SEM images. Hatsukade et al. [231] further demonstrated, that oxygen originates from NMC and not from the electrolyte. Thus, increased gas generation at the cathode might be accompanied with irreversible damage of the NMC structure leading to loss of capacity by LAM_{PE}, which is in good agreement with the results of the ICA and the half-cell capacity loss.

Hence, capacity reduction of NMC stored at high SOC could be driven not only by deposition of oxidative electrolyte decomposition products but also structural damage through cation mixing, oxygen escaping from the layered NMC structure by forming CO_2, CO and O_2, and gas induced surface cracking.

7.5 Conclusion of the SOC-dependent degradation effects

Storing NMC|LTO cells at different SOCs at 80 °C causes several degradation effects. ICA reveals an activation of aging processes at a storage temperature of 80 °C whereas hardly any irreversible aging could be observed at 60 °C. Predominant degradation modes are LLI and LAM_{PE}, depending on the storage SOC.

Calendar aging at low and medium SOCs causes a continuous rise in capacity which exceeds the effects of the PEE in the 10 Ah cells. ICA and the investigation of the electrodes in half-cells indicate that this capacity increase can be ascribed to an extension of the LTOs typical voltage plateau at 1.55 V, which leads to a capacity rise in higher voltage regions. Various gassing induced mechanical and pressure-related sources, such as electrochemical milling or improved electrical contacting, are potential explanations for the capacity increase of LTO. Further investigations are needed to draw reliable conclusions and to fully understand this aging phenomenon.

Storage at 80 °C at high SOCs clearly reveals the most intense degradation effects. According to the ICA a severe LLI and intensive LAM_{dePE} can be observed. The latter might be induced by cation mixing or surface passivation through oxidative decomposition. The comparison of SEM images of NMC (fresh vs. aged) further shows local dark spots and increased surface cracking at the electrode probably related to gassing reactions of NMC especially at a higher degree of lithiation. Hence, capacity reduction of NMC stored at a high SOC could be driven not only by deposition of oxidative electrolyte decomposition products and structural damage through cation mixing but also by oxygen escaping from the layered NMC structure by forming gases which further induce surface cracking.

By comparing the gassing behavior of the calendar aged cells stored at 60 °C (test series 1) and 80 °C (test series 1 and 2) noticeable differences in volume expansion can be found. Cells stored at 60 °C do not show a strong gassing behavior whereas at 80 °C intensive gassing is observed. One reason could be a thermal induced decomposition of electrolyte and $LiPF_6$, which is dramatically accelerated at elevated temperatures. Another reason for this behavior could be a surface layer formation on the LTO electrodes during the formation process by the cell manufacturer, which is stable up to 60 °C. This protective surface layer suppresses gassing of the cells. At a temperature of 80 °C the surface film might start to decompose. Consequently, electrolyte gets in contact with the bare LTO surface and gassing reactions start.

Ex-situ surface observation of the electrodes by XPS measurements show that an increased deposition layer is formed both on the LTO and the NMC electrodes with an increasing SOC mainly composed of organic decomposition products. The formation of a thicker deposition layer on LTO is proven by increasing overpotentials in the half-cell potential curves and an extending CV step in the end by increasing the storage SOC.

The reported findings offer the potential for a series of subsequent investigations. Apart from the still not fully understood capacity increase of LTO at low SOCs, further investigations of the surface layer formation are necessary. Determination of its compounds could allow for insights into both the formation process and the passivating characteristics. In addition, the stability of the surface layer against extreme operating conditions, such as high temperatures, ΔDODs or current rates, should be investigated. Here, an improvement of the passivation layer could minimize side reactions enhancing cell lifetime as well as safety.

8 Extent of reversibility in calendar aging tests

The results of the calendar aging tests in Section 7 and the corresponding IC analyses in Section 7.1 clearly revealed that capacity retention is affected by reversible and irreversible effects. At a storage temperature of 80 °C different degradation modes were observed and surface layer formation on the active materials was demonstrated. Shifts in cell balancing caused by the PEE were detected at 60 °C and 80 °C by IC analysis.

However, at temperatures below 80 °C, the high calendar life of the examined NMC|LTO cells hinders the differentiation of irreversible and reversible capacity effects. This chapter aims to investigate the calendar aging behavior on an experimental level in more depth and to evaluate different examination methods for these effects. The following research questions are of primary interest:

- Is the change in usable capacity, which occurs during calendar aging at a storage temperature of 60 °C mainly caused by reversible or irrversible effects?
- Can reversibility of the PEE be experimentally proven? Further, is the impact of this effect precisely quantifiable?
- How does the impact of the PEE change dependent on the aging state of the cell?
- At 60 °C, does a surface layer form on the electrode materials similar to 80 °C? If so, is it possible to observe such side reactions by non-destructive measurements?

To investigate these questions, the storage SOC has been varied during the course of the calendar aging test at 60 °C. The resulting effects on capacity retention are presented below. In addition, the floating currents needed to maintain the constant cell voltage during the calendar aging phases are analyzed. The periodic check-ups are examined regarding differences in charge capacities in CV phases. The results of an ICA allow for a differentiation between degradation modes and illustrate characteristic shifts due to SOC changes.

8.1 Capacity retention upon adjustment of the storage SOC

The storage SOC of the two cells aged at 60 °C and 20% respectively 90% SOC was swapped after just over 300 days. Thus, the cell initially kept at 20% SOC was then stored at 90% SOC and vice versa. After 100 days in this state, the SOC was switched back to its original value at test start.

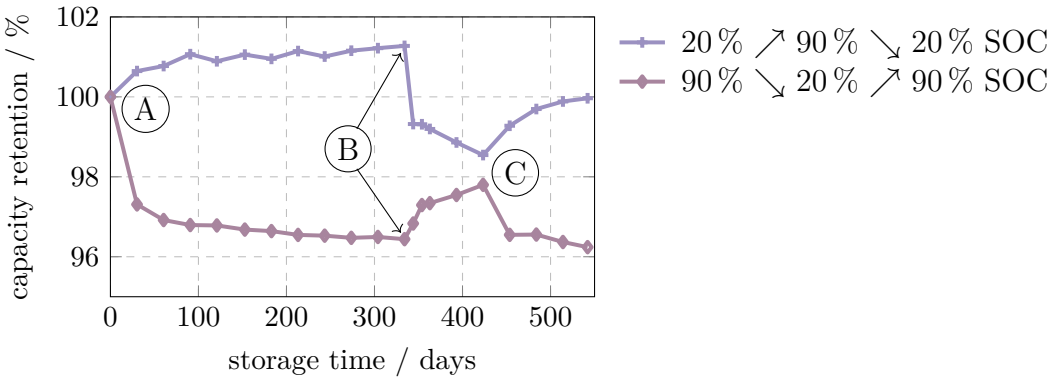

(a)

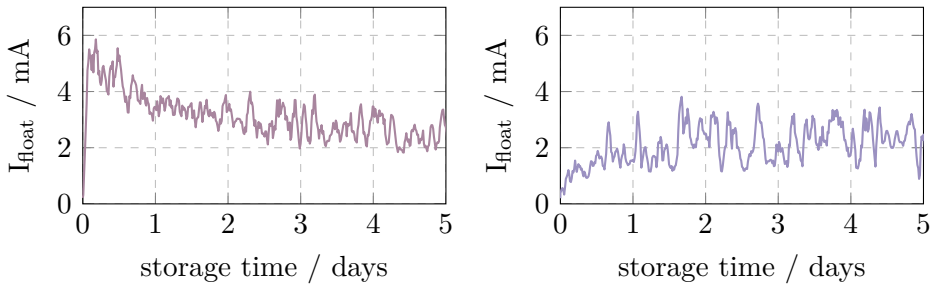

(b) Floating currents at time A after SOC setting (left: 90%; right: 20%)

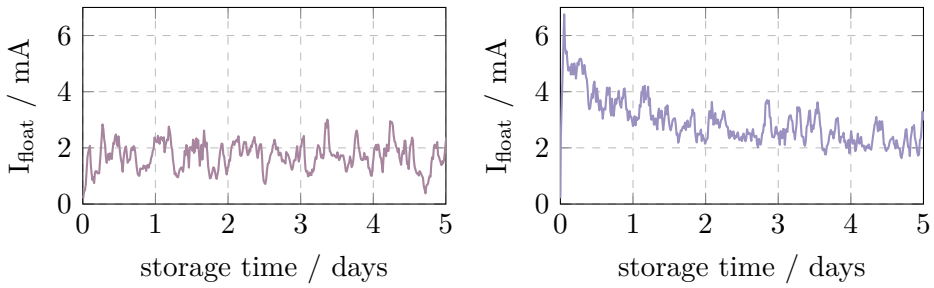

(c) Floating currents at time B after SOC swap (left: 20%; right: 90%)

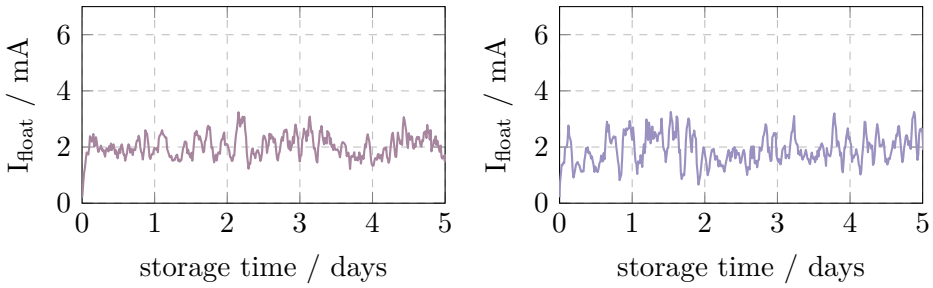

(d) Floating currents at time C after SOC swap (left: 90%; right: 20%)

Figure 8.1: a) Impact of SOC changes on capacity retention of the two calendar-aged cells. Besides the pronounced PEE, irreversible loss of capacity occurs at high SOC. b)-d) Floating currents required to keep the cell voltage constant. Upon first-time storage at high SOC, intense side reactions take place, which seem to form a stable passivation layer.

In Figure 8.1a the capacity retention of the two calendar-aged cells, measured in the check-up, is shown up to about 500 days. Here, marker A indicates the initial setting of the storage SOC at the end of the first check-up. Marker B refers to the SOC switch and marker C to the return to the initial SOC adjusted at the test start.

The cell that started the aging test at 90% SOC loses over 3% of its usable capacity in the first 300 days, as described in the previous chapters. By changing the SOC from 90% to 20% the capacity rises by about 1.5%. An increase in capacity was expected according to the previously described PEE. However, the extent of capacity rise is astonishing. The capacity neither increases to 100% nor reaches similar capacity values as expected after 400 days extrapolation of the cell at 20% SOC. This suggests that a storage temperature of 60 °C at 90% SOC causes irreversible, capacity-reducing aging effects in addition to the PEE. Since the storage SOC of 20% is approximately the same as the SOC before test start (PEE approximately negligible), the cell shows a capacity retention of 98% after 400 days and an irreversible capacity loss of 2% due to calendar aging. At a temperature of 60 °C such a low value is outstanding and confirms the excellent suitability of the investigated NMC|LTO cells for commercial applications with long product lifetimes.

After about 90 days, the amount of reversible capacity due to the change from 90% to 20% SOC is about 1.4%. This percentage is significantly smaller than the loss of capacity that occurred during the first storage phase. Reasons for this phenomenon will be discussed in the further course of this chapter. After the SOC change back to the initial 90% SOC (marker C) until the end of the observation period, the capacity increase is almost fully reversible. This clearly visualizes the impact of the PEE. Compared to the minor calendar aging after the inital drop, the capacity effects of the passive electrode areas predominate.

Switching the SOC of the cell stored at 20% SOC at test start affects the cell capacity differently. Until the time of the SOC change the capacity of this cell increases continuously. This increase occurs most probably due to a rise in capacity in higher voltage ranges identified in the previous chapter, though less pronounced at 60 °C. After the SOC change to 90%, the cell capacity drops rapidly by about 2% and in total drops by almost 2.8% until marker C is reached. After the change back to 20% SOC, the capacity increases by only about 1.4% till the end of the observation period. This reversible capacity difference is almost identical to the one observed for the other cell when changing from 90% to 20% SOC.

This once again highlights the influence of the PEE, which is approximately path-independent for the investigated cell and SOCs. However, it can be assumed that the strict monotonically rising potential curve of the geometrically oversized NMC is the reason for this observation. Active materials such as graphite or LFP show clear phase transitions and potential plateaus. With these materials it can be expected that an equalization process is less continuous and that it shows significantly stronger dependencies on the working potentials of active and passive areas.

8.2 Floating currents as indicator for irreversible aging effects

In the following, the calendar aging phases after a SOC change are analyzed in more detail. Basis for the analysis are the floating currents, which had to be provided by the cell tester during these phases in order to keep the cell voltage constant. Due to electrochemical side reactions within the cell, balancing processes between active and passive electrode areas and a cell-specific self-discharge rate, the cell voltage declines with increasing time. The floating currents compensate for these losses and thus, can contain valuable information concerning the ongoing processes. The occurring floating currents are very low and exhibit a high level of noise making it difficult to analyze the precise magnitude. However, clear trends can be derived qualitatively, which will be described in the following.

Figure 8.1b, 8.1c and 8.1d show the floating currents of the first five days after the SOC changes. Directly after the test start (marker A, see Figure 8.1b), the magnitude of the floating currents varies greatly depending on the storage SOC. The cell starting at 90% SOC requires higher currents for voltage control at the beginning, which flattens out with increasing test time. The high current need is consistent with the results of the capacity analysis showing both irreversible capacity loss and the PEE. After the change from 90% to 20% SOC and also after the change back to 90%, the floating currents are at a constant level. The SOC changes do not seem to initiate sudden aging processes, which supports the assumption of high reversibility of the PEE described in the last chapter.

Interestingly, the cell that started the calendar aging test with 20% SOC exhibits a slightly lower floating current on the first day compared to the following days. Whether this is a measurement inaccuracy or, for example the effects of the PEE, cannot be clarified at this point. However, after changing the SOC to 90% (marker B, see Figure 8.1c), the floating currents are significantly higher at the beginning of the aging phase. The course of the current is similar to that of the other cell at the beginning of the aging test (see Figure 8.1b).

The results confirm that an increase from 20% to 90% triggers additional aging mechanisms. As shown in Section 8.1, these mechanisms have a direct impact on the usable cell capacity. Since the LTO limits the capacity of the examined cell in an unaged state, $\mathrm{LAM_{NE}}$ must be mainly responsible for the capacity reduction of 1% to 1.5%.

This material degradation, as illustrated in Figure 8.1d, does not occur repeatedly. Therefore, it is assumed that a passivating surface layer is formed on LTO when its potential drops below a critical threshold. The remarks made in the last chapter must be expanded to the extent that a destinct formation of a passivating surface layer on lithiated LTO already occurs at 60 °C.

8.3 Impact of SOC changes on constant voltage phases

In Section 6.1.2 it has already been described that the capacities of the CV charging phase can indicate the homogeneity of the lithiation state of the NMC material and thus can confirm the existence of the PEE. Figure 8.2 gives an overview of the capacities of the CV charging phase in the first capacity test of the check-up. The changes in the storage SOCs clearly reveal that the measured capacities in the CV phase depend on the SOC during the calendar aging phase. For the cell at initial 20% SOC, the CV capacity at marker B rises sharply and reaches approximately the level of the cell at 90% SOC. For the cell at 90% SOC, the capacity decreases more slowly when changing from 90% to 20% SOC after a peak in the following check-up. However, the difference in the capacities arising from the SOC change is approximately identical for both cells.

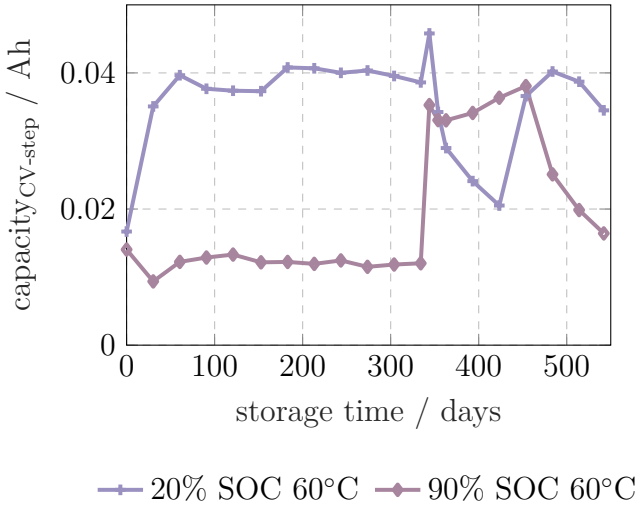

Figure 8.2: Capacities added in the CV phase of the CC-CV charge during the first capacity test of the check-up. The SOC changes lead to voltage potential gradients between active and passive electrode regions resulting in inhomogeneities in the lithiation or delithiation process. These large gradients cause longer CV phases identifiable by sharp rises and peaks. Based on the CV capacities a reversibility is given after the formation of the passivation layer.

Interestingly, when switching to 20% SOC, both cells do not reach the CV capacities measured for the storage SOC of 20% in the first 300 days of testing. This might be caused by additional overvoltages that occur as a consequence of the surface layer formation described above. Further, it is noticeable that after each change in SOC, the CV capacity values sharply increase. Even with a SOC change from 90% to 20%, where a reduction of the CV capacities is expected due to the PEE, the CV capacities first increase and then decrease in the second check-up after the change. An explanation might be the degree of inhomogeneity between the active and passive regions immediately after the SOC change. At this point in time, the gradient of the voltage potential between the two areas is the highest. During the following equalization processes, the middle and the outer active electrode area experience the greatest voltage potential difference. The homogeneity of

the lithiation of the geometrically oversized electrode decreases significantly directly after the SOC change. Thus, during charging and discharging phases the cell voltage limits are reached earlier which requires more capacity to be charged within the CV phase.

8.4 Impact of SOC changes on incremental capacity analyses

The reversible and irreversible capacity effects described in the previous sections are clearly identifiable by ICA. Figure 8.3 shows the IC curves of the two cells with switched SOC. Only the IC curves before and after the two SOC switches are shown. Major shifts are particularly pronounced in the higher voltage range due to which this area is also shown enlarged.

The IC curves of the cell initially aged at 20% SOC (Figure 8.3a) exhibit a distinct shift with each SOC change. In particular, the first SOC change from 20% to 90% induces a strong left shift of the curve due to both passivation and PEE. As expected, the irreversible contribution to the shift remains until the end of the test, even after the PEE has decayed.

The results of the IC curves of the cell that started with 90% SOC (Figure 8.3b) indicate minor lateral shifts. Since the strong irreversible capacity loss has already occurred at the beginning of the aging test, this cell's IC curve shifts are more gradual and reflect the slow equalization process caused by the PEE. However, at the end of the test, the IC curve is not completely congruent with the one before switching to 20% SOC (before B). On the one hand, this could indicate that the equalization processes were not fully completed at the end of the test. On the other hand, the 90-day aging phase at 20% SOC might have led to a slight increase in capacity in higher voltage ranges (see Section 7.1).

A high degree of reversibility is confirmed by these ICA results. Nevertheless, due to the high calendar robustness of the investigated NMC|LTO cells, the overall changes of the IC curves are minor. Specifically, these minor aging-related changes cause an ICA to be sensitive to misinterpretation. For example, unintended, longer rest periods prior to check-ups might induce changes in the IC curves when the SOC during this time strongly deviates from the SOC in the aging test. However, for the purpose of studying the impact of PEE, the ICA provides a valuable method.

One question that could not be fully addressed by this experimental study relates to the impact of the PEE in the course of ongoing cell aging. For an extended analysis, several SOC changes at different aging states would have needed during the calendar aging test. Due to the high calendar lifetime of the NMC|LTO cells such a test procedure could not be accomplished within the course of this thesis. However, it can be expected that even such a test could not completely resolve the raised question. Reason for this is the impact of the PEE. As described in Section 6.1.2 and experimentally proven in Section 7.1, the PEE changes the cell balancing between anode and cathode. Depending on the voltage limits and the arrangement of the potential curves, the usable cell capacity is obtained.

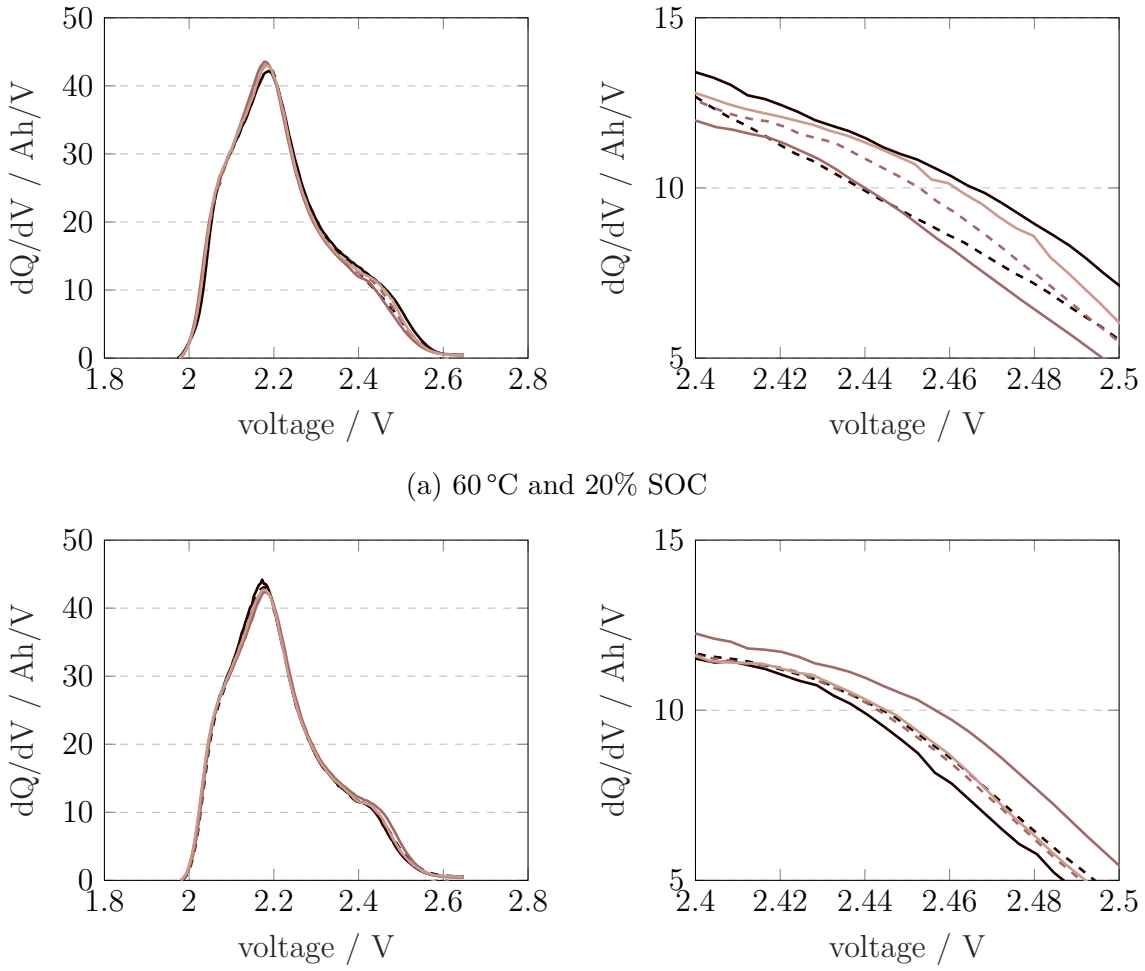

(a) 60 °C and 20% SOC

(b) 60 °C and 90% SOC

Figure 8.3: Results of the ICA of the calendar aged 10 Ah NMC|LTO cells at 60 °C at a) 20% SOC and b) 90% SOC. Only IC curves are shown, which were obtained from the qOCVs before and after the specific SOC changes (markers A, B, C) and at the end of the test (left: complete IC curve; right: enlargement of higher voltage range). Both reversible and irreversible shifts can be identified. Overall, results of the ICAs exhibit a strong dependency on the previous aging condition.

If the voltage potential curves of the active materials change over aging, this influences the shift in cell balancing caused by the PEE. As shown in Section 7.2, the occuring degradation effects, which for example depend on SOC, differ greatly in their effect on the half-cell potentials and available capacity. Therefore, it can be assumed that the capacity changes due to the PEE depend both on the initial cell balancing at begin-of-life and on the aging state of the active materials in the aged cells. Thus, a general statement about the intensity of the PEE for aged cells, even with experimentally tested SOC changes,

becomes more difficult.

8.5 Conclusion of the extent of reversibility

To investigate the differentiation between reversible and irreversible capacity effects, the routine of the ongoing calendar aging tests has been modified. Alternating back and forth between storage SOCs pursued the goal to provoke the appearance of the PEE in order to allow for a distinct analysis of the individual effects.

For the change from 20% to 90% SOC and vice versa, a similar reversible capacity change of about 1.4% was observed. In addition, the test results show that the PEE is fully reversible. Throughout the test period, the PEE is superimposed by irreversible aging effects that both decrease (high storage SOC) and increase (low storage SOC) the capacity.

At high SOC, side reactions occur at the beginning of the aging test. These side reactions were identified by analyzing the floating currents during calendar aging phases. It seems that raising the SOC from 20% to 90% increases the degree of lithiation of the LTO to a level where a surface layer is formed on the LTO. In addition, when the SOC is repeatedly changed to 90%, the floating currents reveal that this surface layer formation is non-recurring indicating a passivating effect. The capacity loss associated with this material degradation is approximately 1% to 1.5%.

The evaluation of the charge capacities in the CV phases demonstrates the reversibility of the PEE and impressively illustrates the effects of the PEE on the homogeneity of the charge distribution within the cathode.

The experimental results of this chapter significantly improve the understanding of capacity degradation of the investigated NMC|LTO cells as a result of calendar aging. Moreover, by intentionally inducing the PEE, its impact on different methods applied for aging analyses (capacity retention, floating currents, CV phases, ICA) has been revealed. Future studies should take these implications into account when evaluating data obtained from such methods.

Further studies are needed to investigate the origin of the surface layer formation and its composition. Whether the formed surface layer is stable and whether it has a permanent passivating effect, comparable to the SEI on graphite, is uncertain. More in-depth knowledge of this surface layer could advance the optimization of LTO not only with respect to aging behavior, but also with respect to the suppression of gassing reactions at the electrode/electrolyte interface.

9 Conclusion and outlook

Extending the 12 V vehicle electrical system by a 48 V voltage level offers automotive manufacturers an attractive opportunity to improve the efficiency of conventional combustion vehicles while maintaining existing vehicle architecture platforms. The requirements for the 48 V lithium-ion batteries needed for such a system are very high, for instance related to power capability, temperature stability and lifetime. However, due to the limited market presence to date, specific load characteristics for such an application are not available. This hinders effective product validation in the development process of 48 V batteries.

LTO-based cells represent promising candidates for use in 48 V systems due to their cell chemistry specific properties. For this reason, this dissertation focused on such a cell type (NMC|LTO). For application-specific measurements of this high-power optimized lithium-ion cell, the arising battery loads in development vehicles with 48 V system were characterized. For this purpose, driving data of more than 7000 km were analyzed and characteristic as well as critical operating parameters of the 48 V battery were identified.

The 48 V battery data showed that the cells are exposed to temperatures ranging from −20 °C to 70 °C. Due to the battery location in the engine compartment or the trunk, average temperatures during driving are high. As indicated by small ΔDODs, current loads are highly dynamic. In addition, high recuperation and boost currents occur, reaching up to 24C (charging) and 30C (discharging). Given the high lifetime requirements for an MHEV and the operating strategy implemented in the investigated vehicles, the lifetime-relevant energy throughputs are expected to be very high. Assuming a vehicle lifetime of 200,000 km, an energy throughput of up to 600 kWh or, related to cyclization, up to 27,000 equivalent full cycles can be expected at the cell level.

The obtained battery stress factors represented the basis for the application-specific investigations of this dissertation. Serving as a set of requirements, they defined the operating points which were used for both performance and aging analysis.

For a comprehensive benchmark analysis, the begin-of-life performance of the 10 Ah NMC|LTO cells was compared to two other high-power optimized graphite-based cells (16 Ah NMC|C, 20 Ah LFP|C). All three cell types showed outstanding electrical performance (<1 mΩ, 1 s, 20% to 90%) at ambient temperatures greater than 10 °C. For a 12 V lithium starter battery application, the LFP|C cell is particularly attractive due to its discharge capability and characteristic operating voltage window. At all temperatures the LFP|C cell offered almost SOC independent discharge performance as well as high capacity and energy availability, positively contributing to the cold-start capability of the system. Accurate battery state detection, which is necessary for reliable SOC and power predictions, is impeded by the presence of pronounced voltage hysteresis. Here, the test results for the

graphite-based cells showed a most pronounced hysteresis behavior, which depended on cell balancing and declined with decreasing temperature. The NMC|LTO cell exhibited an approximately constant and less pronounced hysteresis behavior. Its internal resistance showed the lowest current dependency but increased strongly at low SOC. Due to the high potential of the LTO material, the charge capability of the NMC|LTO cell at low temperatures is significantly higher. Thus, higher recuperation currents and consequently greater CO_2 savings potential could be obtained in a 48 V system if NMC|LTO cells were used.

A comprehensive calendar, cyclic and drive-cycle aging study was performed on NMC|LTO cells. A total of 39 cells were tested, some of them for more than two years. Despite high storage and cyclization temperatures up to 60 °C, the cells exhibited excellent cyclic and calendar lifetimes. For calendar aging at 80 °C, gassing reactions occurring at both high and low SOC were most critical for cell lifetime. The capacity loss during calendar aging was strongly SOC-dependent. A major part of this SOC dependency was caused by equalization processes between active and passive electrode regions. For the first time, the underlying PEE was described for a cell with geometrically oversized cathode. Using a descriptive explanatory model, it is illustrated that the PEE causes a shift in the operating voltage potential of one or both electrode materials. This shift corresponds to a change in cell balancing. Thus, depending on the potential curves and voltage limits, the extractable cell capacity varies. The analysis of capacities in CV charge phases revealed that equalization processes induced by the PEE lead to inhomogeneous lithiation of the active material. These observations can be transferred to graphite-based electrodes and highlight the increased risk of lithium plating in edge regions of the active area of the graphite anode.

For cyclic aging, the dependency of both the loss in capacity and the internal resistance increase on ΔDOD (mean SOC 55%) was most pronounced. However, for a 48 V application with small ΔDODs, the rise in internal resistance during cyclization only slightly exceeds those during calendar aging. Depending on the requirements of the high-power application, the increase in internal resistance can be more lifetime-critical than the capacity loss. Based on the conducted aging studies, it was concluded that the investigated cells are well suited for a 48 V application and that these cells meet the vehicle relevant lifetime requirements of 200,000 km.

Compared to the calendar aging at 60 °C, storing at 80 °C caused large capacity loss (high SOC) as well as strong capacity increase (low and medium SOC). In-situ and ex-situ investigations were performed to analyze these capacity effects and the material degradation. Results of the ICA revealed a distinct initial shift of the IC curves caused by the PEE arising at the beginning of the test. This demonstrates the influence of the PEE on the cell balancing, which is reflected in a change of the characteristic OCV of the cell. Thus, ICA is an effective technique for detecting a PEE. However, ICA results need to be interpreted under consideration of such PEE induced shifts. Depending on the storage SOC, degradation modes were observed during the aging process, mainly indicating LLI and LAM at the positive electrode. The capacity enhancements were attributable to an increase in capacity in higher voltage ranges.

Further, cell opening followed by post-mortem investigation was performed on the aged electrode material. The cell opening showed deterioration effects of active and passive cell materials such as separator discoloration, increased separator cracking or staining of the active materials. The separate measurement of the aged electrodes in half-cells showed that the capacity loss at high SOC was mainly caused by material degradation of the NMC. A capacity increase of the LTO at low SOC was confirmed at least for medium SOC. The XPS measurements demonstrated a surface layer formation on both active materials independent of SOC. Thickness of the surface layer rose with increasing SOC and consisted mainly of organic decomposition products.

For an investigation of reversible and irreversible capacity effects at 60 °C calendar aging, a PEE was intentionally induced in ongoing calendar aging tests by changing the storage SOC. Based on the capacity retention, full reversibility of the PEE was demonstrated. Switching the storage SOC from 20% to 90% and vice versa caused a PEE-induced change in extractable capacity of 1.4%. In addition, when the storage SOC was increased from 20% to 90%, a irreversible capacity loss of 1% to 1.5% occurred. Analysis of the floating currents for maintaining constant cell voltage revealed intensified side reactions at the beginning of the storage phases following such a SOC change. These side reactions and thus the capacity loss occurred only once even with repeated SOC changes during the period under consideration. It can be assumed that the LTO material is responsible for the capacity loss and that it is caused by the formation of a passivating surface layer. These results illustrate that the electrolyte decomposes at the LTO surface despite the characteristic LTO potential of 1.55 V.

The findings of this thesis provide multiple opportunities for future investigations. Shifts in cell balancing caused by the PEE could be integrated into physico-chemical simulation models. A spatially resolved accounting of the operating points on the potential curves of anode and cathode could serve to minimize local lithium plating risk and to enhance cell lifetime. In addition, this could improve the accuracy of the simulation of extractable cell capacities. With electrode-resolved material degradation, the effects of PEE over lifetime could be modeled and thus reversible capacity effects could be addressed in simulations.

The investigations of the aging behavior of the NMC|LTO cells have significantly extended the understanding of the degradation processes. However, some peculiarities remained unexplained within the scope of this thesis such as the observed SOC-dependent surface layer formation on LTO. Additional material studies could aim at investigating the lithiation process of LTO with respect to the critical decomposition potentials of the electrolyte. Further, it is unclear whether the passivating surface layer has a permanent protective effect and, if not, which operating points cause destruction/renewal of the surface layer. A deeper understanding of the electrochemical processes involved could improve the excellent lifetime of LTO-based cells even further and mitigate potential side reactions.

The aging results during calendar aging at low SOC reported in this thesis clearly revealed that the increase in capacity grows with increasing storage temperature. An explanation for this increase in capacity is needed. One hypothesis is that the gassing-induced pressure inside the cell causes this observation. This could be examined by specific aging tests at well-defined external pressure. Material investigations of these obtained LTO test samples

could assess, for example, changes in the material porosity or the electrical contacting of LTO particles.

The extensive investigations in this thesis emphasize the unique properties and attractiveness of the LTO technology and demonstrate its suitability for the use in 48 V vehicle electrical systems. The obtained findings are transferable to other potential fields of application, such as stationary energy storages or battery powered trains, and highlight the need for further development of this battery technology.

Glossary

ΔDOD	cycle depth
BEV	battery electric vehicle
BSG	belt-driven starter generator
C	graphite
CAN	controller area network
CC	constant current
CC-CV	constant current-constant voltage
CE	coulombic efficiency
CV	constant voltage
DC	direct current
DMC	dimethyl carbonate
DV	differential voltage
DVA	differential voltage analysis
EC	ethylene carbonate
EE	energy efficiency
EMC	ethyl methyl carbonate
FHEV	full hybrid electric vehicle
HEV	hybrid electric vehicle
HF	hydrofluoric acid
IC	incremental capacity
ICA	incremental capacity analysis
ICE	internal combustion engine
LAM	loss of active material
LAM_{dePE}	loss of active material at the positive electrode in the delithiated state
LAM_{liPE}	loss of active material at the positive electrode in the lithiated state
LAM_{NE}	loss of active material at the negative electrode
LAM_{PE}	loss of active material at the positive electrode

LFP	lithium iron phosphate
LiF	lithium fluoride
$LiPF_6$	lithium hexafluorophosphate
LLI	loss of lithium inventory
LMO	lithium manganese oxide
LTO	lithium titanate oxide
MHEV	mild hybrid electric vehicle
NMC	lithium nickel manganese cobalt oxide
OCV	open circuit voltage
PC	propylene carbonate
PE	polyethylene
PEE	passive electrode effect
PF_5	phosphorus pentafluoride
PHEV	plug-in hybrid electric vehicle
PP	polypropylene
qOCV	quasi-stationary open circuit voltage
SEI	solid electrolyte interface
SEM	scanning electron microscopy
SOC	state of charge
XPS	X-ray photoelectron spectroscopy

Bibliography

[1] The European Parliament and Council. *Regulation (EU) 2019/631 of the European Parliament and of the Council of 17 April 2019 setting CO2 emission performance standards for new passenger cars and for new light commercial vehicles, and repealing Regulations (EC) No 443/2009 and (EU) No 510/2011*. 2019.

[2] Enang, W. and Bannister, C. 'Modelling and control of hybrid electric vehicles (A comprehensive review)'. In: *Renewable and Sustainable Energy Reviews* 74 (2017), pp. 1210–1239. ISSN: 13640321. DOI: 10.1016/j.rser.2017.01.075.

[3] Hasan, S. and Simsekoglu, Ö. 'The role of psychological factors on vehicle kilometer travelled (VKT) for battery electric vehicle (BEV) users'. In: *Research in Transportation Economics* 82 (2020), p. 100880. ISSN: 07398859. DOI: 10.1016/j.retrec.2020.100880.

[4] Ou, S. et al. 'Quantifying the impacts of micro- and mild- hybrid vehicle technologies on fleetwide fuel economy and electrification'. In: *eTransportation* 4 (2020), p. 100058. ISSN: 25901168. DOI: 10.1016/j.etran.2020.100058.

[5] Cardoso, D. S. et al. 'A review of micro and mild hybrid systems'. In: *Energy Reports* 6 (2020), pp. 385–390. ISSN: 23524847. DOI: 10.1016/j.egyr.2019.08.077.

[6] Oh, Y. et al. 'Estimation of CO2 reduction by parallel hard-type power hybridization for gasoline and diesel vehicles'. In: *The Science of the total environment* 595 (2017), pp. 2–12. DOI: 10.1016/j.scitotenv.2017.03.171.

[7] Gewald, T. et al. 'Accelerated Aging Characterization of Lithium-ion Cells: Using Sensitivity Analysis to Identify the Stress Factors Relevant to Cyclic Aging'. In: *Batteries* 6.1 (2020), p. 6. DOI: 10.3390/batteries6010006.

[8] Gewald, T. and Lienkamp, M. 'A systematic method for accelerated aging characterization of lithium-ion cells in automotive applications'. In: *Forschung im Ingenieurwesen* 83.4 (2019), pp. 831–841. ISSN: 1434-0860. DOI: 10.1007/s10010-019-00318-9.

[9] Schröer, P. et al. 'Challenges in modeling high power lithium titanate oxide cells in battery management systems'. In: *Journal of Energy Storage* 28 (2020), p. 101189. DOI: 10.1016/j.est.2019.101189.

[10] Xu, G. et al. 'Li4Ti5O12-based energy conversion and storage systems: status and prospects'. In: *Coordination Chemistry Reviews* 343 (2017). DOI: 10.1016/j.ccr.2017.05.006.

[11] Nemeth, T. et al. 'Lithium titanate oxide battery cells for high-power automotive applications – Electro-thermal properties, aging behavior and cost considerations'. In: *Journal of Energy Storage* 31 (2020), p. 101656. DOI: 10.1016/j.est.2020.101656.

[12] Schmuch, R. et al. 'Performance and cost of materials for lithium-based rechargeable automotive batteries'. In: *Nature Energy* 3.4 (2018), pp. 267–278. DOI: 10.1038/s41560-018-0107-2.

[13] International Energy Agency. 'Technology Roadmaps: Electric and Plug-in Hybrid Electric Vehicles'. In: (2009). DOI: 10.1787/9789264088177-en.

[14] Aravindan, V. et al. 'Insertion-type electrodes for nonaqueous Li-ion capacitors'. In: *Chemical reviews* 114.23 (2014), pp. 11619–11635. ISSN: 0009-2665. DOI: 10.1021/cr5000915.

[15] Quinn, J. B. et al. 'Energy Density of Cylindrical Li-Ion Cells: A Comparison of Commercial 18650 to the 21700 Cells'. In: *Journal of The Electrochemical Society* 165.14 (2018), A3284–A3291. ISSN: 0013-4651. DOI: 10.1149/2.0281814jes.

[16] Tomaszewska, A. et al. 'Lithium-ion battery fast charging: A review'. In: *eTransportation* 1.15 (2019), p. 100011. ISSN: 25901168. DOI: 10.1016/j.etran.2019.100011.

[17] Löbberding, H. et al. 'From Cell to Battery System in BEVs: Analysis of System Packing Efficiency and Cell Types'. In: *World Electric Vehicle Journal* 11.4 (2020), p. 77. DOI: 10.3390/wevj11040077.

[18] Korthauer, R. *Handbuch Lithium-Ionen-Batterien*. Berlin, Heidelberg: Springer Berlin Heidelberg, 2013. ISBN: 978-3-642-30652-5. DOI: 10.1007/978-3-642-30653-2.

[19] Jossen, A. and Weydanz, W. *Moderne Akkumulatoren richtig einsetzen*. 1. Auflage. Neusäß: Ubooks-Verlag, 2006. ISBN: 978-3-939-35911-1.

[20] Garche, J. *Encyclopedia of electrochemical power sources*. Amsterdam: Elsevier, 2009. ISBN: 9780444520937.

[21] Daniel, C. and Besenhard, J. O. *Handbook of Battery Materials*. Weinheim: Wiley, 2012. ISBN: 978-3-527-32695-2.

[22] Zhang, Z. and Zhang, S. S., eds. *Rechargeable batteries: Materials, technologies and new trends*. Green energy and technology. Cham et al.: Springer, 2015. ISBN: 978-3-319-15457-2.

[23] Korthauer, R., ed. *Lithium-Ion Batteries: Basics and Applications*. Berlin, Heidelberg: Springer Berlin Heidelberg, 2018. ISBN: 978-3-662-53071-9. DOI: 10.1007/978-3-662-53071-9.

[24] Schmalstieg, J. 'Physikalisch-elektrochemische Simulation von Lithium-Ionen-Batterien: Implementierung, Parametrierung und Anwendung'. Dissertation. Aachen: RWTH Aachen University, 2017. DOI: 10.18154/RWTH-2017-04693.

[25] Tarascon, J. M. and Armand, M. 'Issues and challenges facing rechargeable lithium batteries'. In: *Nature* 414.6861 (2001), pp. 359–367. ISSN: 0028-0836. DOI: 10.1038/35104644.

[26] Liu, C. et al. 'Understanding electrochemical potentials of cathode materials in rechargeable batteries'. In: *Materials Today* 19.2 (2016), pp. 109–123. ISSN: 13697021. DOI: 10.1016/j.mattod.2015.10.009.

[27] Xu, W. et al. 'Lithium metal anodes for rechargeable batteries'. In: *Energy Environ. Sci.* 7.2 (2014), pp. 513–537. ISSN: 1754-5692. DOI: 10.1039/C3EE40795K.

[28] Nitta, N. et al. 'Li-ion battery materials: present and future'. In: *Materials Today* 18.5 (2015), pp. 252–264. ISSN: 13697021. DOI: 10.1016/j.mattod.2014.10.040.

[29] He, M. et al. 'In Situ Gas Analysis of Li4Ti5O12 Based Electrodes at Elevated Temperatures'. In: *Journal of The Electrochemical Society* 162.6 (2015), A870–A876. ISSN: 0013-4651. DOI: 10.1149/2.0311506jes.

[30] Aurbach, D. 'A short review of failure mechanisms of lithium metal and lithiated graphite anodes in liquid electrolyte solutions'. In: *Solid State Ionics* 148.3-4 (2002), pp. 405–416. ISSN: 01672738. DOI: 10.1016/S0167-2738(02)00080-2.

[31] Warnecke, A. J. 'Degradation Mechanisms in NMC-Based Lithium-Ion Batteries'. Dissertation. Aachen: RWTH Aachen University, 2017. DOI: 10.18154/RWTH-2017-09646.

[32] Wu, B. et al. 'Good Practices for Rechargeable Lithium Metal Batteries'. In: *Journal of The Electrochemical Society* 166.16 (2020), A4141–A4149. ISSN: 0013-4651. DOI: 10.1149/2.0691916jes.

[33] Wu, X. et al. 'Safety Issues in Lithium Ion Batteries: Materials and Cell Design'. In: *Frontiers in Energy Research* 7 (2019), p. 65. ISSN: 2296-598X. DOI: 10.3389/fenrg.2019.00065.

[34] Zheng, F. et al. 'Review on solid electrolytes for all-solid-state lithium-ion batteries'. In: *Journal of Power Sources* 389 (2018), pp. 198–213. ISSN: 03787753. DOI: 10.1016/j.jpowsour.2018.04.022.

[35] Winter, M. et al. 'Insertion electrode materials for rechargeable lithium batteries'. In: *Advanced Materials* 10 (1998), p. 725. ISSN: 0935-9648.

[36] Zaghib, K. et al. 'Advanced Electrodes for High Power Li-ion Batteries'. In: *Materials (Basel, Switzerland)* 6.3 (2013), pp. 1028–1049. ISSN: 1996-1944. DOI: 10.3390/ma6031028.

[37] Nishi, Y. 'Lithium ion secondary batteries; past 10 years and the future'. In: *Journal of Power Sources* 100.1-2 (2001), pp. 101–106. ISSN: 03787753. DOI: 10.1016/S0378-7753(01)00887-4.

[38] Loeffler, B. N. et al. 'Secondary Lithium-Ion Battery Anodes: From First Commercial Batteries to Recent Research Activities'. In: *Johnson Matthey Technology Review* 59.1 (2015), pp. 34–44. ISSN: 20565135. DOI: 10.1595/205651314X685824.

[39] Fong, R. et al. 'Studies of Lithium Intercalation into Carbons Using Nonaqueous Electrochemical Cells'. In: *Journal of The Electrochemical Society* 137.7 (1990), pp. 2009–2013. ISSN: 0013-4651. DOI: 10.1149/1.2086855.

[40] Dahn, J. R. et al. 'Mechanisms for Lithium Insertion in Carbonaceous Materials'. In: *Science* 270.5236 (1995), pp. 590–593. ISSN: 0036-8075. DOI: 10.1126/science.270.5236.590.

[41] Linden, D. and Reddy, T. B., eds. *Handbook of batteries*. 3. ed. McGraw-Hill handbooks. New York, NY: McGraw-Hill, 2002. ISBN: 978-0071359788.

[42] Heß, M. and Novák, P. 'Shrinking annuli mechanism and stage-dependent rate capability of thin-layer graphite electrodes for lithium-ion batteries'. In: *Electrochimica Acta* 106 (2013), pp. 149–158. ISSN: 00134686. DOI: 10.1016/j.electacta.2013.05.056.

[43] Dahn. 'Phase diagram of LixC6'. In: *Physical review. B, Condensed matter* 44.17 (1991), pp. 9170–9177. ISSN: 0163-1829. DOI: 10.1103/PhysRevB.44.9170.

[44] Huggins, R. A. *Energy Storage*. Boston, MA: Springer Science+Business Media LLC, 2010. ISBN: 1441910239. DOI: 10.1007/978-1-4419-1024-0.

[45] Schlögl, R. 'Graphite — A Unique Host Lattice'. In: *Progress in Intercalation Research*. Ed. by Lévy, F. et al. Vol. 17. Physics and Chemistry of Materials with Low-Dimensional Structures. Dordrecht: Springer Netherlands, 1994, pp. 83–176. ISBN: 978-94-010-4385-4. DOI: 10.1007/978-94-011-0890-4.

[46] Peled, E. 'The Electrochemical Behavior of Alkali and Alkaline Earth Metals in Nonaqueous Battery Systems—The Solid Electrolyte Interphase Model'. In: *Journal of The Electrochemical Society* 126.12 (1979), pp. 2047–2051. ISSN: 0013-4651. DOI: 10.1149/1.2128859.

[47] Flandrois, S. and Simon, B. 'Carbon materials for lithium-ion rechargeable batteries'. In: *Carbon* 37.2 (1999), pp. 165–180. ISSN: 00086223. DOI: 10.1016/S0008-6223(98)00290-5.

[48] Yamada, Y. et al. 'Kinetics of lithium ion transfer at the interface between graphite and liquid electrolytes: effects of solvent and surface film'. In: *Langmuir: the ACS journal of surfaces and colloids* 25.21 (2009), pp. 12766–12770. DOI: 10.1021/la901829v.

[49] Zhao, M. et al. 'Electrochemical Stability of Copper in Lithium-Ion Battery Electrolytes'. In: *Journal of The Electrochemical Society* 147.8 (2000), p. 2874. ISSN: 0013-4651. DOI: 10.1149/1.1393619.

[50] Myung, S.-T. et al. 'Electrochemical behavior and passivation of current collectors in lithium-ion batteries'. In: *Journal of Materials Chemistry* 21.27 (2011), p. 9891. ISSN: 0959-9428. DOI: 10.1039/c0jm04353b.

[51] Schmidt, J. P. 'Verfahren zur Charakterisierung und Modellierung von Lithium-Ionen Zellen'. Dissertation. 2013. DOI: 10.5445/KSP/1000036622.

[52] Amine, K. et al. 'Nanostructured anode material for high-power battery system in electric vehicles'. In: *Advanced materials (Deerfield Beach, Fla.)* 22.28 (2010), pp. 3052–3057. DOI: 10.1002/adma.201000441.

[53] Belharouak, I. et al. 'Electrochemistry and safety of Li4Ti5O12 and graphite anodes paired with LiMn2O4 for hybrid electric vehicle Li-ion battery applications'. In: *Journal of Power Sources* 196.23 (2011), pp. 10344–10350. ISSN: 03787753. DOI: 10.1016/j.jpowsour.2011.08.079.

[54] Chen, Z. et al. 'Titanium-Based Anode Materials for Safe Lithium-Ion Batteries'. In: *Advanced Functional Materials* 23 (2013). DOI: 10.1002/adfm.201200698.

[55] Sun, X. et al. 'Advances in spinel Li4Ti5O12 anode materials for lithium-ion batteries'. In: *New Journal of Chemistry* 39.1 (2015), pp. 38–63. ISSN: 1144-0546. DOI: 10.1039/C4NJ01390E.

[56] Zhao, B. et al. 'A comprehensive review of Li4Ti5O12-based electrodes for lithium-ion batteries: The latest advancements and future perspectives'. In: *Materials Science and Engineering R: Reports* 98 (2015), pp. 1–71. DOI: 10.1016/j.mser.2015.10.001.

[57] Liu, J. et al. 'Lithium Titanate-Based Lithium-Ion Batteries'. In: *Advanced Battery Materials*. Ed. by Sun, C. Vol. 5. Hoboken, NJ, USA: John Wiley & Sons, Inc, 2019, pp. 87–157. ISBN: 9781119407713. DOI: 10.1002/9781119407713.ch2.

[58] Bresser, D. et al. 'The importance of "going nano" for high power battery materials'. In: *Journal of Power Sources* 219 (2012), pp. 217–222. ISSN: 03787753. DOI: 10.1016/j.jpowsour.2012.07.035.

[59] Ohzuku, T. et al. 'Zero–Strain Insertion Material of Li[Li1/3Ti5/3]O4 for Rechargeable Lithium Cells'. In: *Journal of The Electrochemical Society* 142.5 (1995), pp. 1431–1435. ISSN: 0013-4651. DOI: 10.1149/1.2048592.

[60] Kitta, M. et al. 'Characterization of two phase distribution in electrochemically-lithiated spinel Li4Ti5O12 secondary particles by electron energy-loss spectroscopy'. In: *Journal of Power Sources* 237 (2013), pp. 26–32. ISSN: 03787753. DOI: 10.1016/j.jpowsour.2013.03.022.

[61] Lv, W. et al. 'Review-Gassing Mechanism and Suppressing Solutions in Li4Ti5O12-Based Lithium-Ion Batteries'. In: *Journal of The Electrochemical Society* 164.9 (2017), A2213–A2224. ISSN: 0013-4651. DOI: 10.1149/2.0031712jes.

[62] Ding, Y.-L. et al. 'Automotive Li-Ion Batteries: Current Status and Future Perspectives'. In: *Electrochemical Energy Reviews* (2019), pp. 1–28. DOI: 10.1007/s41918-018-0022-z.

[63] Yao, X. L. et al. 'Comparisons of graphite and spinel Li1.33Ti1.67O4 as anode materials for rechargeable lithium-ion batteries'. In: *Electrochimica Acta* 50.20 (2005), pp. 4076–4081. ISSN: 00134686. DOI: 10.1016/j.electacta.2005.01.034.

[64] Sandhya, C. P. et al. 'Lithium titanate as anode material for lithium-ion cells: a review'. In: *Ionics* 20.5 (2014), pp. 601–620. ISSN: 0947-7047. DOI: 10.1007/s11581-014-1113-4.

[65] Sun, Y. et al. 'Promises and challenges of nanomaterials for lithium-based rechargeable batteries'. In: *Nature Energy* 1.7 (2016), p. 652. DOI: 10.1038/nenergy.2016.71.

[66] Wang, S. et al. 'Recent progress in Ti-based nanocomposite anodes for lithium ion batteries'. In: *Journal of Advanced Ceramics* 8.1 (2019), pp. 1–18. ISSN: 2226-4108. DOI: 10.1007/s40145-018-0292-2.

[67] Hong, Z. and Wei, M. 'Layered titanate nanostructures and their derivatives as negative electrode materials for lithium-ion batteries'. In: *Journal of Materials Chemistry A* 1.14 (2013), p. 4403. ISSN: 2050-7488. DOI: 10.1039/c2ta01312f.

[68] He, Y.-B. et al. 'Gassing in Li(4)Ti(5)O(12)-based batteries and its remedy'. In: *Scientific reports* 2 (2012), p. 913. DOI: 10.1038/srep00913.

[69] Lopez, S. et al. 'Acid–Base Properties of Passive Films on Aluminum: II. An X–Ray Photoelectron Spectroscopy and X–Ray Absorption Near Edge Structure Study'. In: *Journal of The Electrochemical Society* 145.3 (1998), pp. 829–834. ISSN: 0013-4651. DOI: 10.1149/1.1838352.

[70] Iwakura, C. et al. 'Electrochemical characterization of various metal foils as a current collector of positive electrode for rechargeable lithium batteries'. In: *Journal of Power Sources* 68.2 (1997), pp. 301–303. ISSN: 03787753. DOI: 10.1016/S0378-7753(97)02538-X.

[71] Yang, H. et al. 'Aluminum Corrosion in Lithium Batteries An Investigation Using the Electrochemical Quartz Crystal Microbalance'. In: *Journal of The Electrochemical Society* 147.12 (2000), p. 4399. ISSN: 0013-4651. DOI: 10.1149/1.1394077.

[72] Klamor, S. 'Insights into Aging Mechanisms and Optimization of Electrode Materials for Lithium-Ion Batteries via In Situ Nuclear Magnetic Resonance and 1D Magnetic Resonance Imaging Techniques'. Dissertation. Westfälische Wilhelms-Universität Münster, 2015.

[73] Bresser, D. et al. 'Lithium-ion batteries (LIBs) for medium- and large-scale energy storage'. In: *Advances in Batteries for Medium and Large-Scale Energy Storage*. Elsevier, 2015, pp. 125–211. ISBN: 9781782420132. DOI: 10.1016/B978-1-78242-013-2.00006-6.

[74] Roscher, M. A. et al. 'OCV Hysteresis in Li-Ion Batteries including Two-Phase Transition Materials'. In: *International Journal of Electrochemistry* 2011.9 (2011), pp. 1–6. DOI: 10.4061/2011/984320.

[75] Prosini, P. P. et al. 'Long-term cyclability of nanostructured LiFePO4'. In: *Electrochimica Acta* 48.28 (2003), pp. 4205–4211. ISSN: 00134686. DOI: 10.1016/S0013-4686(03)00606-6.

[76] Herle, P. S. et al. 'Nano-network electronic conduction in iron and nickel olivine phosphates'. In: *Nature materials* 3.3 (2004), pp. 147–152. ISSN: 1476-1122. DOI: 10.1038/nmat1063.

[77] Chung, S.-Y. et al. 'Electronically conductive phospho-olivines as lithium storage electrodes'. In: *Nature materials* 1.2 (2002), pp. 123–128. ISSN: 1476-1122. DOI: 10.1038/nmat732.

[78] Zhuang, D. et al. 'One-step Solid-state Synthesis and Electrochemical Performance of Nb-doped LiFePO4/C'. In: *Acta Physico-Chimica Sinica* 22.7 (2006), pp. 840–844. ISSN: 18721508. DOI: 10.1016/S1872-1508(06)60037-5.

[79] Park, O. K. et al. 'Who will drive electric vehicles, olivine or spinel?' In: *Energy Environ. Sci.* 4.5 (2011), p. 1621. ISSN: 1754-5692. DOI: 10.1039/C0EE00559B.

[80] Zaghib, K. et al. 'Enhanced thermal safety and high power performance of carbon-coated LiFePO4 olivine cathode for Li-ion batteries'. In: *Journal of Power Sources* 219 (2012), pp. 36–44. ISSN: 03787753. DOI: 10.1016/j.jpowsour.2012.05.018.

[81] Andre, D. et al. 'Future generations of cathode materials: an automotive industry perspective'. In: *Journal of Materials Chemistry A* 3.13 (2015), pp. 6709–6732. ISSN: 2050-7488. DOI: 10.1039/c5ta00361j.

[82] Ferg, E. E. et al. 'The challenges of a Li-ion starter lighting and ignition battery: A review from cradle to grave'. In: *Journal of Power Sources* 423 (2019), pp. 380–403. ISSN: 03787753. DOI: 10.1016/j.jpowsour.2019.03.063.

[83] Dahn, J. et al. 'Thermal stability of LixCoO2, LixNiO2 and lambda-MnO2 and consequences for the safety of Li-ion cells'. In: *Solid State Ionics* 69.3-4 (1994), pp. 265–270. ISSN: 01672738. DOI: 10.1016/0167-2738(94)90415-4.

[84] Gummow, R. J. et al. 'Improved capacity retention in rechargeable 4 V lithium/lithium-manganese oxide (spinel) cells'. In: *Solid State Ionics* 69.1 (1994), pp. 59–67. ISSN: 01672738. DOI: 10.1016/0167-2738(94)90450-2.

[85] Han, A. R. et al. 'Soft Chemical Dehydration Route to Carbon Coating of Metal Oxides: Its Application for Spinel Lithium Manganate'. In: *The Journal of Physical Chemistry C* 111.30 (2007), pp. 11347–11352. ISSN: 1932-7447. DOI: 10.1021/jp0725230.

[86] Sadeghi, B. et al. 'Surface Modification of LiMn2O4 for Lithium Batteries by Nanostructured LiFePO4 Phosphate'. In: *Journal of Nanomaterials* 2012.1 (2012), pp. 1–7. ISSN: 1687-4110. DOI: 10.1155/2012/743236.

[87] Thackeray, M. M. 'Exploiting the Spinel Structure for Li–ion Battery Applications: A Tribute to John B. Goodenough'. In: *Advanced Energy Materials* 29 (2020), p. 2001117. ISSN: 1614-6832. DOI: 10.1002/aenm.202001117.

[88] Löffler, N. 'Towards Greener and Environmentally Friendly Lithium-Ion Batteries: Aqueous Electrode Processing'. Dissertation. Westfälische Wilhelms-Universität Münster, 2016.

[89] Wang, Z. et al. 'Study on decrystallization of cathode material and decomposition of electrolyte in LiNi1/3Co1/3Mn1/3O2-based cells'. In: *Journal of Solid State Electrochemistry* 18.6 (2014), pp. 1757–1762. ISSN: 1432-8488. DOI: 10.1007/s10008-014-2419-x.

[90] Ohzuku, T. et al. 'Comparative study of LiCoO2, LiNi12Co12O2 and LiNiO2 for 4 volt secondary lithium cells'. In: *Electrochimica Acta* 38.9 (1993), pp. 1159–1167. ISSN: 00134686. DOI: 10.1016/0013-4686(93)80046-3.

[91] Yin, S.-C. et al. 'X-ray/Neutron Diffraction and Electrochemical Studies of Lithium De/Re-Intercalation in Li1-xCo1/3Ni1/3Mn1/3O2 (x = 0 → 1)'. In: *Chemistry of Materials* 18.7 (2006), pp. 1901–1910. ISSN: 0897-4756. DOI: 10.1021/cm0511769.

[92] Dahbi, M. et al. 'Electrochemical behavior of LiNi1−y−zCoyMnzO2 probed through structural and magnetic properties'. In: *Journal of Applied Physics* 111.2 (2012), p. 023904. ISSN: 0021-8979. DOI: 10.1063/1.3676434.

[93] Whittingham, M. S. 'Lithium batteries and cathode materials'. In: *Chemical reviews* 104.10 (2004), pp. 4271–4301. ISSN: 0009-2665. DOI: 10.1021/cr020731c.

[94] Li, D. et al. 'Synthesis and electrochemical properties of LiNi0.85−xCoxMn0.15O2 as cathode materials for lithium-ion batteries'. In: *Journal of Solid State Electrochemistry* 12.3 (2008), pp. 323–327. ISSN: 1432-8488. DOI: 10.1007/s10008-007-0394-1.

[95] Arora, P. and Zhang, Z. J. 'Battery separators'. In: *Chemical reviews* 104.10 (2004), pp. 4419–4462. ISSN: 0009-2665. DOI: 10.1021/cr020738u.

[96] Deimede, V. and Elmasides, C. 'Separators for Lithium-Ion Batteries: A Review on the Production Processes and Recent Developments'. In: *Energy Technology* 3.5 (2015), pp. 453–468. ISSN: 2194-4288. DOI: 10.1002/ente.201402215.

[97] Zhang, S. S. 'A review on the separators of liquid electrolyte Li-ion batteries'. In: *Journal of Power Sources* 164.1 (2007), pp. 351–364. ISSN: 03787753. DOI: 10.1016/j.jpowsour.2006.10.065.

[98] Lee, H. et al. 'A review of recent developments in membrane separators for rechargeable lithium-ion batteries'. In: *Energy Environ. Sci.* 7.12 (2014), pp. 3857–3886. ISSN: 1754-5692. DOI: 10.1039/C4EE01432D.

[99] Xu, K. 'Nonaqueous liquid electrolytes for lithium-based rechargeable batteries'. In: *Chemical reviews* 104.10 (2004), pp. 4303–4417. ISSN: 0009-2665. DOI: 10.1021/cr030203g.

[100] Song, J. Y. et al. 'Review of gel-type polymer electrolytes for lithium-ion batteries'. In: *Journal of Power Sources* 77.2 (1999), pp. 183–197. ISSN: 03787753. DOI: 10.1016/S0378-7753(98)00193-1.

[101] Cheng, X. et al. 'Gel Polymer Electrolytes for Electrochemical Energy Storage'. In: *Advanced Energy Materials* 8.7 (2018), p. 1702184. ISSN: 1614-6832. DOI: 10.1002/aenm.201702184.

[102] Zhao, Q. et al. 'Designing solid-state electrolytes for safe, energy-dense batteries'. In: *Nature Reviews Materials* 5.3 (2020), pp. 229–252. DOI: 10.1038/s41578-019-0165-5.

[103] Marcinek, M. et al. 'Electrolytes for Li-ion transport – Review'. In: *Solid State Ionics* 276 (2015), pp. 107–126. ISSN: 01672738. DOI: 10.1016/j.ssi.2015.02.006.

[104] Haregewoin, A. M. et al. 'Electrolyte additives for lithium ion battery electrodes: progress and perspectives'. In: *Energy Environ. Sci.* 9.6 (2016), pp. 1955–1988. ISSN: 1754-5692. DOI: 10.1039/C6EE00123H.

[105] Zhang, S. S. 'A review on electrolyte additives for lithium-ion batteries'. In: *Journal of Power Sources* 162.2 (2006), pp. 1379–1394. ISSN: 03787753. DOI: 10.1016/j.jpowsour.2006.07.074.

[106] Dahbi, M. et al. 'Comparative study of EC/DMC LiTFSI and LiPF6 electrolytes for electrochemical storage'. In: *Journal of Power Sources* 196.22 (2011), pp. 9743–9750. ISSN: 03787753. DOI: 10.1016/j.jpowsour.2011.07.071.

[107] Baum, C. et al. *Future Energy Storage Systems For Mobility Applications*. 2020. DOI: 10.24406/ipt-n-590461.

[108] Lain et al. 'Design Strategies for High Power vs. High Energy Lithium Ion Cells'. In: *Batteries* 5.4 (2019), p. 64. DOI: 10.3390/batteries5040064.

[109] Schmidt, P. A. 'Laserstrahlschweißen elektrischer Kontakte von Lithium-Ionen-Batterien in Elektro- und Hybridfahrzeugen'. Dissertation. Herbert Utz Verlag GmbH, 2015.

[110] Shawn Lee, S. et al. 'Characterization of Joint Quality in Ultrasonic Welding of Battery Tabs'. In: *Journal of Manufacturing Science and Engineering* 135.2 (2013), p. 541. ISSN: 1087-1357. DOI: 10.1115/1.4023364.

[111] Pouraghajan, F. et al. 'Quantifying Tortuosity of Porous Li-Ion Battery Electrodes: Comparing Polarization-Interrupt and Blocking-Electrolyte Methods'. In: *Journal of The Electrochemical Society* 165.11 (2018), A2644–A2653. ISSN: 0013-4651. DOI: 10.1149/2.0611811jes.

[112] Käbitz, S. 'Untersuchung der Alterung von Lithium-Ionen-Batterien mittels Elektroanalytik und elektrochemischer Impedanzspektroskopie'. Dissertation. Aachen: Rheinisch-Westfälische Technische Hochschule Aachen, 2016. DOI: 10.18154/RWTH-2016-12094.

[113] Lee, K. and Kum, D. 'The impact of inhomogeneous particle size distribution on Li-ion cell performance under galvanostatic and transient loads'. In: *2016 IEEE Transportation Electrification Conference*, pp. 454–459. DOI: 10.1109/ITEC-AP.2016.7512997.

[114] Bank, T. et al. 'Extensive aging analysis of high-power lithium titanate oxide batteries: Impact of the passive electrode effect'. In: *Journal of Power Sources* 473 (2020). ISSN: 03787753. DOI: 10.1016/j.jpowsour.2020.228566.

[115] Lin, C. et al. 'Aging Mechanisms of Electrode Materials in Lithium-Ion Batteries for Electric Vehicles'. In: *Journal of Chemistry* 2015.4 (2015), pp. 1–11. ISSN: 2090-9063. DOI: 10.1155/2015/104673.

[116] Broussely, M. et al. 'Main aging mechanisms in Li ion batteries'. In: *Journal of Power Sources* 146.1-2 (2005), pp. 90–96. ISSN: 03787753. DOI: 10.1016/j.jpowsour.2005.03.172.

[117] Bloom, I. et al. 'An accelerated calendar and cycle life study of Li-ion cells'. In: *Journal of Power Sources* 101.2 (2001), pp. 238–247. ISSN: 03787753. DOI: 10.1016/S0378-7753(01)00783-2.

[118] Saxena, S. et al. 'Quantifying EV battery end-of-life through analysis of travel needs with vehicle powertrain models'. In: *Journal of Power Sources* 282 (2015), pp. 265–276. ISSN: 03787753. DOI: 10.1016/j.jpowsour.2015.01.072.

[119] Han, X. et al. 'A comparative study of commercial lithium ion battery cycle life in electric vehicle: Capacity loss estimation'. In: *Journal of Power Sources* 268 (2014), pp. 658–669. ISSN: 03787753. DOI: 10.1016/j.jpowsour.2014.06.111.

[120] Saxena, S. et al. 'Charging ahead on the transition to electric vehicles with standard 120 V wall outlets'. In: *Applied Energy* 157 (2015), pp. 720–728. ISSN: 03062619. DOI: 10.1016/j.apenergy.2015.05.005.

[121] Keil, P. 'Aging of Lithium-Ion Batteries in Electric Vehicles'. Dissertation. Technische Universität München, 2017.

[122] Birkl, C. R. et al. 'Degradation diagnostics for lithium ion cells'. In: *Journal of Power Sources* 341 (2017), pp. 373–386. ISSN: 03787753. DOI: 10.1016/j.jpowsour.2016.12.011.

[123] Vetter, J. et al. 'Ageing mechanisms in lithium-ion batteries'. In: *Journal of Power Sources* 147.1-2 (2005), pp. 269–281. ISSN: 03787753. DOI: 10.1016/j.jpowsour.2005.01.006.

[124] Keil, P. and Jossen, A. 'Calendar Aging of NCA Lithium-Ion Batteries Investigated by Differential Voltage Analysis and Coulomb Tracking'. In: *Journal of The Electrochemical Society* 164.1 (2017), A6066–A6074. ISSN: 0013-4651. DOI: 10.1149/2.0091701jes.

[125] Kassem, M. et al. 'Calendar aging of a graphite/LiFePO4 cell'. In: *Journal of Power Sources* 208 (2012), pp. 296–305. ISSN: 03787753. DOI: 10.1016/j.jpowsour.2012.02.068.

[126] Dubarry, M. et al. 'Calendar aging of commercial Li-ion cells of different chemistries – A review'. In: *Current Opinion in Electrochemistry* 9 (2018), pp. 106–113. ISSN: 24519103. DOI: 10.1016/j.coelec.2018.05.023.

[127] Jalkanen, K. et al. 'Cycle aging of commercial NMC/graphite pouch cells at different temperatures'. In: *Applied Energy* 154 (2015), pp. 160–172. ISSN: 03062619. DOI: 10.1016/j.apenergy.2015.04.110.

[128] Schmalstieg, J. et al. 'A holistic aging model for Li(NiMnCo)O2 based 18650 lithium-ion batteries'. In: *Journal of Power Sources* 257 (2014), pp. 325–334. ISSN: 03787753. DOI: 10.1016/j.jpowsour.2014.02.012.

[129] Schmidt, A. et al. 'Power capability and cyclic aging of commercial, high power lithium ion battery cells with respect to different cell designs'. In: *Journal of Power Sources* 425 (2019), pp. 27–38. ISSN: 03787753. DOI: 10.1016/j.jpowsour.2019.03.075.

[130] Ceraolo, M. et al. 'Aging evaluation of high power lithium cells subjected to micro-cycles'. In: *Journal of Energy Storage* 6 (2016), pp. 116–124. DOI: 10.1016/j.est.2016.03.006.

[131] Liu, Z. et al. 'Aging characterization and modeling of nickel-manganese-cobalt lithium-ion batteries for 48V mild hybrid electric vehicle applications'. In: *Journal of Energy Storage* 21 (2019), pp. 519–527. DOI: 10.1016/j.est.2018.11.016.

[132] Gao, Y. et al. 'Lithium-ion battery aging mechanisms and life model under different charging stresses'. In: *Journal of Power Sources* 356 (2017), pp. 103–114. ISSN: 03787753. DOI: 10.1016/j.jpowsour.2017.04.084.

[133] Dubarry, M. et al. 'Synthesize battery degradation modes via a diagnostic and prognostic model'. In: *Journal of Power Sources* 219 (2012), pp. 204–216. ISSN: 03787753. DOI: 10.1016/j.jpowsour.2012.07.016.

[134] Barré, A. et al. 'A review on lithium-ion battery ageing mechanisms and estimations for automotive applications'. In: *Journal of Power Sources* 241 (2013), pp. 680–689. ISSN: 03787753. DOI: 10.1016/j.jpowsour.2013.05.040.

[135] Anseán, D. 'High power li-Ion battery performance: a mechanistic analysis of aging'. Dissertation. Universidad de Oviedo, 2015.

[136] Sarre, G. et al. 'Aging of lithium-ion batteries'. In: *Journal of Power Sources* 127.1-2 (2004), pp. 65–71. ISSN: 03787753. DOI: 10.1016/j.jpowsour.2003.09.008.

[137] Geisbauer, C. et al. 'Review—Review of Safety Aspects of Calendar Aged Lithium Ion Batteries'. In: *Journal of The Electrochemical Society* 167.9 (2020), p. 090523. ISSN: 0013-4651. DOI: 10.1149/1945-7111/ab89bf.

[138] Takami, N. et al. 'High-power and long-life lithium-ion batteries using lithium titanium oxide anode for automotive and stationary power applications'. In: *Journal of Power Sources* 244 (2013), pp. 469–475. ISSN: 03787753. DOI: 10.1016/j.jpowsour.2012.11.055.

[139] Hall, F. et al. 'Experimental investigation of the thermal and cycling behavior of a lithium titanate-based lithium-ion pouch cell'. In: *Journal of Energy Storage* 17 (2018), pp. 109–117. DOI: 10.1016/j.est.2018.02.012.

[140] Han, X. et al. 'Cycle Life of Commercial Lithium-Ion Batteries with Lithium Titanium Oxide Anodes in Electric Vehicles'. In: *Energies* 7.8 (2014), pp. 4895–4909. DOI: 10.3390/en7084895.

[141] Stroe, A.-I. et al. 'Accelerated Lifetime Testing of High Power Lithium Titanate Oxide Batteries'. In: *2018 IEEE Energy Conversion Congress and Exposition (ECCE)*. 2018, pp. 3857–3863. DOI: 10.1109/ECCE.2018.8557416.

[142] Svens, P. et al. 'Analysis of aging of commercial composite metal oxide – Li4Ti5O12 battery cells'. In: *Journal of Power Sources* 270 (2014), pp. 131–141. ISSN: 03787753. DOI: 10.1016/j.jpowsour.2014.07.050.

[143] Dubarry, M. and Devie, A. 'Battery durability and reliability under electric utility grid operations: Representative usage aging and calendar aging'. In: *Journal of Energy Storage* 18 (2018), pp. 185–195. DOI: 10.1016/j.est.2018.04.004.

[144] Fell, C. R. et al. 'Investigation of the Gas Generation in Lithium Titanate Anode Based Lithium Ion Batteries'. In: *Journal of The Electrochemical Society* 162.9 (2015), A1916–A1920. ISSN: 0013-4651. DOI: 10.1149/2.1091509jes.

[145] Nordh, T. *A Quest for the Unseen: Surface Layer Formation on Li4Ti5O12 Li-Ion Battery Anodes*. Digital Comprehensive Summaries of Uppsala Dissertations from the Faculty of Science and Technology. Uppsala: Uppsala University, 2017. ISBN: 978-91-513-0105-1.

[146] Dedryvère, R. et al. 'Electrode/Electrolyte Interface Reactivity in High-Voltage Spinel LiMn1.6Ni0.4O4/Li4Ti5O12 Lithium-Ion Battery'. In: *The Journal of Physical Chemistry C* 114.24 (2010), pp. 10999–11008. ISSN: 1932-7447. DOI: 10.1021/jp1026509.

[147] Belharouak, I. et al. 'Performance Degradation and Gassing of Li4Ti5O12/LiMn2O4 Lithium-Ion Cells'. In: *Journal of The Electrochemical Society* 159.8 (2012), A1165–A1170. ISSN: 0013-4651. DOI: 10.1149/2.013208jes.

[148] Gauthier, N. et al. 'Impact of the cycling temperature on electrode/electrolyte interfaces within Li4Ti5O12 vs LiMn2O4 cells'. In: *Journal of Power Sources* 448 (2020), p. 227573. ISSN: 03787753. DOI: 10.1016/j.jpowsour.2019.227573.

[149] Kitta, M. et al. 'Study of surface reaction of spinel Li4Ti5O12 during the first lithium insertion and extraction processes using atomic force microscopy and analytical transmission electron microscopy'. In: *Langmuir : the ACS journal of surfaces and colloids* 28.33 (2012), pp. 12384–12392. DOI: 10.1021/la301946h.

[150] He, Y.-B. et al. 'Effect of solid electrolyte interface (SEI) film on cyclic performance of Li4Ti5O12 anodes for Li ion batteries'. In: *Journal of Power Sources* 239 (2013), pp. 269–276. ISSN: 03787753. DOI: 10.1016/j.jpowsour.2013.03.141.

[151] Yoon, J. K. et al. 'Highly-Stable Li4Ti5O12 Anodes Obtained by Atomic-Layer-Deposited Al2O3'. In: *Materials (Basel, Switzerland)* 11.5 (2018). ISSN: 1996-1944. DOI: 10.3390/ma11050803.

[152] Han, C. et al. 'A review of gassing behavior in Li4Ti5O12 -based lithium ion batteries'. In: *Journal of Materials Chemistry A* 5.14 (2017), pp. 6368–6381. ISSN: 2050-7488. DOI: 10.1039/C7TA00303J.

[153] Aurbach, D. 'Review of selected electrode–solution interactions which determine the performance of Li and Li ion batteries'. In: *Journal of Power Sources* 89.2 (2000), pp. 206–218. ISSN: 03787753. DOI: 10.1016/S0378-7753(00)00431-6.

[154] Li, R. et al. 'Advanced composites of complex Ti-based oxides as anode materials for lithium-ion batteries'. In: *Advanced Composites and Hybrid Materials* 1.3 (2018), pp. 440–459. ISSN: 2522-0128. DOI: 10.1007/s42114-018-0038-1.

[155] Wang, Y.-Q. et al. 'Rutile-TiO2 nanocoating for a high-rate Li4Ti5O12 anode of a lithium-ion battery'. In: *Journal of the American Chemical Society* 134.18 (2012), pp. 7874–7879. DOI: 10.1021/ja301266w.

[156] Gao, Y. et al. 'Workfunction, a new viewpoint to understand the electrolyte/-electrode interface reaction'. In: *Journal of Materials Chemistry A* 3.46 (2015), pp. 23420–23425. ISSN: 2050-7488. DOI: 10.1039/C5TA07030A.

[157] Käbitz, S. et al. 'Cycle and calendar life study of a graphite|LiNi1/3Mn1/3Co1/3O2 Li-ion high energy system. Part A: Full cell characterization'. In: *Journal of Power Sources* 239 (2013), pp. 572–583. ISSN: 03787753. DOI: 10.1016/j.jpowsour.2013.03.045.

[158] Ecker, M. et al. 'Calendar and cycle life study of Li(NiMnCo)O2-based 18650 lithium-ion batteries'. In: *Journal of Power Sources* 248 (2014), pp. 839–851. ISSN: 03787753. DOI: 10.1016/j.jpowsour.2013.09.143.

[159] Gyenes, B. et al. 'Understanding Anomalous Behavior in Coulombic Efficiency Measurements on Li-Ion Batteries'. In: *Journal of The Electrochemical Society* 162.3 (2015), A278–A283. ISSN: 0013-4651. DOI: 10.1149/2.0191503jes.

[160] Lewerenz, M. et al. 'Systematic aging of commercial LiFePO 4 |Graphite cylindrical cells including a theory explaining rise of capacity during aging'. In: *Journal of Power Sources* 345 (2017), pp. 254–263. ISSN: 03787753. DOI: 10.1016/j.jpowsour.2017.01.133.

[161] Hüfner, T. et al. 'Lithium flow between active area and overhang of graphite anodes as a function of temperature and overhang geometry'. In: *Journal of Energy Storage* 24 (2019), p. 100790. DOI: 10.1016/j.est.2019.100790.

[162] Tang, M. et al. 'Two-Dimensional Modeling of Lithium Deposition during Cell Charging'. In: *Journal of The Electrochemical Society* 156.5 (2009), A390. ISSN: 0013-4651. DOI: 10.1149/1.3095513.

[163] Wilhelm, J. et al. 'Cycling capacity recovery effect: A coulombic efficiency and post-mortem study'. In: *Journal of Power Sources* 365 (2017), pp. 327–338. ISSN: 03787753. DOI: 10.1016/j.jpowsour.2017.08.090.

[164] Dagger, T. et al. 'Performance tuning of lithium ion battery cells with area-oversized graphite based negative electrodes'. In: *Journal of Power Sources* 396 (2018), pp. 519–526. ISSN: 03787753. DOI: 10.1016/j.jpowsour.2018.06.043.

[165] Schnell, J. and Reinhart, G. 'Quality Management for Battery Production: A Quality Gate Concept'. In: *Procedia CIRP* 57 (2016), pp. 568–573. ISSN: 22128271. DOI: 10.1016/j.procir.2016.11.098.

[166] Bank, T. et al. 'Lithium-ion cell requirements in a real-world 48 V system and implications for an extensive aging analysis'. In: *Journal of Energy Storage* 30 (2020), p. 101465. DOI: 10.1016/j.est.2020.101465.

[167] Schindler, M. J. 'Mehr-Batterie-System für Mikro-Hybrid-Fahrzeuge auf Basis von Blei-Säure- und Lithium-Ionen-Technologie'. Dissertation. 2014.

[168] Pischinger, S. and Seiffert, U., eds. *Vieweg Handbuch Kraftfahrzeugtechnik*. 8th ed. ATZ/MTZ-Fachbuch. Wiesbaden: Springer, 2016. ISBN: 978-3-658-09527-7. DOI: 10.1007/978-3-658-09528-4.

[169] Moseley, P. et al. '21 - Lead–acid batteries for future automobiles: Status and prospects'. In: *Lead-Acid Batteries for Future Automobiles*. Ed. by Jürgen Garche et al. Amsterdam: Elsevier, 2017, pp. 601–618. ISBN: 978-0-444-63700-0. DOI: 10.1016/B978-0-444-63700-0.00021-0.

[170] The European Commision. *Commission Directive (EU) 2017/2096 of 15 November 2017 amending Annex II to Directive 2000/53/EC of the European Parliament and of the Council on end-of life vehicles*. 2017.

[171] Gensch, C.-O. et al. *8th adaptation to scientific and technical progress of exemptions 2(c), 3 and 5 of Annex II to Directive 2000/53/EC (ELV)*. 2016. DOI: 10.2779/137742.

[172] Kollmeyer, P. J. and Jahns, T. M. 'Aging and performance comparison of absorbed glass matte, enhanced flooded, PbC, NiZn, and LiFePO4 12V start stop vehicle batteries'. In: *Journal of Power Sources* 441 (2019), p. 227139. ISSN: 03787753. DOI: 10.1016/j.jpowsour.2019.227139.

[173] Bao, R. et al. 'Effect of 48 V Mild Hybrid System Layout on Powertrain System Efficiency and Its Potential of Fuel Economy Improvement'. In: *SAE Technical Paper Series*. SAE Technical Paper Series. 2017. DOI: 10.4271/2017-01-1175.

[174] Dörsam, T. et al. 'Die neue Spannungsebene 48 V im Kraftfahrzeug'. In: *ATZelektronik* 7.1 (2012), pp. 20–25. ISSN: 1862-1791. DOI: 10.1365/s35658-012-0114-1.

[175] Hofmann, P. *Hybridfahrzeuge: Ein alternatives Antriebssystem für die Zukunft*. 2. Aufl. Wien: Springer, 2014. ISBN: 978-3-7091-1779-8. DOI: 10.1007/978-3-7091-1780-4.

[176] Mahr, B. '48 Volt technology – More than a mild hybrid'. In: *16. Internationales Stuttgarter Symposium*. Ed. by Bargende, M. et al. Proceedings. Wiesbaden: Springer Fachmedien Wiesbaden, 2016, pp. 1091–1100. ISBN: 978-3-658-13254-5. DOI: 10.1007/978-3-658-13255-2_81.

[177] Hoffmann, C.-A. 'Komplexitätsmanagement in der Automobilindustrie'. In: *Methodik zur Steuerung modularer Produktbaukästen*. Ed. by Hoffmann, C.-A. Wiesbaden: Springer Fachmedien Wiesbaden, 2018, pp. 27–38. ISBN: 978-3-658-20561-4. DOI: 10.1007/978-3-658-20562-1.

[178] Paul, B. S. 'Analyse der Ausfallwahrscheinlichkeiten von Lithium-Ionen-Energiespeichern in elektrifizierten Fahrzeugen'. Dissertation. Universität Ulm, 2015.

[179] Miller, J. M. 'Hybrid electric vehicle propulsion system architectures of the e-CVT type'. In: *IEEE Transactions on Power Electronics* 21.3 (2006), pp. 756–767. ISSN: 0885-8993. DOI: 10.1109/TPEL.2006.872372.

[180] Abdellahi, A. et al. 'Exploring the Opportunity Space For High-Power Li-Ion Batteries in Next-Generation 48V Mild Hybrid Electric Vehicles'. In: *SAE Technical Paper Series*. SAE Technical Paper Series. SAE International400 Commonwealth Drive, Warrendale, PA, United States, 2017. DOI: 10.4271/2017-01-1197.

[181] Kuypers, M. 'Application of 48 Volt for Mild Hybrid Vehicles and High Power Loads'. In: *SAE Technical Paper Series*. SAE Technical Paper Series. 2014. DOI: 10.4271/2014-01-1790.

[182] Anthony D. Wearing, James Haybittle, Ran Bao, James W. Baxter, Cedric Rouaud, Ozge Taskin. *2018 IEEE Energy Conversion Congress and Exposition (ECCE)*. Piscataway, NJ: IEEE, 2018. ISBN: 9781479973132.

[183] Bae, S. and Park, J.-W. 'A study on optimal operation strategy for mild hybrid electric vehicle based on hybrid energy storage system'. In: *Journal of Electrical Engineering and Technology* 13(2) (2018), pp. 631–636. DOI: 10.5370/JEET.2018.13.2.631.

[184] Liu, Z. et al. 'Impacts of Real-World Driving and Driver Aggressiveness on Fuel Consumption of 48V Mild Hybrid Vehicle'. In: *SAE International Journal of Alternative Powertrains* 5.2 (2016), pp. 249–258. ISSN: 2167-4205. DOI: 10.4271/2016-01-1166.

[185] Campestrini, C. et al. 'Validation and benchmark methods for battery management system functionalities: State of charge estimation algorithms'. In: *Journal of Energy Storage* 7 (2016), pp. 38–51. DOI: 10.1016/j.est.2016.05.007.

[186] Ecker, M. et al. 'Influence of operational condition on lithium plating for commercial lithium-ion batteries – Electrochemical experiments and post-mortem-analysis'. In: *Applied Energy* 206 (2017), pp. 934–946. ISSN: 03062619. DOI: 10.1016/j.apenergy.2017.08.034.

[187] Keil, P. et al. 'Calendar Aging of Lithium-Ion Batteries'. In: *Journal of The Electrochemical Society* 163.9 (2016), A1872–A1880. ISSN: 0013-4651. DOI: 10.1149/2.0411609jes.

[188] Wikner, E. and Thiringer, T. 'Extending Battery Lifetime by Avoiding High SOC'. In: *Applied Sciences* 8.10 (2018), p. 1825. DOI: 10.3390/app8101825.

[189] Ge, H. et al. 'Investigating Lithium Plating in Lithium-Ion Batteries at Low Temperatures Using Electrochemical Model with NMR Assisted Parameterization'. In: *Journal of The Electrochemical Society* 164.6 (2017), A1050–A1060. ISSN: 0013-4651. DOI: 10.1149/2.0461706jes.

[190] Bank, T. et al. 'Performance benchmark of state-of-the-art high-power lithium-ion cells and implications for their usability in low-voltage applications'. In: *Journal of Energy Storage* 36 (2021), p. 102383. ISSN: 2352-152X. DOI: 10.1016/j.est.2021.102383.

[191] Bank, T. et al. 'State of charge dependent degradation effects of lithium titanate oxide batteries at elevated temperatures: An in-situ and ex-situ analysis'. In: *Journal of Energy Storage* (2021 (in review)).

[192] Marongiu, A. et al. 'Comprehensive study of the influence of aging on the hysteresis behavior of a lithium iron phosphate cathode-based lithium ion battery – An experimental investigation of the hysteresis'. In: *Applied Energy* 171 (2016), pp. 629–645. ISSN: 03062619. DOI: 10.1016/j.apenergy.2016.02.086.

[193] Barai, A. et al. 'A study on the impact of lithium-ion cell relaxation on electrochemical impedance spectroscopy'. In: *Journal of Power Sources* 280 (2015), pp. 74–80. ISSN: 03787753. DOI: 10.1016/j.jpowsour.2015.01.097.

[194] Pop, V. et al. 'Modeling Battery Behavior for Accurate State-of-Charge Indication'. In: *Journal of The Electrochemical Society* 153.11 (2006), A2013. ISSN: 0013-4651. DOI: 10.1149/1.2335951.

[195] Barai, A. et al. 'A study of the open circuit voltage characterization technique and hysteresis assessment of lithium-ion cells'. In: *Journal of Power Sources* 295 (2015), pp. 99–107. ISSN: 03787753. DOI: 10.1016/j.jpowsour.2015.06.140.

[196] Barai, A. et al. 'A study of the influence of measurement timescale on internal resistance characterisation methodologies for lithium-ion cells'. In: *Scientific reports* 8.1 (2018), p. 21. DOI: 10.1038/s41598-017-18424-5.

[197] Huang, X. et al. 'A Review of Pulsed Current Technique for Lithium-ion Batteries'. In: *Energies* 13.10 (2020), p. 2458. DOI: 10.3390/en13102458.

[198] Lewerenz, M. et al. 'New method evaluating currents keeping the voltage constant for fast and highly resolved measurement of Arrhenius relation and capacity fade'. In: *Journal of Power Sources* 353 (2017), pp. 144–151. ISSN: 03787753. DOI: 10.1016/j.jpowsour.2017.03.136.

[199] Lewerenz, M. 'Dissection and quantitative description of aging of lithium-ion batteries using non-destructive methods validated by post-mortem-analyses'. Dissertation. Aachen: RWTH Aachen University, 2018. DOI: 10.18154/RWTH-2018-228663.

[200] Riviere, E. et al. 'Innovative Incremental Capacity Analysis Implementation for C/LiFePO4 Cell State-of-Health Estimation in Electrical Vehicles'. In: *Batteries* 5.2 (2019), p. 37. DOI: 10.3390/batteries5020037.

[201] Devie, A. et al. 'Overcharge Study in Li4Ti5O12 Based Lithium-Ion Pouch Cell'. In: *Journal of The Electrochemical Society* 162.6 (2015), A1033–A1040. ISSN: 0013-4651. DOI: 10.1149/2.0941506jes.

[202] Vernon-Parry, K. D. 'Scanning electron microscopy: an introduction'. In: *III-Vs Review* 13.4 (2000), pp. 40–44. ISSN: 09611290. DOI: 10.1016/S0961-1290(00)80006-X.

[203] Hofmann, S. *Auger- and X-Ray Photoelectron Spectroscopy in Materials Science*. Vol. 49. Berlin, Heidelberg: Springer Berlin Heidelberg, 2013. ISBN: 978-3-642-27380-3. DOI: 10.1007/978-3-642-27381-0.

[204] Schröer, P. et al. 'Adaptive modeling in the frequency and time domain of high-power lithium titanate oxide cells in battery management systems'. In: *Journal of Energy Storage* 32 (2020), p. 101966. DOI: 10.1016/j.est.2020.101966.

[205] Andre, D. et al. 'Characterization of high-power lithium-ion batteries by electrochemical impedance spectroscopy. I. Experimental investigation'. In: *Journal of Power Sources* 196.12 (2011), pp. 5334–5341. ISSN: 03787753. DOI: 10.1016/j.jpowsour.2010.12.102.

[206] Farmann, A. et al. 'Application-specific electrical characterization of high power batteries with lithium titanate anodes for electric vehicles'. In: *Energy* 112 (2016), pp. 294–306. ISSN: 03605442. DOI: 10.1016/j.energy.2016.06.088.

[207] Waag, W. et al. 'Experimental investigation of the lithium-ion battery impedance characteristic at various conditions and aging states and its influence on the application'. In: *Applied Energy* 102 (2013), pp. 885–897. ISSN: 03062619. DOI: 10.1016/j.apenergy.2012.09.030.

[208] Baccouche, I. et al. 'Improved OCV Model of a Li-Ion NMC Battery for Online SOC Estimation Using the Extended Kalman Filter'. In: *Energies* 10.6 (2017), p. 764. DOI: 10.3390/en10060764.

[209] Tatsukawa, E. et al. 'Application of Gibbs energy model to equilibrium potential for structural phase transition in lithium intercalation process'. In: *Fluid Phase Equilibria* 357 (2013), pp. 19–23. ISSN: 03783812. DOI: 10.1016/j.fluid.2013.01.013.

[210] Lavigne, L. et al. 'Lithium-ion Open Circuit Voltage (OCV) curve modelling and its ageing adjustment'. In: *Journal of Power Sources* 324 (2016), pp. 694–703. ISSN: 03787753. DOI: 10.1016/j.jpowsour.2016.05.121.

[211] Barai, A. et al. 'A comparison of methodologies for the non-invasive characterisation of commercial Li-ion cells'. In: *Progress in Energy and Combustion Science* 72 (2019), pp. 1–31. ISSN: 03601285. DOI: 10.1016/j.pecs.2019.01.001.

[212] Karthikeyan, D. K. et al. 'Thermodynamic model development for lithium intercalation electrodes'. In: *Journal of Power Sources* 185.2 (2008), pp. 1398–1407. ISSN: 03787753. DOI: 10.1016/j.jpowsour.2008.07.077.

[213] Srinivasan, V. and Newman, J. 'Discharge Model for the Lithium Iron-Phosphate Electrode'. In: *Journal of The Electrochemical Society* 151.10 (2004), A1517. ISSN: 0013-4651. DOI: 10.1149/1.1785012.

[214] Dreyer, W. et al. 'The thermodynamic origin of hysteresis in insertion batteries'. In: *Nature materials* 9.5 (2010), pp. 448–453. ISSN: 1476-1122. DOI: 10.1038/nmat2730.

[215] Meethong, N. et al. 'Strain Accommodation during Phase Transformations in Olivine-Based Cathodes as a Materials Selection Criterion for High-Power Rechargeable Batteries'. In: *Advanced Functional Materials* 17.7 (2007), pp. 1115–1123. ISSN: 1616301X. DOI: 10.1002/adfm.200600938.

[216] Pyun, S.-I. and Ryu, Y.-G. 'Lithium transport through graphite electrodes that contain two stage phases'. In: *Journal of Power Sources* 70.1 (1998), pp. 34–39. ISSN: 03787753. DOI: 10.1016/S0378-7753(97)02616-5.

[217] Ovejas, V. J. and Cuadras, A. 'Effects of cycling on lithium-ion battery hysteresis and overvoltage'. In: *Scientific reports* 9.1 (2019), p. 14875. DOI: 10.1038/s41598-019-51474-5.

[218] Farmann, A. and Sauer, D. U. 'A study on the dependency of the open-circuit voltage on temperature and actual aging state of lithium-ion batteries'. In: *Journal of Power Sources* 347 (2017), pp. 1–13. ISSN: 03787753. DOI: 10.1016/j.jpowsour.2017.01.098.

[219] Barai, A. et al. 'The influence of temperature and charge-discharge rate on open circuit voltage hysteresis of an LFP Li-ion battery'. In: *2016 IEEE Transportation Electrification Conference and Expo (ITEC)*. 2016, pp. 1–4. DOI: 10.1109/ITEC.2016.7520299.

[220] Ovejas, V. J. and Cuadras, A. 'State of charge dependency of the overvoltage generated in commercial Li-ion cells'. In: *Journal of Power Sources* 418 (2019), pp. 176–185. ISSN: 03787753. DOI: 10.1016/j.jpowsour.2019.02.046.

[221] Shin, H. C. et al. 'Electrochemical properties of carbon-coated LiFePO4 cathode using graphite, carbon black, and acetylene black'. In: *Electrochimica Acta* 52.4 (2006), pp. 1472–1476. ISSN: 00134686. DOI: 10.1016/j.electacta.2006.01.078.

[222] Hess, A. et al. 'Determination of state of charge-dependent asymmetric Butler–Volmer kinetics for LixCoO2 electrode using GITT measurements'. In: *Journal of Power Sources* 299 (2015), pp. 156–161. ISSN: 03787753. DOI: 10.1016/j.jpowsour.2015.07.080.

[223] Grimsmann, F. et al. 'Hysteresis and current dependence of the graphite anode color in a lithium-ion cell and analysis of lithium plating at the cell edge'. In: *Journal of Energy Storage* 15 (2018), pp. 17–22. DOI: 10.1016/j.est.2017.10.015.

[224] Lewerenz, M. et al. 'Irreversible calendar aging and quantification of the reversible capacity loss caused by anode overhang'. In: *Journal of Energy Storage* 18 (2018), pp. 149–159. DOI: 10.1016/j.est.2018.04.029.

[225] Dubarry, M. et al. 'Cell degradation in commercial LiFePO4 cells with high-power and high-energy designs'. In: *Journal of Power Sources* 258 (2014), pp. 408–419. ISSN: 03787753. DOI: 10.1016/j.jpowsour.2014.02.052.

[226] Chauque, S. et al. 'Lithium titanate as anode material for lithium ion batteries: Synthesis, post-treatment and its electrochemical response'. In: *Journal of Electroanalytical Chemistry* 799 (2017). DOI: 10.1016/j.jelechem.2017.05.052.

[227] Christensen, J. 'Modeling Diffusion-Induced Stress in Li-Ion Cells with Porous Electrodes'. In: *Journal of The Electrochemical Society* 157.3 (2010), A366. ISSN: 0013-4651. DOI: 10.1149/1.3269995.

[228] Schipper, F. et al. 'Review-Recent Advances and Remaining Challenges for Lithium Ion Battery Cathodes'. In: *Journal of The Electrochemical Society* 164.1 (2016), A6220–A6228. ISSN: 0013-4651. DOI: 10.1149/2.0351701jes.

[229] Takami, N. et al. 'Lithium Diffusion in Li4/3Ti5/3O4 Particles during Insertion and Extraction'. In: *Journal of The Electrochemical Society* 158.6 (2011), A725. ISSN: 0013-4651. DOI: 10.1149/1.3574037.

[230] Li, T. et al. 'Degradation Mechanisms and Mitigation Strategies of Nickel-Rich NMC-Based Lithium-Ion Batteries'. In: *Electrochemical Energy Reviews* 3.1 (2020), pp. 43–80. ISSN: 2520-8489. DOI: 10.1007/s41918-019-00053-3.

[231] Hatsukade, T. et al. 'Origin of Carbon Dioxide Evolved during Cycling of Nickel-Rich Layered NCM Cathodes'. In: *ACS applied materials & interfaces* 10.45 (2018), pp. 38892–38899. DOI: 10.1021/acsami.8b13158.

A Own publications

Within the course of this scientific work, several publications have been prepared which are listed below. Content from these publications is used for this thesis. This is in line with the rules for dissertation of the faculty for Electrical Engineering and Information Technology at RWTH Aachen University and has been agreed with Prof. Dirk Uwe Sauer, the major supervisor of this thesis. Text elements, graphs, pictures or tables from these publications are not explicitly cited within the thesis, as far as they are mainly created by me. If such elements in the listed publications are mainly created by the co-authors, a direct link to the publication is given.

A.1 Scientific journals

[1] T. Bank, S. Klamor, D. U. Sauer. 'Lithium-ion cell requirements in a real-world 48 V system and implications for an extensive aging analysis'. In: Journal of Energy Storage 30 (2020), p. 101465. doi: 10.1016/j.est.2020.101465.

[2] T. Bank, J. Feldmann, S. Klamor, S. Bihn, D. U. Sauer. 'Extensive aging analysis of high-power lithium titanate oxide batteries: Impact of the passive electrode effect'. In: Journal of Power Sources 473 (2020). issn: 03787753. doi: 10.1016/j.jpowsour.2020.228566.

[3] T. Bank, S. Klamor, N. Löffler, D. U. Sauer. 'Performance benchmark of state-of-the-art high-power lithium-ion cells and implications for their usability in low-voltage applications'. In: Journal of Energy Storage 36 (2021), p. 102383. doi: 10.1016/j.est.2021.102383.

[4] T. Bank, L. Alsheimer, N. Löffler, D. U. Sauer. 'State of charge dependent degradation effects of lithium titanate oxide batteries at elevated temperatures: An in-situ and ex-situ analysis'. In: Journal of Energy Storage [in review].

A.2 Conferences

- T. Bank, D. U. Sauer. 'Lithium-ion cell requirements in a real-world 48 V system and implications for an extensive aging analysis'. Kraftwerk Batterie, Aachen, Germany, 2019.

- T. Bank, S. Klamor, D. U. Sauer. ‘Electrical characterisation of state-of-the-art high-power lithium-ion cells and implications for the usability in low-voltage applications (12 V/48 V)’. Advanced Automotive Battery Conference, Wiesbaden, Germany, 2020.

B Guided student theses

Within the course of this scientific work, the following student theses were developed. I specified the topic for these theses and supervised them contentwise and scientifically. Some of the topics are sub-aspects of my dissertation and thus can be found in this thesis. In case of corresponding contents the student theses are not explicitly referenced. Other student theses, which were not written under my supervision, are cited like all other references.

B.1 Master theses

- Feldmann, Jan: 'General analysis and simulation of aging effects in high-power lithium-ion cells used in a 48 V electrical system', master thesis, RWTH Aachen University, 10/2019.
- Strothotte, Philipp: 'Comparison of the aging behavior of different high power lithium-ion batteries with multiple cell chemistries based on semi-empirical simulation models', master thesis, RWTH Aachen University, 12/2020.

B.2 Student assistants

My scientific work was supported by the following student assistants who worked under my scientific supervision:

- Jan Feldmann
- Nataliia Moskvina

ABISEA Band 1
Eßer, Albert
Berührungslose, kombinierte Energie- und Informationsübertragung für bewegliche Systeme
1. Aufl. 1992, 129 S.
ISBN 3-86073-046-0

ABISEA Band 2
Vogel, Ulrich
Entwurf und Beurteilung von Verfahren zur Hochausnutzung des Rad-Schiene-Kraftschlusses durch Triebfahrzeuge
1. Aufl. 1992, 131 S.
ISBN 3-86073-060-6

ABISEA Band 3
Reckhorn, Thomas
Stromeinprägendes Antriebssystem mit fremderregter Synchronmaschine
1. Aufl. 1992, 128 S.
ISBN 3-86073-061-4

ABISEA Band 4
Ackva, Ansgar
Spannungseinprägendes Antriebssystem mit Synchronmaschine und direkter Stromregelung
1. Aufl. 1992, 137 S.
ISBN 3-86073-062-2

ABISEA Band 5
Mertens, Axel
Analyse des Oberschwingungsverhaltens von taktsynchronen Delta - Modulationsverfahren zur Steuerung von Pulsstromrichtern bei hoher Taktzahl
1. Aufl. 1992, 178 S.
ISBN 3-86073-069-X

ABISEA Band 6
Geuer, Wolfgang
Untersuchungen über das Alterungsverhalten von Blei-Akkumulatoren
1. Aufl. 1993, 97 S.
ISBN 3-86073-097-5

ABISEA Band 7
Langheim, Jochen
Einzelradantrieb für Elektrostraßenfahrzeuge
1. Aufl. 1993, 213 S.
ISBN 3-86073-123-8
(vergriffen)

ABISEA Band 8
Fetz, Joachim
Fehlertolerante Regelung eines Asynchron-Doppelantriebes für ein Elektrospeicherfahrzeug
1. Aufl. 1993, 136 S.
ISBN 3-86073-124-6
(vergriffen)

ABISEA Band 9
Schülting, Ludger
Optimierte Auslegung induktiver Bauelemente für den Mittelfrequenzbereich
1. Aufl. 1993, 126 S.
ISBN 3-86073-174-2
(vergriffen)

ABISEA Band 10
Skudelny, H.-Ch.
Stromrichtertechnik
4. Aufl. 1997, 259 S.
ISBN 3-86073-189-0

ABISEA Band 11
Skudelny, H.-Ch.
Elektrische Antriebe
3. Aufl. 1997, 124 S.
ISBN 3-86073-231-5

ABISEA Band 12
Schöpe, Friedhelm
Batterie-Management für Nickel-Cadmium Akkumulatoren
1. Aufl. 1994, 148 S.
ISBN 3-86073-232-3
(vergriffen)

ABISEA Band 13
v. d. Weem, Jürgen
Schmalbandige aktive Filter für Schienentriebfahrzeuge am Gleichspannungsfahrdraht
1. Aufl. 1995, 126 S.
ISBN 3-86073-233-1

ABISEA Band 14
Backhaus, Klaus
Spannungseinprägendes Direktantriebssystem mit schnelllaufender geschalteter Reluktanzmaschine
1. Aufl. 1995, 146 S.
ISBN 3-86073-234-X
(vergriffen)

ABISEA Band 15
Reinold, Harry
Optimierung dreiphasiger Pulsdauermodulationsverfahren
1. Aufl. 1996, 107 S.
ISBN 3-86073-235-8

ABISEA Band 16
Köpken, Hans-Georg
Regelverfahren für Parallelschwingkreisumrichter
1. Aufl. 1996, 125 S.
ISBN 3-86073-236-6

ABISEA Band 17
Mauracher, Peter
Modellbildung und Verbundoptimierung bei Elektrostraßenfahrzeugen
1. Aufl. 1996, 192 S.
ISBN 3-86073-237-4

ABISEA Band 18
Protiwa, Franz-Ferdinand
Vergleich dreiphasiger Resonanz-Wechselrichter in Simulation und Messung
1. Aufl. 1997, 178 S.
ISBN 3-86073-238-2

ABISEA Band 19
Brockmeyer, Ansgar
Dimensionierungswerkzeug für magnetische Bauelemente in Stromrichteranwendungen
1. Aufl. 1997, 175 S.
ISBN 3-86073-239-0

ABISEA Band 20
Apeldoorn, Oscar
Simulationsgestützte Bewertung von Steuerverfahren für netzgeführte Stromrichter mit verringerter Netzrückwirkung
1. Aufl. 1997, 134 S.
ISBN 3-86073-680-9

ABISEA Band 21
Lohner, Andreas
Batteriemanagement für verschlossene Blei-Batterien am Beispiel von Unterbrechungsfreien Stromversorgungen
1. Aufl. 1998, 126 S.
ISBN 3-86073-681-7

ABISEA Band 22
Reinert, Jürgen
Optimierung der Betriebseigenschaften von Antrieben mit geschalteter Reluktanzmaschine
1. Aufl. 1998, 153 S.
ISBN 3-86073-682-5

ABISEA Band 23
Nagel, Andreas
Leitungsgebundene Störungen in der Leistungselektronik: Entstehung, Ausbreitung und Filterung
1. Aufl. 1999, 140 S.
ISBN 3-86073-683-3

ABISEA Band 24
Menne, Marcus
Drehschwingungen im Antriebsstrang von Elektrostraßenfahrzeugen - Analyse und aktive Dämpfung
1. Aufl. 2001, 169 S.
ISBN 3-86073-684-1

ABISEA Band 25
von Bloh, Jochen
Multilevel-Umrichter zum Einsatz in Mittelspannungs-Gleichspannungs-Übertragungen
1. Aufl. 2001, 137 S.
ISBN 3-86073-685-X

ABISEA Band 26
Karden, Eckhard
Using low-frequency impedance spectroscopy for characterization, monitoring, and modeling of industrial batteries
1. Aufl. 2002, 137 S.
ISBN 3-8265-9766-4

ABISEA Band 27
Karipidis, Claus-Ulrich
A Versatile DSP/ FPGA Structure optimized for Rapid Prototyping and Digital Real-Time Simulation of Power Electronic and Electrical Drive Systems
1. Aufl. 2001, 164 S.
ISBN 3-8265-9738-9

ABISEA Band 28
Kahlen, Klemens
Regelungsstrategien für permanentmagnetische Direktantriebe mit mehreren Freiheitsgraden
1. Aufl. 2002, 154 S.
ISBN 3-8322-1222-1

ABISEA Band 29
Inderka, Robert B.
Direkte Drehmomentregelung Geschalteter Reluktanzantriebe
1. Aufl. 2003, 182 S.
ISBN 3-8322-1175-6

ABISEA Band 30
Schröder, Stefan
Circuit-Simulation Models of High-Power Devices Based on Semiconductor Physics
1. Aufl. 2003, 123 S.
ISBN 3-8322-1250-7

ABISEA Band 31
Buller, Stephan
Impedance-Based Simulation Models for Energy Storage Devices in Advanced Automotive Power Systems
1. Aufl. 2003, 138 S.
ISBN 3-8322-1225-6

ABISEA Band 32
Schönknecht, Andreas
Topologien und Regelungsstrategien für das induktive Erwärmen mit hohen Frequenz-Leistungsprodukten
1. Aufl. 2004, 157 S.
ISBN 3-8322-2408-4

ABISEA Band 33
Tolle, Tobias
Konvertertopologien für ein aufwandsarmes, zweistufiges Schaltnetzteil zum Laden von Batterien aus dem Netz
1. Aufl. 2004, 148 S.
ISBN 3-8322-2676-1

ABISEA Band 34
Götting, Gunther
Dynamische Antriebsregelung von Elektrostraßenfahrzeugen unter Berücksichtigung eines schwingungsfähigen Antriebsstrangs
1. Aufl. 2004, 157 S.
ISBN 3-8322-2804-7

ABISEA Band 35
Dieckerhoff, Sibylle
Transformatorlose Stromrichterschaltungen für Bahnfahrzeuge am 16 2/3Hz Netz
1. Aufl. 2004, 147 S.
ISBN 3-8322-3094-7

ABISEA Band 36
Hu, Jing
Bewertung von DC-DC-Topologien und Optimierung eines DC-DC-Leistungsmoduls für das 42-V-Kfz-Bordnetz
1. Aufl. 2004, 148 S.
ISBN 3-8322-3201-X

ABISEA Band 37
Detjen, Dirk-Oliver
Characterization and Modeling of Si-Si Bonded Hydrophobie Interfaces for Novel High-Power BIMOS Devices
1. Aufl. 2004, 135 S.
ISBN 3-8322-2963-9

ABISEA Band 38
Walter, Jörg
Simulationsbasierte Zuverlässigkeitsanalyse in der modernen Leistungselektronik
1. Aufl. 2004, 121 S.
ISBN 3-8322-3481-0

ABISEA Band 39
Schwarzer, Ulrich
IGBT versus GCT in der Mittelspannungsanwendung - ein experimenteller und simulativer Vergleich
1. Aufl. 2005, 170 S.
ISBN 3-8322-4489-1

ABISEA Band 40
Bartram, Markus
IGBT-Umrichtersysteme für Windkraftanlagen: Analyse der Zyklenbelastung, Modellbildung, Optimierung und Lebensdauervorhersage
1. Aufl. 2006, 185 S.
ISBN 3-8322-5039-5

ABISEA Band 41
Ponnaluri, Srinivas
Generalized Design, Analysis and Control of Grid side converters with integrated UPS or Islanding functionality
1. Aufl. 2006, 163 S.
ISBN 3-8322-5281-9

ABISEA Band 42
Jacobs, Joseph
Multi-Phase Series Resonant DC-to-DC Converters
1. Aufl. 2006, 185 S.
ISBN 3-8322-5532-X

ABISEA Band 43
Linzen, Dirk
Impedance-Based Loss Calculation and Thermal Modeling of Electrochemical Energy Storage Devices for Design Considerations of Automotive Power Systems
1. Aufl. 2006, 185 S.
ISBN 3-8322-5706-3

ABISEA Band 44
Fiedler, Jens
Design of Low-Noise Switched Reluctance Drives
1. Aufl. 2007, 176 S.
ISBN 978-3-8322-5864-1

ABISEA Band 45
Fuengwarodsakul, Nisai
Predictive PWM-based Direct Instantaneous Torque Control for Switched Reluctance Machines
1. Aufl. 2007, 141 S.
ISBN 978-3-8322-6210-5

ABISEA Band 46
Meyer, Christoph
Key Components for Future Offshore DC Grids
1. Aufl. 2007, 187 S.
ISBN 978-3-8322-6571-7

ABISEA Band 47
Fujii, Kansuke
Characterization and Optimization of Soft-Switched Multi-Level Converters for STATCOMs
1. Aufl. 2008, 199 S.
ISBN 978-3-8322-6981-4

ABISEA Band 48
Carstensen, Christian
Eddy Currents in Windings of Switched Reluctance Machines
1. Aufl. 2008, 179 S.
ISBN 978-3-8322-7118-3

ABISEA Band 49
Bohlen, Oliver
Impedance-based battery monitoring
1. Aufl. 2008, 190 S.
ISBN 978-3-8322-7606-5

ABISEA Band 50
Thele, Marc
A contribution to the modelling of the charge acceptance of lead-acid batteries - using frequency and time domain based concepts
1. Aufl. 2008, 165 S.
ISBN 978-3-8322-7659-1

ABISEA Band 51
König, Andreas
High Temperature DC-to-DC Converters for Downhole Applications
1. Aufl. 2009, 154 S.
ISBN 978-3-8322-8489-3

ABISEA Band 52
Dick, Christian Peter
Multi-Resonant Converters as Photovoltaic Module-Integrated Maximum Power Point Tracker
1. Aufl. 2010, 182 S.
ISBN 978-3-8322-9199-0

ABISEA Band 53
Kowal, Julia
Spatially resolved impedance of nonlinear inhomogeneous devices: using the example of lead-acid batteries
1. Aufl. 2010, 203 S.
ISBN 978-3-8322-9483-0

ABISEA Band 54
Roscher, Michael Andreas
Zustandserkennung von LiFeP04-Batterien für Hybrid- und Elektrofahrzeuge
1. Aufl. 2011, 186 S.
ISBN 978-3-8322-9738-1

ABISEA Band 55
Hirschmann, Dirk
Highly Dynamic Piezoelectric Positioning
1. Aufl. 2011, 146 S.
ISBN 978-3-8322-9746-6

ABISEA Band 56
Rigbers, Klaus
Highly Efficient Inverter Architectures for Three-Phase Grid Connection of Photovoltaic Generators
1. Aufl. 2011, 244 S.
ISBN 978-3-8322-9816-9

ABISEA Band 57
Kasper, Knut
Analysis and Control of the Acoustic Behavior of Switched Reluctance Drives
1. Aufl. 2011, 205 S.
ISBN 978-3-8322-9869-2

ABISEA Band 58
Köllensperger, Peter
The Internally Commutated Thyristor - Concept, Design and Application
1. Aufl. 2011, 214 S.
ISBN 978-3-8322-9909-5

ABISEA Band 59
Schoenen, Timo
Einsatz eines DC/DC-Wandlers zur Spannungsanpassung zwischen Antrieb und Energiespeicher in Elektro-und Hybridfahrzeugen
1. Aufl. 2011, 128 S.
ISBN 978-3-8440-0622-3

ABISEA Band 60
Hennen, Martin
Switched Reluctance Direct Drive with Integrated Distributed Inverter
1. Aufl. 2012, 141 S.
ISBN 978-3-8440-0731-2

ABISEA Band 61
van Treek, Daniel
Position Sensorless Torque Control of Switched Reluctance Machines
1. Aufl. 2012, 144 S.
ISBN 978-3-8440-1014-5

ABISEA Band 62
Bragard, Michael
The Integrated Emitter Turn-Off Thyristor. An Innovative MOS-Gated High-Power Device
1. Aufl. 2012, 164 S.
ISBN 978-3-8440-1152-4

ABISEA Band 63
Gerschler, Jochen B.
Ortsaufgelöste Modellbildung von Lithium-Ionen-Systemen unter spezieller Berücksichtigung der Batteriealterung
1. Aufl. 2012, 334 S.
ISBN 978-3-8440-1307-8

ABISEA Band 64
Neuhaus, Christoph R.
Schaltstrategien für Geschaltete Reluktanzantriebe mit kleinem Zwischenkreis
1. Aufl. 2012, 133 S.
ISBN 978-3-8440-1487-7

ABISEA Band 65
Butschen, Thomas
Dual-ICT- A Clever Way to Unite Conduction and Switching Optimized Properties in a Single Wafer
1. Aufl. 2012, 168 S.
ISBN 978-3-8440-1771-7

ABISEA Band 66
Plum, Thomas
Design and Realization of High-Power MOS Turn-Off Thyristors
1. Aufl. 2013, 113 S.
ISBN 978-3-8440-1884-4

ABISEA Band 67
Kiel, Martin
Impedanzspektroskopie an Batterien unter besonderer Berücksichtigung von Batteriesensoren für den Feldeinsatz
1. Aufl. 2013, 226 S.
ISBN 978-3-8440-1973-5

ABISEA Band 68
Brauer, Helge
Schnelldrehender Geschalteter Reluktanzantrieb mit extremem Längendurchmesserverhältnis
1. Aufl. 2013, 192 S.
ISBN 978-3-8440-2345-9

ABISEA Band 69
Thomas, Stephan
A Medium-Voltage Multi-Level DC/DC Converter with High Voltage Transformation Ratio
1. Aufl. 2014, 226 S.
ISBN 978-3-8440-2605-4

ABISEA Band 70
Richter, Sebastian
Digitale Regelung von PWM Wechselrichtern mit niedrigen Trägerfrequenzen
1. Aufl. 2014, 126 S.
ISBN 978-3-8440-2641-2

ABISEA Band 71
Bösing, Matthias
Acoustic Modeling of Electrical Drives - Noise and Vibration Synthesis based on Force Response Superposition
1. Aufl. 2014, 188 S.
ISBN 978-3-8440-2752-5

ABISEA Band 72
Waag, Wladislaw
Adaptive algorithms for monitoring of lithium-ion batteries in electric vehicles
1. Aufl. 2014, 232 S.
ISBN 978-3-8440-2976-5

ABISEA Band 73
Sanders, Tilman
Spatially Resolved Electrical In-Situ Measurement Techniques for Fuel Cells
1. Aufl. 2014, 126 S.
ISBN 978-3-8440-3121-8

ABISEA Band 74
Baumhöfer, Thorsten
Statistische Betrachtung experimenteller Alterungsuntersuchungen an Lithium-Ionen Batterien
1. Aufl. 2015, 157 S.
ISBN 978-3-8440-3423-3

ABISEA Band 75
Andre, Dave
Systematic Characterization of Ageing Factors for High-Energy Lithium-Ion Cells and Approaches for Lifetime Modelling Regarding an Optimized Operating Strategy in Automotive Applications
1. Aufl. 2015, 196 S.
ISBN 978-3-8440-3587-2

ABISEA Band 76
Merei, Ghada
Optimization of off-grid hybrid PV-wind-diesel power supplies with multi-technology battery systems taking into account battery aging
1. Aufl. 2015, 184 S.
ISBN 978-3-8440-4148-4

ABISEA Band 77
Schulte, Dominik
Modellierung und experimentelle Validierung der Alterung von Blei-Säure Batterien durch inhomogene Stromverteilung und Säureschichtung
1. Aufl. 2016, 165 S.
ISBN 978-3-8440-4216-0

ABISEA Band 78
Schenk, Mareike
Simulative Untersuchung der Wicklungsverluste in Geschalteten Reluktanzmaschinen
1. Aufl. 2016, 126 S.
ISBN 978-3-8440-4282-5

ABISEA Band 79
Wang, Yu
Development of Dynamic Models with Spatial Resolution for Electrochemical Energy Converters as Basis for Control and Management Strategies
1. Aufl. 2016, 188 S.
ISBN 978-3-8440-4303-7

ABISEA Band 80
Ecker, Madeleine
Lithium Plating in Lithium-Ion Batteries:
An Experimental and Simulation Approach
1. Aufl. 2016, 154 S.
ISBN 978-3-8440-4525-3

ABISEA Band 81
Zhou, Wei
Modellbasierte Auslegungsmethode von Temperierungssystemen für Hochvolt-Batterien in Personenkraftfahrzeugen
1. Aufl. 2016, 175 S.
ISBN 978-3-8440-4589-5

ABISEA Band 82
Lunz, Benedikt
Deutschlands Stromversorgung im Jahr 2050
Ein szenariobasiertes Verfahren zur vergleichenden Bewertung von Systemvarianten und Flexibilitätsoptionen
1. Aufl. 2016, 187 S.
ISBN 978-3-8440-4627-4

ABISEA Band 83
Hofmann, Andreas G.
Direct Instantaneous Force Control: Key to Low-Noise Switched Reluctance Traction Drives
1. Aufl. 2016, 228 S.
ISBN 978-3-8440-4715-8

ABISEA Band 84
Budde-Meiwes, Heide
Dynamic Charge Acceptance of Lead-Acid Batteries for Micro-Hybrid Automotive Applications
1. Aufl. 2016, 157 S.
ISBN 978-3-8440-4733-2

ABISEA Band 85
Engel, Stefan P.
Thyristor-Based High-Power On-Load Tap Changers Control under Harsh Load Conditions
1. Aufl. 2016, 156 S.
ISBN 978-3-8440-4986-2

ABISEA Band 86
Van Hoek, Hauke
Design and Operation Considerations of Three-Phase Dual Active Bridge Converters for Low-Power Applications with Wide Voltage Ranges
1. Aufl. 2017, 231 S.
ISBN 978-3-8440-5011-0

ABISEA Band 87
Diekhans, Tobias
Wireless Charging of Electric Vehicles - a Pareto-Based Comparison of Power Electronic Topologies
1. Aufl. 2017, 151 S.
ISBN 978-3-8440-5048-6

ABISEA Band 88
Lehner, Susanne
Reliability Assessment of Lithium-Ion Battery Systems with Special Emphasis on Cell Performance Distribution
1. Aufl. 2017, 184 S.
ISBN 978-3-8440-5090-5

ABISEA Band 89
Käbitz, Stefan
Untersuchung der Alterung von Lithium-Ionen-Batterien mittels Elektroanalytik und elektrochemischer Impedanzspektroskopie
1. Aufl. 2016, 258 S.
DOI: 10.18154/RWTH-2016-12094

ABISEA Band 90
Witzenhausen, Heiko
Elektrische Batteriespeichermodelle: Modellbildung, Parameteridentifikation und Modellreduktion
1. Aufl. 2017, 266 S.
DOI: 10.18154/RWTH-2017-03437

ABISEA Band 91
Münnix, Jens
Einfluss von Stromstärke und Zyklentiefe auf graphitische Anoden
1. Aufl. 2017, 171 S.
DOI: 10.18154/RWTH-2017-01915

ABISEA Band 92
Pilatowicz, Grzegorz
Failure Detection and Battery Management Systems of Lead-Acid Batteries for Micro-Hybrid Vehicles
1. Aufl. 2017, 212 S.
DOI: 10.18154/RWTH-2017-09156

ABISEA Band 93
Drillkens, Julia
Aging in Electrochemical Double Layer Capacitors: An Experimental and Modeling Approach
1. Aufl. 2017, 179 S.
DOI: 10.18154/RWTH-2018-223434

ABISEA Band 94
Magnor, Dirk
Globale Optimierung netzgekoppelter PV-Batteriesysteme unter besonderer Berücksichtigung der Batteriealterung
1. Aufl. 2017, 210 S.
DOI: 10.18154/RWTH-2017-06592

ABISEA Band 95
Iliksu, Merve
Elucidation and Comparison of the Effects of Lithium Salts on Discharge Chemistry of Nonaqueous Li-O_2 Batteries
1. Aufl. 2018, 160 S.
DOI: 10.18154/RWTH-2018-223782

ABISEA Band 96
Schmalstieg, Johannes
Physikalisch-elektrochemische Simulation von Lithium-Ionen-Batterien: Implementierung, Parametrierung und Anwendung
1. Aufl. 2017, 168 S.
DOI: 10.18154/RWTH-2017-04693

ABISEA Band 97
Soltau, Nils
High-Power Medium-Voltage DC-DC Converters: Design, Control and Demonstration
1. Aufl. 2017, 176 S.
DOI: 10.18154/RWTH-2017-04084

ABISEA Band 98
Stieneker, Marco
Analysis of Medium-Voltage Direct-Current Collector Grids in Offshore Wind Parks
1. Aufl. 2017, 144 S.
DOI: 10.18154/RWTH-2017-04667

ABISEA Band 99
Masomtob, Manop
A New Conceptual Design of Battery Cell with an Internal Cooling Channel
1. Aufl. 2017, 167 S.
DOI: 10.18154/RWTH-2018-223281

ABISEA Band 100
Marongiu, Andrea
Performance and Aging Diagnostic on Lithium Iron Phosphate Batteries for Electric Vehicles and Vehicle-to-Grid Strategies
1. Aufl. 2017, 222 S.
DOI: 10.18154/RWTH-2017-09944

ABISEA Band 101
Gitis, Alexander
Flaw detection in the coating process of lithium-ion battery electrodes with acoustic guided waves
1. Aufl. 2017, 109 S.
DOI: 10.18154/RWTH-2017-099519

ABISEA Band 102
Neeb, Christoph
Packaging Technologies for Power Electronics in Automotive Applications
1. Aufl. 2017, 132 S.
DOI: 10.18154/RWTH-2018-224569

ABISEA Band 103
Adler, Felix
A Digital Hardware Platform for Distributed Real-Time Simulation of Power Electronic Systems
1. Aufl. 2017, 156 S.
DOI: 10.18154/RWTH-2017-10761

ABISEA Band 104
Becker, Jan
Flexible Dimensionierung und Optimierung hybrider Lithium-Ionenbatterie-speichersysteme mit verschiedenen Auslegungs-zielen
1. Aufl., 2017, 157 S.
DOI: 10.18154/RWTH-2017-09278

ABISEA Band 105
Warnecke, Alexander J.
Degradation Mechanisms in NMC Based Lithium-Ion Batteries
1. Aufl. 2017, 158 S.
DOI: 10.18154/RWTH-2017-09646

ABISEA Band 106
Taraborrelli, Silvano
Bidirectional Dual Active Bridge Converter using a Tap Changer for Extended Voltage Ranges
1. Aufl. 2017, 94 S.
DOI: 10.18154/RWTH-2018-228242

ABISEA Band 107
Sarriegi, Garikoitz
SiC and GaN Semiconductors: The Future Enablers of Compact and Efficient Converters for Electromobility
1. Aufl. 2017, 106 S.
DOI: 10.18154/RWTH-2018-227548

ABISEA Band 108
Senol, Murat
Drivetrain Integrated Dc-Dc Converters utilizing Zero Sequence Currents
1. Aufl. 2017, 134 S.
DOI: 10.18154/RWTH-2018-226170

ABISEA Band 109
Kojima, Tetsuya
Efficiency Optimized Control of Switched Reluctance Machines
1. Aufl. 2017, 142 S.
DOI: 10.18154/RWTH-2018-226697

ABISEA Band 110
Lewerenz, Meinert
Dissection and Quantitative Description of Aging of Lithium-Ion Batteries Using Non-Destructive Methods Validated by Post-Mortem-Analyses
1. Aufl. 2018, 139 S.
DOI: 10.18154/RWTH-2018-228663

ABISEA Band 111
Büngeler, Johannes
Optimierung der Verfügbarkeit und der Lebensdauer von Traktionsbatterien für den Einsatz in Flurförderfahrzeugen
1. Aufl. 2018, 171 S.
DOI: 10.18154/RWTH-2018-226569

ABISEA Band 112
Wegmann, Raphael
Betriebsstrategien und Potentialbewertung hybrider Batteriespeichersysteme in Elektrofahrzeugen
1. Auflage 2018, 184 S.
DOI: 10.18154/RWTH-2018-228833

ABISEA Band 113
Nordmann, Hannes
Batteriemanagementsysteme unter besonderer Berücksichtigung von Fehlererkennung und Peripherieanalyse
1. Aufl. 2018, 222 S.
DOI: 10.18154/RWTH-2018-228763

ABISEA Band 114
Engelmann, Georges
Reducing Device Stress and Switching Losses Using Active Gate Drivers and Improved Switching Cell Design
1. Aufl. 2018, 195 S.
DOI: 10.18154/RWTH-2018-228973

ABISEA Band 115
Klein-Heßling, Annegret
Active DC-Power Filters for Switched Reluctance Drives during Single-Pulse Operation
1. Aufl. 2018, 166 S.
DOI: 10.18154/RWTH-2018-231030

ABISEA Band 116
Burkhart, Bernhard
Switched Reluctance Generator for Range Extender Applications - Design, Control and Evaluation
1. Aufl. 2018, 194 S.
DOI: 10.18154/RWTH-2019-00025

ABISEA Band 117
Biskoping, Matthias
Discrete Modeling and Control of a versatile Power Electronic Test Bench with Special Focus on Central Photovoltaic Inverter Testing
1. Aufl. 2018, 236 S.
DOI: 10.18154/RWTH-2019-03346

ABISEA Band 118
Schubert, Michael
High-Precision Torque Control of Inverter-Fed Induction Machines with Instantaneous Phase Voltage Sensing
1. Aufl. 2019, 221 S.
DOI: 10.18154/RWTH-2018-231364

ABISEA Band 119
Van der Broeck, Christoph
Methodology for Thermal Modeling, Monitoring and Control of Power Electronic Modules
1. Aufl. 2019, 290 S.
DOI: 10.18154/RWTH-2019-01370

ABISEA Band 120
Hust, Friedrich Emanuel
Physico-chemically motivated parameterization and modelling of real-time capable lithium-ion battery models – a case study on the Tesla Model S battery
1. Aufl. 2019, 203 S.
DOI: 10.18154/RWTH-2019-00249

ABISEA Band 121
Ralev, Iliya
Accurate Torque Control of Position Sensorless Switched Reluctance Drives
1. Aufl. 2019, 154 S.
DOI: 10.18154/RWTH-2019-03071

ABISEA Band 122
Ayeng'o, Sarah Paul
Optimization of number of PV cells connected in series for a direct-coupled PV system with lead-acid and lithium-ion batteries
1. Aufl. 2019, 114 S.
DOI: 10.18154/RWTH-2019-01843

ABISEA Band 123
Koschik, Stefan Andreas
Permanenterregte Synchronmaschinen mit verteilter Einzelzahnsteuerung - Regelkonzepte und Betriebsstrategien für hochintegrierte Antriebssysteme
1. Aufl. 2019, 158 S.
DOI: 10.18154/RWTH-2019-03446

ABISEA Band 124
Farmann, Alexander
A comparative study of reduced-order equivalent circuit models for state-of-available-power prediction of lithium-ion batteries in electric vehicles
1. Aufl. 2019, 214 S.
DOI: 10.18154/RWTH-2019-04700

ABISEA Band 125
Mareev, Ivan
Analyse und Bewertung von batteriegetriebenen, oberleitungsversorgten und brennstoffzellengetriebenen Lastkraftwagen für den Einsatz im Güterfernverkehr in Deutschland
1. Aufl. 2019, 158 S.
DOI: 10.18154/RWTH-2019-04698

ABISEA Band 126
Qi, Fang
Online Model-predictive Thermal Management of Inverter-fed Electrical Machines
1. Aufl. 2019, 154 S.
DOI: 10.18154/RWTH-2019-08304

ABISEA Band 127
Kairies, Kai-Philipp
Auswirkungen dezentraler Solarstromspeicher auf Netzbetreiber und Energieversorger
1. Aufl. 2019, 140 S.
DOI: 10.18154/RWTH-2019-06706

ABISEA Band 128
Fleischer, Michael
Traction control for Railway Vehicles
1. Aufl. 2019, 162 S.
DOI: 10.18154/RWTH-2019-10570

ABISEA Band 129
Teuber, Moritz
Lifetime Assessment and Degradation Mechanisms in Electric Double-Layer Capacitors
1. Aufl. 2019, 150 S.
DOI: 10.18154/RWTH-2019-10071

ABISEA Band 130
Bußar, Christian
Investigation of Optimal Transformation Pathways towards 2050 for the Successful Implementation of a Sustainable Reduction of Carbon Emissions from Power Generation
1. Aufl. 2019, 204 S.
DOI: 10.18154/RWTH-2019-09975

ABISEA Band 131
Wienhausen, Arne Hendrik
High Integration of Power Electronic Converters enabled by 3D Printing
1. Aufl. 2019, 146 S.
DOI: 10.18154/RWTH-2019-08746

ABISEA Band 132
Kwiecien, Monika
Electrochemical Impedance Spectroscopy on Lead-Acid Cells during Aging
1. Aufl. 2019, 138 S.
DOI: 10.18154/RWTH-2019-09480

ABISEA Band 133
Titiz, Furkan Kaan
A Three-phase Low-voltage Grid-connected Current Source Inverter
1. Aufl. 2019, 128 S.
DOI: 10.18154/RWTH-2020-00458

ABISEA Band 134
Wünsch, Martin
Separation der Kathoden-alterung in Lithium-Ionen-Batteriezellen mittels elektrochemischer Impedanzspektroskopie
1. Aufl. 2019, 177 S.
DOI: 10.18154/RWTH-2019-11017

ABISEA Band 135
Badeda, Julia
Modeling and Steering of Multi-Use Operation with Uninterruptible Power Supply Systems - utilizing the example of lead-acid batteries
1. Aufl. 2020, 282 S.
DOI: 10.18154/RWTH-2020-05456

ABISEA Band 136
Kleinsteinberg, Björn
Energy Efficiency Increase of a Vanadium Redox Flow Battery with a Power-Based Model
1. Aufl. 2020, 163 S.
DOI: 10.18154/RWTH-2020-06092

ABISEA Band 137
Cai, Zhuang
Optimization of dimension and operation strategy for a wind-battery energy system in German electricity market under consideration of battery ageing process
1. Aufl. 2020, 144 S.
DOI: 10.18154/RWTH-2020-06525

ABISEA Band 138
Sabet, Pouyan Shafiei
Analysis of Predominant Processes in Electrochemical Impedance Spectra and Investigation of Aging Processes of Lithium-Ion Batteries with Layered Oxide Cathodes and Graphitic Anodes
1. Aufl. 2020, 136 S.
DOI: 10.18154/RWTH-2020-07683

ABISEA Band 139
Angenendt, Georg
Operation, Optimization and Additional Market Participation of Households with PV Battery Storage System and Power-to-Heat Application
1. Aufl. 2020, 221 S.
DOI: 10.18154/RWTH-2020-05200

ABISEA Band 140
Oberdieck, Karl Friedrich
Measurement and Mitigation of Electromagnetic Emissions of Propulsion Inverters for Electric Vehicles
1. Aufl. 2020, 181 S.
DOI: 10.18154/RWTH-2020-09215

ABISEA Band 141
Bubert, Andreas Martin
Optimierung des elektrischen Antriebsstrangs von Elektrofahrzeugen mit Betrachtung parasitärer Ströme innerhalb der elektrischen Maschine
1. Aufl. 2020, 215 S.
DOI: 10.18154/RWTH-2020-09556

ABISEA Band 142
Fleischer, Christian Georg
Model-Driven Software Development and Verification Solutions for Safety Critical Battery Management Systems
1. Aufl. 2021, 356 S.
DOI: 10.18154/RWTH-2021-00436

ABISEA Band 143
Arzberger, Arno
Thermografische Methoden zur zerstörungsfreien Messung der anisotropen Wärmeleitfähigkeit von Lithium-Ionen Zellen
1. Aufl. 2020, 131 S.
DOI: 10.18154/RWTH-2021-00479

ABISEA Band 144
Lange, Tobias
Oberwellenbasierte Modellierung, Regelung und Auslegung von Permanentmagnet- und Reluktanz-Synchronmaschinen
1. Aufl. 2020, S.
DOI: 10.18154/RWTH-2021-

ABISEA Band 145
Weiss, Claude
Fault Tolerant Switched Reluctance Machines with Distributed Inverters – Modeling and Control
1. Aufl. 2020, S.
DOI: 10.18154/RWTH-2021-

ABISEA Band 146
Huck, Moritz
Modelling the Transient Behaviour of Lead-Acid Batteries: Electrochemical Impedance of Adsorbed Species
1. Aufl. 2020, 151 S.
DOI: 10.18154/RWTH-2020-08362

ABISEA Band 147
Willenberg, Lisa
Volumenausdehnung und ihre Auswirkungen auf die Alterung einer zylindrischen Lithium-Ionen-Batterie
1. Aufl. 2020, S.
DOI: 10.18154/RWTH-2021-

ABISEA Band 148
Rogge, Matthias
Electrification of Public Transport Bus Fleets with Battery Electric Busses
1. Aufl. 2020, 161 S.
DOI: 10.18154/RWTH-2021-02146

ABISEA Band 149
Münderlein, Jeanette
Numerische Methodik zur Auslegung eines Hybriden Speichersystems mit Multinutzen“
1. Aufl. 2020, 221 S.
DOI: 10.18154/RWTH-2021-00867

ABISEA Band 150
Merten, Michael
Participation of Battery Storage Systems in the Secondary Control Reserve Market
1. Aufl. 2020, 187 S.
DOI: 10.18154/RWTH-2021-01029

ABISEA Band 151
Ge, Lefei
Performance Enhancement of Switched Reluctance Machines for High-speed Back-up Generators
1. Aufl. 2020, 152 S.
DOI: 10.18154/RWTH-2020-11546

ABISEA Band 152
Neubert, Markus
Modeling, Synthesis and Operation of Multiport-Active Bridge Converters
1. Aufl. 2020, 227 S.
DOI: 10.18154/RWTH-2020-10814

ABISEA Band 153
Schülting, Philipp
Optimierte Auslegung von hochintegrierten und bidirektionalen Onboard GaN-Ladegeräten
1. Aufl. 2020, 158 S.
DOI: 10.18154/RWTH-2020-09771

ABISEA Band 154
Sewergin, Alexander
Design Challenges and Solutions for the Practical Application of SiC Power Moduls – Exemplified by an Automotive DC-DC Converter. 1. Aufl. 2021, 154 S.
DOI: 10.18154/RWTH-2021-04498

ABISEA Band 155
Stippich, Alexander
Exploiting the Full Potential of Silicon Carbide Devices via Optimized Highly Integrated Power Modules
1. Aufl. 2021, 188 S.
DOI: 10.18154/RWTH-2021-08122

ABISEA Band 156
Gottschlich, Jan
Hilfsspannungsversorgungskonzepte für Mittelspannungs-DC/DC-Wandler
1. Aufl. 2021, S.
DOI: 10.18154/RWTH-2021-

ABISEA Band 157
Hollstegge, Philipp
Injektion raumzeigerzerlegter Stromharmonischer zur Minderung tonaler Geräuschanteile in asymmetrisch sechsphasigen Permanentmagnetsynchronmaschinen
1. Aufl. 2021, S.
DOI: 10.18154/RWTH-2021-

ABISEA Band 158
Grau, Vivien
Development of a Test Bench to Investigate the Impact of Steep Voltage Slopes on the Lifetime of Insulation Systems for Coil Windings
1. Aufl. 2021, S.
DOI: 10.18154/RWTH-2021-

ABISEA Band 159
Ringbeck, Florian
Optimized Charging of Lithium-Ion Batteries with Physico-Chemical Models
1. Aufl. 2021, S.
DOI: 10.18154/RWTH-2021-

Partial electrification of vehicles with conventional combustion engines is an effective method to enhance efficiency and reduce CO2 emissions. One way of adding a so-called mild hybridization to existing vehicle architectures is to extend the conventional 12 V vehicle electrical system by a 48 V voltage level that contains a 48 V lithium-ion battery.

A promising anode material for such a battery is lithium titanate oxide (LTO), which possesses several outstanding material properties including high-power capability, inherent safety and excellent lifetime performance. Extensive scientific studies on mass-produced LTO-based cells are rare, resulting in a lack of essential information on performance and aging behavior of LTO-based cells.

Based on characteristic 48 V battery operating conditions this thesis addresses this knowledge gap. It assesses the suitability of an LTO-based cell type for low voltage vehicle systems by reporting essential performance and aging characteristics.

The investigated LTO-based cells show excellent power capability and cycle stability, even at high ambient temperatures and high current rates, and meet the vehicle relevant lifetime requirements of 200,000 km. The calendar aging behavior is strongly dependent on temperature and state of charge. This can be attributed to both reversible capacity effects caused by an overhang of the electrodes as well as irreversible aging mechanisms such as (passivating) surface layer formation and gas formation.

ISSN 1437-675X